UNIVERSIDADE D
COIMBRA

Adriana Filipa da Silva Fontes

MUSHROOM-ENRICHED DIETS TO AMELIORATE MITOCHONDRIAL DYSFUNCTION IN WILSON DISEASE

Tese no âmbito do Doutoramento em Biociências, ramo de especialização em Bioquímica, orientada pela Professora Doutora Anabela Marisa Azul, Professor Doutor João Ramalho-Santos e Professor Doutor Hans Zischka, e apresentada ao Departamento de Ciências da Vida, Faculdade de Ciências e Tecnologia da Universidade de Coimbra

Janeiro de 2023

Departamento de Ciências da Vida,

Faculdade de Ciências e Tecnologia da

Universidade de Coimbra

MUSHROOM-ENRICHED DIETS TO AMELIORATE MITOCHONDRIAL DYSFUNCTION IN WILSON DISEASE

Adriana Filipa da Silva Fontes

Tese no âmbito do Doutoramento em Biociências, ramo de especialização em Bioquímica, orientada pela Professora Doutora Anabela Marisa Azul, Professor Doutor João Ramalho-Santos e Professor Doutor Hans Zischka, e apresentada ao Departamento de Ciências da Vida, Faculdade de Ciências e Tecnologia da Universidade de Coimbra

Janeiro de 2023

UNIVERSIDADE D
COIMBRA

This doctoral thesis was hosted at the Centre for Neuroscience and Cell Biology, University of Coimbra, Portugal; and at both Institute of Molecular Toxicology and Pharmacology (TOXI), Helmholtz Centre Munich, German Research Centre for Environmental Health (HMGU) and Institute for Toxicology and Environmental Hygiene, Technical University of Munich (TUM), Munich, Germany, as part of the individual research project entitled "Mushroom-enriched diets for Non-alcoholic fatty liver disease (NAFLD)", under the European Training Network "Bioenergetic Remodelling in the Pathophysiology and Treatment of Non-Alcoholic Fatty Liver Disease (NAFLD)" (Foie Gras, ID 722619), that received funding from the Marie Sklodowska-Curie Actions program in the European Union's Horizon 2020, and the Helmholtz Centre Munich, German Research Centre for Environmental Health (HMGU). This thesis was also funded as a PhD research studentship from the Portuguese public agency Fundação para a Ciência e Tecnologia (FCT) entitled "*A bio-nutritive strategy against transition metal toxicity*" (SFRH/BD/05623/202).

HELMHOLTZ MUNICH

CENTER FOR NEUROSCIENCE
AND CELL BIOLOGY
UNIVERSITY OF COIMBRA
PORTUGAL

FoieGras
European Training Network | H2020-MSCA

Fundação
para a Ciência
e a Tecnologia

REPÚBLICA
PORTUGUESA
CIÊNCIA, TECNOLOGIA
E ENSINO SUPERIOR

Publications

Inês C. M. Simões, **Adriana Fontes**, Paolo Pinton, Hans Zischka, Mariusz R. Wieckowski, "Mitochondria in non-alcoholic fatty liver disease", *The International Journal of Biochemistry & Cell Biology*, Volume 95, 2018:93-99, ISSN 1357-2725.
Available at https://www.sciencedirect.com/science/article/pii/S1357272517303321

Adriana Fontes, Mireia Alemany-Pagès, Paulo J. Oliveira, João Ramalho-Santos, Hans Zischka, Anabela Marisa Azul, "Antioxidant Versus Pro Apoptotic Effects of Mushroom-Enriched Diets on Mitochondria in Liver Disease", *International Journal of Molecular Sciences*, Volume 20 (16), 2019, 3987.
Available at https://www.mdpi.com/1422-0067/20/16/3987

Yaschar Kabiri, Christine von Toerne, **Adriana Fontes**, Percy A. Knolle, Hans Zischka. "Isolation and Purification of Mitochondria from Cell Culture for Proteomic Analyses", In: *Methods in Molecular Biology*, 2021, 2261:411-419.
Available at https://doi.org/10.1007/978-1-0716-1186-9_25

Adriana Fontes, João Ramalho-Santos, Hans Zischka, Anabela Marisa Azul, "Mushrooms on the plate: Trends towards NAFLD treatment, health improvement and sustainable diets", *European Journal of Clinical Investigation*. 2022;52(3):e13667.
Available at https://onlinelibrary.wiley.com/doi/10.1111/eci.13667

"Intestinal integrity impairment in Wilson disease"
Adriana Fontes, Hannah Pierson, Carola Eberhagen, Jennifer Kinschel, Tamara Rieder, Andree Zibert, Christine von Toerne, Bernhard Michalke, Hartmut H. Schmidt, João Ramalho-Santos, Anabela Marisa Azul, Svetlana Lutsenko and Hans Zischka.
Article in preparation

Author’s declaration

The author states to have afforded a major contribution to the conceptual design, technical execution, interpretation of the results and manuscript preparation of the work included in this thesis.

Acknowledgements

Agradecimentos

Esta secção será predominantemente escrita na minha língua materna, o português, mas também em inglês, para que todos os visados neste agradecimento possam desfrutar do mesmo, da melhor forma possível.

O termo Ph.D. é uma abreviação que provem do latim *Philosophiae doctor*, em que *Philo* significa amigo ou amante, e *sophiae* significa sabedoria. O amor pelo conhecimento é a base de todo aquele que escolhe este percurso, que escolhe ser *Doctor of Philosophy*.

Considero que o meu percurso não foi de todo comum, ou simples, mas sem dúvida que fez jus ao sentido da sigla. Antes de iniciar esta jornada tive o privilégio de ensinar Ciência aos mais pequenos, que todos os dias vibram com a aprendizagem e descoberta de novas coisas. Foi aí que percebi que ser cientista é como ser criança, em que cada novo dia é uma oportunidade de conhecimento, de acrescentar algo que no dia anterior não existia....

E com essa determinação decidi embarcar nesta aventura. Ninguém disse que ia ser fácil. Muitos dias foram difíceis, muitos dias vinha a questão: Será que consigo? Mas para cada problema, veio sempre uma solução. Se ficou mais fácil? Não. Mas fiquei eu, mais forte.

E uma boa parte dessa força veio também daqueles com quem partilhei esta jornada, porque um doutoramento não é um processo solitário, mas sim de comunhão e partilha. E assim, quero endereçar um agradecimento especial às pessoas e instituições sem as quais este trabalho não teria sido possível:

Ao Consortium FOIE GRAS e a todas as pessoas nele envolvidas. Um agradecimento especial ao Doutor Paulo Oliveira pela condução deste projeto. Obrigado por ter acreditado em nós, jovens cientistas. Agradecer também aos Project Managers, Liljana e Daniel, cujo trabalho foi indispensável e por vezes ingrato.

À Fundação para a Ciência e Tecnologia, pelo suporte financeiro concedido durante dois anos através de uma bolsa de Doutoramento (SFRH/BD/05623/202), que me permitiu finalizar esta etapa importante da minha vida.

Aos meus orientadores, pelo papel preponderante que tiveram durante todo o meu doutoramento, quer a nível a científico, quer a nível pessoal:

To my supervisors, for the preponderant role they played throughout my doctorate, for supporting my growth as a scientist and as a person:

To Doctor Hans Zischka, thank you for introducing a whole new scientific world to this young colleague. Since day one, there were never problems, only solutions. The enthusiasm was contagious, and even when I thought the week, or month, have been bad, you always had something positive to say. Thank you for the partnership in this crazy idea with mushrooms, for letting me be creative and explore new ideas, for letting me "hit a couple of scientific walls" and giving me the tools to open a hole in it and see the light again. Thank you for always being an inspiration, for the long scientific discussions, for telling me when things were completely wrong and, at the same time, defending my work. Thank you for believing in me.

À Doutora Anabela Marisa Azul, obrigada pelo desafio que me lançou em 2017. Desafio esse que foi muito mais além do que tinha imaginado. Obrigada por todo o conhecimento científico transmitido, pelas horas de discussão de resultados, pela partilha de ideias, pela paciência na leitura e correção, pelo espaço concedido para errar e melhorar, pela abertura a novos conceitos e novas possibilidades de fazer ciência. Obrigada pela parceria em todo o trabalho desenvolvido com os cogumelos, em que foram longas as horas a recolher corpos frutíferos, limpar micélios e liofilizar....Obrigada pela disponibilidade, entusiasmo e dedicação a este projeto. Obrigada pelo espírito crítico e inconformado, por ver a ciência como uma forma de alcançar o bem comum e não o bem individual, pela confiança e amizade.

Ao Doutor João Ramalho-Santos, obrigado pelo apoio incondicional a este projeto, por alinhar connosco nesta "loucura saudável" e acreditar que, a 2303 km de distância, alguém está a trabalhar para trazer algo de valor à comunidade científica. Obrigado pela transmissão de conhecimento, pela disponibilidade e pela partilha. Obrigado pelo exemplo de integridade, trabalho e dedicação à ciência que é para mim uma inspiração diária. Obrigado por quebrar barreiras e estereótipos, e lutar por um futuro melhor na investigação. É nesse futuro que quero continuar a minha carreira científica.

Aos meus colegas foiegrinos: Inês Simões, Sara, Inês Mateus, Getachew, Gabriella, Bárbara, Emilio, Tawhidul, Rui, Jelena, Harshita, Mireia, Raquel e Sravan, obrigada por todos

os momentos que passámos juntos e nos apoiámos mutuamente! Mireia e Inês Mateus, um obrigado especial pela partilha de conhecimento e amizade.

A todo o grupo MitoXT - Mitochondrial Toxicology and Experimental Therapeutics Laboratory, no UC-Biotech em Cantanhede, em especial ao Doutor José Teixeira, que foi o meu grande apoio durante os oito meses de trabalho desenvolvido no laboratório. Agradeço o tempo disponibilizado para me introduzir ao trabalho prático, discutir resultados, pensar em novas experiências e corrigir relatórios. Agradeço ainda a quem trabalhou mais diretamente comigo, ao Ricardo Amorim, à Caroline Veloso, à Susana Pereira, à Cláudia Deus e à Luciana Ferreira, pela boa disposição, criatividade, contínuo apoio no laboratório e input científico.

Às pessoas que concordaram em fazer parte desta aventura com os cogumelos, ao Rui Coelho e ao Bruno Belchior, obrigado pela disponibilidade, interesse e simpatia que demonstraram durante todo o trabalho que fizemos juntos.

To my colleagues at the AG Zischka, thank you for welcoming a strange Portuguese girl into the group. It is never easy to start a new job and a new life away from home, but finding good people along the way makes it easier. To Carola, thank you for the kindness and patience, for always being present and available to help with anything. Thank you for the hard work and for taking care of all of us. To Yaschar, thank you for the long hours of scientific teaching and discussion, for guiding me through the do's and don'ts. For being a beacon of light in some dark moments and for all the fun we had in the lab, despite the daily struggle. For the coffee breaks, for the lunch breaks, for having such a big heart. Thank you for the friendship. To Judith Nagel, thank you for the knowledge exchange and the scientific discussions, for the trust, for the inspiration, for the friendship and for being a pillar in the group. To Judith Sailer, thank you for your positivity, your selfness, your availability to work and improve, for always be there to help with anything, for the inspiration and for the friendship. To Banu, thank you for all the hard work, the commitment to group, for always striving to improve, even the little things, for the companionship. To Quirin and Tamara, thank you for all the support in the laboratory. Without you, it would be impossible to accomplish all the work.

To the former members, Sabine Borchard, Sabine Schmitt and Claudia, thank you for laying the foundations and giving me the scientific knowledge that would allow the development of a big part of this work.

À Ana Carvalho, por ser para mim um exemplo de força, dedicação, e trabalho. Por fazer parecer que nada é impossível e que se sonharmos conseguimos alcançar aquilo que

desejamos. Pelo apoio e incentivo que me deu para me lançar nesta viagem de fazer um doutoramento. Obrigada pela amizade.

À Soraia e à Diana, duas irmãs que a vida me deu. Quero agradecer por toda a amizade, por estarem sempre presentes nos bons e maus momentos, pelas palavras amigas e de conforto. Por nunca desistirem de mim, mesmo estando longe.

Aos meus pais e avós, quero agradecer todo o carinho, apoio e entusiasmo com que acompanharam esta minha etapa. Sem vocês, nada disto seria possível. Vocês são a minha base de vida, o meu porto de abrigo e o exemplo que sigo para todos os dias dar o melhor de mim.

Ao meu marido Aléxis, que aceitou este desafio e se mudou para Munique comigo. Começámos namorados, ficámos noivos e este ano casámos. Quero agradecer o teu apoio incondicional, a tua capacidade para me animares em dias menos bons, por compreenderes este meu gosto pela ciência e sentires orgulho no meu trabalho. Obrigada pela pessoa que és, e por nunca me teres faltado. Sem ti, tudo teria sido muito mais difícil.

À Josie, pela companhia e suporte emocional na reta final da escrita da tese.

A todos aqueles que sempre me encorajaram ao longo deste caminho, que me ajudaram a melhorar com as suas críticas, sugestões, ideias, ou simplesmente com uma palavra amiga.

A todos, o meu mais sincero obrigado

To all of you, my deepest thank you

Dedico esta tese aos meus pais,

Por todo o apoio e incentivo que me deram desde o início,

e por todos os sacríficos que a mesma implicou.

Ao Aléxis, por todos os momentos menos bons

E pela capacidade de os ultrapassarmos juntos

“Never put your work down

Others will do that for you”

Hans Zischka

Index

List of figures

List of tables

Abbreviations

ALT	Alanine aminotransferase
AST	Aspartate aminotransferase
ANOVA	Analysis of variance
ATOX1	Antioxidant copper chaperone 1
ATP7A	Adenosinetriphosphatase copper transporting alpha
ATP7B	Adenosinetriphosphatase copper transporting beta
BBB	Blood brain barrier
Bili	Bilirubin
BSA	Bovine serum albumin
C_{cl}	Capacitance
CCO	Cytochrome c oxidase
Cp	Ceruloplasmin
CCS	Copper chaperone for superoxide dismutase 1
CTR1/2	High affinity copper transporter 1/2
Cu	Copper
DPA	D-Penicillamine
EB	Erythrosine B
ECAR	Extracellular acidification rate
Fe	Iron
FFA	Free fatty acids
GI/GIT	Gastrointestinal tract
GSH	Glutathione
HCC	Hepatocellular carcinoma
HCD	High-caloric diet
H&E	Hematoxylin and Eosin
IEC	Intestinal epithelial cells
LEC	Long-Evans Cinnamon
M-Ctrl(PO)	*Pleurotus ostreatus* mycelium protein extract control
MB	Methanobactin

MT	Metallothioneins
MS	Mass spectrometry
NAFLD	Non-alcoholic fatty liver disease
NASH	Non-alcoholic steatohepatitis
OCR	Oxygen consumption rate
OXPHOS	Oxidative phosphorylation
PAS	Periodic acid-Schiff
PET	Polyethylene terephthalate
ZM(PO)	*Pleurotus ostreatus* zinc-enriched mycelium protein extract
Zn	*Zinc*
PVDF-membrane	Polyvinylidene fluoride-membrane
ROS	Reactive oxygen species
Se	Selenium
SOD1	Cu/Zn superoxide dismutase
TAGs	Triacylglycerol
TEER	Transepithelial electrical resistance
TG	Triglyceride
TGN	Trans-Golgi network
TJ	Tight-junction
TTM	Tetrathiomolybdate
WD	Wilson disease
Zn	Zinc
ZO-1/TJP1	Zona-occludens 1/Tight-junction protein 1

Abstract

The role played by copper is a topic of research with new evidence pointing to alterations in lipid metabolism and protein-linked damage that ultimately can lead to cell death (cuproptosis) upon copper misbalance. In Wilson disease (WD), impaired hepatic copper excretion, due to mutations in the copper-transporting ATPase ATP7B, causes mitochondrial alterations and steatosis, shared features with the metabolic disorder non-alcoholic fatty liver disease (NAFLD). At the present, zinc salts is considered an effective treatment in patients with WD, however, it has a very strict treatment regimen with gastrointestinal (GIT) side effects being associated to gastritis, erosions and ulcers.

With this in mind, the present work details the development of a new dietary "bio-zinc" approach to potentially improve the therapeutic outcome in the WD condition. This nutritional therapy based on a zinc-enriched mushroom has the premise that, on one hand, mushrooms are recognized as a healthy food, with bioactive compounds that can be hepatoprotective and have beneficial effects in the gut-liver axis and, on the other hand, with the zinc enrichment, they have the potential to directly bind copper in the diet and/or promote copper retention in the enterocytes via metallothionein upregulation, with less GIT irritation.

Edible and medicinal mushrooms have long been consumed as food or as a dietary supplement, and have proven health beneficial effects in several metabolic conditions, from type 2 diabetes mellitus, to obesity, hyperlipidemia, hypertension and cancer. Moreover, the capacity of mushrooms to sequestrate and accumulate metals, namely copper and zinc, is also becoming well documented. Thus, the consumption of a zinc-enriched mushroom would provide a metal exchange in the GIT, decreasing copper absorption.

Yet, whereas the hepatic phenotype is well known in WD, the ATP7B malfunction, copper accumulation and its phenotypical consequences in the intestine have been largely overlooked. Therefore, to better understand the putative benefits of a zinc-enriched mushroom therapy, it also implies a better understanding of the intestinal pathology in WD. This brought two scientific open questions: 1) Can a zinc-enriched mushroom diet be beneficial as a therapy in a copper-linked toxicity scenario, more precisely in WD?, and 2) What are the intestinal pathophysiologic alterations associated with the mutation in the copper transporter ATP7B?

Thus, this work aimed to evaluate intestinal copper levels, mitochondria structure and functional alterations, together with potential proteome changes in two WD models; to select

a mushroom species that could be efficient sequestering zinc; to develop a zinc-enriched mushroom and, to study the beneficial effects of a mushroom-enriched diet in the WD condition.

The results in WD animals (LPP rats, which are *Atp7b*$^{-/-}$), with emphasis on its intestinal phenotype, and in the human cell line Caco-2, with its correspondent ATP7B Knockout (KO), were structural changes in mitochondria without a significant increase in copper content, changes/alterations in the expression of proteins related to mitochondria function, energy metabolism and lipid processing, and decreased intestinal barrier tightness. In the ATP7B KO cellular model, mitochondrial function and barrier integrity were improved upon treatment with the high affinity copper chelator Methanobactin (MB).

From an initial set of seven edible and/or medicinal species: *Agaricus bisporus*, *Boletus edulis*, *Cantharellus cibarius*, *Ganoderma lucidum*, *Lentinula edodes*, *Macrolepiota procera* and *Pleurotus ostreatus*, the aqueous extract of the species *Pleurotus ostreatus* presented a promising clear-cut protective effect in an *in vitro* model for hepatic lipotoxicity, promoting an increase in cellular metabolic activity and ATP content, with a decreased cellular lipid accumulation. This species was therefore selected for the development of a zinc-enriched mushroom, which involved an extensive protocol optimization, either for the production and validation of the enrichment, with a significant increase of zinc observed in the mycelium, but not in the fruiting bodies. The evaluation of the protective effects of the diet showed that the zinc-enriched mycelium protein extract was protective against copper toxicity in Caco-2 cells, with a positive effect in barrier integrity and metallothionein expression. Additionally, in LPP rats, a short feeding study demonstrated that this nutritional “bio-zinc” approach can change metal values (zinc and copper) in the upper intestine of these animals, together with a potential increase in zinc uptake.

In conclusion, a reduced ATP7B expression in the intestine was shown to induce mitochondrial dysfunction and increased barrier leakiness, without a significant increase in copper levels. These alterations were first described here, showing that, in contrast with the hepatic phenotype in WD, damage to the intestine is not paralleled with copper overload. The promising results observed in the cells after treatment with the “bio-zinc” protein extract, as well as the modulation of metal levels in the intestine after the feeding of LPP rats with the mushroom-enriched diet, prospect exciting alternatives for a new nutritional “bio-zinc” treatment aiming to improve the life quality of patients with Wilson disease but also other metal-related pathologies.

Keywords: Wilson disease, copper, intestine, mitochondrion, steatosis, zinc, mushroom

Resumo

O papel desempenhado pelo cobre é um tema de investigação com novas evidências científicas a apontarem para alterações no metabolismo dos lípidos e interações com proteínas, impactando na sua função e/ou estrutura, o que pode conduzir à morte celular (cuproptose) pelo desequilíbrio nos níveis de cobre. Na doença de Wilson (DW), a excreção hepática do cobre é reduzida devido a mutações no transportador de cobre ATPase ATP7B, o que se traduz em alterações mitocondriais e esteatose, características partilhadas com distúrbios metabólicos como é o caso da doença do fígado gordo não-alcoólico (FIGNA). Os tratamentos aprovados atualmente para a DW, especialmente os sais de zinco, têm um regime de tratamento muito rigoroso e causam frequentemente problemas gastrointestinais tais como gastrite, erosões e úlceras.

Assim sendo, neste projeto de investigação foi desenvolvida uma nova abordagem nutritiva, baseada num cogumelo enriquecido em zinco, "bio-zinco", com o objetivo de criar uma terapia alternativa para ajudar no tratamento de doentes com DW.

Esta terapia de base nutricional assenta na premissa de que, por um lado, os cogumelos têm vindo a ser reconhecidos como um alimento saudável e que contem compostos bioativos hepatoprotetores e com potencial terapêutico no eixo intestino-fígado e, por outro lado, com o enriquecimento em zinco, poderão diminuir a absorção do cobre no trato gastrointestinal, quer ligando diretamente o metal no lúmen e promovendo a sua excreção através das fezes, quer imitando o mecanismo promovido pelos sais de zinco, de uma forma menos pro-inflamatória.

O consumo de espécies de cogumelos comestíveis e/ou medicinais como alimento ou suplemento é uma prática comum desde à vários séculos, e os seus efeitos benéficos para a saúde já foram comprovados em doenças como a diabetes mellitus tipo 2, obesidade, colesterol elevado, hipertensão e cancro. Além disso, a capacidade dos cogumelos para sequestrar e acumular metais, nomeadamente cobre e zinco, está também a ser documentada. Desta forma, o "bio-zinco" representa uma opção terapêutica que ajudaria a reduzir a absorção de cobre a nível intestinal. Contudo, enquanto o fenótipo hepático seja bem conhecido na DW, a disfunção do transportador ATP7B, a acumulação de cobre, e as consequências fenotípicas no intestino têm sido largamente negligenciadas. Assim sendo, de forma a compreender melhor as implicações de uma dieta com cogumelo enriquecido em zinco num cenário de DW, a investigação do fenótipo intestinal tornou-se imperativa neste trabalho de investigação. Neste contexto, duas questões científicas foram definidas: 1) Se o

cogumelo enriquecido com zinco é benéfico como terapia num cenário de toxicidade ligada ao cobre, mais precisamente na DW, e 2) Quais são as alterações fisiopatológicas no intestino associadas à mutação no transportador de cobre ATP7B.

No seguimento das questões, este trabalho de investigação teve como objetivos avaliar os níveis intestinais de cobre, a estrutura e função mitocondrial, juntamente com potenciais alterações do proteoma em dois modelos de DW; selecionar uma espécie de cogumelo que pudesse ser eficiente na captura do zinco; desenvolver um cogumelo enriquecido com zinco, e por último estudar os seus efeitos benéficos como uma dieta enriquecida na condição de DW.

Os resultados no modelo animal para a DW (ratos LPP, *Atp7b*$^{-/-}$), com ênfase no seu fenótipo intestinal, e na linha celular humana Caco-2, e a sua correspondente linha celular mutada para a proteína ATP7B (ATP7B KO), foram alterações estruturais nas mitocôndrias, sem um aumento significativo do teor de cobre, alterações na expressão de proteínas relacionadas com a função das mitocôndrias, metabolismo energético e processamento lipídico, e diminuição da permeabilidade da barreira intestinal. No modelo celular ATP7B KO, a função mitocondrial e a integridade da barreira foram melhoradas após tratamento com o quelante de cobre Metanobactina (MB).

De um conjunto inicial de sete espécies de cogumelos comestíveis e/ou medicinais: *Agaricus bisporus*, *Boletus edulis*, *Cantharellus cibarius*, *Ganoderma lucidum*, *Lentinula edodes*, *Macrolepiota procera* e *Pleurotus ostreatus*, o extrato aquoso do *Pleurotus ostreatus* foi o que demonstrou efeitos protetores contra a lipotoxicidade hepática *in vitro*, promovendo um aumento da atividade metabólica celular e do conteúdo em ATP, assim como uma diminuição da acumulação intracelular de ácidos gordos. Esta espécie foi selecionada para o desenvolvimento de um cogumelo enriquecido com zinco, o que implicou uma extensa otimização protocolar, quer para a produção, quer para a validação do enriquecimento, observando-se um aumento significativo de zinco no micélio, mas não no corpo frutífero. A avaliação dos efeitos benéficos da dieta demonstrou que o extrato proteico do micélio enriquecido com zinco foi protetor contra a toxicidade do cobre nas Caco-2, com efeitos positivos na integridade da barreira, e na expressão da proteína metalotioneína. Adicionalmente, num primeiro estudo em que os ratos LPP foram alimentados com o "bio-zinco", observou-se alterações nos níveis de metais (zinco e cobre), no intestino superior, e um potencial aumento na absorção de zinco.

Em conclusão, a expressão reduzida do transportador de cobre ATP7B no intestino resulta em disfunção mitocondrial e aumento da permeabilidade da barreira intestinal, sem um aumento

significativo do nível de cobre. Estas alterações foram primeiro descritas neste trabalho de investigação, demostrando que, em contraste com o fenótipo hepático na DW, os danos no intestino não são paralelos à sobrecarga de cobre nas células. Os resultados promissores observados nas células após o tratamento com o extrato proteico do "bio-zinco", assim como as indicações da modulação dos níveis de metais no intestino após a alimentação de ratos LPP com o micélio enriquecido com zinco, reforçam a importância de desenvolver alternativas nutricionais, como o "bio-zinco", por forma a melhorar a qualidade de vida dos doentes com Doença de Wilson, ou outras patologias relacionadas com o desequilíbrio dos níveis de metais.

Palavras-chave: Doença de Wilson, cobre, intestino, mitocôndria, esteatose, zinco, cogumelos

1. Introduction

1.1 **Copper – the friend and the foe**

Copper (Cu) is an essential transition trace element, that serves as a cofactor for several important redox enzymes[1]. Copper is taken up by the diet, with a daily average intake of around 1 mg, and a bioavailability of 65 to 70%[2]. In the body, Cu content can be around 100 mg, mainly distributed amongst the liver (≈10 mg), muscle (≈28 mg) and bone tissue (≈46 mg)[1]. Copper is an essential enzymatic co-factor and approximatly 54 Cu-binding proteins have been identified[3], with the most important/studied cuproenzymes being cytochrome c oxidase (CCO), tyrosinase, dopamine-B-hydroxylase, amine oxidase, lysyl oxidase, Cu/Zn superoxide dismutase (SOD1), hephaestin and ceruloplasmin (Cp). These enzymes are fundamental in different metabolic pathways such as cellular respiration, melanin synthesis, dopamine conversion, oxidoreductase activity and iron metabolism[4]. For this reason, maintaining Cu homeostasis is of outmost importance since, on the one hand, low Cu levels can compromise the activity of these key cellular enzymes and, on the other hand, high Cu levels can be toxic. Copper deficiency is associated with several pathologies such as anemia, neurologic and connective tissue defects, oxidative stress and hypopigmentation[5]. Furthermore, Cu misbalance, meaning either deficiency or excess, is observed in different neurological conditions (Alzheimer's, Parkinson´s, Huntington´s and Amyotrophic Lateral Sclerosis)[6], cardiovascular disease[7], and metabolic syndrome, especially non-alcoholic fatty liver disease (NAFLD)[8-10]. However, the molecular mechanisms behind the relation between Cu and these diseases are not fully understood.

In the realm of Cu-linked genetic inherited disorders, Menkes and Wilson disease (WD) are the most widely study diseases[11]. Both comprise mutations in specific Cu-transporting ATPases: ATP7A in Menkes, and ATP7B in WD, that result in the loss of protein function[12]. In Menkes disease, the lack of ATP7A in placenta, gastrointestinal tract (GIT) and blood-brain barrier (BBB) causes Cu deficiency, leading to premature death, or resulting in growth deficiencies and severe neurodegenerative disease[13]. Conversely, in WD, non-functional ATP7B causes impaired biliary Cu excretion in the liver, with excessive accumulation of Cu in the hepatocytes resulting in cellular necrosis and liver damage, which in turn, may cause Cu to leak and accumulate in other organs (Figure 1), like the brain[12, 14]. In a scenario of dangerous intracellular elevation of Cu levels, metal-responsive proteins, such as glutathione (GSH) and metallothioneins (MT), bind Cu with high affinity (Figure 1)[15, 16], largely avoiding non-bound Cu^{1+} that can be involved in Fenton based reactions (1.$Fe^{3+}/Cu^{2+} + O_2^{\bullet -} \leftrightarrow Fe^{2+}/Cu^{1+} + O_2$; 2.

$Fe^{2+}/Cu^{1+} + H_2O_2 \rightarrow Fe^{3+}/Cu^{2+} + OH^{\bullet} + OH^-$). The cycling between the oxidized state Cu(II) and the reduced state Cu(I) generates hydroxyl radicals ($OH^{\bullet}$) causing damage towards proteins, lipids and nucleic acids in the cells[17-19]. For a long time, oxidative stress was considered as the main mechanism of cellular damage in Cu overload toxicity, as happens in WD. However, decreased activity of antioxidant enzymes, with increased lipid peroxidation and DNA damage were only observed at later stages of the disease, in both WD patients and animal models[20, 21]. Moreover, studies in yeast showed that free Cu concentration is less than 10^{-18} M, which corresponds to less than one free Cu atom per cell, rendering the cellular free Cu pool practically non existent[22]. Therefore, even in Cu stress conditions as occurs in WD, the cellular response capacity towards Cu-related oxidative damage has proven efficient, at least in an early disease state[20]. Thus, excess Cu has been recently linked to its toxic inactivation of essential enzymes, culminating in the recently proposed Cu-driven cell death mechanism, cuproptosis[23].

1.1.1 Copper metabolism – uptake, distribution and excretion

The balance between Cu uptake, distribution and excretion is well accomplished by our body, with two major players involved: the intestine and the liver. Copper is mainly taken up via nutrition as a divalent ion, at the proximal part of the intestine. At the apical site of the enterocytes, Cu is reduced by a specific family of metalloreductases, the STEAP proteins, and afterwards transported by the high affinity Cu transporter 1 (CTR1). Other transporters, like the divalent metal ion transporter (DMT1)[24], or the low-affinity Cu transporter 2 (CTR2), have been suggested to have a role in Cu uptake as well, however, their exact mechanisms remains unclear[25]. For distribution throughout the body, Cu is first delivered via ATP7A from the enterocytes to the blood circulation where it binds to serum proteins, such as macroglobulin and albumin, or amino acids, like histidine[26]. Afterward, it is removed from the blood compartment an enters the liver via the portal vein[27], where again, CTR1 is responsible for Cu uptake into the hepatocytes (Figure 1). Intracellular Cu binding and transfer amongst Cu-dependent proteins is regulated based on a gradient of increasing Cu-binding affinity. Copper-chaperones bind Cu^{1+} and transport them to either cytosolic enzymes, or transporters that deliver Cu to different enzymes in the cellular organelles[28]. For instance, antioxidant protein 1 (ATOX1) is responsible for the transport of Cu to ATP7A and ATP7B in the trans-Golgi network (TGN). There, apo-ceruloplasmin is able to bind up to six Cu atoms per each molecule, turning into holo-ceruloplasmin, that is released into plasma and distributed to other tissues

(Figure 1) [27, 29]. Ceruloplasmin (Cp) is the main Cu distributor to other organs in the body. Also, ATOX1 is responsible for transferring Cu to the nucleus and secretory pathways via ATP7B. The Cu chaperone for SOD1 (CCS), distributes Cu to SOD1 in the cytosol and mitochondria, while a myriad of other different proteins (Cox17, Cox11, Sco1 and Sco2) are responsible for Cu delivery to CCO, in the mitochondria (Figure 1). In a scenario of Cu excess, Cu-ATPases (ATP7A and ATP7B) increase Cu transport to the secretory pathways to be incorporated into cuproenzymes, or translocate from the TGN to the vesicular compartment for Cu sequestration[29-31]. The most efficient route of Cu excretion is via the biliary system, into the GIT lumen[32]. Daily, and under physiological conditions, the bile transports around 0.6-6 mg Cu into the GIT, with saliva, gastric and pancreatic juices accounting for 0.8 mg, and duodenum secretions with 0.16 mg Cu. Through the faecal route, 0.6-1.6 mg Cu are eliminated, whereas only 0.05 mg are gone via the urine[33, 34]. Thus, biliary/faecal excretion is the predominant Cu excretion route, which is severely impaired in WD[35, 36] (see below).

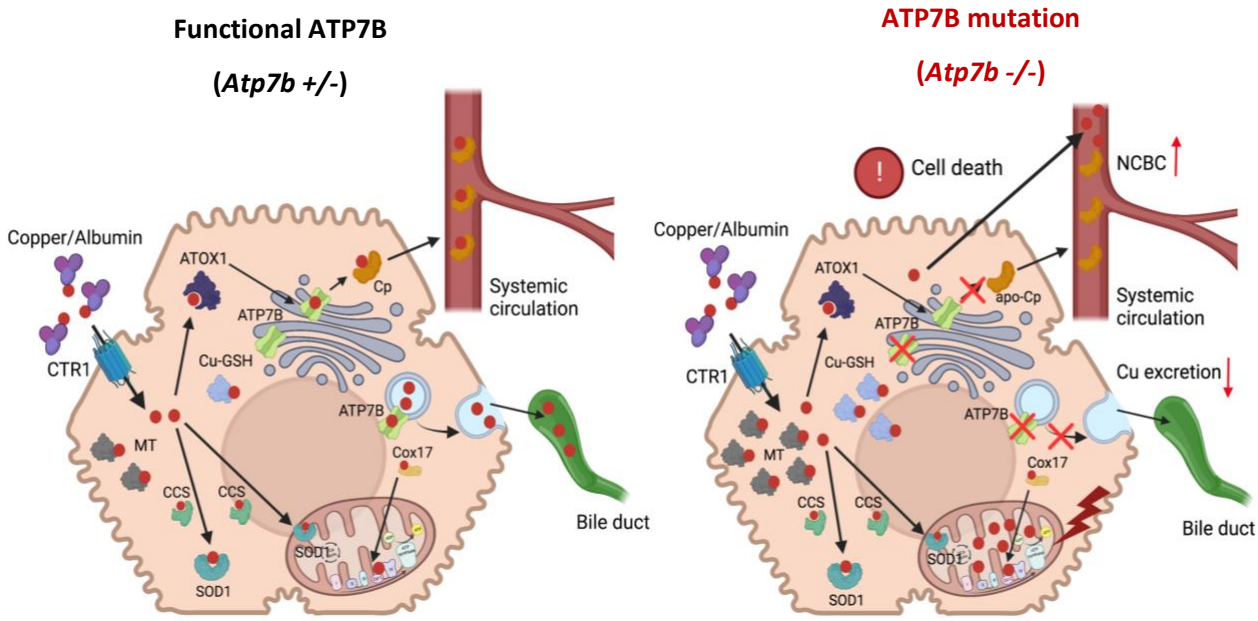

Figure 1. **Copper metabolism in the liver.** Dietary copper (Cu) reaches the liver via the portal circulation and enters the hepatocytes through the copper transporter CTR1, directly binding to chaperones in the cytosol, like ATOX1, CCS and Cox17. Under physiological conditions (functional ATP7B), ATOX1 transfers Cu to the trans Golgi network (TGN) to be incorporated into ceruloplasmin (Cp) by ATP7B, followed by its secretion into the systemic circulation. Excess Cu increases ATP7B trafficking from the TGN to lysosomes, promoting its subsequent excretion into the bile. The chaperone CCS transports Cu to SOD1 in the cytosol and mitochondria, while Cox17 is responsible for Cu transport to cytochrome c oxidase (CCO), in the mitochondria. Other Cu-binding proteins (MT, GSH) are responsible for protecting the intracellular environment from Cu toxicity, serving as a buffering system to avoid cell damage. In Wilson disease, ATP7B mutation results in reduced Cu incorporation into Cp, increasing the amount of non-ceruloplasmin bound Cu (NCBC). Moreover, Cu excretion into the bile is strongly inhibited, leading to Cu accumulation in the hepatocytes. Consequentially, MT and GSH levels increase and Cu accumulates in the mitochondria leading to mitochondrial dysfunction. Subsequent cell death increases the levels of circulating NBCB and Cu, that can affect other organs such as the heart and brain. Created in Biorender.

Abbreviations: ATOX1: Antioxidant copper chaperone 1; ATP7B: ATPase copper transporting beta; CCS: Copper chaperone for superoxide dismutase 1; Cp: Ceruloplasmin; CTR1: High affinity copper transporter 1; Cu: Copper; GSH: Glutathione; MT: Metallothioneins; NCBC: Non-ceruloplasmin bound copper; SOD1: Superoxide dismutase 1; TGN: trans Golgi network

1.2 Wilson disease – a copper overload condition

1.2.1 Epidemiology and pathophysiology of Wilson disease

Wilson disease (WD) is a rare autosomal recessive disorder of Cu metabolism, linked to the dysfunction of ATP7B. In the liver, this dysfunction leads to a deficient incorporation of the metal into apo-Cp and decreased Cu excretion into the bile[37-40] . The disease was first described, and named after the neurologist Samuel Wilson, in 1912. In his doctoral thesis, he described the pathologic finding of "lenticular degeneration" in brain, associated with liver cirrhosis[41]. In 1985, the genetic mutations responsible for WD were located in the long arm of the chromosome 13[42]. So far, more than 500 mutations in the *ATP7B* gene have been identified, many associated within isolated communities[43]. The prevalence of WD worldwide is estimated to be 1 case per 30.000 live births[44]. However, the incidence can vary greatly in different populations. Some examples are Asia (from 2:100.000 to 1:3.000)[45], United Kingdom (1:7.026)[46] and Gran Canaria (1:2.600)[47]. The clinical phenotypes of WD patients may vary from asymptomatic (with hepatomegaly and steatosis) to chronic liver disease, neurologic or psychiatric symptoms and acute liver failure. Liver cancer may occur, mostly associated with advanced fibrosis and cirrhosis, increasing the need for liver transplantation[14, 48-51]. Also, kidney failure and cardiac dysfunction are observed in WD patients, as consequence of Cu deposits in extra-hepatic tissues, aside from the brain[52]. Currently, diagnosis is done based on the presence of Kayser-Fleischer Rings (i.e., golden to greenish-brown annular deposition of Cu located in the periphery of the cornea Descemet's membrane), low serum Cp levels, increased urinary Cu excretion and elevated liver Cu content, accompanied or not, by typical signs of neurological WD. The diagnosis may be confirmed by genetic testing[53]. Time of diagnosis depends on the symptoms and disease pathology, with the majority of the patients with liver problems being diagnosed in the first decades of life (5-35 years old), and the ones with neurologic symptoms later in time[53].

1.2.2 Mitochondrial damage and steatosis as early features of hepatic Wilson Disease

As cofactor for CCO[54], Cu is essential for cellular respiration[55]. Localized in the mitochondrial inner membrane (IM), CCO serves as a terminal enzyme in the respiratory chain, being essential for ATP production via ATP synthase[56]. Apart from the process of oxidative phosphorylation (OXPHOS), Cu and mitochondria overlap in other essential cellular functions like heme and Iron-Sulfur (Fe/S) clusters synthesis, oxidative stress and apoptosis[4, 57, 58]. Furthermore, mitochondria have the capacity to store Cu by transporting it into the matrix compartment, also serving as a cellular buffer organelle for the transition metal [59, 60].

Copper misbalance is also correlated with lipid metabolism dysregulation in the hepatocytes[17, 61]. Histologic analysis of liver biopsies from WD patients revealed the presence of steatosis, with mitochondrial structure changes and cellular inflammation. These WD features are common to NAFLD[39, 62-65] and, in more advanced stages, focal necrosis and fibrosis can also be present in both diseases, ultimately leading to liver damage[35, 53, 66]. For this reason, WD is frequently misdiagnosed for NAFLD. In an animal model for WD (LPP rats - *Atp7b*$^{-/-}$)[67], these WD features were encountered, with increased liver Cu content, mitochondrial structure and functional impairment and, upon disease (i.e. increase in blood levels of liver transaminases), liver inflammation and fibrosis[68, 69]. Moreover, upon high-caloric feeding (HCD) mimicking a Western diet, the disease onset in LPP *Atp7b*$^{-/-}$ rats developed early, with increased mitochondrial damage, oxidative stress and steatosis present in the liver. Even though steatosis was also present in HCD-fed LPP *Atp7b*$^{+/-}$ control animals, only LPP *Atp7b*$^{-/-}$ developed steatohepatitis[70]. In agreement, in *Atp7b*$^{-/-}$ mice, several reports suggested alterations in lipid metabolism, even without a change in diet[71-74], as well as mitochondria dysfunction[75]. In NAFLD patients, Cu misbalance is associated with the risk of disease to progress to non-alcoholic steatohepatitis (NASH) and cirrhosis. NAFLD-cirrhotic patients had increased serum Cu levels, with increased expression of CTR1 in the liver[76]. Increased serum Cu levels significantly correlated with the risk of NAFLD and insulin resistance in a cross-sectional study with more than 3000 subjects[77]. In contrast, low Cu levels were also associated with dysregulation of lipid metabolism and development of hepatic steatosis[8, 9]. In the liver of NAFLD patients, Cu levels were lower in comparison to control subjects, but were also low in comparison to chronic hepatitis, hemochromatosis, alcoholic liver disease and autoimmune hepatitis patients. Furthermore, in the same study, NASH patients had even lower hepatic Cu

content in comparison to NAFLD patients[10]. In a diet-induced NAFLD mouse model, a lower hepatic Cu content was observed[78], whereas the combination of a Cu-deficient diet with fructose or sucrose supplementation induced a typical NAFLD disease scenario, with increased *de novo* lipogenesis, fat accumulation, lipid peroxidation and liver damage[79, 80]. Thus, both Cu excess and deficit are linked to a dysregulation of lipid metabolism.

Mitochondrial dysfunction and alterations in lipid metabolism are the first early findings in the liver of WD, in parallel to rising hepatic Cu levels. Furthermore, in line with the "multi-hit" hypothesis that recognizes the role of different insults (insulin resistance, hormone secretion, gut microbiota, nutritional factors and genetic/epigenetic aspects) for the development of metabolic syndrome/NAFLD[81], Cu levels are also changed in NAFLD patients and animal models, with low hepatic Cu and increased serum Cu levels in comparison to controls. While the mechanisms behind disease progression and Cu dyshomeostasis in NAFLD/NASH are not fully understood, the overlap of shared symptoms with WD clearly argues for similar pathognomonic processes in NAFLD and WD.

1.2.3 Copper toxicity: mitochondrial proteins as first targets of cuproptosis

Mitochondria structural alterations, observed in WD patients and WD animal models are early indications of Cu toxicity, long before any oxidative stress or hepatic failure are observed[20]. Therefore, the question is: What is the mechanism behind early mitochondrial Cu toxicity? New evidences showed that specific proteins in the mitochondria could be targets for Cu, namely thiol-rich[69, 82] or lipoylated[23] proteins, resulting in proteotoxic stress and cell death. Since this mechanism for cell death is different from other described mechanisms, such as apoptosis, necroptosis or ferroptosis, the new concept of cuproptosis has been introduced by Tsvetkov *et al*. in 2022[23, 83]. In an *in vitro* study, isolated mitochondria from wild-type rats treated with Cu experienced mitochondrial swelling, that was blocked by the addition of thiol-bearing antioxidants (GSH, dithiothreitol-DTT and dithioerythritol-DTE). Furthermore, a complete reversion of swelling was observed with the treatment with Cu chelators[82]. Increasing Cu doses, in the presence of DTT (mimicking a physiologic reducing milieu), induced mitochondria structural alterations that were comparable to the ones observed in the mitochondria of clinically apparent LPP *Atp7b*$^{-/-}$ rats. In this scenario, different mitochondrial proteins were identified as being targets for Cu-DTT, forming a complex as a result of intermolecular thiol bridges. The formation of this complex might be the molecular mechanisms behind the typical intramitochondrial contracted phenotype, characteristic in WD, in contrast to the typical phenotype observed in the case of oxidative stress, i.e. swelling of the mitochondrial matrix and cristae disruption[69]. Borchard *et al.* also proposed mitochondrial protein thiols as major targets of mitochondrial Cu toxicity[82]. In their study, isolated mitochondria from brain tissue were more sensitive to Cu challenges (in comparison to heart, kidney and liver), with structural alterations already present upon *in vitro* treatments with a Cu/GSH ratio of 1:10, i.e. at reducing conditions, thereby out ruling a Fenton-chemistry based mechanisms of destruction. A further significant emergence of ROS was only detected upon treatment with a Cu/GSH ratio of 5:10, that would hardly occur *in vivo*. These results clearly argue for a thiol/protein directed attack of Cu as toxic mechanism, and not for a undirect overwhelming oxidative stress via Cu induced Fenton chemistry. Therefore, a lower expression of GSH in the brain was pointed out as a possible explanation for the increased sensitivity to Cu, in comparison to the other tissues. In line with these results, Tsvetkov and co-workers[23] observed that cells which rely on mitochondria for energy production have increased levels of lipoylated tricarboxylic acid cycle (TCA) enzymes, such as the pyruvate dehydrogenate complex. Upon an increase in intracellular Cu levels, in this case induced by

the treatment with a Cu ionophore, lipoylated protein aggregation was observed with a loss of Fe-Su cluster-containing proteins and induction of acute proteotoxic stress, resulting in cell death, termed cuproptosis.

1.2.4 The intestinal phenotype in Wilson disease

The intestine and the liver are connected by anatomy via the portal vein and the biliary tract. As a result, in several chronic liver diseases (i.e. alcohol-associated liver disease, NAFLD/NASH, cirrhosis), the role of the gut-liver axis was shown to be preponderant in the progression of disease state[84-86].

1.2.4.1 Intestinal barrier and the role of tight junctions

The intestinal mucosa is composed by different layers that work together to build a physical and immunological barrier towards the gut lumen. These layers are roughly composed by 1) an outer mucus layer, containing highly glycosylated mucin proteins that form a gel-like structure covering the intestinal epithelium, 2) the epithelial cells, that are responsible for the formation of the intestinal barrier; and 3) a pool of multipotent cells located at the crypts, which give rise to different types of cells, including absorptive enterocytes, goblet cells, enteroendocrine cells, Paneth cells and tuft cells (Figure 2.A, B). A continuous and polarized cellular monolayer is formed, that separates the lumen from the lamina propria, where innate and adaptive immune cells, i.e. macrophages and dendritic cells, are located[87, 88]. The intestinal barrier is not a static structure, but highly dynamic in response to both external stimuli like dietary factors, pathogens and drugs, or internal stimuli like inflammatory cytokines[89]. Regulation of the paracellular transport of different substances is accomplished by three important complexes in the intestinal epithelial cells (IEC): tight junctions (TJs), adherens junctions (AJs) and desmosomes (Figure 2.C)[87]. The TJs are located at the most apical end of the IEC, and have two major functions: to keep the structure of the barrier, and to regulate diffusion of water, ions and small molecules through the paracellular space[90]. They are composed by transmembrane proteins (JAM, claudins, occludin/tricellulin), peripheral proteins (zonula-occludens - ZO and catenins) and regulatory proteins[87, 90, 91]. Occludin, ZO-1 and claudin-5 are all expressed in the small intestine section of the GIT[91]. In particular, the claudin family[92, 93] and occludin[94] are thought to be responsible for the selective paracellular permeability in the intestine. The loss of TJs proteins is directly related to the barrier

dysfunction, which is a feature of diseases such as inflammatory bowel disease, colon carcinoma, obesity, NAFLD, diabetes, amongst others[88, 90].

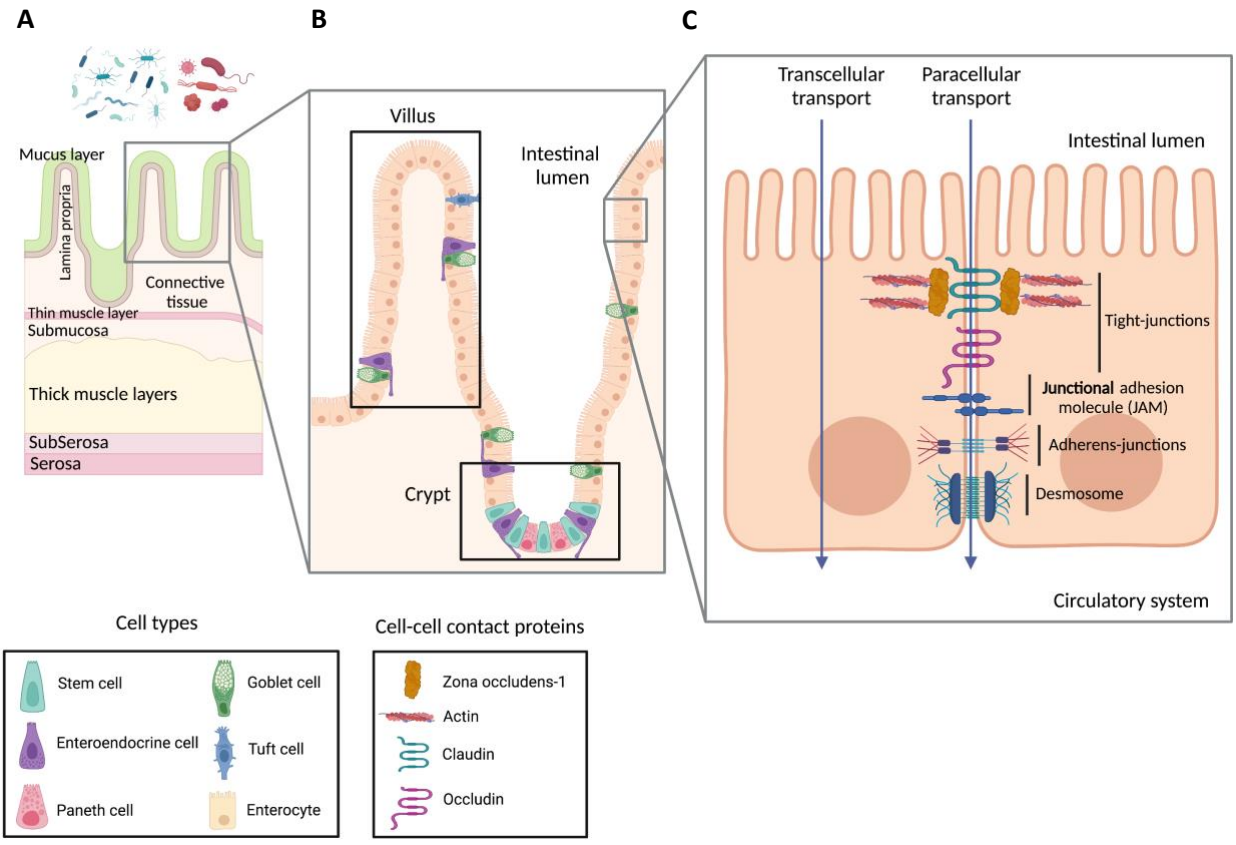

Figure 2. **Scheme of the of the gastrointestinal tract (GIT) barrier** with a focus on the small intestine (duodenum), displaying the **(A)** different layers forming the intestinal epithelium, **(B)** the distribution of different cell types on the intestinal villus, and **(C)** a simplified organization of the inter and intracellular proteins (tight-junctions, adherens junctions and desmosome) that maintain the enterocytes as a tight monolayer. Created in Biorender.

1.2.4.2 ATP7B malfunction in the intestine - What is known?

Malfunction of hepatic ATP7B in Wilson disease (WD), has been repeatedly addressed in the context of Cu overload. In contrast, its function in the gastrointestinal tract (GIT), more precisely in the small intestine, is just recently starting to be unravelled. Weiss and co-workers[95] quantified ATP7B mRNA and protein expression in murine kidney, liver (wild-type (WT) and *Atp7b*$^{-/-}$ mice), and different sections of the GIT, as well as in two different human cell lines: Caco-2 and HepG2. They observed the highest mRNA expression in WT liver, followed by HepG2 cells, duodenum and kidney, in comparison with colon, jejunum, stomach and Caco-2 cells. Protein expression was highest in WT liver, Caco-2 cells, jejunum and kidney.

The authors also suggested that ATP7B is responsible for sequestration of excess Cu into cytoplasmic vesicles in the enterocytes, possibly facilitating apical excretion. Furthermore, they observed a co-expression of ATP7B and ATP7A in the enterocytes which might be suggestive of a cooperative effort to regulate Cu levels. Pierson and co-workers[74] observed that ATP7B was more abundant in the crypts of mice duodenum, while its presence in the villi was restricted to enterocytes, presenting a non-polarized vesicular distribution. Moreover, Cu localization was correlated with the ATP7B patterns, also pointing to a role in storage and distribution. In the intestine of *Atp7b*$^{-/-}$ mice, Cu tissue levels were decreased, while mitochondria shape was altered and their number increased, together with lipid accumulation, indicating changes in dietary fat processing[74]. In Long-Evans Cinnamon (LEC) rats, with an age of 3 months old, a significant elevation of hepatic Cu was observed, in comparison to Long-Evans Agouti (LEA) controls (223.1 vs 3.7 μg/g wet weight), but with no significant changes in brain or small intestine Cu levels[96]. The LEC rats, and the derived LPP rat strain[67], is a widely used and accepted animal model for WD. The homozygous animals bearing the mutation (*Atp7b*$^{-/-}$), progressively accumulate Cu in the liver, reaching a plateau at around 70 days of age. Consequentially, the animals develop acute liver disease at around 90 days of age, with a survival expectancy of less than 20% at 120 days of age[69]. More recently, Guttmann and co-workers[97] demonstrated that ATP7B knockout Caco-2 cells are more sensitive to Cu and have disturbed lipid metabolism with reduced triglyceride (TG) storage and secretion**.** In WD patients, a limited amount of information on intestinal ATP7B function and/or intestinal Cu levels is available. However, Przybyłkowski *et al*., showed that in the enterocytes of WD patientes, there is a decrease CTR1 mRNA and protein expression, and an increased ATP7A mRNA and protein production[98]. These results point towards an active role of the intestinal ATP7B protein in the regulation of Cu levels in the enterocytes.

In comparison to hepatic ATP7B, a low number of studies have turned their attention to intestinal ATP7B. While in the liver, this Cu transporter is well known for its role in Cu excretion via the bile, its function in the intestine appears to be more related to intracellular Cu storage and distribution. Of note, in both *in vivo* and *in vitro* intestinal models of Wilson disease, mitochondrial alterations and changes in lipid metabolism were observed, despite no significant *in vivo* changes in intestinal Cu content.

1.2.5 Current treatment options and developments in Wilson disease

1.2.5.1 Copper chelators

The first line treatments for WD patients are Cu chelators (D-penicillamine or DPA, Trientine and Ammonium tetrathiomolybdate or TTM) that aim to establish Cu homeostasis. DPA contains amino, thiol and carboxylate groups which are able to chelate both Cu^{1+} and Cu^{2+}, whereas trientine is an acyclic amino chelator with four amino nitrogen groups. DPA binds intracellular Cu in the liver, while trientine mostly chelates non-Cp bound Cu in plasma, both promoting its elimination via the urine[27, 35, 43, 99]. Trientine is usually prescribed for patients that are intolerant to DPA, however its absorption in the GIT is lower in comparison. The Cu chelator DPA is taken in 2 or 3 daily doses, while trientine requires only 1 dose, all taken apart from meals[35, 100]. Neurological worsening has been observed upon treatment with Cu chelators, especially DPA, as well as other severe side effects because of long treatment periods, affecting approximately 30% of the patients. Amongst the various described, bone marrow toxicity, lupus-like syndrome and kidney disease are the most life threatening ones[101-103]. The Cu chelator TTM has superior Cu affinity than DPA and Trientine, or even in comparison to metallothioneins (MT). In the GIT, TTM prevents Cu absorption and, in circulation, it renders Cu unavailable for cellular uptake by forming a stable complex with Cu and proteins, such as albumin. TTM is currently in clinical trials and has shown less incidence of neurological damage in comparison to DPA and Trientine[35, 100]. More recently, Bis-choline TTM has been developed and it proved to be more bioavailable in the GIT, more efficient in the targeting of hepatocellular Cu and in the decrease of non-Cp bound Cu[104-106]. As a new, under development therapeutic strategy, the high-affinity Cu chelator methanobactin (MB), a peptide produced by *Methylocystis* Strain SB2[107], is a promising candidate with *in vivo* studies proving its capacity to de-Cu liver mitochondria and ameliorate the disease condition[70, 108].

1.2.5.2 Zinc salts

Zinc (Zn) salts are often considered a maintenance, or a second line therapy for WD patients, i.e. prevents further Cu absorption in the GIT, with no significant changes in liver Cu content. Target groups for Zn as a single therapy are asymptomatic or pregnant patients, as well as patients that do not respond to chelation therapy, or have serious side effects shortly after the beginning of the treatment[109]. Side effects are indeed more uncommon with Zn treatment, including neurological deterioration.[110, 111]. The mechanisms by which Zn helps to decrease Cu levels in the body are different from the Cu chelators[112]. Their action is focused on the intestine, where Zn promotes a lower Cu net intake and higher excretion via the faeces[35, 100]. In the enterocytes, Zn induces the expression of MT, cysteine-rich proteins that are endogenous metal chelators with a higher affinity for Cu than Zn. They bind Cu preventing its transport to the blood, thereby promoting its excretion via the faeces during the desquamation of the intestinal epithelium[111, 113]. Changes in hepatic MT expression can also be induced by Zn that is absorbed via the GIT. However, the de-coppering process of this therapy is rather slow in the liver, which makes it not ideal for patients with advanced liver damage. Zinc therapy is also challenging from a schedule point of view with 3 daily doses. Zinc has to be taken apart from meals and apart from Cu chelators in patients that undergo both therapies[35], which is usually applied in cases of transition to Zn salts. This overlap is necessary since the efficacy of Zn can take several months to reach its peak and establish a negative Cu balance[114, 115]. Therefore, one of the problems associated to Zn therapy is patient compliance. Another problem is the potential development of GIT symptoms such as dyspepsia and gastric irritation (gastritis, erosions and ulcers) that is observed in approximately 30% of the Zn-treated patients[111, 116, 117]. In sum, although it might be perceived as a WD therapy with less side effects (in comparison to Cu chelators) and good patient treatment outcome in milder cases, there is still no consensus with respect to its use in patients with more advanced liver disease, and/or neurologic symptoms[43].

1.3 Mushroom-enriched diets and their benefits in liver disease

1.3.1 Mushrooms in the diet – food as therapy

Mushrooms (and truffles) correspond to the fruiting bodies of higher fungi, and most belong to the divisions Ascomycota and Basidiomycota that, may include over 140 000 species[118]. They have been important dietary components since the hunter-gathering communities and their use for nutritional or medicinal purposes is well documented by Theophrastus (circ. BC 300) and early civilizations like Mesopotamians, Egyptians, Romans and Mesoamericans[119-122]. Mushrooms are increasingly recognized as a healthy food due to their role in disease prevention and, in some cases, in the suppression or remission of a diseased state[123, 124].

The nutritional benefits of mushrooms are related with the low content in fat, the richness of proteins, carbohydrates, low-digestible and non-digestible carbohydrates (known as dietary fibres), vitamins (niacin, folates and traces of B2, C, B1, B12, D, E), minerals (mainly potassium, phosphorus, magnesium, calcium, copper, iron, and zinc), and polyunsaturated fatty acids (PUFAs)[125]. Moreover, primary and secondary metabolites present in mushrooms have proven antioxidant, anti-obesogenic, antidiabetic, anti-inflammatory, antitumor, immunomodulation, and hepatoprotective effects[126, 127]. For example, phenolic compounds, such as phenolic acids (hydroxybenzoic and hydroxycinnamic acids) and flavonoids, tocopherols, ascorbic acid and carotenoids confer antioxidant capacities[128], while polysaccharides, such as ß-D-glucans, and glycoproteins provide immunomodulatory and antitumor properties[129-131].

The increased awareness towards mushrooms beneficial health-related effects might have prompted the exponential 30-fold growth in production of edible and medicinal species observed between 1978 and 2013 (from 1 billion kg to 34 billion kg)[132], with a current global consumption of around 12.7 million tonnes, and a predicted global production of 20.8 million tonnes by 2026[133].

1.3.2 Hepatoprotective effects of edible and medicinal mushrooms

Beneficial health effects of mushrooms in humans' and in *in vivo* models were reported for different edible and medicinal species. The capacity of whole carpophores (i.e. fruiting bodies) and mycelium, extracts or specific isolated compounds, to modulate lipid and sugar metabolism, insulin resistance, gut microbiota, oxidative stress and autophagy were comprehensively described in two published reviews by Fontes *et al*.[134, 135], in which the mechanisms associated to these effects were further described and found to be synergetic in the prevention and treatment of liver disease. Special attention will be given to the seven edible and medicinal species selected for the research study, *Agaricus bisporus* (J.E.Lange) Imbach (Champignon, Portobello)[136, 137], *Boletus edulis* Bull. (Porcini, King bolete)[138], *Cantharellus cibarius* Fr. (Chanterelle)[49, 139, 140], *Ganoderma lucidum* (Curtis) P. Karst. (Reishi, Ling-zhi)[141-144], *Lentinula edodes* (Berk.) Singer (Shiitake)[145, 146], *Macrolepiota procera* (Scop.) Singer (Parasol mushroom)[147, 148] and *Pleurotus ostreatus* (Jacq. ex Fr.) P.Kumm (Oyster mushroom)[149-151], described to have hepatoprotective, antioxidant, anti-inflammatory and immunomodulatory properties, when consumed in the diet or administered as supplements.

Improvement of liver damage in middle-aged human volunteers with mild liver dysfunction was reported for the medicinal mushroom *G. lucidum*. In this clinical trial, decreased activity of serum liver transaminases (alanine aminotransferase – ALT, and aspartate aminotransferase - AST) was observed in patients upon supplementation, and steatosis was improved in three of them. An overall decrease in hepatic oxidative stress, suggested that the amelioration of the liver damage may be correlated with a decrease in free radicals' overproduction or with an improvement of the cellular antioxidant defenses[152]. In animal models with induced liver damage, treatment with extracts from *A. bisporus*, *L. edodes* and *P. ostreatus* significantly reverted the condition. In an *in vivo* model susceptible to high-fat diet (HFD)-induced dyslipidemia, hepatic inflammation and/or fibrosis (*Ldlr-/-* mice), a water soluble extract from *A. bisporus* inhibited the increase in body weight, glycaemia and AST levels, in comparison to mice fed an HFD alone. Liver fibrosis, inflammation, apoptosis and oxidative stress were also decreased with the treatment[137]. *Lentinula edodes* methanol extract decreased ALT and AST, alkaline phosphatase and bilirubin levels in the serum of mice with paracetamol-induced hepatotoxicity[153]. The same effect was observed with *P. ostreatus* ethanolic extract in CCl_4-induced liver damage in rats[154]. Protective effects against oxidative stress and inflammation were also reported for *P. ostreatus, Pleurotus eryngii* and *G. lucidum*

in rodents showing liver damage caused by chemical compounds or HFD feeding[134, 155] (Figure 3). Furthermore, liver damage in chemically-induced diabetic mice fed a HFD[156] was improved with polysaccharides from *B. edulis*. Fasting blood glucose, AST and ALT serum levels, as well as circulating lipids were significantly decreased in treated animals, in comparison to diabetic, HFD-fed controls. Moreover, an increase in the protein expression levels of SOD, catalase (CAT), GSH and glutathione peroxidase (GPx) was observed in the liver of animals treated with the polysaccharides, in comparison to the controls. Immunomodulatory and antitumoral properties were described for polysaccharides and extracts from *C. cibarius* and *M. procera*, respectively, reported in *in vitro* models. A novel acidic β-glucan extracted from the fruiting body of *C. cibarius* induced the activation of RAW264.7 cells, as well as mouse peritoneal and bone marrow macrophages, via MAPK signalling (ERK, JNK and p38 phosphorylation). Excretion of TNF-α, nitric oxide (NO) and IL-6 was also observed in treated macrophages in comparison to non-treated contriols[140]. Methanolic extracts obtained from *M. procera* fruiting body contain high amounts of phenolic compounds that confer antioxidant and antitumoral properties[157]. These effects were observed in different cancer cells lines: human epithelial carcinoma (HeLa), breast cancer (MCF-7), human colon cancer (SW-480, LS174), human lung carcinoma (A549), amongst others, and macrophage-like cells (RAW 264.7).

Besides improving overall oxidative cellular defences and having immunomodulatory capacity, mushrooms can also decrease inflammation, regulate glucose and lipid metabolism via leptin and adiponectin, downregulate *de novo* lipogenesis and prevent lipid peroxidation (Figure 3)[135].

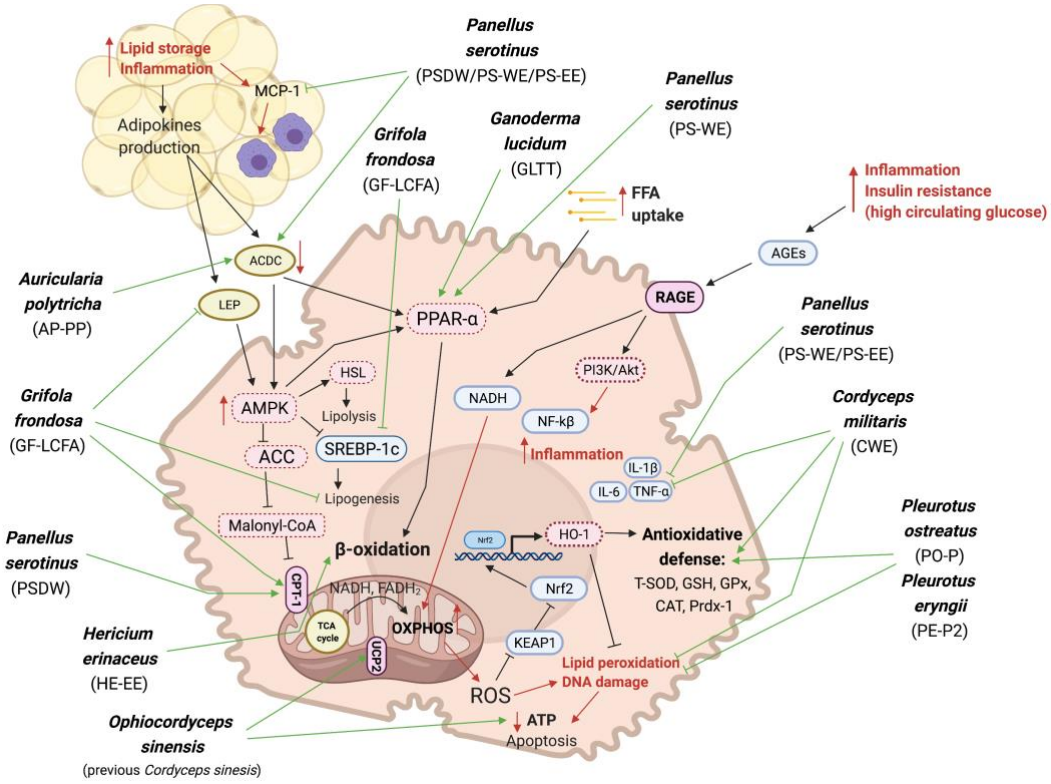

Figure 3. **Molecular mechanisms of the anti-inflammatory, anti-hyperlipidaemic and antioxidant effects of medicinal and edible mushrooms on the liver-white adipose tissue (WAT) axis, in animal models for obesity, diabetes and NAFLD.** The continuous lipid uptake and increase in circulating glucose (resulting from insulin resistance) triggers inflammation in the liver and WAT. β-oxidation in hepatic mitochondria is upregulated via AMP-activated protein kinase (AMPK) and peroxisome proliferator-activated receptor alpha (PPAR-α), in response to lipid overload and production of adipokines in the WAT. The upregulation of β-oxidation can lead to OXPHOS damage, which, in parallel to substrate saturation, causes accumulation of electrons at the electron transport chain (ETC), thereby resulting in ROS emergence which ultimately promotes lipid peroxidation and DNA damage. Medicinal and edible mushrooms can ameliorate or prevent NAFLD progression via different mechanisms: (1) regulation of leptin (LEP) and adiponectin (ACDC) levels, which infer on glucose and lipid metabolism, (2) downregulation of de novo lipogenesis via the transcription factor SREBP-1c and prevention of lipid peroxidation through the upregulation of the cellular anti-oxidative defence and (3) downregulation of inflammatory cytokines, such as IL-6, IL-1ß and TNF- α. Created in Biorender. *Abbreviations: ACDC: adiponectin; ACC: acetyl-CoA carboxylase; AGEs: advanced glycation end products; AMPK: AMP-activated protein kinase; Akt: RAC-beta serine/threonine-protein kinase; ATP: adenosine triphosphate; CAT: catalase; CPT-1: carnitine palmitoyltransferase I; EE: ethanol extract; DW: dried whole powder; FADH2: flavin adenine dinucleotide; FFA: free fatty acid; GSH: glutathione; GPx: glutathione peroxidase; HO-1: heme oxygenase-1; HSL: hormone-sensitive lipase; KEAP1: kelch-like ECH-associated protein 1; IL-1ß: interleukin 1 beta; IL-6: interleukin 6; LCFA: long chain fatty acids; LEP: leptin; Malonyl-CoA: malonyl coenzyme A; MCP-1: monocyte chemoattractant protein-1; NADH: nicotinamide adenine dinucleotide; NF-kB: nuclear factor kappa B; Nrf2: nuclear factor erythroid 2; OXPHOS: oxidative phosphorylation; P/P2: polysaccharide; PI3K: phosphoinositide 3-kinase; PP: polysaccharides-peptide; PPAR-α: peroxisome proliferator-activated receptor alpha; Prdx-1: peroxiredoxin-1; RAGE: receptor for advanced glycation end products; ROS: reactive oxygen species; SREBP-1c: sterol regulatory element-binding proteins 1-c; TCA: tricarboxylic acid cycle; T-SOD: total superoxide dismutase; TT: triterpenoid; TNF-α: tumor necrosis factor alpha; UCP2: mitochondrial uncoupling protein 2; WE: water extract; W: whole. Adapted from Fontes et al.[135], with permission.*

A positive regulation of insulin metabolism is also a feature reported in pre-diabetic and Type 2 diabetes mellitus (T2DM) patients after ingestion of *A. bisporus*, which improved insulin resistance, oxidative stress and inflammation[158]. In T2DM and healthy patients, the combined powder of the mushroom *P. ostreatus* and *Pleurotus cystidiosus* decreased glucose levels and increased postprandial insulin in the serum[159]. Supplementation with *P. ostreatus* also improved the lipid profile, with a decrease in triacylglycerols (TAGs), oxidized low density lipoproteins (oxLDL) and cholesterol levels in a clinical trial with healthy human volunteers [160]. Hypoglycaemic effects were observed in rats fed an enriched *Lentinus edodes* diet[161], and HFD-fed mice supplemented with an extract from *Lepista nuda*[162]. In both studies, serum TG and glucose levels were decreased, while serum insulin levels were increased.

The protective effects against obesity and steatosis were described on a postmenopausal female model, which has a higher predisposition to develop NAFLD. In this model, co-feeding of a HFD and *A. bisporus* improved hepatic steatosis, glucose clearance and lowered serum ALT levels in comparison to postmenopausal HFD-fed animals[163] (Figure 4, AB-DP). Supplementation with the mushroom *Hericium erinaceus* in the same animal model, fed a normal chow-diet, decreased fat tissue, total cholesterol and leptin plasma levels[164]. The modulation of lipid metabolism was also reported upon treatment with ergosterol-enriched extracts from *A. bisporus* (Ergo-E)[165], polysaccharides from *L. edodes* (LE-P)[166] and *P. eryngii* (PE-P)[167], and a dietary fraction from *P. ostreatus* (PO-DF)[168] (Figure 4), further supporting the role of these macro fungi as a nutritional approach to help in the amelioration of steatosis-related conditions[127, 134, 169].

The maintenance of the gut-liver axis homeostasis, including the microbiota, is of major importance in NAFLD since the gut barrier is the first agent against dietary insults and pathogens that can promote liver, and white adipose tissue inflammation (Figure 4). In Wilson disease (WD), the same holds true, in addition to the fact that dietary Cu is mostly absorbed via the upper GIT. As a diet, the positive effects of mushrooms on the gut-liver axis and gut microbiota[170, 171] are demonstrated for different species such as *A. bisporus*, *G. lucidum*, *L. edodes* and *Grifola frondosa* (Figure 4). In healthy human volunteers, gut microbiota composition (*Bacteroidetes* > *Firmicutes*) was improved with an *A. bisporus*-enriched diet, in comparison to a beef diet [172, 173]. Moreover, extracts from *G. lucidum* promoted an improvement of gut dysbiosis, which was correlated with an improvement of tight-junctions (TJs) protein expression, a decrease in total cholesterol (TC), low density lipoproteins (LDL) and TAGs, and an increase in high density lipoproteins (HDL) (Figure 4, GL-WE) [174-176].

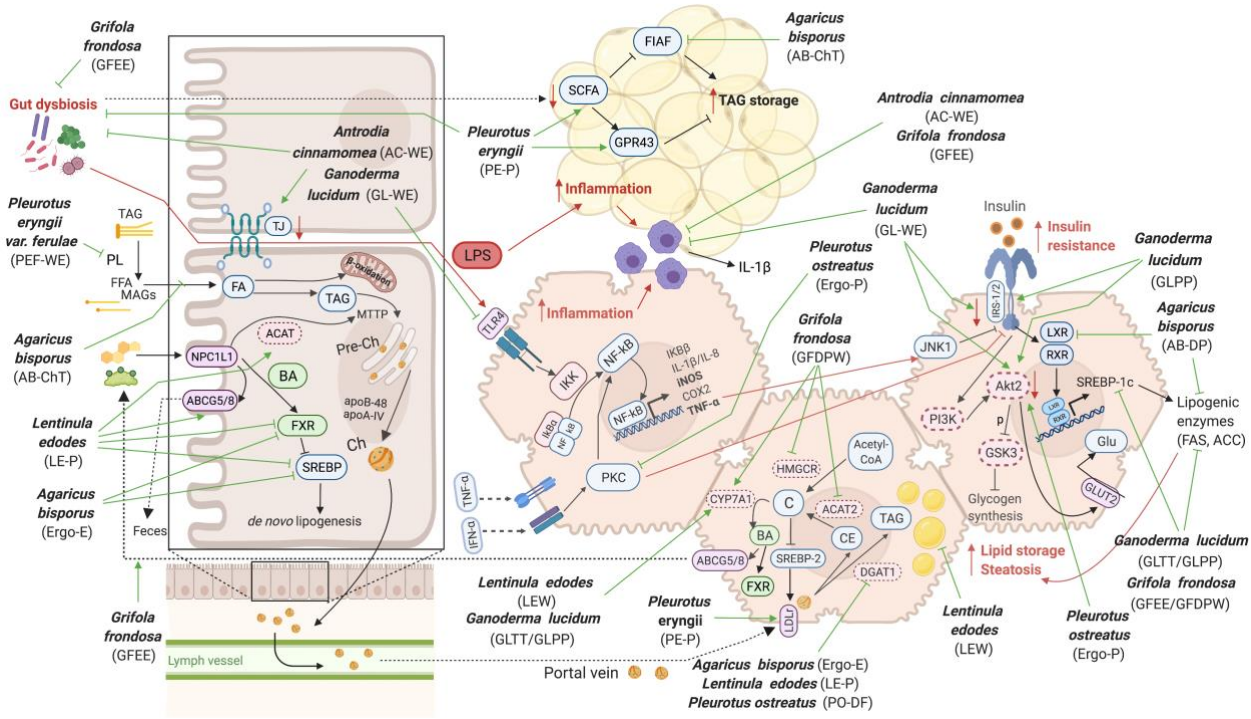

Figure 4. **Molecular mechanisms of the antidiabetic, antisteatotic, anti-inflammatory and gut modulation effects of medicinal and edible mushrooms on the gut-liver and liver-white adipose tissue (WAT) axis, in animal models for obesity, diabetes and NAFLD.** Interactions between the GIT, liver and WAT ensures the homeostasis of lipid and sugar metabolism. Consumption of HFD creates metabolic imbalances that are in close relation with the development of obesity, diabetes and NAFLD. Absorption of fat and sugar, as well as bile acids reabsorption, is controlled in the GIT, with a preponderant role of the gut microbiota. The integrity of the gut barrier is important to avoid blood endotoxemia (LPS) which triggers inflammation of the liver and WAT. The liver is the central hub for lipid and glucose metabolism, while the WAT is mainly responsible for fat storage and plays an important role in the inflammatory process. Medicinal and edible mushrooms ameliorate the effects of HFD in animal models by reversing the imbalances in gut microbiota, decreasing gut permeability via upregulation of TJs protein, promoting bile acids excretion into the faeces and decreasing fat absorption in the GIT. In the WAT, medicinal and edible mushrooms decrease fat storage and consequent inflammation (production of adipokines) and, in the liver, acts in (1) the reduction of fat storage via the suppression of TAG synthesis and *de novo* lipogenesis; (2) upregulation of the bile acids excretion pathway, and (3) the improvement of insulin resistance by regulating the phosphoinositide 3-kinase-Protein kinase B (PI3k-Akt) pathway and the expression of the insulin receptor (IR) and insulin receptor substrates (IRS1/2). Created in Biorender. *Abbreviations: ABCG5/8: ATP-binding cassette sub-family G member 5/8; ACAT/ACAT2: acetyl-CoA acetyltransferase (cytosolic); ACC: acetyl-CoA carboxylase; Acetyl-CoA: acetyl coenzyme A; Akt2: Protein kinase B (PKB); apoB-48: apolipoprotein B-48; apoB-IV: apolipoprotein B-IV; BA: bile acids; C: cholesterol; CE: cholesterol esters; Ch: chylomicron; ChT: chitosan; COX2: cyclooxygenase-2; CYP7A1: cholesterol 7 alpha-hydroxylase; DF: dietary fraction; DGAT1: diacylglycerol O-acyltransferase 1; DP: dried powder; DPW: dried powder in water; EE: ethanol extract; Ergo: ergosterol; Ergo-E: ergosterol enriched extract; FA: fatty acid; FAS: fatty acid synthase; FIAF: fasting-induced adipose factor; FFA: free fatty acid; FXR: farnesoid X receptor; Glu: glucose; GLUT2: glucose transporter type 2; GPR43: g protein-coupled receptor 43; GSK3: glycogen synthase kinase-3 alpha; HMGCR: 3-hydroxy-3-methylglutaryl-coenzyme A reductase; IFN-α: interferon-alpha; IkBα: nuclear factor of kappa light chain gene enhancer in B-Cells alpha; IKK: IκB kinase; IL-1β: interleukin 1 beta; IL-8: interleukin 8; iNOS: nitric oxide synthase 2 ; IRS1/2: insulin receptor substrate 1 ; JNK1: c-Jun terminal protein kinase 1; LDLr: low-density lipoprotein receptor; LPL: lipoprotein lipase; LPS: lipopolysaccharide; LXR: liver X receptors; MAGs: monoacylglycerols; MTTP: microsomal triglyceride transfer protein; NF-kB: nuclear factor kappa B; NPC1L1: niemann-Pick C1-Like 1; P: polysaccharide; PI3K: phosphoinositide 3-kinases; PKC: protein Kinase C Theta; PL: pancreatic lipase; PP: polysaccharides-peptide; RXR: retinoid X receptor; SCFA: short-chain fatty acids; SREBP/SREBP-1c/SREBP-2: sterol regulatory element-binding*

proteins/1-c/2; TAG: triacylglycerol; TJ: tight junctions; TT: triterpenoid; TLR4: toll-like receptor 4; TNF-α: tumor necrosis factor alpha; WE: water extract; W: whole. Adapted from Fontes et al.[135], with permission.

Together with steatosis and dysregulation of lipid metabolism, the decline in hepatic mitochondrial function is also a hallmark of both WD and NAFLD pathology. However, few studies have reported beneficial effects of mushrooms in mitochondria function, apart from their pro-apoptotic effects in a hepatocellular carcinoma scenario (Fontes *et al*.[134]). In extrahepatic tissues, isolated polysaccharides from *G. lucidum* (GLP) inhibited mitochondria-related apoptosis in high fat-fed mice splenic lymphocytes and improved serum, and small intestinal levels of antioxidative enzymes, lipid peroxidation and overall lipid profile[177]. In an intestinal porcine epithelial cell line (IPEC-J2) treated with palmitic acid, GLP rescued mitochondrial membrane potential, citrate synthase activity, improved ATP levels and suppressed the activation of AMPK[178].

1.3.3 Chelating activity of fungi as a new nutritional approach for Wilson Disease

The capacity of several mushroom species to accumulate metals, such as Cu and Zn, is well documented[179-181]. Their high metal tolerance is believed to be related with intracellular metal chelation in the cytosol, by ligands such as GSH and MT[182, 183]. The presence of increased amounts of heavy metals in mushrooms, particularly in wild species, has been associated with health issues in consumers[184, 185]. However, metal-enriched edible mushrooms, grown under controlled conditions, are emerging as promising nutritional approach against oxidative stress and hyperlipidaemia, in the improvement of GIT health and to decreased metal overload. The zinc-enriched mycelia of *Pleurotus eryngii* showed a higher reducing power, 2,2-diphenyl-1-picrylhydrazyl (DPPH) and $OH^{\bullet}$ radical scavenging ability *in vitro*, than non-enriched mycelia[186], while polysaccharides extracted from the *P. djamor* zinc-enriched mycelium increased the activity of antioxidant enzymes (SOD, GSH and CAT), and significantly reduced lipid peroxidation and liver damage (ALT and AST serum levels) in two different chemically induced *in vivo* liver damage models[187, 188]. Metal accumulation in the mycelium of *P. ostreatus* was reported for selenium (Se)[189, 190] in submerged culture, and iron (Fe)[191] in solid substrate. Zinc bioaccumulation in the mycelium and fruiting bodies was also described for *P. florida*[192]. In hyperlipidaemic mice, supplementation with polysaccharides obtained from the zinc-enriched mycelium of *Pholiota nameko* improved blood and liver lipid profile, as well as liver and serum antioxidant status (SOD content and total antioxidant capability (T-AOC))[193]. Selenium-enriched polysaccharides from *Catathelasma ventricosum* improved the activity of antioxidant enzymes, and simultaneously reduced lipid peroxidation in a mouse model with chemical-induced liver damage[194-196]. Moreover, Se-enriched *A. bisporus* mushroom powder improved the gastrointestinal health of pigs, with no changes on GIT morphology, meaning villus height, crypt depth and their ratio (villus height/crypt depth), with a positive regulation of the gut microbiota. The selenium transporter SELENOP was upregulated in the jejunum, and mucin-1 (MUC1) was downregulated in the ileum. Selenium content was increased in the muscle and liver tissues[197]. In Fe overloaded mice, a significant decrease in liver Fe content was observed upon treatment with ethyl acetate and methanolic extracts obtained from the mushroom *Cantharellus cibarius*[198].

1.4 Hypothesis and Aims

Growing evidence on the benefits of mushrooms in metabolism opens new doors towards biotherapeutic approaches. In Wilson disease (WD), zinc salts are considered an effective treatment due its capacity to block copper (Cu) absorption in diet. However, zinc treatment is associated to some side effects, such as gastric irritation that can result gastritis, erosions and ulcers.

The hypothesis of this research work is that **a bio and food friendly option with a mushroom-enriched diet, using a zinc-enriched mushroom, may potentially improve the metal dyshomeostasis in WD condition. We assume that a zinc-enriched mushroom may directly bind copper and/or promote the copper binding in the enterocytes with lower gastrointestinal tract irritation (GIT)**. In addition, the mushroom-enriched diet provide bio compounds that can be protective to liver.

Due to a clear lack of knowledge in respect to the ATP7B malfunction in the intestine in WD, the **first objective** of the research was to shed light into the intestinal impairment in WD. To this end, the following specific scientific objectives were pursued:

- To assess copper levels, mitochondrial structure, proteome alterations and barrier integrity in the animal model for WD rats (LPP *Atp7b*$^{-/-}$), and in Caco-2 wild-type (WT) cells, and cells bearing the ATP7B mutation: Caco-2 ATP7B knockout (KO);
- To evaluate copper toxicity in Caco-2 WT and Caco-2 ATP7B KO cells non-differentiated, and differentiated in enterocyte-like cells;
- To critically compare the results in both models, and infer on the validity of the Caco-2 ATP7B KO cells as an *in vitro* model for intestinal WD.

The **second objective** was to select a mushroom species to develop the biotherapy approach: a zinc-enriched mushroom. To that, seven edible and medicinal mushrooms, *Agaricus bisporus, Boletus edulis, Cantharellus cibarius, Ganoderma lucidum, Lentinula edodes, Macrolepiota procera* and *Pleurotus ostreatus*, with reported health beneficial effects in liver disease were considered, and the following goal pursued:

- To estimate the hepatoprotective effects of the seven mushrooms in an *in vitro* model for hepatic lipotoxicity and select the most prominent species.

The **third objective** consisted in the development of the zinc-enriched mushroom. To this end, the following goals were pursued:

- To evaluate the capacity of the selected mushroom to accumulate inorganic zinc in their fruiting body and/or mycelium;
- To optimize a protocol to obtain a zinc-enriched mycelium protein extract.

The **fourth objective** was to develop a new dietary approach to help reduce copper absorption in the GIT. Thus, the following goals were pursued:

- To study the protective effects of the zinc-enriched mycelium protein extract against copper toxicity (in Caco-2 WT cells);
- To evaluate the potential *in vitro* de-coppering effect, and enterocyte-like barrier protection of the zinc-enriched mycelium protein extract in Caco-2 WT and ATP7B KO cells, after differentiation;
- To establish a mushroom-enriched diet formulation with the zinc-enriched mycelium for the treatment of WD rats (LPP *Atp7b*$^{-/-}$) and to evaluate its putative beneficial effects in terms of zinc and copper absorption/excretion.

2. Materials and Methods

2.1 Reagents and technical equipment

Table 1. **Chemicals, reagents, dyes and kits**

Reagent	*Manufacturer*
Adenosine-5'-diphosphate (ADP)	Sigma-Aldrich, Taufkirchen, Germany
Acetic acid 100%	Merck, Darmstadt, Germany
Acetone	Serva Electrophoresis GmbH, Heidelberg, Germany
Acrylamide Rotiphorese 30 %	Carl Roth, Karlsruhe, Germany
Albumin Fraction V, fatty acid-free	Carl Roth, Karlsruhe, Germany
Alpha-Linolenic acid	Sigma-Aldrich, Taufkirchen, Germany
Ammonium persulfate (APS)	Sigma-Aldrich, Taufkirchen, Germany
Antimycin A	Sigma-Aldrich, Taufkirchen, Germany
Antibiotic-antimycotic solution	Life Technologies, Darmstadt, Germany
Ascorbic acid (Vitamin C)	Sigma-Aldrich, Taufkirchen, Germany
ß-Mercaptoethanol	Sigma-Aldrich, Taufkirchen, Germany
Bleicitrate 3%	Leica Microsystems, Wetzlar, Germany
BODIPY FL (N-(4,4-difluoro-5,7-dimethyl-4-bora-3a,4a-diaza-s-indacene-3-yl)methyl)iodoacetamide)	Invitrogen, Karlsruhe, Germany
Bromophenol Blue sodium salt	Sigma-Aldrich, Taufkirchen, Germany
Carbonyl cyanide m-chloro-phenylhydrazone (CCCP)	Sigma-Aldrich, Taufkirchen, Germany
Cacodylate buffer	EMS, Science Services
CellTiter-Glo® Luminescent Cell Viability Assay	Promega, Fitchburg, USA
CHAPS (3-((3-cholamidopropyl) dimethylammonio)-1-propanesulfonate)	Abcam, Cambridge, UK
Cholesterol	Sigma-Aldrich, Taufkirchen, Germany
Chloramphenicol	Sigma-Aldrich, Taufkirchen, Germany
Chloroform	Sigma-Aldrich, Taufkirchen, Germany
Copper(II) chloride dihydrate 99.99%	Sigma-Aldrich, Taufkirchen, Germany
CyQuant™ Cell Proliferation assay	ThermoFisher Scientific GmbH, Dreieich, Germany
DDSA	Serva Electrophoresis GmbH, Heidelberg, Germany

Digitonin	Calbiochem, Sigma-Aldrich, Taufkirchen, Germany
Dimethyl sulfoxide (DMSO) (>99,9 %)	Merck, Darmstadt, Germany
DMEM, high glucose, GlutaMAX™ Supplement	Gibco™, ThermoFisher Scientific GmbH, Dreieich, Germany
DMP30	Serva Electrophoresis GmbH, Heidelberg, Germany
DPBS (Dulbecco's phosphate buffered saline)	Biochrom, Berlin, Germany
Ethanol 99.9 % (technical grade)	Storage HMGU
Ethylene glycol-bis(2-amino-ethylether)- tetraacetic acid (EGTA)	Fluka, Sigma-Aldrich, Taufkirchen, Germany
Erythrosine B (C.I. 45430)	Sigma-Aldrich, Taufkirchen, Germany
FCS (fetal calf serum)	Biochrom, Berlin, Germany
Fluorescein (Dextran, 10,000 MW, Anionic)	Sigma-Aldrich, Taufkirchen, Germany
Glucose	Sigma-Aldrich, Taufkirchen, Germany
L-Glutamic acid	Fluka, Sigma-Aldrich, Taufkirchen, Germany
Glutaraldehyde 2.5% in 0.1M Sodium-Cacodylatpuffer	EMS, Science Services
Glutaraldehyde 25% solution in H_2O	Sigma-Aldrich, Taufkirchen, Germany
Glycerol	Sigma-Aldrich, Taufkirchen, Germany
Glycerol phosphate (disodium salt hydrate)	Sigma-Aldrich, Taufkirchen, Germany
Glycidether 100	Serva Electrophoresis GmbH, Heidelberg, Germany
Glycin	Sigma-Aldrich, Taufkirchen, Germany
Hanks balanced salts solution (HBSS)	Sigma-Aldrich, Taufkirchen, Germany
HEPES (4-(2-hydroxyethyl)piperazine-1- ethansulfonic acid)	Sigma-Aldrich, Taufkirchen, Germany
Hoechst 33342	Thermo Fisher Scientific
Human IL8/CXCL8 ELISA kit	Sigma-Aldrich, Taufkirchen, Germany
Hydrogen chloride (HCl) 32%	Merck, Darmstadt, Germany
Isopropanol	VWR, Ismaning, Germany
20x LumiGlo® reagent and 20x peroxide	Cell Signaling, Frankfurt a.M., Germany
Lactobionate	Sigma-Aldrich, Taufkirchen, Germany
L-Histidine	Sigma-Aldrich, Taufkirchen, Germany
Linoleic acid	Sigma-Aldrich, Taufkirchen, Germany
Magnesium chloride (MgCl2)	Sigma-Aldrich, Taufkirchen, Germany

Magnesium sulphate (MgSO4)	PanReaC, AppliChem, Darmstadt, Germany
Malate (disodium salt)	Merck, Darmstadt, Germany
Malt extract	ThermoFisher Scientific GmbH, Dreieich, Germany
Methanol	Merck, Darmstadt, Germany
MNA	Serva Electrophoresis GmbH, Heidelberg, Germany
NEAA (non-essential amino acids)	Life Technologies, Darmstadt, Germany
Neutral red	Sigma-Aldrich, Taufkirchen, Germany
Nile Red	Sigma-Aldrich, Taufkirchen, Germany
Nitric acid 65%	Merck, Darmstadt, Germany
N,N,N',N-Tetramethyl-p-phenylenediamine (TEMED)	Sigma-Aldrich, Taufkirchen, Germany
N,N,N',N'-Tetramethyl-p-phenylenediamine dihydrochloride (TMPD)	Sigma-Aldrich, Taufkirchen, Germany
Oleic acid	Sigma-Aldrich, Taufkirchen, Germany
Oligomycin	Sigma-Aldrich, Taufkirchen, Germany
Osmiumtetroxid 4%	EMS, Science Services
Palmitic acid	Sigma-Aldrich, Taufkirchen, Germany
Paraformaldehyde 4%	Sigma-Aldrich, Taufkirchen, Germany
Percoll®	GE Healthcare, Munich, Germany
Phenylmethylsulfonyl fluoride (PMSF)	Sigma-Aldrich, Taufkirchen, Germany
Poly-D-Lysine hydrobromide	Sigma-Aldrich, Taufkirchen, Germany
Ponceau S	Sigma-Aldrich, Taufkirchen, Germany
Potassium dihydrogen phosphate (KH_2PO_4)	Merck, Darmstadt, Germany
Potassium hydroxide (KOH)	Merck, Darmstadt, Germany
Potassium phosphate dibasic (K_2HOP_4)	Sigma-Aldrich, Taufkirchen, Germany
Potato dextrose agar	Sigma-Aldrich, Taufkirchen, Germany
Protease inhibitor cocktail (EDTA-free)	Merck, Darmstadt, Germany
Propylenoxid	Serva Electrophoresis GmbH, Heidelberg, Germany
Resazurin salt	Sigma-Aldrich, Taufkirchen, Germany
RIPA buffer	Cell Signaling, Frankfurt a.M., Germany
Rotiphorese 10x SDS-PAGE	Carl Roth, Karlsruhe, Germany
Roti®-Nanoquant (Bradford reagent)	Carl Roth, Karlsruhe, Germany
Rotenone	Sigma-Aldrich, Taufkirchen, Germany

Seahorse FluxPak (102601-100)	Agilent, Waldbronn, Germany
Seahorse XF media (103575-100)	Agilent, Waldbronn, Germany
Skim milk powder	Carl Roth, Karlsruhe, Germany
Sodium azide (NaN_3)	Sigma-Aldrich, Taufkirchen, Germany
Sodium chloride (NaCl)	Merck, Darmstadt, Germany
Sodium dodecyl sulfate (SDS)	Serva Electrophoresis GmbH, Heidelberg, Germany
Sodium hydroxide (NaOH)	Merck, Darmstadt, Germany
Sodium pyruvate ($C_3H_3NaO_3$	Life Technologies, Darmstadt, Germany
Succinate (sodium salt)	Sigma-Aldrich, Taufkirchen, Germany
Stearic acid	Fluka, Sigma-Aldrich, Taufkirchen, Germany
Sucrose	Fluka, Sigma-Aldrich, Taufkirchen, Germany
Sulforhodamine B	Sigma-Aldrich, Taufkirchen, Germany
Taurine	Sigma-Aldrich, Taufkirchen, Germany
TES	Sigma-Aldrich, Taufkirchen, Germany
Tris (tris(hydroxymethyl)aminomethane)	VWR, Ismaning, Germany
Triton X-100	Sigma-Aldrich, Taufkirchen, Germany
Trypan blue	Sigma-Aldrich, Taufkirchen, Germany
Tween-20	Sigma-Aldrich, Taufkirchen, Germany
UranyLess	EMS, Science Services
Vectashield HardSet™	Vector Laboratories, Maravai Life Sciences, US
Yeast extract	Sigma-Aldrich, Taufkirchen, Germany
Zinc acetate ($Zn(CH_3CO_2)_2$)	Sigma-Aldrich, Taufkirchen, Germany
Zinc sulphate heptahydrate ($ZnSO_4.7H_2O$)	Sigma-Aldrich, Taufkirchen, Germany

Table 2. **Technical equipment**

Equipment/Software	*Model*	*Manufacturer*
Analytical scaler	MC210S	Sartorius AG, Göttingen, Germany
Automated cell counter	LUNA IITM	Logos biosystems, Anyang, South Korea
Biophotometer		Eppendorf, Hamburg, Germany
Blot system	MiniProtean 3 CelL	Bio-Rad Laboratories, Inc, California, US
ClarioStar plate reader		BMG Labtech, Ortenberg, Germany
Centrifuge	Centrifuge 5415R	Eppendorf, Hamburg, Germany
Centrifuge cell culture	Centrifuge 5702R	Eppendorf, Hamburg, Germany
CO_2 Incubator	Heraeus BBD6220	ThermoFisher Scientific GmbH, Dreieich, Germany
DatLab		Oroboros Instruments, Innsbruck, Austria
Electron microscope	JEM 1200-EXII	Jeol Solutions for Innovation USA, Inc
Electrophoresis chamber	XCell SureLock	Invitrogen, Karlsruhe, Germany
Fluorescence microscope	ECLIPSE Ti-S	Nikon Instruments Inc. Melville, US
Heating block	Thermoshaker Ts1	Biometra GmbH, Göttingen, Germany
ImageJ		National Institutes of Health (NIH)
Incubator	Heratherm Cmpct Microbio	ThermoFisher Scientific GmbH, Dreieich, Germany
Infusion pump	Pump 11 Elite	Harvard Apparatus
Inverted light microscope	Labovert	Leica Microsystems, Wetzlar, Germany
Metabolic cages	3007M071	Tecniplast, Hohenpeissenberg, Germany
Oxygraph	Oxygraph-2k	Oroboros Instruments, Innsbruck, Austria
pH-Meter	pHenomenal® pH 1100L	VWR, Ismaning, Germany
Photo Imager	Fusion FX7	Vilber Smart Imaging, France
Prism		GraphPad Software, Inc.
Power source	Power Pac™ Basic	Bio-Rad Laboratories, Inc, California, US
Sterile work bench	LaminAIR® HB 2472	ThermoFisher Scientific GmbH, Dreieich, Germany
Seahorse XF Analyzer	XFe96	Agilent Technologies, US
TEER (transepithelial/ -endothelial resistance) meter	cellZscopeE	nanoAnalytics, Münster, Germany

Tissue homogeneizer	Minilys Personal homogeneizer	Bertin Technologies SAS, France
Transwell® inserts	PET-TW permeable supports (0.4μm pore size)	Corning, New York, USA; ThermoFisher Scientific GmbH, Dreieich, Germany
Ultra-centrifuge	Optima™ MAX-XP Ultracentifuge	Beckman Coulter Inc., California, US
Ultrasonic Processor	UP100H	Hielscher Ultrasonics GmbG, Teltow, Germany
Reflotron system		Roche Diagnostics, Penzberg, Germany
8-well ibidi slides		ibidi GmbH, Gräfelfing, Germany
96-well plates	White, flat bottom	ThermoFisher Scientific GmbH, Dreieich, Germany
96-well plates	Clear, flat bottom	ThermoFisher Scientific GmbH, Dreieich, Germany

Table 3. **Antibodies list**

Antibody	*Species*	*Dilution*	*Application*	*Supplier*	*Catalog number*	*Storage*
Primary antibodies						
Metallothionein	Mouse	1:500	WB	Abcam, Cambridge, US	Ab12228	-20°C
Citrate synthase	Rabbit	1:50	ICC	Proteintech, Rosemont, USA	16131-1-AP	-20°C
Zona-occludens 1	Rabbit	1:250	ICC	ThermoFisher Scientific GmbH, Dreieich, Germany	61-7300	-20°C (aliquoted)
Occludin	Mouse	1:500	ICC	Zytomed Systems, Berlin, Germany	Clone 3G217	-20°C (aliquoted)
Claudin-5	Rabbit	1:250	ICC	Abcam, Cambridge, U	ab15106	-20°C (aliquoted)
GAPDH	Rabbit	1:1000	WB	Cell Signaling, Frankfurt a.M., Germany	2118	-20°C
Secondary antibodies						
Anti-biotin, HRP	Goat	1: 2000	WB	Cell Signaling, Frankfurt a.M., Germany	7075S	-20°C
Anti-mouse, HRP	Goat	1: 2000	WB	Cell Signaling, Frankfurt a.M., Germany	7076S	-20°C
Anti-rabbit, HRP	Goat	1: 2000	WB	Cell Signaling, Frankfurt a.M., Germany	7074S	-20°C
Alexa Fluor ™ 488 anti-mouse IgG (H+L)	Goat	1:1000	ICC	Invitrogen, Karlsruhe, Germany	1810948	4°C

Alexa Fluor ™ 568 anti-rabbit IgG (H+L)	Goat	1:1000	ICC	Invitrogen, Karlsruhe, Germany	1811756	4°C

2.2 Mushroom extracts

Mushroom extracts (ethanol and water) of *Agaricus bisporus*, *Boletus edulis*, *Cantharellus cibarius*, *Ganoderma lucidum*, *Lentinula edodes*, *Macrolepiota procera* and *Pleurotus ostreatus*, where kindly provided by Professor Isabel Ferreira, Laboratory of Applied Chemistry and Biochemistry (LQBA) of Polytechnic Institute of Bragança (IPB). The aqueous extractions were obtained by performing a decoction preparation. The sample (1g) was added to 200 mL of distilled water, heated (heating plate, VELP scientific) and boiled for 5 min. The mixture was left to stand for 5 min and then filtered under reduced pressure. The obtained decoctions were frozen and lyophilized. The ethanol extraction was performed by maceration using the dry powdered mushroom (1g) and stirring with 30 mL of ethanol at 25°C, 150 rpm for 1 hour, and filtered through Whatman No. 4 paper. The residue was then re-extracted with one additional 30 mL portion of ethanol. The combined extracts were evaporated at 35°C under reduced pressure (rotary evaporator Büchi R-210, Flawil, Switzerland).

The ethanol extracts were solubilized in dimethyl sulfoxide cell culture grade (DMSO, 99.9%). For *C. cibarius*, *G. lucidum* and *P. ostreatus*, the powder from ethanol extraction (aliquoted and kept at -80ºC) were solubilized into a final concentration of 70.19mg/mL, 60.97mg/mL and 57.55mg/mL, respectively; and for *A. bisporus*, *B. edulis*, *L. edodes* and *M. procera*, the solution from the ethanol extracts were solubilized into a final concentration of 100mg/mL. Aqueous extracts from *A. bisporus*, *B. edulis*, *C. cibarius*, *L. edodes*, *M. procera*, and *P. ostreatus*, were solubilized in MiliQ water to a final concentration of 200mg/mL, while the aqueous extract of *G. lucidum* was solubilized in 77.1% MiliQ water and 22.9% DMSO.

2.3 Production of *Pleurotus ostreatus* in solid substrate

2.3.1 Strain and culture

Pleurotus ostreatus pure mycelium culture (strain 382-POSP, obtained from Mycelia - code M2191) used in the experiment was provided by the Quadrante Natural - Micologia e Ambiente, Lda. The strain was maintained in agar-based medium and also preserved in cryotubes with perlite in liquid malt, in refrigeration. For mycelium growth, the strain was transferred to petri dishes (90 mm x 16,2 mm) with 25 mL of potato dextrose agar (PDA) media, at 22.5°C in the dark, until the mycelium covered most of the medium, approximately 8 days. This experiment was done by Rui Coelho (Quadrante Natural - Micologia e Ambiente, Lda, Lisbon, Portugal) and Bruno Belchior (Mushrooms Mountain, Lda, Alcanede, Portugal)

2.3.2 Zinc solutions

Zinc solutions were prepared from zinc sulphate heptahydrate: $ZnSO_4.7H_2O$ (from Sigma-Aldrich Chemical Co., Saint Louis, MO, USA, CAS number: 7446-20-0), in concentrations of 0, 0.200, 0.300, 0.500, 0.800, 1.000, 1.500 and 2.000g/L using distilled water.

2.3.3 Preparation of the substrate

The substrate for *Pleurotus ostreatus* (382-POSP) fructification was prepared with 68% water and 32% substrate composed by 80% pine pellets (from Pinewells) supplemented with 20% biologic lucerne pellets (formulation: LU20 – w/calcium carbonate from Diamantino Coelho) in polyethylene bags (maximum 35 cm, drilled every 10 to 15 cm). In zinc-treated substrate, mixtures were moistened to 68% of distilled water containing the different concentrations of zinc (0, 0.200, 0.300, 0.500, 0.800, 1.000, 1.500 and 2.000g/L). Sterilization of the bags was conducted in an autoclave for 3 hours with the temperature of the centre of the bags reaching 115.3°C for 28 minutes, with an over-elevation of 7.6°C (122.9°C) until the temperature is achieved, dropping to 115.3°C in the exterior of the bags until the end of the cycle. The substrate was let to cooled down for 12 hours to a temperature of 30°C and inoculated with 50g of mycelium to each 2000g of substrate. This experiment was done together with Dr. Anabela Marisa Azul, Rui Coelho (Quadrante Natural - Micologia e Ambiente, Lda, Lisbon, Portugal) and Bruno Belchior (Mushrooms Mountain, Lda, Alcanede, Portugal)

2.3.4 Incubation, mycelium colonization and fructification

The inoculation of *Pleurotus ostreatus* pure mycelium culture was performed in sterile conditions in a laminar flux chamber. To induce mycelia colonization, bags were placed in a room with a controlled temperature between 20-22°C, with a substrate temperature between 25-30°C and 60-70% relative humidity. After full mycelia colonization of the substrates, the bags were changed to the fructification room and opened. To induce fructification, temperature was set to 20°C with a relative humidity of 90 to 95%, until the primordia appearance, being changed to 85% for the sporocarp formation. The relative air humidity was achieved with an ultrasonic membrane using de-mineralized water (Desmiwater system). The concentration of CO_2 is less than 1000 ppm and the light 100 to 200 lux (white LED light system) for 24 hours. This experiment was done by Rui Coelho (Quadrante Natural - Micologia e Ambiente, Lda, Lisbon, Portugal) and by Bruno Belchior (Mushrooms Mountain, Lda, Alcanede, Portugal).

2.3.5 Harvesting of carpophores and mycelia

Fructification was induced has abovementioned (2.3.4), and both carpophores and mycelia recovered from the bags. Carpophores were weight and saved in clean bags, according to zinc conditions, for later lyophilization (freeze-drying). In the first study, mycelia were recovered, together with substrate, dried, and afterwards separated from the remaining substrate. In the second study, mycelia were collected from the bags under a laminar flux chamber, directly weight and stored in clean 50 mL falcon tubes for later lyophilization (freeze-drying). Harvesting of carpophores and mycelia was done together with Dr. Anabela Marisa Azul, Rui Coelho (Quadrante Natural - Micologia e Ambiente, Lda, Lisbon, Portugal) and Bruno Belchior (Mushrooms Mountain, Lda, Alcanede, Portugal). Lyophilization of carpophores and mycelia was done by Cristina Barosa and Dr. Anabela Marisa Azul, at the Centre for Neurosciences and Cell Biology (CNC), Intermediary Metabolism Group, University of Coimbra, Biotech-Biocant, Cantanhede, Portugal.

2.4 Production of *Pleurotus ostreatus* mycelium in liquid substrate

2.4.1 Strain and culture

Pleurotus ostreatus pure mycelium culture (obtained from Mycelia - code M2191-MCUP) was maintained in agar-based media at 4°C, and also preserved in cryotubes in a 20% glycerol solution in liquid nitrogen. For mycelium growth, the strain was transferred to petri dishes (90 mm x 16,2 mm) with 25 mL of potato dextrose agar (PDA) media (see Table 4), at 25°C in the dark, until the mycelium covered most of the medium, approximately 8 days. After, the plates were kept at 4°C.

2.4.2 Mycelium growth in liquid substrate

To grow the mycelium in liquid substrate, 2 pieces from the stock agar plates, with approximately 4 cm x 4 cm, were inoculated in a 2 L Erlenmeyer flask containing 1 L of medium (see Table 4), supplemented, or not (controls), with 0.2mM zinc sulphate heptahydrate ($ZnSO_4.7H_2O$). The mycelium was allowed to grow for 7-9 days with an agitation of 120 rpm at RT, in the dark. The newly grown mycelia were harvest using a 450-mm diameter sieve (stainless steel, 500 µm aperture width, VWR, Serial-No: 71194820), washed twice with PBS 1x (without calcium and magnesium), followed by 2 steps of centrifugation (10 min, 3.000g) and stored at -80°C until freeze drying.

Table 4. **Composition of liquid medium for *Pleurotus ostreatus* mycelia growth**

Chemical	*Concentration*	*Company*	*Order number*
Glucose	20 g/L	Sigma-Aldrich	G7021-1KG
Malt extract	20 g/L	Thermo Scientific	10188572-1000G
Potato dextrose agar	39 g/L	Sigma-Aldrich	70139-500G
Yeast extract	3 g/L	Sigma-Aldrich	Y1625-250G
KH_2PO_4	0.46 g/L	Sigma-Aldrich	P5655-500G
K_2HPO_4	1 g/L	Merck	105104.1000
$MgSO_4$	0.5 g/L	PanReac AppliChem	142486.1211
$ZnSO_4.7H_2O$	58 mg/L	Sigma-Aldrich	Z0251-500G
Chloramphenicol	25 mg/L	Sigma-Aldrich	C0378-5G

*solid and liquid media had a pH between 5.5 and 6, and were autoclaved (15 min, 121ºC) before adding chloramphenicol and/or $ZnSO_4.7H_2O$.

2.4.3 Freeze drying of mycelia

The mycelia were lyophilized under the following conditions: freezing phase 10min @5°C, -50°C @ 1°/min for 30 min hold; drying phase PD:74mTorr/0.1 mbar, -5°C, @ 1°/min, delta p=5mTorr, SD: +40°C @ 1°/min, 8h. Freeze drying was performed by Ivonne Seifert and Elena Richert at the Institute of Pharmaceutical Technology & Biopharmaceutics, Department of Pharmacy, Ludwig-Maximilians University of Munich (LMU), Munich, Germany.

2.5 Protein extraction from *Pleurotus ostreatus* mycelia

The dried mycelia was lysed using the Precellys lysing kit VK05 for tough micro-organisms, containing 0.5mm glass beads (Bertin Instruments, REF P000913-LYSK0-A), in the Minilys tissue homogeniser (Bertin Instruments). A total amount of 34-36 mg of dried mycelium was weight in the tubes and 0.8 mL of lysis buffer (see Table 5) added. In the Minilys, the tubes were subjected to 3 cycles of 20 seconds each with 30 seconds interval, at 6500 rpm. The tubes were centrifuge twice for 10 min at 16.000g and 4°C. The supernatant was recovered and centrifuge for 10 min at 16.000g and 4°C. The protein extract was used for protein determination (see Bradford method) and dialysed or used for protein determination and stored at -80°C.

Table 5. **Composition of the lysis buffer used for *Pleurotus ostreatus* mycelium protein extraction**

Chemical	*Concentration*	*MW (g/mol)*	*Weight*	*Volume (mL)*	*Company*	*Order number*
Tris Base	50mM	124.14	0.151 g	25	VWR	103156X
CHAPS	2%	614.88	0.5 g	25	Abcam	Ab141396
Protease inhibitor cocktail (EDTA-free)	½ tablet	----	----	25	Merck-Roche	11873580001

*pH 7.4

2.6 Dialysis assays

The dialysis assays were performed using the Float-A-Lyzer® G2 Dialysis Devices (Spectra/Por® Dialysis Membrane, Spectrum Laboratories, Inc, USA) with different molecular weight cut-offs (0.5-1, 20 and 100KDa), 1:500 against dialysis buffer. Before dialysis, the Float-A-Lyzer® G2 were remove by firmly holding the collar of the top-piece with one hand and the packaging tube with the other hand. The cap of the devices was removed, the device filled and subsequently submerged in 10% ethanol for 10 min. After, the solution was removed and the device flush thoroughly with deionized water (DI), followed by 20 min incubation with DI. The solution was removed from the device and 1 mL of *P. ostreatus* protein extract added for overnight dialysis at 4°C with stirring.

2.7 Cell culture

2.7.1 HepG2 cell line (ATCC® HB-8065TM)

The HepG2 cell line is derived from a liver hepatocellular carcinoma of a 15-year-old Caucasian male (Organism: Homo sapiens, human). HepG2 cells are widely used as an *in vitro* model alternative to primary human hepatocytes, in drug metabolism and to study hepatotoxicity, free fatty acids lipotoxicity and steatosis[199, 200].

2.7.1.1 Initiating a new cell culture

A frozen cell vial was thawed at 37°C and the content transferred to a falcon containing 10 mL of fresh, pre-warmed cell culture medium. The HepG2 cells were centrifuged at 250g for 5 min and the supernatant discarded. The cells were transferred to a 25 cm^2 flask with fresh Minimum Essential medium (MEM, ThermoFisher Scientific, 11900073) cell culture medium, supplemented with sodium bicarbonate (2.2g/L), sodium pyruvate (0.11g/L), 10% fetal bovine serum (FBS) (50 mL) or 2% fetal bovine serum (FBS) (10 mL), 1% penicillin-streptomycin (5 mL) and 1% NEAA (5 mL). Fetal bovine serum (FBS), penicillin-streptomycin (10.000 U/mL), 0.05% Trypsin– EDTA, Non-essential amino acids (NEAA) were purchased from Gibco-Invitrogen, Grand Island, New York, USA.

The cells were incubated in a humid atmosphere with 5% CO_2 at 37°C. After 24 hours, the medium was replaced to remove dead cells. When the cellular confluency was approximately

80%, a 1:2 dilution was performed into a 10 cm cell culture dish, and the cells incubated in MEM medium (5mM glucose, 10% FBS) in a humid atmosphere with 5% CO_2 at 37°C until used.

2.7.1.2 Cell passage

HepG2 cells were sub-cultured when reached, approximately, 80% confluence. The cells were washed with PBS 1X (no magnesium, no calcium) and treated with 0.05% trypsin-EDTA for 5 min at 37°C. After the detachment of the cells, they were collected in MEM medium (5mM glucose, 10% FBS) and centrifuged for 5 min at 250g. HepG2 cells were re-suspended in adequate volume of medium and cell number evaluated by counting them in the presence of trypan blue dye in the BioRad TC20TM Automated Cell Counter. Afterwards, cells were seeded in 10 cm cell culture dishes with a density of $2x10^6$ cells/plate.

2.7.1.3 Seeding the cells

HepG2 cells were re-suspended in MEM medium (5mM glucose, 10% FBS) and seeded in 96-well plates for 24 hours, with a density of $2x10^4$ cells/well, 150 µL per well ($1.33x10^5$ cell/mL).

2.7.2 HepG2 cells treatment

HepG2 cells were seeded in 96-well plates for 24 hours (as previously described). To evaluate the mushroom extracts cytotoxicity, cell culture medium was replaced by MEM medium (5mM glucose, 10% FBS) after 24 hours plus mushroom extracts (ethanol and aqueous) in the following concentrations: 1.95, 3.9, 7.8, 15.62, 31.25, 62.5, 125, 250, 500 and 1000µg/mL.

To establish the *in vitro* model to study hepatic steatosis, cell culture medium was replaced by MEM medium (5mM glucose, 2% FBS) after 24 hours, plus 125µM free fatty acids (FFA)-Bovine serum albumin (BSA) mixture. The FFA mixture was composed by palmitic acid (C16:0), stearic acid (C18:0), oleic acid (C18:1), linoleic acid (C18:2) and arachidonic acid (C20:4), purchased from Sigma-Aldrich Chemical Co., Saint Louis, MO, USA. The free fatty acids were dissolved in 25mM KOH at 70°C, to a final concentration of 10mM. After cooled at room temperature (RT), the FFA were mixed in the amounts indicated in Table 6. Afterwards, an equal volume of 20% BSA solution was added to the fatty acid mixture and incubated for 10 min at 56°C. The FFA-BSA mixture was filtered (0.2 µm filter) in sterile conditions and stored -20°C. The FFA-BSA solution, with a final concentration of 5mM, could be stored several months at -20°C. The 20% BSA solution was prepared by dissolving 4g of fatty acid free BSA in

20 mL of DPBS 1x (no magnesium and calcium) and heated up to 37°C to improve solubilization. The pH of the BSA solution was adjusted to 7.4 with 1M sodium hydroxide (NaOH) and stored at -20°C. Additionally, a solvent control (BSA-KOH) was prepared out of 20% BSA in PBS 1x (no magnesium and calcium) in an equal ratio with KOH, following the same heating, filtration and storing process.

Table 6. **Composition of fatty acids mixture for HepG2 cells treatment**

Fatty acids	*Abbreviation*	*[%]*	*mL*
Palmitic acid	C-16:0	39	3,9
Stearic acid	C-18:0	5.5	0,55
Oleic acid	C-18:1	50	5,0
Linoleic acid	C-18:2	3.7	0,37
Arachidonic acid	C-20:4	1.8	0,18

To evaluate the hepatoprotective effect of the mushrooms aqueous extracts in the *in vitro* model of hepatic steatosis, cell culture medium was replaced after 24 hours by MEM medium (5mM glucose, 2% FBS) containing 125µM of the FFA-BSA mixture, and the cells incubated for a 24 hours period. Afterwards, culture medium was replaced, and new medium was added containing 125 µM FFA-BSA plus mushroom aqueous extracts in the following concentrations: 250, 500 and 1000µg/mL for another 24 hours' time period. Total assay duration was 48 hours.

2.7.3 The Caco-2 cell line (ECACC® 86010202)

Caco-2 cell line is derived from a colorectal adenocarcinoma of a 72-year-old Caucasian male (Organism: Homo sapiens, human). This cell line was established at the Sloan-Kettering Institute for Cancer Research by Jorgen Fogh[201]. The Caco-2 cells, when seeded in a Transwell® system (Figure 5), are able to differentiate in enterocyte-like cells and form a tight monolayer resembling the gut barrier with microvilli formation on the apical side, as well as tight junctions between cells[202, 203]. This model is widely used as an *in vitro* model to study the absorption and transport of compounds through the intestinal barrier[48, 204, 205]. The ATP7B Caco-2 knockout cell line was gratefully received from Dr. rer. nat. Andree Zibert (UKM Münster), where the ATP7B knockout was created using CRISPR/Cas9 technique[97]. The Caco-2 cell line used to generate the ATP7B knockout cell line was acquired from the American Type Culture Collection (ATCC, Manassas, USA).

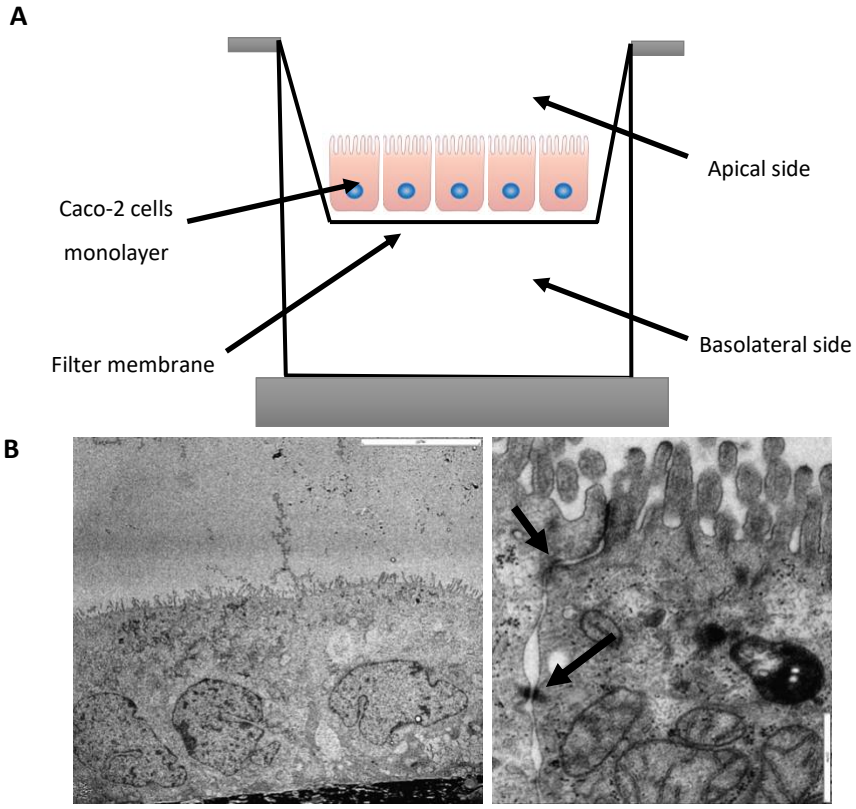

Figure 5. **Differentiation of Caco-2 cells in enterocyte-like cells forming a monolayer**. **(A)** The Caco-2 cells can differentiate in enterocyte-like cells on a filter membrane to form a monolayer. This *in vitro* model can be used to analyse passing of compounds through the biological barrier, or their impact on the barrier per se. **(B)** Caco-2 cells differentiated for 21 days, in a trans-well system. Electron micrographs of the epithelial cell barrier (scale bar: 10 µm, right image, and 0.5 µm, left image), black arrows: tight-junctions.

2.7.3.1 Initiating a new cell culture

A frozen cell vial was thawed at 37°C and the content transferred to a falcon containing 10 mL of fresh, pre-warmed cell culture medium. The Caco-2 cells were centrifuged at 200g for 5 min and the supernatant discarded. The cells were transferred to a 10 cm plate with fresh culture medium (DMEM, 25mM glucose, 10% FCS) and incubated in a humid atmosphere with 5% CO_2 at 37°C. When the cells reached a confluence of approximately 80%, a first cell passaging was performed as described below.

2.7.3.2 Cell passage and seeding

Caco-2 cells were sub-cultured when reached, approximately, 80% confluence. The cells were washed twice with PBS 1X (no magnesium, no calcium) and treated with 0.05% trypsin-EDTA for 5 min at 37°C. After detachment of the cells, they were collected in 10% FCS culture medium (Table 7) and centrifuged for 5 min at 200g. Caco-2 cells were re-suspended in adequate volume of medium and cell number evaluated by counting them in the presence of erythrosine B or trypan blue dye in the LUNA^{II} Cell Counter. For passaging and maintenance, cells were seeded in 10 cm cell culture dishes with a density of $1x10^6$ cells/plate for 4 days, or $7.5x10^5$ cells/plate for 3 days, in DMEM (25mM glucose, 10% FCS).

Table 7. **Medium composition**

Media	*10 % FCS*	*2 % FCS*
DMEM high glucose (25 mM)		
Fetal Calf Serum (FCS)	56.0 mL	10.2 mL
Non-Essential Amino Acids (NEAA) (100X)	5.6 mL	5.6 mL
Penicillin Streptomycin (10 000 U/mL)	5.6 mL	5.6 mL

2.7.3.3 Cell differentiation

For differentiation, $2x10^6$ cells, $3.3x10^5$ and $2.8x10^4$ cells were cultivated in Corning™ Costar Transwell® PET (Polyethylene terephthalate) permeable supports (pore size 0.4 μm) with 44 cm^2, 4.67 cm^2 and 0.33 cm^2, respectively; $5x10^4$ cells were cultivated in Nunc™ Polycarbonate Cell Culture Inserts with 0.47 cm^2 (pore size 0.4 μm).

2.7.3.4 Evaluation of cellular differentiation: Transepithelial electrical resistance (TEER) and capacitance (C_{cl}) measurements

Principle of the assay: The transepithelial electrical resistance (TEER) measurement is a technique that provides information about the integrity of the epithelial barrier upon differentiation of the Caco-2 cells in a Transwell® system[204]. The TEER values are directly correlated with the permeability of the cellular monolayer[206]. To measure the TEER, trans-wells are transferred to the CellZscope (nanoAnalytics®) Transwell® system in which two electrodes are placed in the cell culture medium, one at the apical compartment, and the other at the basolateral compartment, that measure the resistance of the cellular monolayer by a voltmeter[203, 204]. In parallel, the capacitance of the membrane (C_{cl}) is also measured, which is proportional to the cell surface[207]. In this system, the plasma membrane acts as a capacitor, where the phospholipid bilayer is a thin isolator, separating two electrolytic media, the extracellular compartment from the cytoplasm. This parameter can also be measured and is an indicator for the microvilli expression and extrusions of other membranes[206, 207]. Only wells with a TEER higher than 200 Ω.cm^2 and a C_{cl} between 2-6 μF/ cm^2 were selected for analysis and/or treatments. After differentiation for 14 or 21 days, Caco-2 cells were transferred to the Transwell® system and incubated at 37°C with 5% CO_2. The measurement of TEER and C_{cl} were initiated 24 hours before any treatments to reach signal stability.

2.7.4 Caco-2 cells treatments

For treatments, Caco-2 cells were re-suspended in medium (DMEM, 25mM glucose, 10% FCS) after centrifugation, and seeded in different plates with the respective cell densities, volumes and time of incubation, before the starting of the treatment, listed in Table 8. A DMEM 25mM glucose, 2% FCS medium was used for all treatments, except for the ones applied to differentiated Caco-2 cells in a Transwell® system. Cells were maintained at 37°C with 5% CO_2.

Table 8. **Caco-2 cells seeding information**

Plate	*Density (cells/mL)*	*Volume/ well (µL)*	*Number of cells/well*	*Days until confluence/ differentiation*
96-wells	$2.0x10^5$	100	$2.0x10^4$	4 days
96-wells (Seahorse XFe96 FluxPak mini - 102601-100)	$5.0*10^4$	100	$5.0*10^3$	2 days
6-wells	$5.0*10^5$	1000	$5.0*10^5$	3 days
8-well ibidi	$2.0x10^5$	200	$4.0x10^4$	4 days
PET-TW permeable supports (12 well inserts, 6.5 mm, 0.4 µm pore size)	$5.6*10^5$	200	$2.8*10^4$	4, 7, 14 or 21 days
PET-TW permeable supports (6 well inserts, 24 mm, 0.4 µm pore size)	$1.87*10^5$	2000	$3.3x10^5$	7, 14 or 21 days
PET-TW permeable supports (75 mm, 0.4 µm pore size)	$2.0*10^6$	1000	$2.0*10^6$	7, 14 or 21 days
10 cm	$0.5\text{-}1.0*10^5$	10000	$0.5\text{-}1.0*10^6$	4 days

PET: Polyethylene terephthalate; TW: Trans-well

2.7.4.1 Copper toxicity

Caco-2 WT and Caco-2 ATP7B KO cells were seeded into 96 well plates and treated for 24 hours with increasing doses of copper chloride, $CuCl_2$ (20 – 500µM) or Copper-Histidine, Cu-His (20 – 1000µM). Caco-2 WT and Caco-2 ATP7B KO cells, seeded in Transwell® PET permeable supports with 6.5 or 24 mm (pore size 0.4 µm), were treated with DMEM (25mM glucose, 10% FCS) alone or containing 100µM $CuCl_2$, from the 7th day, until the 21st day of differentiation, with medium exchange performed every 2 days, with the abovementioned treatment. The stock solution of copper(II)chloride dihydrate ($CuCl_2.2H_2O$) was prepared in

Milli-Q water to a final concentration of 50mM. The Cu-His stock solution was prepared by dissolving 0.108g $CuCl_2.2H_2O$ and 0.3336g L-Histidine in a 0.9% sodium chloride (NaCl) solution to a final concentration of 6.34mM, as it was described earlier by Hoppe-Tichy and co-workers[208]. The pH was adjusted to 7.4 using a 0.2M NaOH solution. Both stock solutions were sterile filtrated using a 0.2 µm filer and stored at 4°C.

2.7.4.2 Free fatty acids

Caco-2 WT and Caco-2 ATP7B KO cells seeded in 96 well or 8 well ibidi plates were treated with a free fatty acids (FFA) mixture (Table 9) complexed with bovine serum albumin (BSA), in a concentration of 500µM, with the aim of mimicking the composition of an obesity-inducing diet. Treatments lasted either 24 or 48 hours in DMEM (25mM glucose, 2% FCS), at 37°C with 5% CO_2.

Table 9. **Fatty acid composition resembling a high fat diet (Altromin™ C1090-45)**

Fatty acid	*Abbreviation*	*[%]*	*mL*
α-Linolenic acid	C-18:3	7.95	0.795
Linoleic acid	C-18:2	21.85	2.185
Palmitic acid	C-16:0	61.6	6.160
Stearic acid	C:-18:0	3.58	0.358
Oleic acid	C-18:1	2.51	0.251

The FFA listed on Table 9 were dissolved in 25mM potassium hydroxide (KOH) and prepared in stock solutions of 10mM. For homogenous solutions, the stocks were saponified for a few minutes at 70°C before storing at -20°C for up to several months. For complexation, a 20% BSA solution was prepared by dissolving 4g of fatty acid free BSA in 20 mL of DPBS 1x (no magnesium and calcium) and heating the solution up to 37°C to improve solubilization. The pH of the BSA solution was adjusted to 7.4 with 1M NaOH and stored at -20°C. To prepare the FFA-BSA solution, the FFA listed on Table 9 were mixed in the respective concentrations with an equal volume of BSA solution and heated in a water bath at 56°C for 10 minutes. The final 5mM FFA-BSA solution was sterile filtered through a 0.2 µm filter and could also be stored at -20°C for a several months. Additionally, a solvent control (BSA-KOH) was prepared out of 20% BSA in DPBS 1x (no magnesium and calcium) in an equal ratio with KOH, following the same heating, filtration and storing process.

2.7.4.3 Methanobactin (MB) treatment

Caco-2 ATP7B KO cells, seeded in Transwell® PET permeable supports with 6.5 or 24 mm (pore size 0.4 μm), were treated with DMEM (25mM glucose, 10% FCS) alone or containing 50μM MB (Zn stabilized), from the 7th day, until the 21st day of differentiation, with media exchanges performed every 2 days, with the abovementioned treatment. Methanobactin (MB) was isolated from the spent media *of Methylocystis* as described previously [107]. For stabilization[68], pre-labelling of MB with Zn was done by mixing equal volumes of an 18mM zinc acetate solution with a 20mM MB solution, prepared in 100mM Tris buffer (pH 7.4). The solution was sterile filtrated using a 0.2 μm filter and stored at 4°C.

2.7.4.4 Zinc toxicity

Caco-2 WT cells were seeded into 96 well plates and treated for 24 hours with increasing doses of zinc(II)sulphate heptahydrate, $ZnSO_4.7H_2O$ (125 – 2000 μM). The $ZnSO_4.7H_2O$ stock solution was prepared in Milli-Q water to a final concentration of 5mM, sterile filtrated using a 0.2 μm filter and stored at 4°C.

2.7.4.5 Pleurotus ostreatus protein extract and Zinc salt treatments

Caco-2 WT cells were seeded in 96 well or 6 well plates and treated with *P. ostreatus* zinc-enriched mycelia protein extract - ZM(PO), and control mycelia protein extract - M-Ctrl(PO), in an equivalent volume to the treatment of the cells with ZM(PO), which corresponds to a zinc concentration of 18.5 or 37μM. Co-treatments with $CuCl_2$ were performed for 48 hours in the following concentrations: 200μM $CuCl_2$ + ZM(PO) 18.5μM. Caco-2 WT cells were seeded in a PET Trans-well system (24 or 6.5 mm), maintained for 21 days in culture medium and incubated in a humid atmosphere with 5% CO_2 at 37 °C, with a medium change every 2-3 days. Afterwards, Caco-2 WT cells were treated with 100μM $CuCl_2$ and 100μM $CuCl_2$ + 20μM ZM(PO), from the 14th day of differentiation on, up to 20 days of differentiation, with fresh treatment added every 48 hours. Caco-2 ATP7B KO cells were treated with 100μM $CuCl_2$, 20μM ZM(PO) and 100μM $CuCl_2$ + 20μM ZM(PO), from the 4th day of differentiation on, up to 21 days of differentiation, with fresh treatment added every 48 hours.

2.8 Toxicity assays

2.8.1 Resazurin assay

Principle of the assay: Resazurin acts as an intermediary acceptor of electrons, being reduced to resorufin (pink and highly fluorescent) through the dehydrogenases in living cells. The fluorescence is proportional to the number of metabolically active cells[209, 210].

A stock solution of resazurin was prepared by dissolving 10mg of resazurin sodium salt in 10 mL of PBS 1X. Afterwards, the solution was filtered with a 0.2 µm pore filter and stored at -20°C. The resazurin working solution was prepared by adding 0.1 mL of the stock solution (10µg/mL) to 9.9 mL of culture media. The cell culture medium was completely removed and cells were incubated with 80µL of the prepared resazurin solution in a humid atmosphere with 5% CO_2 at 37°C for 1 hour. The amount of resazurin reduced to resorufin was measured fluorometrically at an excitation wavelength of 540 nm and emission set at 590 nm in a ClarioStar plate reader (BMG-Labtech, Germany).

2.8.2 CellTiter-Glo Luminescent Cell Viability assay

Principle of the assay: Indicates the ATP levels of metabolically active cells. The enzyme luciferase uses ATP as a co-factor, and acts on luciferin to produce oxyluciferin, in which energy is converted in luminescence. The luminescence produced is proportional to the amount of ATP present, and it relates directly to the number of living cells present in culture[211].

The ATP levels in living cells were measured using a commercial kit (Promega, Fitchburg, WI, USA) according to the manufacturer's protocols. An aliquot of CellTiter-Glo Reagent was thawed to RT and 50µL added to the cells after total removal of the cell culture medium. The cells were incubated at RT for 2 min (constant shake) to induce cell lysis. Afterwards, cells were incubated for 10 min, at RT to stabilize the luminescence signal. Luminescence was recorded in a ClarioStar plate reader (BMG-Labtech, Germany).

2.8.3 Sulforhodamine B assay

Principle of the assay: Sulforhodamine B (SRB) is a pink dye that binds to basic amino acids of cellular proteins[212, 213], and the amount of dye extracted from stained cells is proportional to the amount of living cells after treatment.

The culture medium was completely removed and the cells washed once with PBS 1X, followed by fixation with 1% acetic acid in ice-cold methanol during, at least, 2 hours at -20°C. Afterwards, the fixed cells were removed from -20°C and the 1% acetic acid in ice-cold methanol solution let to evaporate under the chemical hood. After, the fixed cells were incubated with 0.05% SRB in 1% acetic acid solution at 37°C for 1 hour, washed with 1% acetic acid in MiliQ H_2O and dried at 37°C. To re-suspend the dye (SRB), 150µL of Tris (pH 10) were added to the fixed cells followed by 10-15 min constant shake at RT, until complete solubilization. The SRB content was measured fluorometrically at an excitation wavelength of 510 nm and emission set at 620 nm, in a ClarioStar plate reader (BMG-Labtech, Germany). The Tris-NaOH solution was prepared by dissolving 0.64g of Tris base in 400 mL of MiliQ-H_2O and the pH adjusted to 10 with 1 M NaOH.

2.8.4 Nile red - fatty acid content

Principle of the assay: Nile red (9-diethylamino-5H-benzo[a]phenoxazine-5-one), is a vital stain that acts as a lysochrome binding to lipids including triglycerides, fatty acids and lipoproteins. Since it does not bind to any other substance it allows the quantification of lipids when applied to cells in aqueous conditions[214, 215].

A Nile red stock solution was prepared to a final concentration of 0.5mg/mL in acetone. The working solution was freshly diluted 1:200 in DMEM medium and 100µL added to the cells after medium removal. The cells were incubated for 2 hours, in a humid atmosphere with 5% CO_2 at 37°C. Afterwards, the Nile red solution was removed, the cells washed once with PBS 1X and new PBS 1X was added. Fluorescence was measured at an excitation wavelength of 520 nm and emission set at 640 nm in a ClarioStar plate reader (BMG-Labtech, Germany).

2.8.5 Live-death staining/Dye exclusion test

Principle of the assay: Viable cells present with intact cell membranes that exclude certain dyes, such as Trypan blue and Erythrosine B. Therefore, upon incubation with the dye, viable cells will present with a clear, translucent cytoplasm under the light microscope, while non-viable cells will have a blue/pink cytoplasm[216, 217].

Caco-2 cells were harvested by washing the 6 wells/10 cm plates twice with PBS 1X (no magnesium, no calcium) and treated with 0.05% trypsin-EDTA for 5 min at 37°C. After detachment, the cells were collected in new cell culture medium and centrifuged for 5 min at 200g. The cells were re-suspended in adequate volume of medium and incubate for 2 minutes with Trypan blue/Erythrosine B (EB) in a 1:2 dilution followed by counting in a Neubauer chamber or in the LUNA^{II} Cell Counter (Logos, Biosystems).

2.8.6 Neutral red assay

Principle of the assay: Neutral red is a weakly cationic dye that is able to cross the cell membrane via passive diffusion and concentrate in the lysosomes. The uptake of neutral red depends on the capacity of the cells to maintain pH gradients, through the production of ATP. The dye presents a net charge close to zero at pH 7.4, but becomes charged inside lysosomes, or other acidic compartments, and remains trapped. The extraction of the dye from viable cells can be achieved by using an acidified ethanol solution, after washing all the non-bound dye[218].

A Neutral red stock solution was prepared to a final concentration of 4mg/mL in PBS 1X. The treatment medium was removed from the cells and 100µl of a 1:100 neutral red working solution, in new culture medium (2% FCS) was added to the wells. After 2 hours' incubation in a humid atmosphere with 5% CO_2 at 37°C, the neutral red solution was removed and the cells washed twice with 150µl PBS 1X. Afterwards, 150µl of a de-staining solution (50% ethanol plus 1% acetic acid in MilliQ-H_2O) was added, and the cells incubated for 10 min at RT with agitation. The relative fluorescence units were measured at an excitation wavelength of 520 nm and an emission wavelength of 620 nm, in a ClarioStar plate reader (BMG-Labtech, Germany).

2.9 Protein determination (Bradford method)

Principle of the assay: Positively charged proteins bind to the Coomassie Brilliant Blue causing a shift in the maximum absorption of the dye from its cationic form at 465 nm, to its anionic form at 595 nm. This shift is accompanied by a colour change from brown to blue which is detected spectrophotometrically at a wavelength of 595 nm[219].

For quantification of protein content in a giving sample, a standard curve was prepared using BSA standards in concentrations of 0, 0.5, 1, 2 and 5µg/µL in ddH_2O. A volume of 5µL of both standards and samples was added to plastic cuvettes containing 1 mL of a 1:5 diluted Bradford solution, with a beam path of d = 1 cm at 590 nm and 450 nm. The values were recorded in duplicate. To calculate the protein content, the average of both measured values was calculated and then divided by the dilution factor five.

2.10 Animal Studies

Animals were maintained under the Guidelines for the Care and Use of Laboratory Animals of the Helmholtz Centre Munich. Animal experiments were approved by the government authorities of the Regierung von Oberbayern, Munich, Germany. The rats of both sexes (strain name LPP[67]), heterozygous controls (LPP *Atp7b*$^{+/-}$) and LPP *Atp7b*$^{-/-}$ were fed ad libitum on 1314, Altromin Spezialfutter GmbH, Germany (Cu content, 13.9 mg/kg), and tap water. Serum ALT, AST and bilirubin levels were measured with the Reflotron system (Roche Diagnostics, Penzberg, Germany) and liver damage in animals was considered clinically apparent if serum AST level is above 200 U/L and/or bilirubin level is above 0.5 mg/dL [68, 70].

2.10.1 The pilot study of *Pleurotus ostreatus* zinc-enriched mycelia diet

Feeding of LPP *Atp7b*$^{-/-}$ animals with a *P. ostreatus* zinc-enriched mycelium diet was approved (AZ_55.2-2532.Vet_02-21-105) by the government authorities of the Regierung von Oberbayern, Munich, Germany. A total of three LPP *Atp7b*$^{-/-}$ females (84 days old) were fed a zinc-enriched mycelium diet (see Table 10.) for 6 days. Afterwards, the animals were 24 hours in a metabolic cage (Figure 6.B) to 1) access body weight (BW), food and water intake (FI), and b) collect urine and faeces for metal analysis. Afterwards, animals were switched back to a normal chow diet (Altromin^{TM} 1310, see Table 10). A blood sample (BS) was collected from the animals via the sublingual vein under narcosis (isoflurane) at key time points (Figure 6.A)

to track animal values of AST, ALT and Bilirubin. Upon elevation of AST values above 100 U/L, animals started the second feeding cycle that lasted 7 days, ending with 24 hours in a metabolic cage (Figure 6.A). Treated animals and correspondent non-treated LPP *Atp7b*$^{+/-}$ controls were sacrificed after isoflurane overdose and bleeding. Small intestine was recovered, and tissue homogenates were prepared for mitochondria isolation and metal content determination. Isolated mitochondria was used for imaging via transmission electron microscopy (TEM, see 2.15) and metal content determination. Liver, kidney, heart, spleen and brain were recovered for homogenate preparation and metal content determination. This experiment was done together with Tamara Rieder, Judith Sailor, Judith Nagel and Quirin Reinold (Institute for Molecular Toxicology and Pharmacology (HMGU) and Institute of Toxicology and Environmental Hygiene (TUM), Munich, Germany).

Table 10. **Composition of a normal rat chow diet (Altromin™ 1310) and the mycelia-enriched food paste.**

	Pellets (% of total weight)	*Water (% of total weight)*	*Mycelia (% of total weight)*	*Copper content (mg/100g)*	*Zinc content (mg/100g)*
Altromin™ 1310	100	0	0	1,389	8,499
Mycelia-enriched food	38,6	54,5	7	0,229	21,46

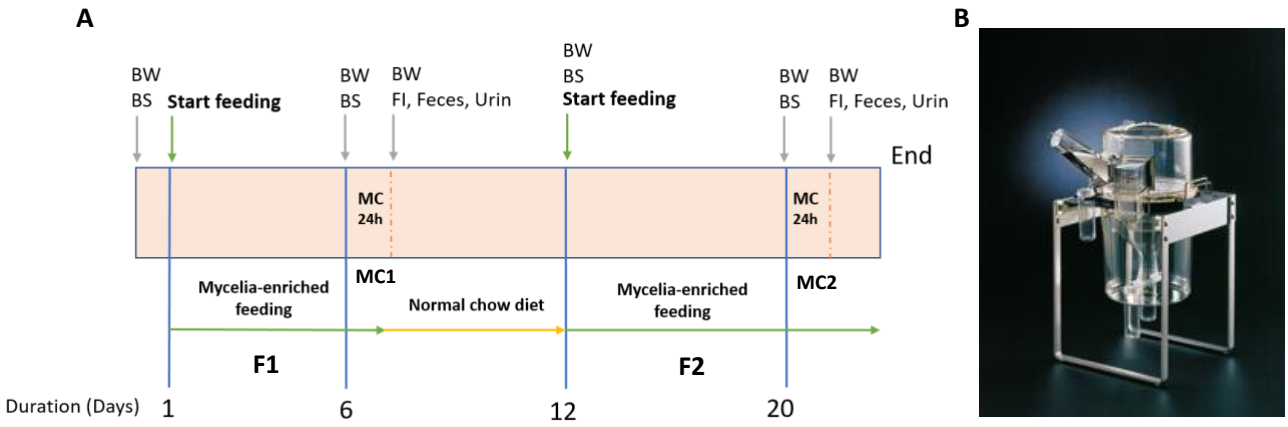

Figure 6. **(A) Scheme of the Pilot study: *Pleurotus ostreatus* zinc-enriched mycelia feeding. (B) Metabolic cage used during the pilot study.** F1: 1st feeding cycle; F2: 2nd feeding cycle; MC: metabolic cage; MC1: 1st metabolic cage; MC2: 2nd metabolic cage; BS: blood sample; BW: body weight; FI: food and water intake

2.11 Metal analysis

Principle of the assay: Inductively coupled plasma optical emission spectroscopy (ICP-OES) was used for the determination of copper, zinc and iron. This analytical method relies on the excitation of electrons to a higher energy level caused by the acceleration and collision with argon atoms. This process creates ionized atoms within a plasma. Upon relaxation, the electrons return from the excited state to the "ground state" with a photon emission at specific wavelengths that is measured to obtain the concentration of a specific element in a sample [220].

Samples were analysed by ICP Optical Emission Spectrometry (Ciros Vision, SPECTRO Analytical Instruments GmbH, Kleve, Germany) by Peter Grill (from the Department of Environmental Science, Research Unit Analytical BioGeoChemistry, HMGU, Munich, Germany), after wet-ashing of samples with 1.5 mL of 65% Nitric acid.

2.12 Mitochondria isolation from cell culture

Isolation of mitochondria from cells was performed using a pump-controlled cell rupture system (PCC), a cell homogeniser (Isobiotec™, Germany) combined with 1 mL syringes (internal diameter 4.608 mm, SGE Supelco, USA) and a high precision pump (pump 11, Harvard apparatus, USA). A 6-micron tungsten carbide ball was inserted in the cell homogeniser, and a delivery speed of 1000 µl/min was applied to 1 mL cell suspension in order to rupture the cell membrane, but not the nucleus, and release the mitochondria[221, 222]. Caco-2 WT and ATP7B KO cells were harvest after respective treatments and counted in the LUNA^{II} Cell Counter (Logos, Biosystems). A suspension of 5.5-6x10^6 cells/mL was prepared in isolation buffer (300mM sucrose, 5mM TES, 200µM EGTA, pH 7.2). The sample was loaded in the syringe and passed 3 times through the system at a constant rate (1000 µl/min). In order to recover the whole homogenate, the system was rinsed once with 1 mL isolation buffer. Afterwards, the sample was centrifuged (800g, 5 min at 4°C), followed by a second centrifugation (9.000g,10 min at 4°C) of the recovered supernatant. The mitochondria-enriched pellet was re-suspended in isolation buffer and kept on ice until protein content determination (see 2.9) or storage at -80°C.

2.13 Analysis of rat intestine tissue

2.13.1 Swiss roll technique

Intestine from LPP *Atp7b*$^{+/-}$, still healthy and diseased LPP *Atp7b*$^{-/-}$, was cut free from the stomach and transferred to a clean petri dish containing PBS 1X. The cecum was removed, as well as mesenteric connective and fat tissue. The small intestine and colon were gently unravelled and flushed with a 10 mL syringe containing modified Bouin's fixative (50% ethanol and 5% acetic acid in ddH_2O) for simultaneous cleaning and fixation. Afterwards, the small intestine was longitudinally cut open along the mesenteric line and separated in 3 equal segments: duodenum, jejunum and ileum. For each segment, the proximal and distal ends were marked. Using clean petri dishes, the intestinal segments were placed with the luminal side facing upward. For the colon, the luminal side was identified by the variegations/ridges running across its width. Handling one segment at a time, each one was flat opened with the luminal side up and pulled with forceps from its proximal end toward the edge of the Petri dish. The edge of the proximal end was wrapped around a toothpick using a pair of forceps,

and slightly pinched to start the rolling step. Carefully, all the intestinal sections were rolled and afterwards removed from the toothpick into a tissue-processing/-embedding cassette with 10% buffered formalin. The samples were kept at RT in formalin for up to 48 hours. This protocol was updated from Bialkowska *et al.*[223].

2.13.2 Haematoxylin and Eosin (H&E) staining

The sections of the intestine prepared by swiss rolling and fixed in 10% buffered formalin were embedded in paraffin and sectioned using a microtome. The obtained sections were deparaffinized using xylene and rehydrated in isopropanol and descending alcohol series (Table 11). Next, the sections were stained in Mayer´s haematoxylin and exposed to eosin followed by dehydration using different ethanol solutions, isopropanol and xylol.

Table 11. **Procedure for H&E staining of intestinal section**

Chemical	*Time*
100% xylene	2 x 5 min
Isopropanol	2 x 5 min
96% ethanol	2 x 1 min
70% ethanol	2 x 1 min
ddH_2O	25 s
Mayer´s haematoxylin solution	8 min
Tap water	10 min
1% aqueous eosin solution	4 min
ddH2O	1 min
70% ethanol	30 s
96% ethanol	30 s
Isopropanol	2 x 25 s
100% xylene	2 x 1.5 min

2.13.3 Periodic acid-Schiff (PAS) staining

The sections of the intestine prepared by swiss rolling and fixed in 10% buffered formalin were embedded in paraffin and sectioned using a microtome. The obtained sections were deparaffinized using xylol and rehydrated in descending alcohol series (Table 12). Next, the sections were stained with periodic acid 0.5%, washed and exposed to Schiff reagent, followed

by washing and staining with Mayer´s haematoxylin. Afterwards, the sections were again dehydration using different ethanol solutions and xylol.

Table 12. **Procedure for PAS staining of intestinal section**

Chemical	*Time*
Xylol	3 x 2 min
100% ethanol	25 s
96% ethanol	2 x 25 s
70% ethanol	25 s
ddH_2O	25 s
0.5% periodic acid	15 min
Tap water	3 min
ddH_2O	10 s
Schiff reagent	15 min
Tap water	3 min
ddH_2O	10 s
Mayer´s haematoxylin solution	8 min
Tap water	6 min
96% ethanol	30 s
100% ethanol	2 x 25 s
Xylol	2 x 1.5 min

Paraffin-embedding, cutting and staining (H&E and PAS) of the intestinal sections was performed by the technicians at the Comparative Experimental Pathology Department, Institute for General Pathology and Pathological Anatomy, Technical University of Munich (TUM), Munich, Germany.

2.13.4 Preparation of rat duodenum homogenates and mitochondria isolation

Duodenum from LPP *Atp7b*$^{+/-}$, still healthy and diseased LPP *Atp7b*$^{-/-}$ was rinsed 2-3 times with ice-cold 0.9 % NaCl, the mesenteric connective and/or fat tissue removed, and the duodenum cut opened along the mesenteric line. The tissue was minced, directly placed in ice-cold isolation buffer (0.3M sucrose, 5mM TES, 0.2mM EGTA, 0.1% BSA (w/v), pH 7.2) and homogenized using a semi-automatic homogenizer (Schuett Biotec^{TM} Homgen^{Plus}, Göttingen, Germany), equipped with a Teflon-glass potter (Glas-Co, Cole-Palmer, UK), with 5 strokes at

1000 rpm. The homogenates were kept on ice until protein content determination (see 2.9), storage or mitochondria isolation. Mitochondria isolation was adapted from the protocol to isolate mitochondria liver, kidney and heart as recently reported[224]. Briefly, the homogenates were centrifuged twice (800g, 10 min, 4°C) for clearance of cell debris and nuclei and the supernatant centrifuged (9.000xg, 10 min, 4°C) to obtain the mitochondria-enriched pellet. The resulting crude pellet was further purified by a density gradient centrifugation (9.000g, 10 min, 4°C) using an 18/30/60% Percoll™ gradient system. The purified mitochondria were washed twice in BSA-free isolation buffer via centrifugation (9.000g, 10 min, 4°C) and re-suspended in the same buffer. The samples were kept on ice until protein content determination (see 2.9) and storage at -80°C.

2.13.5 Preparation of rat duodenum cytosol

Frozen duodenum tissue was homogenized by hand with a Teflon-glass homogenizer (Kontes glass Co., USA) in ice-cold BSA-free isolation buffer (0.3M sucrose, 5mM TES, 0.2mM EGTA, pH 7.2). Approximately 1 mL of the homogenate was centrifuged (100.000g, 1 h, 4°C) and the supernatant (duodenal cytosol) collected. For metal analysis, it was submitted 300µL of sample and the rest stored at -80°C.

2.14 Proteome analysis

2.14.1 Sample preparation

Caco-2 and Caco-2 ATP7B knockout cells were lysed with RIPA buffer 1X (10X #9806, Cell Signaling, Massachusetts, US) plus 1 mM phenylmethylsulfonyl fluoride (PMSF) for 30 min at 4°C, followed by a brief sonication and 10 min centrifugation at 800g, 4°C. LPP rat duodenum samples, homogenised in isolation buffer without BSA, were kept on ice. A total of 10 µg protein per replicate, from both cell lysates (N=6) and duodenum homogenates (N=3), was submitted to proteome analysis. Equal amounts were subjected to trypsin treatment applying a modified filter aided sample preparation (FASP)[225]. Peptides were collected by centrifugation (10 min at 14.000g), acidified with trifluoroacetic acid (TFA), and stored at -20°C.

2.14.2 Mass spectrometric measurements

Liquid chromatography with tandem mass spectrometry (LC-MS/MS) analysis was performed in data-dependent acquisition (DDA) mode. MS data were acquired on a Q-Exactive HF-X mass spectrometer (Thermo Scientific) online coupled to a nano-RSLC (Ultimate 3000 RSLC; Dionex). Tryptic peptides were loaded on a C18 trap column (300 µm inner diameter (ID) × 5 mm, Acclaim PepMap100 C18, 5 µm, 100 Å, LC Packings) at 30 µl/min flow rate. For chromatography, a C18 reversed phase analytical column (nanoEase MZ HSS T3 Column, 100Å, 1.8 µm, 75 µm x 250 mm, Waters) at 250nl/min flow rate in a 95 min non-linear acetonitrile gradient from 3 to 40% in 0.1% formic acid was used. The high-resolution MS spectrum was acquired within a mass range from 300 to 1500 m/z with automatic gain control target set to 3×10^6 and a maximum of 30 ms injection time. From the MS pre-scan, the 15 most abundant peptide ions were selected for fragmentation (MS/MS) if at least doubly charged, with a dynamic exclusion of 30 s. MSMS spectra were recorded at resolution 15.000 with automatic gain control target set to 5×10^2 and a maximum of 50 ms injection time. The normalised collision energy was 28, and the spectra were recorded in profile mode.

2.14.3 Data Processing – Protein Identification

Proteome Discoverer 2.5 software (Thermo Fisher Scientific; version 2.5.0.400) was used for peptide and protein identification via a database search (Sequest HT search engine) against Swissprot rat data base (Release 2020_02, 8096 sequences), considering full tryptic specificity, allowing for one missed tryptic cleavage sites, precursor mass tolerance 10 ppm, fragment mass tolerance 0.02 Da. Carbamidomethylation of Cys was set as a static modification. Dynamic modifications included deamidation of Asn, Gln, oxidation of Met, and a combination of Met loss with acetylation on protein N-terminus. The software Percolator was used for validating peptide spectrum matches and peptides, accepting only the top-scoring hit for each spectrum, and satisfying the cut-off values for FDR < 1%, and posterior error probability < 0.05. The Sequest HT Xcorr filter was set to 1 removing identifications below this threshold. The final list of proteins complied with the strict parsimony principle.

2.14.4 Data processing – Label-free quantification

The quantification of proteins was based on abundance values for unique peptides. Abundance values were normalized on total peptide amount to account for sample loading errors. The protein abundances were calculated summing up the abundance values for admissible peptides and the data analysed following Navarro P., *et al*[226].

2.14.5 Pathway analysis

A functional annotation analysis of changes in rat duodenum (LPP WT, still healthy and diseased LPP *Atp7b*$^{-/-}$), and Caco-2 cell proteins (WT and KO) was performed with the whole set of proteins identified, using the Ingenuity Pathway Analysis program (IPA, Qiagen). For canonical pathway analysis, a threshold of z>2 (-log(p-value)) was considered, which refers to a p-value lower than 0.05. For animal samples, analysis was performed by comparing LPP WT data set with either still healthy or diseased LPP *Atp7b*$^{-/-}$. For the *in vitro* samples, Caco-2 WT cell and Caco-2 KO cells were compared.

The last step of sample preparation (trypsinization and acidification), mass spectrometric measurements and data processing were performed by Dr. Christine Von Törne, at the Metabolomics and Proteomics Core (MPC), HMGU, Munich, Germany.

2.15 **Transmission electron microscopy**

Principle of the assay: Transmission electron microscopy (TEM) is a microscopy technique used to visualize cellular components *in situ* or isolated, as is the case for mitochondria [227]. Pre-stained embedded samples are cut in ultrathin sections and images are obtained when an electron beam is transmitted through these ultrathin samples. The interaction between the electron beam and the biological components in the sample leads to absorption and scattering of the beam, generating contrast that allows the visualization of the different cellular structures [228].

Isolated mitochondria (50µg) from rat duodenum and $3x10^5$ cells (Caco-2 WT and ATP7B KO) were loaded into BEEM capsules and centrifuged at 10.000g for 10 min at 4°C and at 400g for 10 min at RT, respectively. The obtained pellets were fixed with 600µL of 2.5% Glutaraldehyde in cacodylat buffer, post-fixed with 1% osmium tetroxide, dehydrated and embedded in epoxy resin. Duodenum tissue samples were also fixed with 2.5% glutaraldehyde in cacodylate buffer, post-fixed with 1% osmium tetroxide, dehydrated and embedded in epoxy resin. Caco-2 cell monolayers, grown on a Transwell® system, were dehydrated in ethanol, and gradually embedded in epoxy resin in ethanol (1:2, 1:1, 2:1 for 20 min each). After embedded in 100% epoxy resin for 48 hours at 60°C, 50 to 70 nm sections from all samples were cut using the Reichert-Jung Ultracut E microtome (now Leica Biosystems) and positive-stained with Uranyless and lead citrate. Images were acquired using a JEM1200 EXII electron microscope (Akishima, Tokyo, Japan) at 60 kv, equipped with a KeenView II digital camera (Olympus, Hamburg, Germany) and processed with the iTEM software package (analysis Five, Olympus, Germany). Sample preparation and imaging were performed by Carola Eberhagen, Institute for Molecular Toxicology and Pharmacology (HMGU), Munich, Germany.

2.16 High resolution respirometry – Oxygraph-2k

Principle of the assay: The Oroboros O2k-FluroRespirometer enables high resolution respirometry and quantitative evaluation of mitochondria function in living cells, tissue and isolated mitochondria. Through the utilization of different substrates and OXPHOS-target inhibitors in an oxygen controlled chamber, it is possible to determine different mitochondrial bioenergetics parameters upon different pre-treatments[229]. The NADH-linked pathway (N-pathway), the Succinate-linked pathway (S-pathway), a combination of both (NS-pathway), and the maximum respiratory capacity of the mitochondria electron transport system (ET or ET-pathway state) are the most common parameters evaluated.

Caco-2 WT and Caco-2 ATP7B knockout cells were treated for 24 hours with DMEM (25mM glucose, 2% FCS) alone or containing 100µM $CuCl_2$. Oxygen consumption was assessed by high-resolution respirometry using the Oxygraph-2k and DatLab 7.0 (Oroboros Instruments GmbH) as previously described [230], with adaptations. Per chamber, 1.5×10^6 living cells were supplied in 2 ml of MiR05 buffer (0.5mM EGTA, 3mM $MgCl_2$, 60mM lactobionic acid, 20mM taurine, 10mM KH_2PO_4, 20mM HEPES, 110mM sucrose, 1g/l albumin, pH 7.1) and routine respiration was measured. For cellular permeabilization, digitonin (4µM) was added to both chambers. Addition of substrates (Glutamate 10mM, Pyruvate 5mM, Malate 2mM) without ADP enabled the measurement of Leak respiration (O_2 consumption without ATP production). Complex I-linked respiration (N-pathway) was assessed after ADP (2.5mM) addition, and stepwise addition (1 µl steps from 1mM stock solution) of carbonyl cyanide m-chlorophenyl hydrazone (CCCP) allowed the determination of the maximum O_2 flux, corresponding to the maximum capacity of the mitochondria electron transport system (ET-pathway state). Addition of Succinate (10mM) allowed the determination of overall ET-pathway maximum capacity linked to the NS-pathway, with subsequent addition of rotenone (0.5 µM) blocking Complex-I activity, with O_2 consumption now corresponding to the Complex-II linked respiration (S-pathway). An alternative pathway was evaluated by adding glycerol-3-phosphate (G3P, 10mM), which feeds electrons directly to ubiquinone (Complex-II). To finalize the measurement, Antimycin A (1µM) was added to block Complex-III linked respiration, and Complex IV-linked respiration was determined by addition of Ascorbate (2mM)/TMPD (0.5mM) with subsequent inhibition with Sodium azide (100mM). Table 13 summarizes the substrates and inhibitors used to performed this assay.

Table 13. **List of substrates and inhibitors used in the High resolution respirometry analysis of mitochondria**

Substance	*Stock solution*	*Final conc. in the chamber*	*Volume (µL)*	*Solvent*
Digitonin	10 mg/mL	4 µM	1µL	MilliQ-H_2O
Glutamate	2 M	10 mM	10 µL	MilliQ-H_2O
Malate	0.5 M	2 mM	8µL	MilliQ-H_2O
Pyruvate	2 M	5 mM	5 µL	MilliQ-H_2O
Succinate	1 M	10 mM	20 µL	MilliQ-H_2O
Glycerol-3-phosphate (G3P)	1 M	10 mM	20 µL	MilliQ-H_2O
ADP	500mM	2.5 mM	10 µL	MilliQ-H_2O
Rotenone	1 mM	0.5 µM	1 µL	Ethanol
CCCP	1 mM	0.5 µM	1 µL	Ethanol/DMSO
Antimycin A	1 mM	1 µM	2µL	Ethanol
TMPD	200 mM	0.5 mM	5 µL	MilliQ-H_2O
Ascorbate	800 mM	2 mM	5 µL	MilliQ-H_2O
Azide (Sodium azide)	4 M	100 mM	50 µL	MilliQ-H_2O

2.17 Cellular oxygen consumption and extracellular acidification rate measurements

Principle of the assay: The Seahorse XF Cell Mito Stress Test uses modulators of mitochondrial function that target components of OXPHOS to reveal key parameters of metabolic function. The compounds: oligomycin, CCCP, and a mix of rotenone (Rot) and antimycin A (AA) are serially injected to measure ATP production-linked respiration, maximal respiratory capacity and non-mitochondrial respiration, respectively. Proton leak and spare respiratory capacity are then calculated using these parameters and the basal respiration, measured before adding the inhibitors.

Caco-2 WT and ATP7B KO were seeded in a 96-well plate (Seahorse XFe96 FluxPak mini - 102601-100), at a density of 5000 cells/well until confluence (48 hours). Afterwards, they were treated with 100μM $CuCl_2$ for 24 hours. Caco-2 ATP7B KO were also treated with 50μM MB (Zn) for 24 hours. In parallel, an XFe96 sensor cartridge was placed in a 96-well calibration plate containing 200μL of ultra-pure H_2O, and left to hydrate overnight at 37°C, in a CO_2-free incubator. On the day of the experiment, the XFe96 sensor cartridge was incubated with XF calibration buffer for 1 hour at 37°C, in a CO_2 free-incubator, and the cells washed once with 180 μL Seahorse XF DMEM medium, pH 7.4 (supplemented with 1mM pyruvate, 2mM glutamine, and 10mM glucose). Afterwards, 180 μL of medium was added to the wells and the cells incubated for 30 min at 37°C, in a CO_2-free incubator. Oligomycin, CCCP, Rot and AA stocks were prepared in Dimethyl sulfoxide (DMSO). Loading volumes of the stock solutions in the XF96 sensor cartridges were the following: 20 μL (Port A – 2.5μM oligomycin), 22 μL (Port B – 1μM CCCP), 25 μL (Port C – 0.5μM Rot/AA). The sensor cartridge and the calibration plate were loaded into the XFe96 Extracellular Flux Analyzer for calibration. When calibration was complete, the study plate was introduced. Three baseline rate measurements of oxygen consumption rate (OCR) and extracellular acidification rate (ECAR) of the cells were made using a 3 min mix, 2 min pause and 3 min measuring cycles. The compounds were then pneumatically and sequentially injected by the XFe96 Analyzer into each well, mixed, and both OCR and ECAR measured simultaneously using 3 min mix, 2 min pause and 3 min measuring cycles. Data was normalized against fluorescence related to DNA content (CyQUANT® Cell Proliferation Assay Kit, Invitrogen), following the manufacturer instructions. Seahorse Analysis was performed together with Julia Zuber, at the Institute for Cancer and Diabetes (IDC, HMGU), Munich, Germany.

2.18 Fluorescence microscopy

Principle of the assay: Fluorescence microscopy is a technique that uses fluorescence to generate an image of targeted cellular organelles/compartments as a way to study and monitor cell physiology [231]. Different labelling methods can be used such as fluorescent proteins or dyes, that bind/accumulate in specific organelles, or antibodies that are conjugated with fluorescent molecules (Immunocytochemistry, ICC). The specimen is illuminated with light of a specific wavelength that is absorbed by these fluorophores, which then will emit light of longer wavelengths. The excitatory light, which is reflected, reaches the detector with a high signal-to-noise ratio (SNR) [232].

Previous to cell seeding, 8-well Ibidi microscopy slides were coated with Poly-D-Lysine (stored at -20°C, thawed before use) and incubated for at least 1 hour in the clean bench. After, the coating solution was removed and the plate left for drying for an additional 1-2 hours. Thereupon, the plate was washed twice with sterile DPBS 1x (with magnesium and calcium) and left to dry. Immediately after, Caco-2 WT and ATP7B KO cells were seeded in a density of $4x10^4$ cells/well, and left to adhere and grow for 4 days at 37°C in a humidified atmosphere with 5% CO_2. Afterwards, cells were treated with 200μM Cu-His, BSA-KOH, 500μM FFA or 200μM Cu-His + 500μM FFA, for 24 or 48 hours, after 4 days in non-treated DMEM (25 mM glucose, 10% FCS) medium. Afterwards, cells were washed with 250 μL of DPBS 1x (no magnesium and calcium) before fixation with 4% paraformaldehyde (PFA) (10 min, RT, under the chemical fume hood). For mitochondrial staining via ICC, cells were permeabilized with 0.2% Triton X-100 (10 min, RT) after a second washing step with DPBS 1x (no magnesium and calcium). Once again, the wells were washed and unspecific binding sites were blocked by adding 1% BSA in DPBS 1x (no magnesium and calcium) and incubated for 30 min at RT with agitation. The primary antibody for citrate synthase was diluted 1:50 in a solution of 1% BSA in DPBS 1x (no magnesium and calcium), and the cells incubated for 2 hours at RT with agitation, or at 4°C overnight whilst shaking. Afterwards, the cells were washed thrice with 1% BSA in DPBS 1x (no magnesium and calcium) and the secondary antibody (Goat anti-rabbit IgG, Alexa Fluor™ 568), prepared in 1% BSA in DPBS 1x (no magnesium and calcium), was added in a final dilution of 1:1000 followed by a 30 minutes' incubation at RT, with agitation and covered from light. After three further washing steps with 1% BSA in DPBS 1x (no magnesium and calcium), BODIPY was used for neutral lipid staining in a concentration of 0.1 μg/mL, and the cells incubated for 10 minutes, at RT with agitation. For nuclei staining, cells were incubated with Hoechst (10 μg/mL) for 5 minutes, at RT with agitation. To remove unbound

dyes, the slides were washed twice with DPBS 1x (no magnesium and calcium) and kept in the same solution for imaging. The samples were acquired using the Eclipse Ti-S Inverted Research Microscope from Nikon. Two to three fields were chosen randomly from the top to the bottom of every well and pictures were taken in a magnification of 60x.

For tight junctions (TJs) proteins immunocytochemical staining, Caco-2 WT and ATP7B KO cells differentiated, and treated in trans-well membrane inserts, were washed twice with DPBS 1x (with magnesium and calcium), in both apical and basolateral compartments, after media removal. Afterwards, they were fixed with 4% PFA (20 min, 4°C), permeabilized with 0.2% Triton X-100 (10 min, RT) and washed with DPBS 1x (no magnesium and calcium). Blocking of unspecific binding sites was prevented by incubation with a 3% BSA solution followed by incubation with the primary antibodies (30 min, 37°C): anti–Claudin-5 (Abcam, Cambridge, UK), anti-Occludin (Zytomed Systems GmbH) or anti-ZO-1 (Thermofischer Scientific, US). After, a second blocking step with 3% BSA solution was performed before washing with DPBS 1x (with magnesium and calcium) and incubate with the secondary antibodies: Alexa Fluor 488 or 568–conjugated secondary antibody (Invitrogen, Molecular Probes Inc.). Hoechst 33342 (Invitrogen, Molecular Probes Inc) was used to stain cell nuclei (30 seconds at RT, in the dark), followed by a second fixation step with 4% PFA (10 min, RT, in the dark). Subsequently, membranes were washed (DPBS 1x, with magnesium and calcium) cut out of the inserts and mounted in Vectashield HardSet^{TM} (Vector Laboratories, Maravai Life Sciences, US). After a solidification period of, at least, 24 hours, the samples were analysed using a Nikon ECLIPSE Ti-Series fluorescence microscope (Nikon Instruments) in combination with the NIS-Elements imaging software. Two to three fields were chosen randomly from the top to the bottom of every well and pictures were taken in a magnification of 60x. The slides were kept at 4°C in the dark for storage.

2.19 **Permeability assays**

Principle of the assay: The transport of substances across biological membranes is of great interest for the pharmaceutical industry. Models that mimic organ barriers, like the Caco-2 cells upon differentiation in permeable filters, are of great value to study this process. Most models assume that transport of molecules can occur via passive diffusion in restricted aqueous spaces between cells (*paracellular*), which is tight-junction's dependent, and across the cell membrane *(transcellular*). Passive diffusion is the most significant transport mechanism for the majority of the compounds[233, 234]. Therefore, changes in the apparent paracellular permeability (Papp) can be related to a decrease in barrier function. Measuring the flux of fluorescence dyes, such as Fluorescein Isothiocyanate-Dextran (FITC-Dextran), from apical to basolateral compartments, allows the determination of the Papp and, consequentially, the evaluation of the barrier permeability[235, 236].

Caco-2 WT and Caco-2 ATP7B KO cells, seeded in Corning™ Costar Transwell® PET permeable supports with 44 cm^2 (pore size 0.4 μm) were treated with DMEM (25mM glucose, 10% FCS) alone or containing 100μM $CuCl_2$, from the 7th day, until the 21st day of differentiation, with medium change performed every 2 days, with the abovementioned treatment. For Papp determination, medium was removed from both apical and basolateral compartments, and the trans-wells washed once with PBS 1X. Afterwards, the cells were equilibrated in Hanks balanced salts solution (HBSS) buffer for 1 hour at 37°C in a humidified atmosphere with 5% CO_2. A FITC-Dextran (10kDa) solution of 1 μM, prepared in HBSS, was added to the apical compartment. Samples were collected from the basolateral media at 0, 15, 30 and 90 minutes of incubation with the dye, and the fluorescence intensity measured at 490 nm excitation and 520 nm emission in a ClarioStar plate reader (BMG-Labtech, Germany). The P_{app} (cm/s) was calculated according to Hubatsch *et al.*[235].

2.20 ELISA measurement of Interleukin-8

Principle of the assay: ELISA stands for enzyme-linked immunosorbent assay and is a technique used to detect the presence of antigens in biological samples. In a sandwich ELISA assay, an antigen is immobilized to a solid surface, which complexes to the target in the biologic sample followed by a biotin labelled detection antibody. As a final step, the samples are incubated with a molecule amenable for detection such as an enzyme or a fluorophore[237].

Concentration of excreted interleukin 8, a chemokine expressed in endothelial cells and key mediator in inflammatory processes[238], was determined by ELISA according to the manufacturer instructions (Human IL8/CXCL8 ELISA kit – RAB0319, Sigma–Aldrich) on the basolateral compartment media of Caco-2 WT and Caco-2 ATP7B KO cells, seeded in Corning™ Costar Transwell® PET permeable supports with 44 cm^2 (pore size 0.4 μm). The cells were treated with DMEM (25mM glucose, 10% FCS) alone or containing 100μM $CuCl_2$, from the 7th day, until the 21st day of differentiation, with medium change performed every 2 days, with the abovementioned treatment.

2.21 SDS-PAGE and Western Blot

Principle of the assay: This method consists on the separation of the proteins by sodium dodecyl sulfate (SDS) gel electrophoresis and then transfer of the proteins onto a polyvinylidene fluoride-membrane (PVDF-membrane), followed by immunodetection and chemiluminescence. The immunological protein detection is based on antigen-antibody interactions[239-241]. The first step of this method is the separation of the proteins by SDS-polyacrylamide gel electrophoresis (SDS-PAGE). In this step, proteins are negatively charged and separated based on of their molecular weight. Proteins can also be separated in denaturing or non-denaturing conditions. Addition of β-mercaptoethanol during sample preparation reduces the proteins and cleaves possible disulfide bridges, while heating denatures and unfolds them. After separation, the proteins are transferred from the gel to a PVDF-membrane. The following immunological protein detection is based on an antigen-antibody reaction. The membrane is first incubated with a protein-specific first antibody followed by a species-specific antibody incubation. The secondary antibody is labelled with the marker enzyme horseradish peroxidase (HRP), which allows detection via chemiluminescence. The HRP catalyses the hydrogen peroxide-dependent reaction of luminol, which generates light and allows the quantification of the protein bands.

2.21.1 Gel casting

For protein separation, discontinuous gels consisting of a separation and a stacking gel were used. For the separation of smaller proteins, higher-percentage gels (15% acrylamide) were used, since smaller pores are formed in the gel during polymerization. For the separation gels, chemicals listed in Table 14 were mixed together with a 10% APS solution and Tetramethyl-p-phenylenediamine (N,N,N',N-) (TEMED), added last to started the polymerization. The solution was gently inverted in the falcon tube and then pipetted into the gel cassettes. The separation gel was layered with isopropanol until the gel was even and free of air bubbles. After the separation gel was fully polymerized, the isopropanol was discarded, and the top of the gel was washed with ddH_2O. The remaining water was dried with a piece of Whatman paper. For the stacking gel, the solutions from Table 14 were mixed in a falcon tube. Again, the 10% APS and TEMED were added last. The stacking gel was gently inverted and pipetted onto the solid separation gel until the cassette was completely filled. A sample comb with 12 sample bags was inserted into the cassette. After the stacking gel polymerized completely, the solid gel could be stored for up to two weeks at 4°C, in a humid environment to avoid drying.

Table 14. **Composition of separation and stacking gels for Western blot analysis**

Substances	*Volume (mL) - 3 gels*
Separation gel (15%)	
ddH_2O	7.2
1.5 M Tris/ HCl pH 8.8	7.5
30 % Acrylamide solution	15.0
20 % SDS [µL]	150
10% APS [µL]	150
TEMED [µL]	15
Total volume	30
Stacking gel	
ddH_2O	6.1
0.5 M Tris/ HCl pH 6.8	2.5
30 % Acrylamide solution	1.3
20 % SDS [µL]	50
10% APS [µL]	50
TEMED [µL]	10
Total volume	10

2.21.2 Sample preparation for SDS-PAGE

After determination of sample protein content (see 2.9), the samples were adjusted to a final protein concentration of 2µg/µL with ddH_2O. The samples were mixed with 4x Laemmli buffer (Table 15), without β-mercaptoethanol, in a ratio of 1:4 and heated for 30 min at 50°C. If the samples were lysed cells, they were centrifuged at 16.000g for 10 min at 4°C and the supernatants were applied to the gel.

Table 15. **Composition of 4x Laemmli-Buffer**

Substances/Buffer	*Weight/volume*	*Final concentration*	*Volume final*
1 M Tris/HCl pH 6.8	10 mL	200 mM	50 mL fill up with ddH_20
SDS	4 g	8 %	
Bromophenol blue	0.2 g	0.4 %	
Glycerol	20 mL	40 %	

2.21.3 SDS-PAGE

The electrophoresis chamber was assembled, filled with running buffer (Table 16) and put on ice. A sample volume of 20 µL was pipetted into the gel wells. In case of remaining empty wells, a mixture of running buffer and 4x Laemmli buffer was pipetted instead of sample. In addition to the samples, 10 µL of a size marker and 10 µL of a biotinylated protein marker were added in opposite sides of the gel. The electrophoresis was started at 100 V for about 10 minutes until the protein band reached the end of the stacking gel. Then the proteins were separated at 180 V for about 1 hour.

Table 16. **Composition of buffers used in SDS-PAGE, protein transferring, membrane staining and washing.**

Substances/Buffer	*Weight /volume*	*Final concentration*	*Volume final*
		10x TBS	
1 M Tris/ HCl pH 8.0	100 mL	100 mM	1 L
NaCl	87.75 g	1.5 M	fill up with ddH_2O
		1x TBS-T	
10x TBS	100 mL	1x	1 L
Tween-20	500 µL	0.05 %	fill up with ddH_2O
		Electrophoresis running buffer	
Rotiphorese 10x	100 mL	1x	1 L fill up with ddH_2O
		Transfer buffer	
Glycin	2.9 g	39 mM	2 L fill up with ddH_2O
Tris	5.8 g	48 mM	
Ethanol	400 mL	20%	
SDS 20 %	0.250 mL	0.0025 %	
$CaCl_2$	0,443 g	2 mM	
		Glutaraldehyde fixing solution	
25% Glutaraldehyde	1 mL	2.5%	10 mL ddH_2O
		Ponceu S	
Ponceau S	0.5 g	0.1 % w/v	500 mL
Acetic acid 100 %	25 mL	5 % v/v	fill up with ddH_2O
		Ponceau S destainer	
Acetic acid 100 %	200 mL	10 %	2 L fill up with ddH_2O
Ethanol technical	800 mL	40 %	
ddH_2O	1000 mL	50 %	
		Skim milk 5 %	
Skim milk 5 %	25 g	5 % w/v	500 TBS-T

2.21.4 Western Blot – transferring of the proteins

After SDS-PAGE, the gel was placed in transfer buffer for 15 min to lower the SDS concentration. In parallel, the PVDF-membrane was first activated in methanol and then transferred to a bowl with transfer buffer (Table 16). Two fiber pads, and two Whatman papers per gel, were also placed in transfer buffer. The blotting cassette was assembled as shown in Figure 7 and possible air bubbles were displaced by a roll. The blotting cassette was then placed in the blotting chamber, which was filled up with transfer buffer and put on ice. The proteins were transferred to the PVDF-membrane for 1 hour at 80 V.

Figure 7 **Scheme of the blotting cassette assembling for protein transfer into the PVC membrane**

2.21.5 Glutaraldehyde fixing

After the transfer, the PVDF-membrane was washed in ddH_2O to remove the remaining SDS and incubated with a 2.5% glutaraldehyde solution (Table 16) for 1 hour, at RT with agitation.

2.21.6 Ponceau S staining

The PVDF-membrane was washed in ddH_2O to remove the remaining glutaraldehyde and stained with the Ponceau S solution (Table 16) for 1 – 5 min on the shaker. The PVDF-membrane was then swirled up to 3 times in the distaining solution (Table 16) for 1 – 2 min, until the background of the PVDF-membrane was almost white. The PVDF-membrane was dried and scanned for documentation.

2.21.7 Immunodetection of proteins of interest

The dried PVDF-membrane was reactivated in methanol and washed in TBS-T (Table 16) for 5 min. Then, the PVDF-membrane was incubated for 30 min on the shaker with 20 mL of 5 % skim milk (Table 16, blocking solution). Afterwards, 10 mL of the first antibody (Table 3), prepared in skim milk, was applied to the PVDF-membrane and incubated overnight at 4°C on the shaker. The PVDF-membrane was then washed 2 times with TBS-T for 5-10 min and after incubated with 10 mL of the matching secondary antibody and biotinylated antibody (Table 3), both diluted 1:2000 in 5% skim milk, for 1 hour on the shaker at RT. After the second incubation, the PVDF-membrane was washed 3 times with TBS-T for 10 min. After the last washing step, the PVDF-membrane was swirled in developing solution, which consisted of 4.5 mL ddH_2O and 250 µL of each LuminoGlo solutions. The PVDF-membrane was swirled in the developing solution for at least 10 seconds and placed directly into a transparent foil and the air bubbles were carefully removed. The chemiluminescence was measured in the Fusion FX (Vilber®). This was followed by quantitative evaluation with Fusion Capt.

2.22 Statistical analysis

Throughout this study, N refers to the number of biological replicates, and n to the number of technical replicates. Data are presented as means ± SD. When appropriated, data were tested for Gaussian distribution and outlier analysis was performed by the ROUT method. Statistical significance was analysed using 1-way analysis of variance with the nonparametric Kruskal–Wallis test when comparing 2 sample sets. When comparing 3 or more data sets, a 2-way analysis of variance was used (Dunnett’s or Sidak's multiple comparisons test) using GraphPad Prism 6 (GraphPad Software, Inc, San Diego, CA).

3. Results

3.1 Intestinal alterations and impairments in Wilson Disease animal and cell models

3.1.1 Intestinal damage is present in LPP animals, an *in vivo* model for Wilson disease.

In the liver of LPP *Atp7b*$^{-/-}$ diseased animals (i.e., ALT/AST/bilirubin plasma levels above normal), inflammation, tissue necrosis and fibrosis were present, which mimics the situation of liver failure in WD patients[68]. Increased liver Cu content is the hallmark of the disease and the main cause of liver damage[102, 103]. To better understand if ATP7B malfunction has a similar impact on the intestine of LPP animals, tissue samples from the small (duodenum) and large (colon) intestine were stained (Haematoxylin and eosin-H&E and Periodic acid/Schiff-PA) to evaluate changes in overall tissue structure from two comparable sets of LPP *Atp7b*$^{+/-}$ and LPP *Atp7b*$^{-/-}$ animals (Figure 8.A, B). The PAS-stained cross section through the small and large intestine at different anatomical levels gave a regular distribution of goblet cells within the epithelia, and normal mixed lympho-plasma cellular infiltrate within the lamina propria in LPP *Atp7b*$^{+/-}$ animals. In comparison, both LPP *Atp7b*$^{-/-}$ animals presented with a reduction in mucin content, which could be related to a decreased content of goblet cells within the duodenal epithelia, as well as a reduced cell content within the lamina propria at duodenal level (Figure 8.A, B). With regards to PAS/H&E stained cross sections through the large intestine of LPP *Atp7b*$^{+/-}$ and LPP *Atp7b*$^{-/-}$ animals, no obvious difference in epithelial (mucosal) thickness, crypt-length or goblet-cell distribution was visible. Nonetheless, LPP *Atp7b*$^{-/-}$ displayed an increased content of mucosal associated lymphatic tissue (MALT-Tissue) in the colon (Figure 8.B)

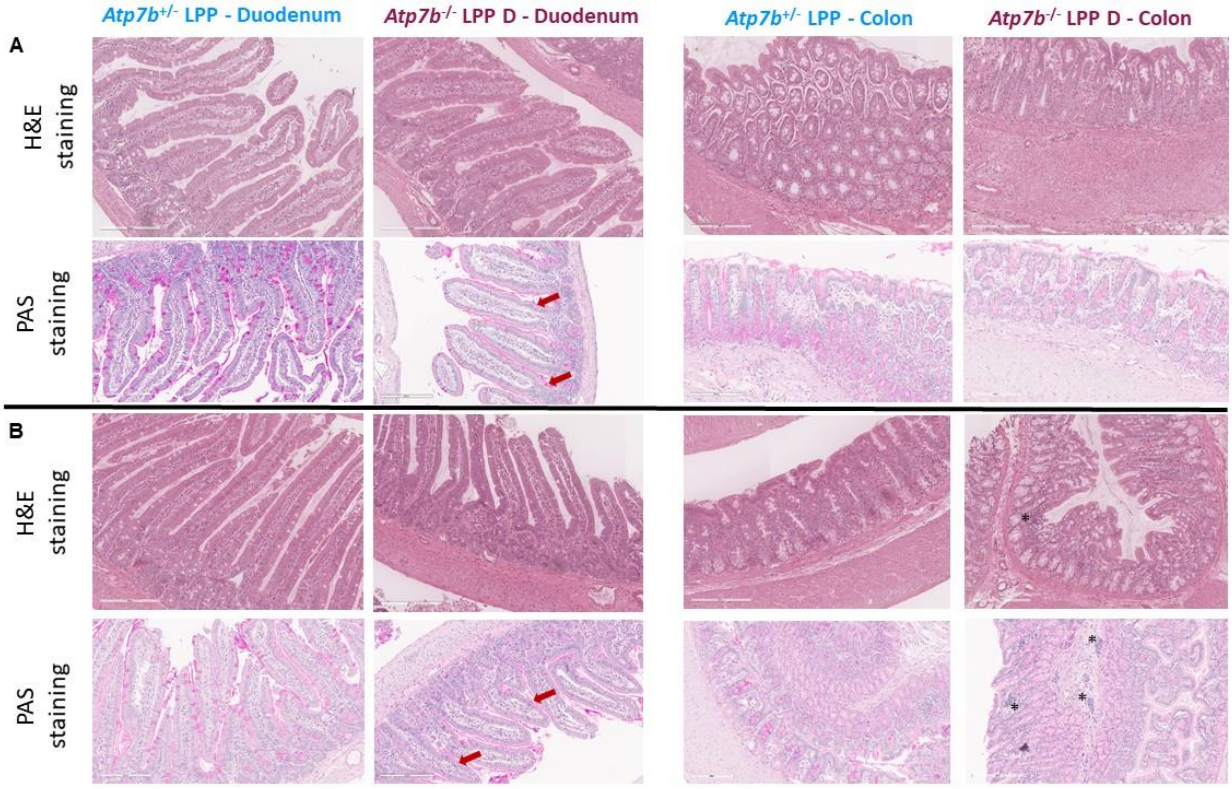

Figure 8. **Intestine histology depicted differences in diseased LPP *Atp7b*$^{-/-}$ rats (D) in comparison to heterozygous controls (LPP *Atp7b*$^{+/-}$).** Polysaccharides and mucosubstances, such as glycoproteins and mucins, were reduced in the duodenum of diseased *Atp7b*$^{-/-}$, as shown by the decreased in Periodic acid/Schiff (PAS) staining (red arrows), in comparison to *Atp7b*$^{+/-}$ controls. Alterations in the large intestine (colon) were observed by H&E staining that showed an increased content of mucosal associated lymphatic tissue (MALT-Tissue) (black asterisks). Scale bar: 200 μm; **(A)** Comparable pair of LPP *Atp7b*$^{+/-}$ and LPP *Atp7b*$^{-/-}$ diseased (D); and **(B)** a second comparable pair of LPP *Atp7b*$^{+/-}$ and LPP *Atp7b*$^{-/-}$ diseased. Data are N=2.

In LPP *Atp7b*$^{-/-}$, liver Cu accumulation was significant at 40 days of age, reaching a plateau at around 70-80 days of age, far preceding liver damage, that is observed around 100 days of age, assessed by increased serum AST levels[69]. Since Cu homeostasis in the enterocytes may also depend on ATP7B[74, 95, 97], we investigated intestinal Cu levels in LPP *Atp7b*$^{-/-}$ rats. In comparison to homozygous still healthy animals (i.e., with ALT/AST/bilirubin plasma levels still in the normal range), LPP *Atp7b*$^{-/-}$ diseased animals had significantly elevated duodenal Cu, but normal Zn and Fe levels (Figure 9.A-C). However, in LPP *Atp7b*$^{-/-}$ rats that were still healthy, intestinal Cu levels were not significantly changed in comparison to non-affected LPP control *Atp7b*$^{+/-}$ rats (Figure 9.A). Nonetheless, proteome analysis of duodenum tissue revealed significant elevated metallothioneins (MT1 and MT2) presence in still healthy LPP *Atp7b*$^{-/-}$ rats, and a significant depletion in the Cu transporter CTR1 and in the Cyclin and CBS domain divalent metal cation transport mediator 4 (CNNM4) (Figure 9.D). CNNM4 is a transporter for

Cu, magnesium and cobalt, and it was described to interact with cytochrome c oxidase Cu chaperone COX11, therefore possibly playing a role on Cu delivery in the mitochondria[242].

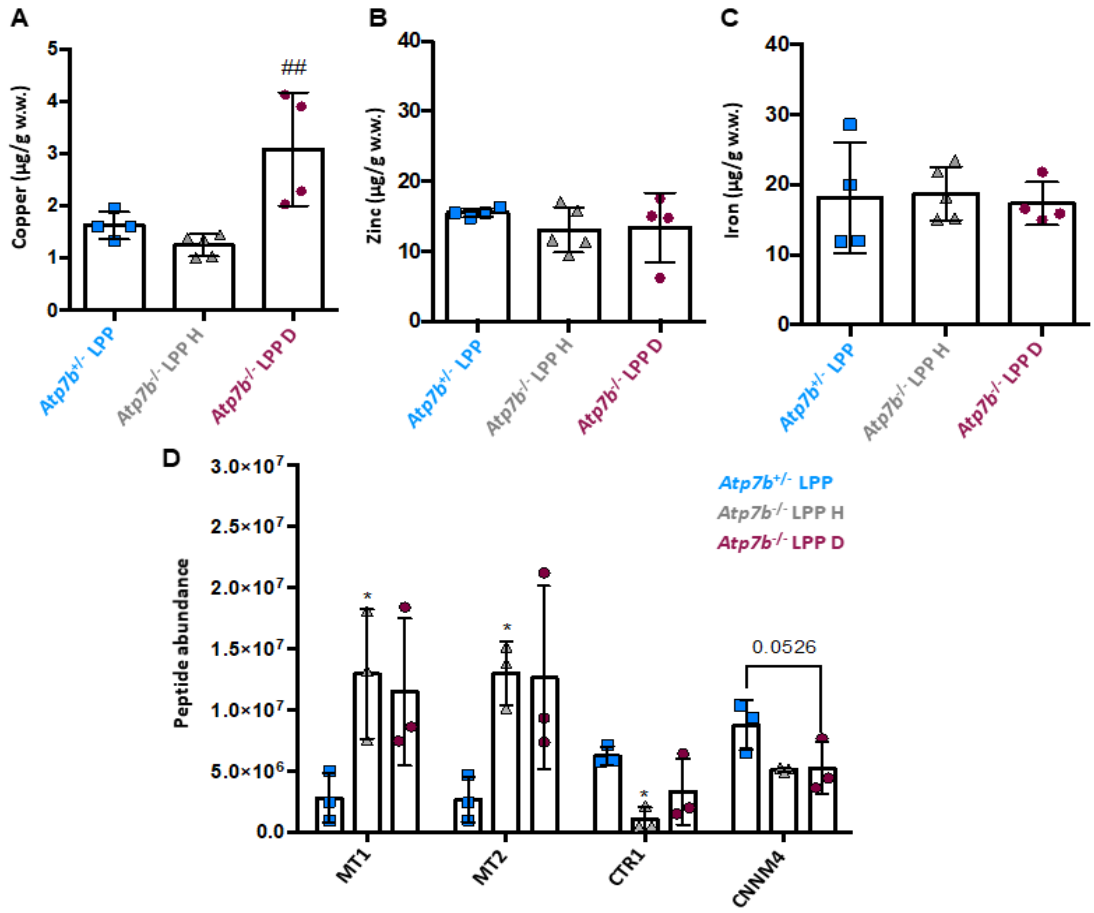

Figure 9. **Copper intestinal metabolism changed in Wilson disease LPP *Atp7b*$^{-/-}$ rats . (A)** Copper levels increased in the duodenum of *Atp7b*$^{-/-}$ animals, but only upon disease (D). Still healthy (H) *Atp7b*$^{-/-}$ animals had no significant changes in intestinal Cu, **(B)** Zn and Fe **(C)** content in comparison to *Atp7b*$^{+/-}$ animals. **(D)** The peptide abundance of metallothioneins 1 and 2 (MT1, MT2) was increased, while CTR1 and CNNM4 abundance was decreased in H animals. Peptide abundance: total amount of identified peptides normalized towards the total amount of peptides in 10µg of protein. Data are the mean ± SD of N=5-4 (A-C). One-way analysis of variance with the Kruskal-Wallis test (Dunn's multiple comparisons), after column analysis (identify outliers). *Significance to LPP *Atp7b*$^{+/-}$ animals. #Significance to LPP *Atp7b*$^{-/-}$ H. *P<.05, ##P<.001

Thus, already at a still healthy state, WD rat enterocytes were counteracting systemic Cu uptake. Elevated MT1/2 levels correlated with an increase in cytosolic Cu content, that was significant in LPP *Atp7b*$^{-/-}$ diseased animals (Figure 10.A), but also with the increase in the percentage of Cu located in the cytosol, observed in still healthy LPP *Atp7b*$^{-/-}$ animals (Figure 10.D). No significant changes were observed for Zn or Fe content levels in duodenum (Figure 10.B,C), with a significant increase in cytosolic Fe content in diseased LPP *Atp7b*$^{-/-}$ animals (Figure 10.F)

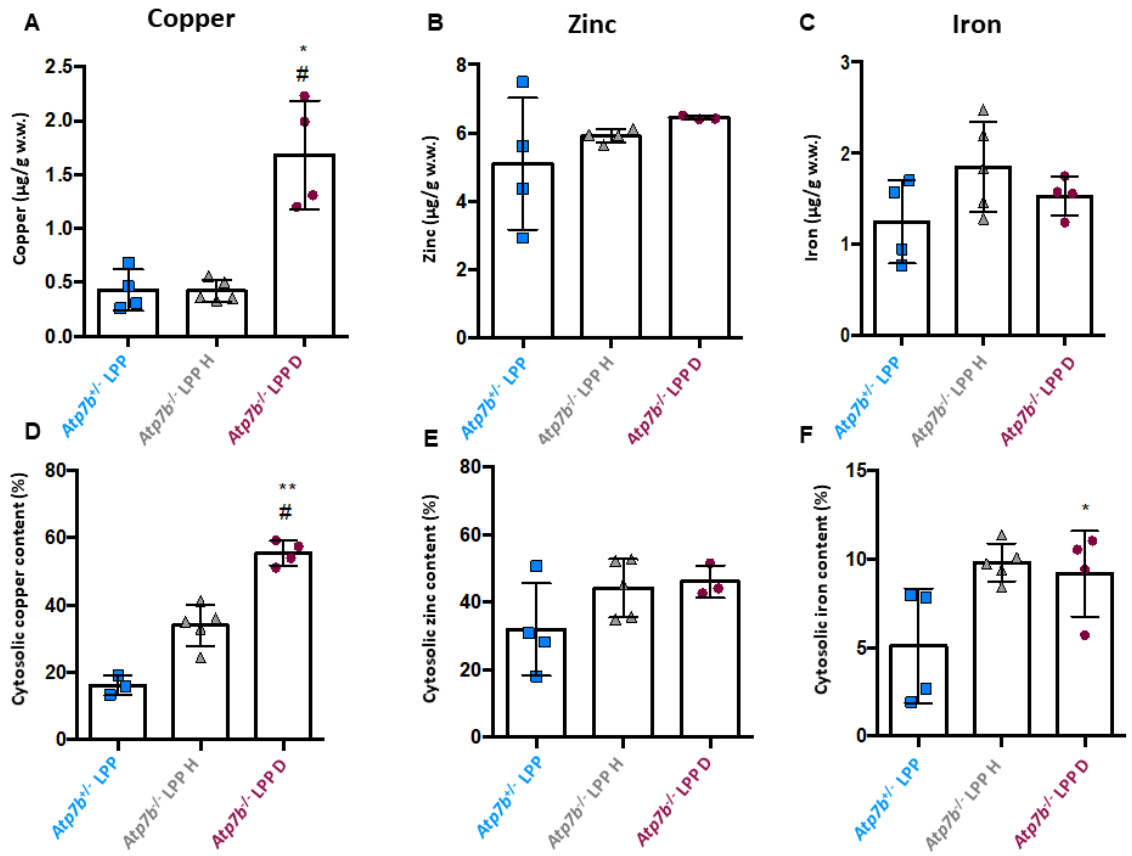

Figure 10. **Duodenal cytosolic copper levels were increased in Wilson disease rats. (A)** Total cytosolic Cu levels in the duodenum were significantly increased in diseased *Atp7b*$^{-/-}$ animals (D), with no significant changes in **(B)** Zn and **(C)** Fe content in comparison to *Atp7b*$^{+/-}$ and still healthy *Atp7b*$^{-/-}$ animals. **(D)** The percentage of Cu in the cytosol, in relation to the total amount of Cu present in the duodenum homogenates, increased in still healthy (H) *Atp7b*$^{-/-}$ animals and was significantly increased in diseased *Atp7b*$^{-/-}$ animals (D), in comparison to both *Atp7b*$^{-/-}$ still healthy and *Atp7b*$^{+/-}$ animals. No significant changes were observed for **(E)** Zn, and a significant increase in the percentage of **(F)** Fe in the cytosol was observed in comparison with *Atp7b*$^{+/-}$ animals . Data are the mean ± SD of N=3-5 (A-F). One-way analysis of variance with the Kruskal-Wallis test (Dunn's multiple comparisons), after column analysis (identify outliers). *Significance to LPP *Atp7b*$^{+/-}$ animals. $^{\#}$Significance to LPP *Atp7b*$^{-/-}$ H. *P<.05, **P<.001, $^{\#\#}$P<.001

3.1.1.1 Mitochondrial structure is altered in the intestine of Wilson disease animals

Hepatic mitochondrial damage due to excess Cu accumulation is another hallmark of WD pathology[69, 243]. We therefore analysed the mitochondrial structure from the small (duodenum, jejunum, ileum) and large (colon) intestine. In the duodenum and jejunum of still healthy LPP *Atp7b*$^{-/-}$ versus controls, mitochondria appeared bigger in size, less electron-dense, with partial membrane deformations and vesicular cristae widening, which were also observed in the ileum section of the intestine (Figure 11). In the LPP *Atp7b*$^{-/-}$ diseased animals, less electron-dense matrixes and loss of cristae structure were observed across all small intestine (Figure 11). No significant alterations in mitochondria structure were observed for the colon, neither in still healthy nor in diseased animals. Isolated mitochondria from the duodenum presented with similar alterations, less electron-dense matrixes, and vesicular cristae widening's, especially in mitochondria from diseased animals (Figure 11). These mitochondrial alterations, however, are distinct from the ones observed in the liver mitochondria of WD patients and LPP rats. In the latter case, they have similar size but appear with more dense matrices, loose outer membranes, cristae widenings, membranous depositions, vacuoles and inclusions[69, 243, 244].

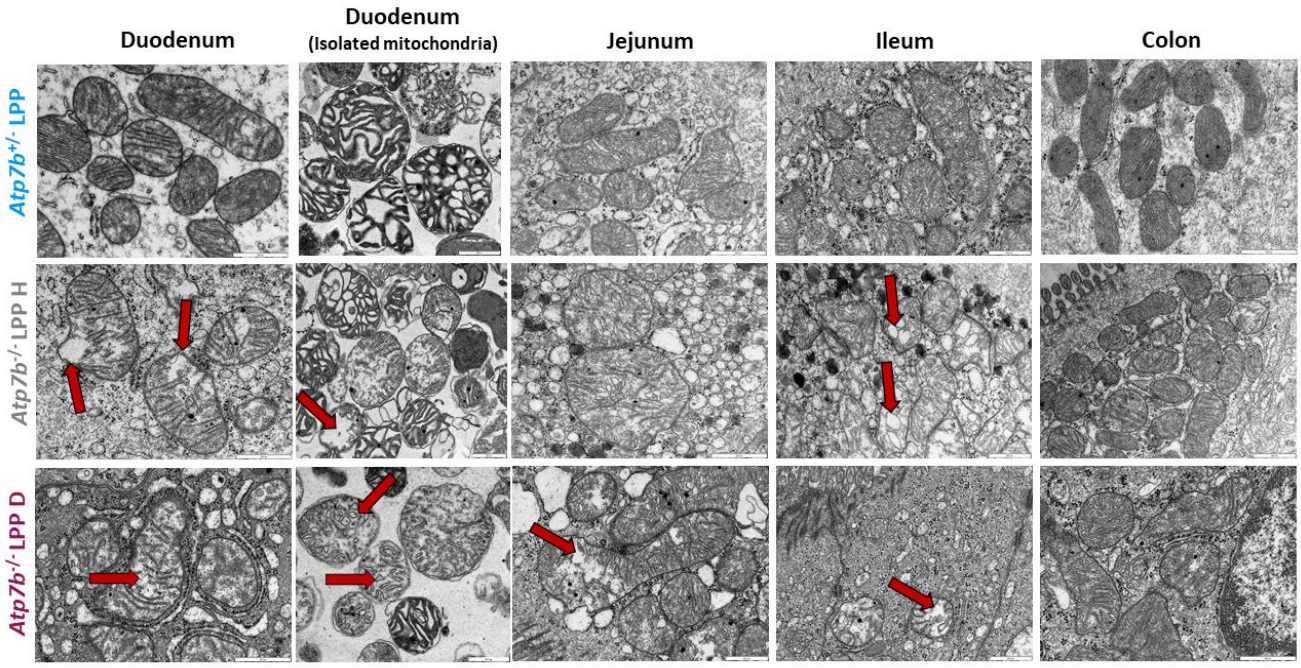

Figure 11. **Mitochondria from the small intestine of Wilson disease rats had mitochondria structural alterations.** Electron micrographs of duodenum (tissue and isolated mitochondria), jejunum, ileum and colon from LPP rats (scale bar: 500 nm). Still healthy *Atp7b*$^{-/-}$(H) animals present mitochondria structure alterations with cristae disorganization, loss of electron dense matrices and presence of vesicular structures (red arrows), more prominent in the duodenum and ileum. In *Atp7b*$^{-/-}$ diseased (D) animals, alterations in mitochondria structure were also evident, with loss of electron dense areas and increased swelling (red arrows) in all small intestine sections and isolated mitochondria (red arrows).

Investigation of the intestinal proteomes of these animals showed that the abundance of proteins related to mitochondrial organization and bioenergetic processes were significantly changed in LPP *Atp7b*$^{-/-}$ animals, in comparison to LPP *Atp7b*$^{+/-}$ non-affected controls (Figure 12.B). These results corroborate the observed mitochondrial structural changes (Figure 11).

3.1.1.2 Alterations in lipid metabolism and intracellular signalling in the duodenum of LPP animals

The abundance of proteins involved in plasma lipoprotein assembly, remodelling and clearing, such as high-density lipoproteins (HDL) and chylomicrons, were significantly downregulated in LPP *Atp7b*$^{-/-}$ rats, especially in diseased ones (Figure 12.B, Table S2). Also, the predicted inhibition of cholesterol transport and efflux, may be counterbalanced by the observed elevation of biosynthetic enzymes linked to cholesterol biosynthesis, such as Lanosterol 14-alpha demethylase (Cyp51a1), and squalene synthase (Fdft1) (Figure 12.A). Pierson and co-workers[74] reported an increase in TG levels in the intestine of *Atp7b*$^{-/-}$ mice, with a clear depletion of chylomicrons, in comparison to WT. Furthermore, although present in similar levels, apolipoprotein B localization in the duodenum was different between WT and *Atp7b*$^{-/-}$ mice. Using enteroids, they observed that Cu levels, either by excess or deficit, affect chylomicrons assembly. Therefore, a proper balance in Cu amounts in the intestine is crucial for lipid metabolism. In agreement with their conclusion, in the duodenum of diseased LPP *Atp7b*$^{-/-}$ animals, we observed a significant Cu increase together with the most significant changes in the proteome analysis.

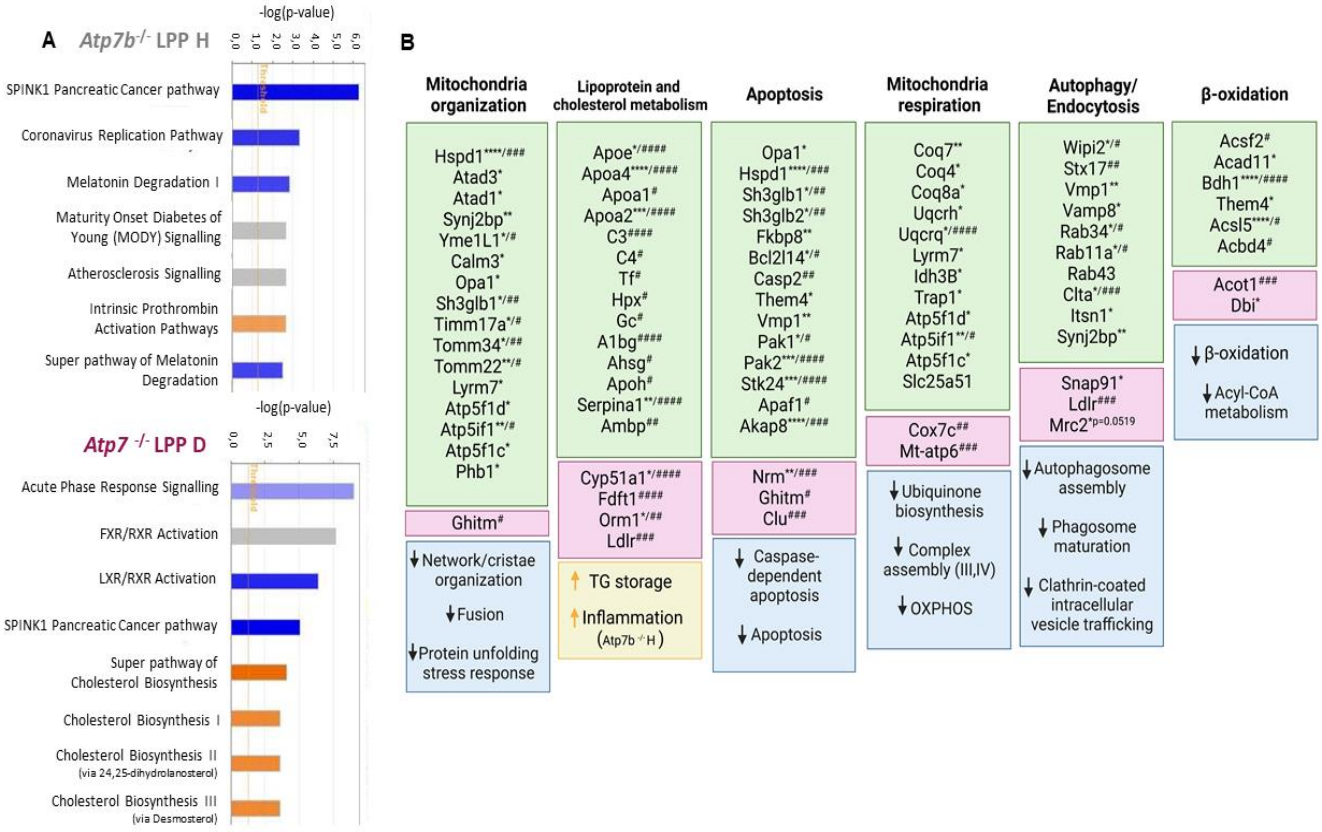

Figure 12. **Proteomics analysis of duodenum homogenates from LPP *Atp7b*$^{-/-}$ still healthy (H) and diseased (D) animals, in comparison with LPP *Atp7b*$^{+/-}$ animals. (A)** Comparison of altered pathways between LPP H or LPP D, in comparison to LPP *Atp7b*$^{+/-}$ using Ingenuity pathway analysis (IPA). The most statistically significant canonical pathways identified (p<0.05) are listed according to their p-value (-log, orange line). Blue bars: negative z-score (predicted inhibition); Orange bars: positive z-score (predicted activation); Grey bars: no activity pattern available. **(B)** Changes in protein expression impact cellular organelle organization (mitochondria and autophagosomes), and important processes for cell homeostasis such as cholesterol metabolism, apoptosis and autophagy. Green: Downregulated proteins in comparison to LPP *Atp7b*$^{+/-}$ animals; Pink: Upregulated proteins in comparison to LPP *Atp7b*$^{+/-}$ animals; Blue/Yellow: affected cellular processes and/or pathways. Proteins are represented with their correspondent gene symbol. *Significance of H animals in comparison to LPP *Atp7b*$^{+/-}$ animals; #Significance of LPP *Atp7b*$^{-/-}$ D animals in comparison to LPP *Atp7b*$^{+/-}$. $^{*,\ \#}$P<.05, $^{**,\ \#\#}$P<.01, $^{***,\ \#\#\#}$P<.001, $^{****,\ \#\#\#\#}$P<.0001. *Abbreviations: A1bg, Alpha-1B-glycoprotein; Acad11, Acyl-CoA dehydrogenase family member 11; Acbd4, Acyl-CoA-binding domain-containing protein 4; Acot1, Acyl-coenzyme A thioesterase 1; Acsf2, Medium-chain acyl-CoA ligase ACSF2; Acsl5, Long-chain-fatty-acid--CoA ligase 5; Ahsg, Alpha-2-HS-glycoprotein; Ambp, Protein AMBP; Akap8, A-kinase anchor protein 8; Apaf1, Apoptotic protease-activating factor 1; Apoa1, Apolipoprotein A-I; Apoa2, Apolipoprotein A-II Apoa4, Apolipoprotein A-IV; Apoe, Apolipoprotein E; Apoh, Beta-2-glycoprotein 1; Atad1, ATPase family AAA domain-containing protein 1; Atad3, ATPase family AAA domain-containing protein 3; Atp5f1c, ATP synthase subunit gamma; Atp5f1d, ATP synthase subunit delta; Atp5if1, ATPase inhibitor; Bcl2l14, Apoptosis facilitator Bcl-2-like protein 14; Bdh1, D-beta-hydroxybutyrate dehydrogenase; C3, Complement C3; C4, Complement C4; Calm3, Calmodulin-3; Casp2, Caspase-2; Clta, Clathrin light chain A; Clu, Clusterin; Coq4, Ubiquinone biosynthesis protein COQ4 homolog; Coq5, 2-methoxy-6-polyprenyl-1,4-benzoquinol methylase; Coq7, 5-demethoxyubiquinone hydroxylase; Coq8a, Atypical kinase COQ8A; Cox7c, Cytochrome c oxidase subunit 7C; Cyp51a1, Lanosterol 14-alpha demethylase; Dbi, Acyl-CoA-binding protein; Fdft1, Squalene synthase; Fkbp8, Peptidyl-prolyl cis-trans isomerase FKBP8; Gc, Vitamin D-binding protein; Ghitm, Growth hormone-inducible transmembrane protein; Hadha, Trifunctional enzyme subunit alpha; Hpx, Hemopexin; Hspd1, 60 kDa heat shock protein; Idh3B, Isocitrate dehydrogenase [NAD] subunit beta; Itsn1, Intersectin-1; Ldlr, Low-density lipoprotein receptor; Lyrm7, Complex III assembly factor LYRM7; Mff, Mitochondrial fission factor; Mrc2, C-type mannose receptor 2; Mt-atp6, ATP synthase subunit a; Mtnd1, NADH-ubiquinone oxidoreductase chain 1; Nrm, Nurim; Oma1, Metalloendopeptidase OMA1; Opa1, Dynamin-like 120 kDa*

protein; Orm1, Alpha-1-acid glycoprotein; Pak1, Serine/threonine-protein kinase PAK 1; Pak2, Serine/threonine-protein kinase PAK 2; Phb1, Prohibitin; Rab11a, Ras-related protein Rab-11A; Rab34, Ras-related protein Rab34; Rab43, Ras-related protein Rab43; Serpina1, Alpha-1-antiproteinase; Sh3glb1, Endophilin-B1; Sh3glb2, Endophilin-B2; Slc25a51, Solute carrier family 25 member 51; Snap91, Clathrin coat assembly protein AP180; Stk24, Serine/threonine-protein kinase 24; Stx17, Syntaxin-17; Synj2bp, Synaptojanin-2-binding protein; Tf, Serotransferrin; Them4, Acyl-coenzyme A thioesterase THEM4; Tmem41, Transmembrane protein 41B; Timm17a, Mitochondrial import inner membrane translocase subunit Tim17-A; Tomm22, Mitochondrial import receptor subunit TOM22 homolog; Tomm34, Mitochondrial import receptor subunit TOM34; Trap1, Heat shock protein 75 kDa; Uqcrh, Cytochrome b-c1 complex subunit 6; Uqcrq, Cytochrome b-c1 complex subunit 8; Vamp8, Vesicle-associated membrane protein 8; Vmp1, Vacuole membrane protein 1; Wipi2, WD repeat domain phosphoinositide-interacting protein 2; Yme1l1, ATP-dependent zinc metalloprotease.

Of note, in still healthy LPP *Atp7b*$^{-/-}$ rats, it was observed a strong predicted activation of cellular acute stress response, and elevated nuclear receptor signalling towards cellular proliferation and inflammation (Figure 12.A, Figure 13.A). Thus, although still being clinically healthy and lacking Cu excess, animal intestines presented clear evidence of cellular stress.

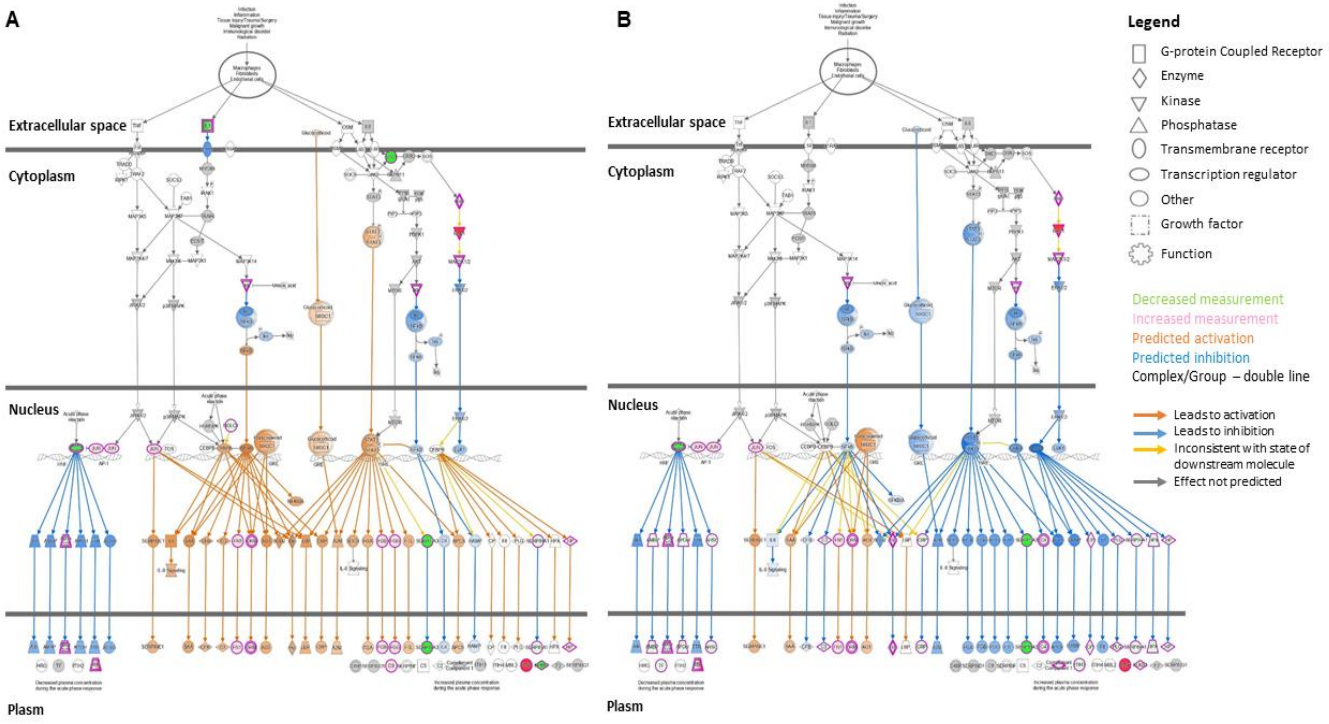

Figure 13. **Cellular acute phase response was changed in the duodenum of Wilson disease rats upon disease onset. (A)** In still healthy (H) LPP *Atp7b*$^{-/-}$ animals, it was observed a predicted activation of pathways directly related to inflammation, proliferation, cellular differentiation and immune response, **(B)** while in diseased (D) LPP *Atp7b*$^{-/-}$ animals, the opposite was observed, with most inflammatory and proliferation responses predicted to be inhibited (Qiagen, Ingenuity pathway analysis)**.** Green: Downregulated proteins in comparison to Atp7b heterozygous animals; Pink: Upregulated proteins in comparison to LPP *Atp7b*$^{+/-}$ animals; Blue: predicted inhibition of the pathway; Orange: predicted activation of the pathway; Grey: no activity pattern available. Proteins are represented with their correspondent gene symbol.

Furthermore, a predicted strong inactivation of the nuclear receptor heterodimer LXR/RXR was observed in diseased animals, in comparison with still healthy ones (Figure 14). Also,

proteins whose function is important in cellular renewal processes such as autophagy and apoptosis, were downregulated in LPP *Atp7b*$^{-/-}$ rats (Figure 12.B), which could have a negative impact on mitochondria renewal, possibly contributing to increased levels of cellular stress in still healthy LPP *Atp7b*$^{-/-}$ intestines.

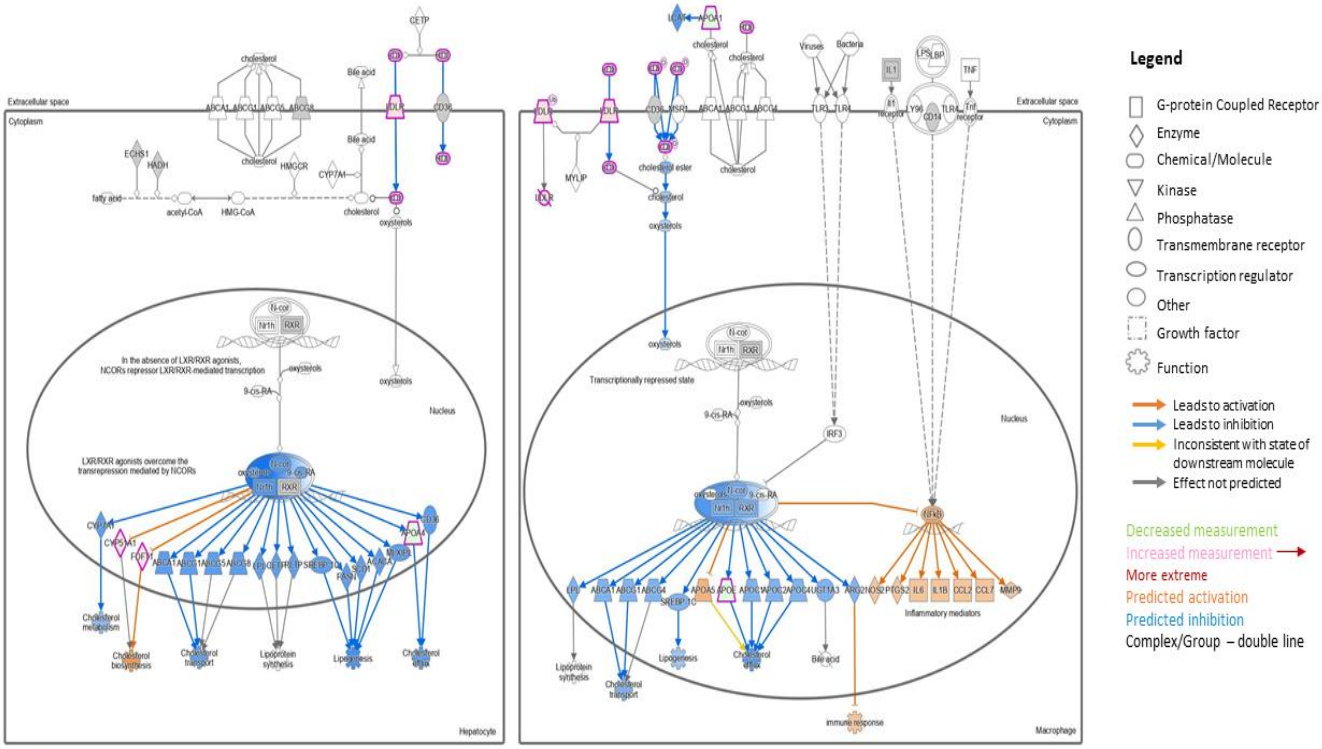

Figure 14. **Alterations in the expression of the nuclear receptors LXR/RXR in the duodenum of Wilson disease rats upon disease, affected cholesterol metabolism and inflammation.** In diseased LPP *Atp7b*$^{-/-}$ animals, cholesterol metabolism was affected with a predicted increase of cholesterol biosynthesis and decrease in cholesterol transport, lipogenesis and cholesterol efflux. Inflammatory response was predicted to be activated via the NF-kB pathway, with a predicted increase of several inflammatory mediators. (Qiagen, Ingenuity pathway analysis)**.** Green: Downregulated proteins in comparison to LPP *Atp7b*$^{+/-}$ animals; Pink: Upregulated proteins in comparison to LPP *Atp7b*$^{+/-}$ animals; Blue: predicted inhibition of the pathway; Orange: predicted activation of the pathway; Grey: no activity pattern available. Proteins are represented with their correspondent gene symbol.

On the other hand, upregulation of proteins linked to carbohydrate, fat and bile salts metabolism was observed in both still healthy and diseased animals (Table S1). Especially hexokinase-1, a key protein in glycolysis was found to be significantly elevated in still healthy LPP *Atp7b*$^{-/-}$ rats, along with ketogenic enzymes, namely 3-hydroxybutyrate dehydrogenase type 2 (BDH2), acetyl-CoA acetyltransferase (ACAT2) and hydroxy-methylglutaryl-CoA synthase (HMGCS1).

3.1.1.3 Cell-cell contacts impairment in the duodenum of LPP animals

In combination with the proteome analysis, electron micrographs of duodenum tissues from still healthy and diseased LPP *Atp7b*$^{-/-}$ animals revealed a significant depletion in proteins forming cell-cell contacts, in comparison to LPP *Atp7b*$^{+/-}$ non-affected controls (Figure 15). The peptide abundance of the cadherin family (5, 1, 17) was significantly downregulated in still healthy LPP *Atp7b*$^{-/-}$, with no significant differences for occludin, claudin-3, 7 and 15, as well as zona occludens-1 (ZO-1) (Figure 15.A). In agreement, electron micrographs demonstrated less electron-dense desmosome areas and severe widenings of enterocyte tight junctions (TJ) in LPP *Atp7b*$^{-/-}$ rats compared to controls (Figure 15.B).

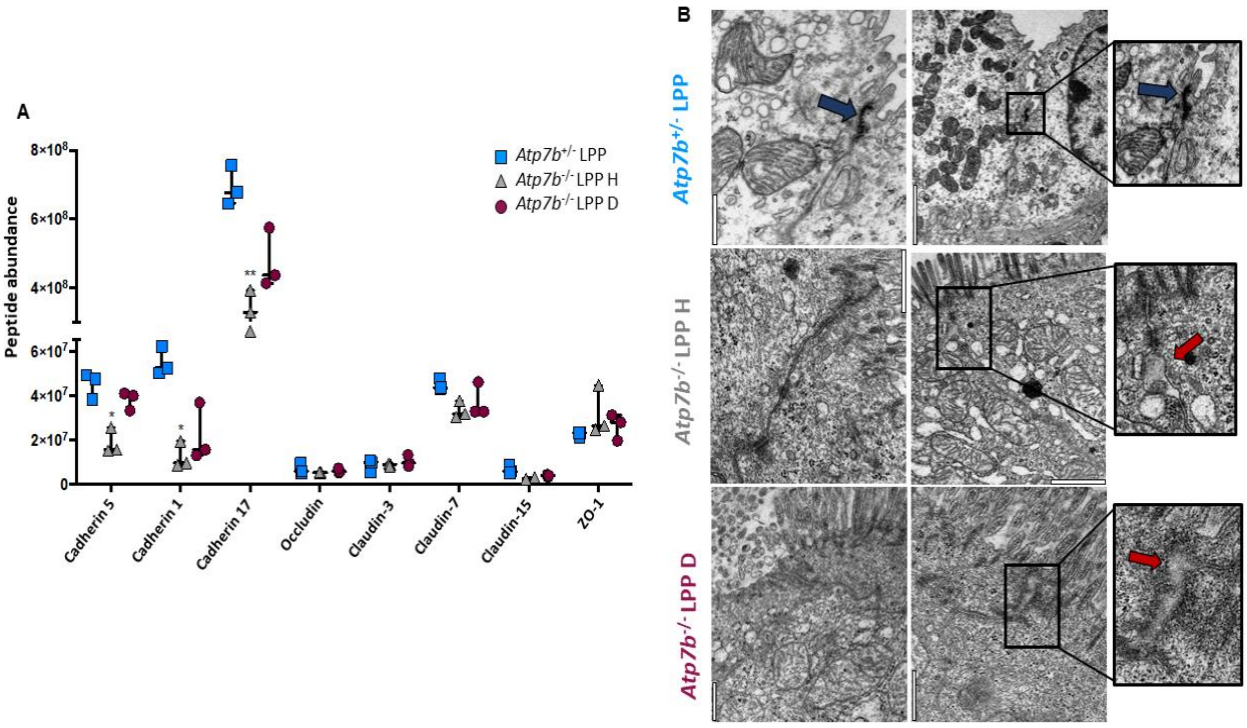

Figure 15. **Duodenum of Wilson disease rats had a decreased expression of tight junctions (TJ) proteins, in comparison to LPP *Atp7b*$^{+/-}$ rats. (A)** Protein abundance of cadherins (5, 1 and 17) was significantly lower in LPP *Atp7b*$^{-/-}$ still healthy (H) animals. **(B)** Electron micrographs of duodenum from LPP *Atp7b*$^{+/-}$ and *Atp7b*$^{-/-}$ animals (scale bar: 500 nm). Duodenum from *Atp7b*$^{-/-}$ still healthy (H) animals had less dense TJ-like areas with widening of the intercellular adhesion spaces (red arrows). In *Atp7b*$^{-/-}$ diseased (D) animals, a similar effect was observed. In contrast, *Atp7b*$^{+/-}$ TJ-like structures were high electron dense, and the border between the cells was tightly closed (blue arrow). Peptide abundance: total amount of identified peptides normalized towards the total amount of peptides in 10µg of protein. One-way analysis of variance with the Kruskal-Wallis test (Dunn's multiple comparisons), after column analysis (identify outliers). *Significance to LPP *Atp7b*$^{+/-}$ animals, *P<.05, **P<.001

Thus, ATP7B mutation induces cellular stress in the duodenum of still healthy LPP *Atp7b*$^{-/-}$ rats, that was not paralleled by a significantly increased tissue Cu content. However, metabolic and bioenergetics changes, most prominently at mitochondrial level, seemed to force enterocytes to utilize alternative energy sources to keep basic cellular functions, possibly neglecting secondary anabolic processes such as the maintenance of cell-cell contacts.

3.1.2 Copper sensitivity and mitochondrial damage in a Wilson disease enterocyte cell model

Indications of mitochondrial impairment, changes in energy metabolism and intestinal barrier irregularities were observed in LPP *Atp7b*$^{-/-}$ animals, already in the absence of a significant increase in Cu levels in the duodenum. To study these effects in more depth, an immortalized human colorectal adenocarcinoma cell line (Caco-2 cells) was employed, together with the ATP7B deficient cell line (Caco-2 KO) generated via CRISPR/Cas9[97], that had a significant decrease in ATP7B protein expression (Figure 16.A). When seeded in a trans-well plate, these cells differentiate in enterocyte-like cells and form a monolayer resembling the gut barrier expressing TJ proteins (see 2.7.3). Electron micrographs of Caco-2 KO cells indicated alterations in mitochondrial structure with apparent loss of cristae organization, in comparison to Caco-2 wild-type (WT) cells (Figure 16.B). Furthermore, Caco-2 KO in comparison to Caco-2 WT cells, were more sensitive to Cu challenges with a significant decrease in metabolic activity (Figure 16.C), ATP cellular content (Figure 16.D), cellular mass content (Figure 16.E) and lysosomal activity (Figure 16.F). In particular, at 100µM $CuCl_2$, overall ATP cellular content was significantly reduced in KO cells, with no differences in cellular mass, i.e. no differences in cell viability (Figure 16.D, E). Of note, a significant decrease in acidification of lysosomes/other acidic vesicular structures was observed upon treatment of the cells with 150µM $CuCl_2$ (Figure 16.F).

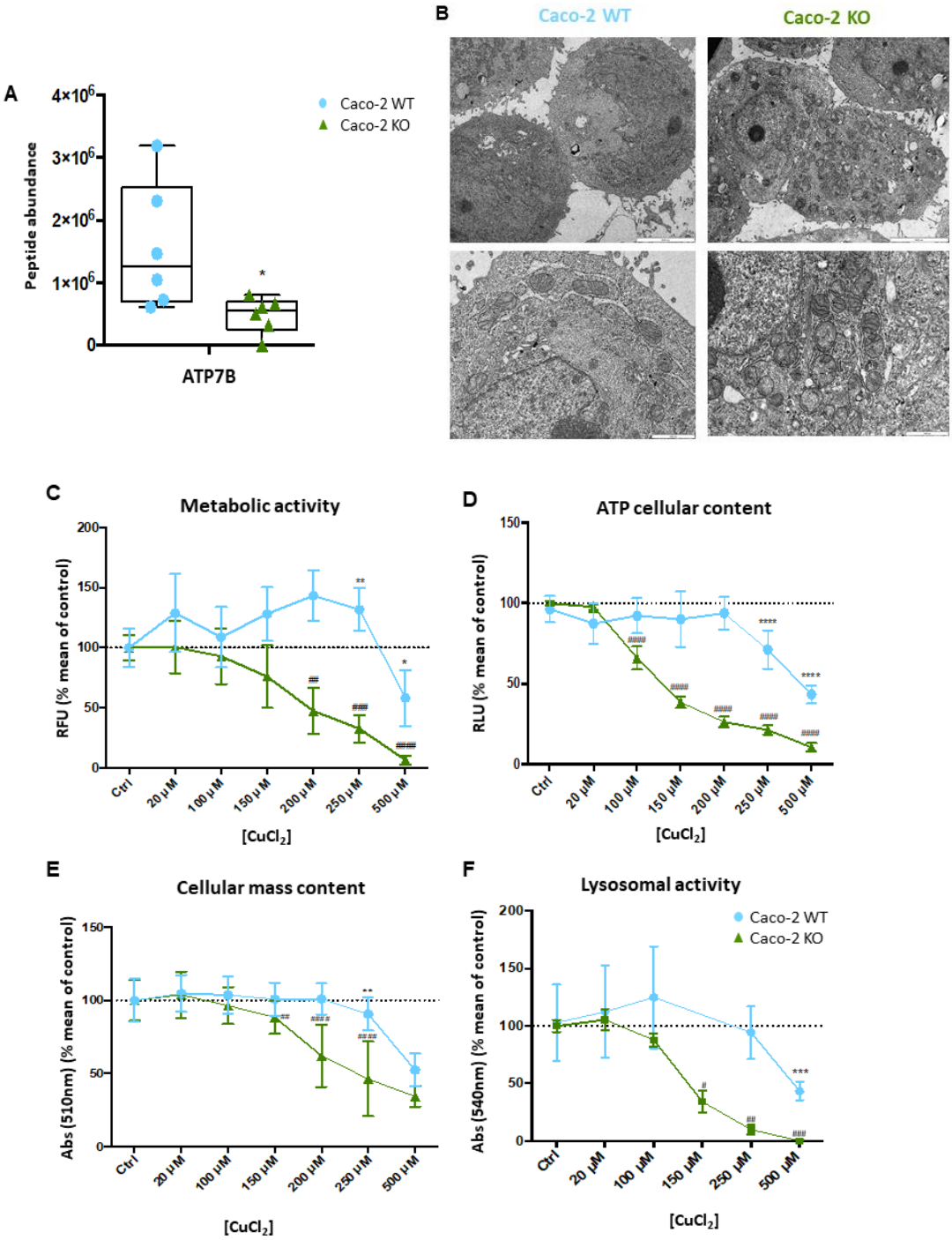

Figure 16. **Caco-2 ATP7B KO cells were more sensitive to copper. (A)** ATP7B protein expression was significantly downregulated in ATP7B KO cells. **(B)** Alterations in mitochondria structure were evident from the electron micrographs of Caco-2 KO cells in comparison to Caco-2 WT cells (scale bar upper panel: 5000 nm; scale bar lower panel: 1000 nm). Increasing $CuCl_2$ concentrations decreased **(C)** Metabolic activity, **(D)** ATP cellular content, **(E)** Cellular mass content and **(F)** Lysosomal activity of Caco-2 WT and KO cells. Data are the mean ± SD of N=4,n=3. One-way analysis of variance (A) with the Kruskal-Wallis test (Dunn's multiple comparisons), or a Two-way analysis of variance with Sidak's multiple comparisons test (C-F), after column analysis (identify outliers). *Significance to Caco-2 WT control. #Significance to Caco-2 KO control. $^{*,\#}$P<.05; $^{**,\#\#}$P<.01; $^{***,\#\#\#}$P<.001; $^{****,\#\#\#\#}$ P<.0001

As observed in the intestine of still healthy LPP *Atp7b*$^{-/-}$, no significant differences in Cu levels were observed between untreated Caco-2 KO and WT cells (Figure 17.A), as well as in isolated mitochondria from both untreated cells lines (Figure 17.D), and similar elevations in KO vs WT were observed upon treatment with 100μM $CuCl_2$ (Figure 17.D). A significant increase in Zn content was observed in treated KO cells (Figure 17.B), whereas no differences were observed in isolated mitochondria (Figure 17.E). Iron content was not significantly changed in either whole cells (Figure 17.C) or isolated mitochondria (Figure 17.F).

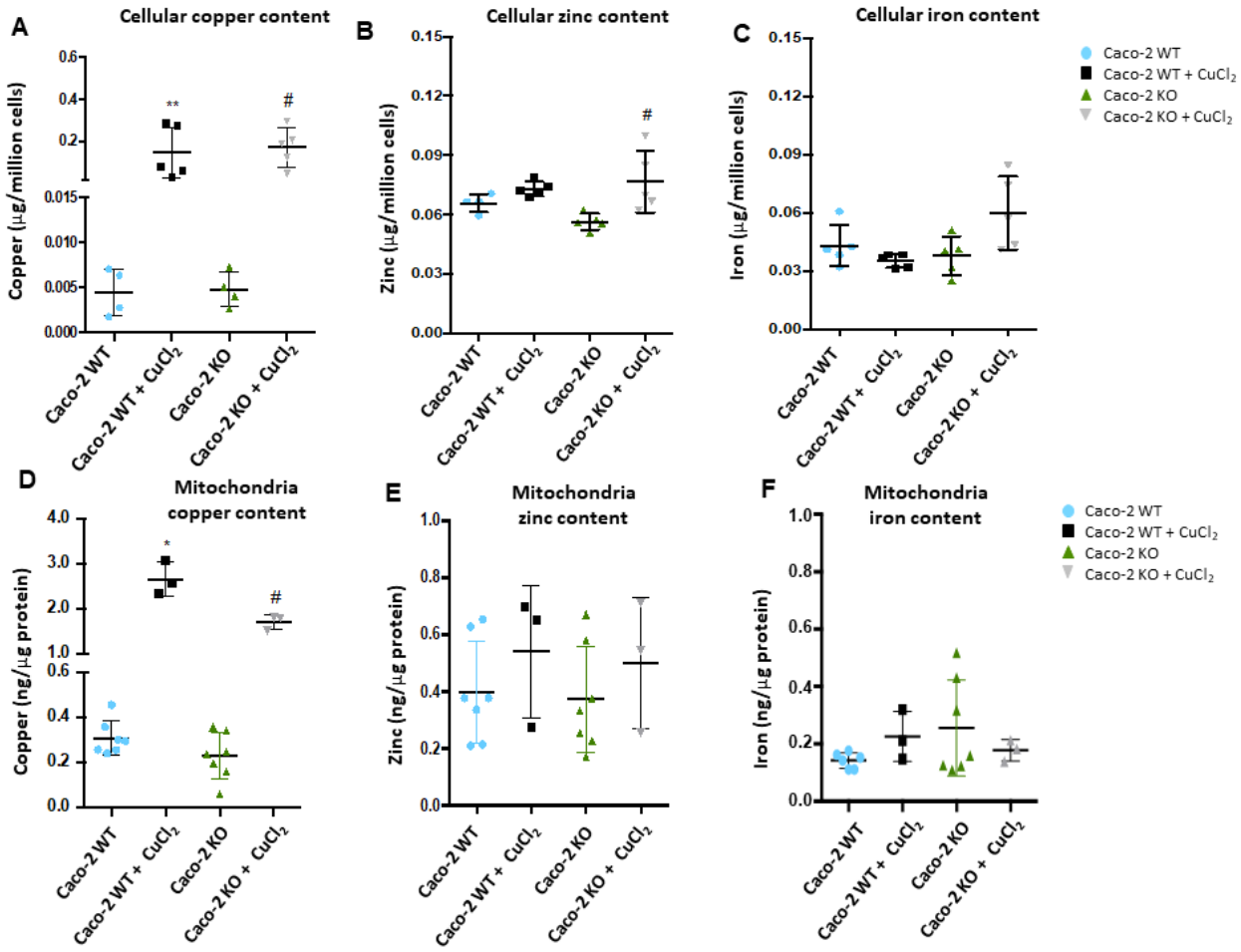

Figure 17. **Copper content in Caco-2 ATP7B KO cells did not significantly differ from Caco-2 WT cells. (A)** Cellular Cu, **(B)** Zn and **(C)** Fe content were not significantly different in between Caco-2 KO and Caco-2 WT cells, as well as in the **(D-F)** mitochondria fractions. Treatment with 100μM $CuCl_2$ significantly increased **(A)** cellular and **(D)** mitochondria Cu content in both cell lines, with a significant increase in **(B)** cellular Zn content in Caco-2 KO cells. Data are the mean ± SD of N=4-5 (A-C) and N=7-3 (D-F). One-way analysis of variance (A-F) with the Kruskal-Wallis test (Dunn's multiple comparisons), after column analysis (identify outliers). *Significance to Caco-2 WT control. #Significance to Caco-2 KO control. *, #P<.05; **P<.01.

In further agreement with the findings in LPP *Atp7b*$^{-/-}$, proteome analyses of Caco-2 WT vs. Caco-2 KO cells validated mitochondrial dysfunction, with a predicted inhibition of OXPHOS

(Figure 18.A-C), decreased network/cristae organization and metabolic changes with a decreased expression of important proteins linked to β-oxidation (Figure 18.C). A predicted increased activation of stress response pathways (EIF2, mTor and Sirtuin signalling) that promote inflammation, glucose metabolism, and an active response to oxidative stress were observed in Caco-2 KO cells (Figure 18.A). Moreover, changes in the expression of proteins related to lysosomal function were additionally observed, as well as in vesicular trafficking and lipid metabolism (Figure 18.C).

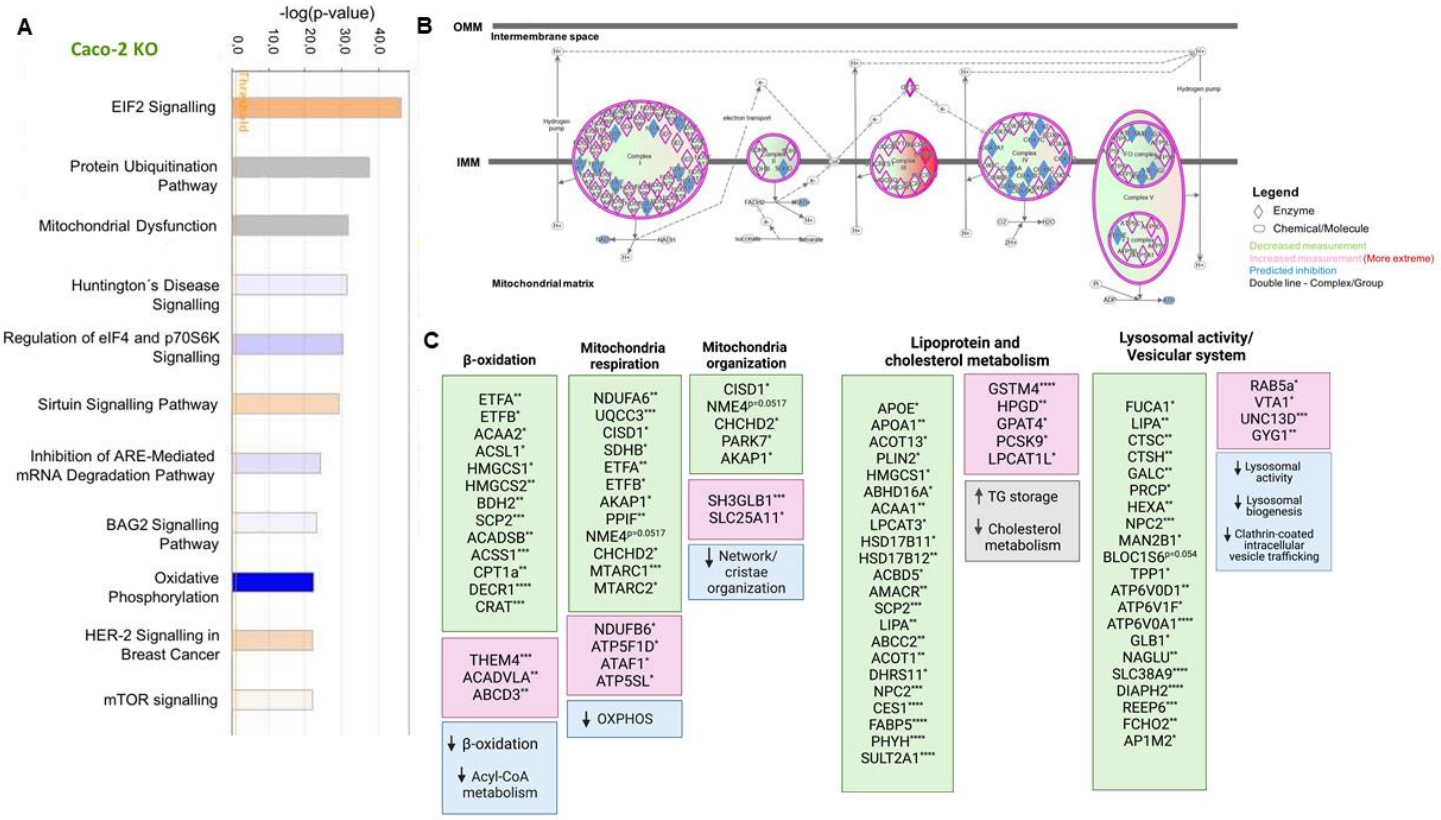

Figure 18. **Proteomics analysis of Caco-2 ATP7B KO cells in comparison to Caco-2 WT cells. (A)** Comparison of altered pathways between Caco-2 KO and Caco-2 WT, using Ingenuity pathway analysis (IPA). The most statistically significant canonical pathways identified ($p<0.05$) were listed according to their p value (-log, orange line). Blue bars: negative z-score (predicted inhibition); Orange bars: positive z-score (predicted activation); Grey bars: no activity pattern available. **(B)** Canonical pathway analysis of proteomics data comparing Caco-2 ATP7B KO and WT cells showed decreased expression (Green), increased expression (Purple to Red) and predicted inhibition (Blue), of several proteins involved in the OXPHOS pathway (Qiagen, Ingenuity pathway analysis). **(C)** Changes in protein expression with an important role in cellular organelle organization (mitochondria and lysosomes), and processes for cell homeostasis such as cholesterol metabolism, cellular respiration and apoptosis. Pink: Upregulated proteins in comparison Caco-2 WT cells; Green: Downregulated proteins in comparison Caco-2 WT cells; Blue/Grey: affected cellular processes and/or pathways. Proteins are represented with their correspondent gene symbol. *Significance of KO cells in comparison to WT cells; *P<.05, **P<.01, ***P<.001, ****P<.0001. *Abbreviations: Abcc2, Canalicular multispecific organic anion transporter 1; Abcd3, ATP-binding cassette sub-family D member 3; Abhd16a, Phosphatidylserine lipase ABHD16A; Acaa1, 3-ketoacyl-CoA thiolase*

(peroxisomal); Acaa2, 3-ketoacyl-CoA thiolase (mitochondrial); Acadsb, Short/branched chain specific acyl-CoA dehydrogenase; Acadvl, Very long-chain specific acyl-CoA dehydrogenase; Acbd5, Acyl-CoA-binding domain-containing protein 5; Acot1, Acyl-coenzyme A thioesterase 1; Acot13, Acyl-coenzyme A thioesterase 13; Acsl1, Long-chain-fatty-acid--CoA ligase 1; Acss1, Acetyl-coenzyme A synthetase 2-like; Akap1, A-kinase anchor protein 1; Amacr, Alpha-methylacyl-CoA racemase; Apoa1, Apolipoprotein A-I; Apoe, Apolipoprotein E; Ap1m2, AP-1 complex subunit mu-2; Atp5sl/Dmac2, Distal membrane-arm assembly complex protein 2; Atp5f1d, ATP synthase subunit delta; Atp6v0a1, V-type proton ATPase 116 kDa subunit a isoform 1; Atp6v0d1, V-type proton ATPase subunit d 1; Atp6v1f, V-type proton ATPase subunit F; Atpaf1, ATP synthase mitochondrial F1 complex assembly factor 1; Bdh2, 3-hydroxybutyrate dehydrogenase type 2; Bloc1s6, Biogenesis of lysosome-related organelles complex 1 subunit 6; Ces1, Liver carboxylesterase 1; Chchd2, Coiled-coil-helix-coiled-coil-helix domain-containing protein 2; Cisd1, CDGSH iron-sulfur domain-containing protein 1; Cpt1a, Carnitine O-palmitoyltransferase 1; Crat, Carnitine O-acetyltransferase; Ctsc, Dipeptidyl peptidase 1; Ctsh, Pro-cathepsin H; Decr1, 2,4-dienoyl-CoA reductase; Dhrs11, Dehydrogenase/reductase SDR family member 11; Diaph2, Protein diaphanous homolog 2; Etfa, Electron transfer flavoprotein subunit alpha; Etfb, Electron transfer flavoprotein subunit beta; Fbp5, Fatty acid-binding protein 5; Fcho2, F-BAR domain only protein 2; Fuca1, Tissue alpha-L-fucosidase; Galc, Galactocerebrosidase; Glb1, Beta-galactosidase; Gpat4, Glycerol-3-phosphate acyltransferase 4; Gstm4, Glutathione S-transferase Mu 4; Gyg1, Glycogenin-1; Hexa, Beta-hexosaminidase subunit alpha; Hmgcs1, Hydroxymethylglutaryl-CoA synthase (cytoplasmic); Hmgcs2, Hydroxymethylglutaryl-CoA synthase (mitochondrial); Hpgd, 15-hydroxyprostaglandin dehydrogenase [NAD(+)]; Hsd17b11, Estradiol 17-beta-dehydrogenase 11; Hsd17b12, Very-long-chain 3-oxoacyl-CoA reductase; Lipa, Lysosomal acid lipase/cholesteryl ester hydrolase; Lpcat1, Lysophosphatidylcholine acyltransferase 1; Lpcat3, Lysophospholipid acyltransferase 5; Man2b1, Lysosomal alpha-mannosidase; Mtarc1, Mitochondrial amidoxime-reducing component 1; Mtarc2, Mitochondrial amidoxime reducing component 2; Naglu, Alpha-N-acetylglucosaminidase; Ndufa6, NADH dehydrogenase [ubiquinone] 1 alpha subcomplex subunit 6; Ndufb6, NADH dehydrogenase [ubiquinone] 1 beta subcomplex subunit 6; Nme4, Nucleoside diphosphate kinase; Npc2, NPC intracellular cholesterol transporter 2; Park7, Parkinson disease protein 7; Pcsk9, Proprotein convertase subtilisin/kexin type 9; Phyh, Phytanoyl-CoA dioxygenase; Plin2, Perilipin-2; Ppif, Peptidyl-prolyl cis-trans isomerase F; Prcp, Lysosomal Pro-X carboxypeptidase; Rab5a, Ras-related protein Rab-5A; Reep6, Receptor expression-enhancing protein 6; Scp2, Non-specific lipid-transfer protein; Sdhb, Succinate dehydrogenase [ubiquinone] iron-sulfur subunit; Sh3glb1, Endophilin-B1; Slc25a11, Mitochondrial 2-oxoglutarate/malate carrier protein; Slc38a9, Sodium-coupled neutral amino acid transporter 9; Sult2a1, Bile salt sulfotransferase; Them4, Acyl-coenzyme A thioesterase THEM4; Tpp1, Tripeptidyl-peptidase 1; Unc13d, Protein unc-13 homolog D; Vta1, Vacuolar protein sorting-associated protein VTA1 homolog;

3.1.2.1 Mitochondria structure and function are impaired in ATP7B KO Caco-2 cells

Mitochondrial structure damage was observed in Caco-2 KO cells, even before additional Cu challenges (Figure 19.A). For quantification, four stages that depict increased mitochondrial structure alterations were defined (Figure 19.B). Thereat, Stage I indicated mitochondria with a distinguishable network of cristae, no visible alterations in the outer or inner membrane and an electron-dense matrix, and Stage IV indicated mitochondria with no distinguishable network of cristae, damage to the inner membrane and visible swelling, whereas Stages II and III presented intermediate changes. Untreated Caco-2 KO cells had a significant decrease of Stage I mitochondria, with an increase in Stage IV (Figure 19.C, D), in comparison to untreated Caco-2 WT cells. Copper treatment did not significantly alter mitochondrial structures in Caco-2 KO cells, however, WT cells had a significant increase in Stage IV mitochondria upon treatment (Figure 19.C, D).

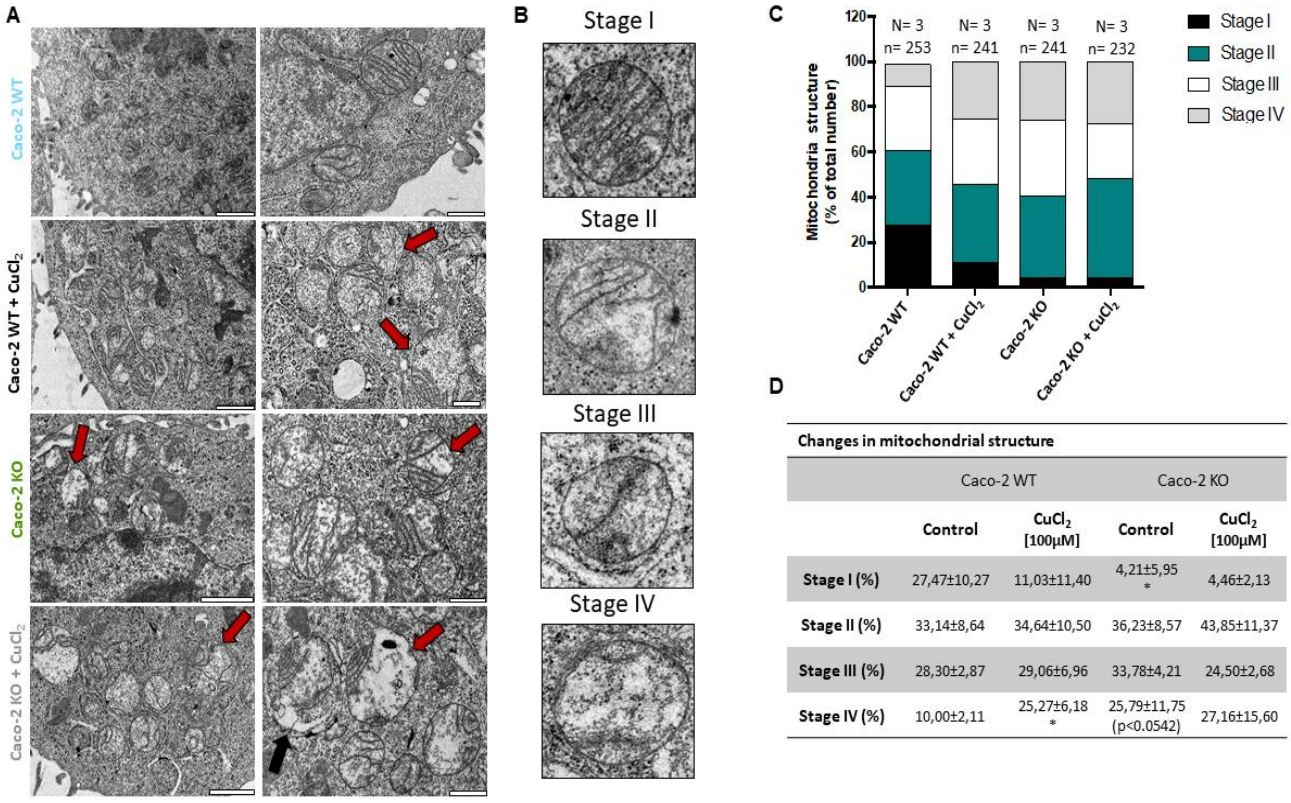

Changes in mitochondrial structure

	Caco-2 WT		Caco-2 KO	
	Control	$CuCl_2$ [100µM]	Control	$CuCl_2$ [100µM]
Stage I (%)	27,47±10,27	11,03±11,40	4,21±5,95 *	4,46±2,13
Stage II (%)	33,14±8,64	34,64±10,50	36,23±8,57	43,85±11,37
Stage III (%)	28,30±2,87	29,06±6,96	33,78±4,21	24,50±2,68
Stage IV (%)	10,00±2,11	25,27±6,18 *	25,79±11,75 (p<0.0542)	27,16±15,60

Figure 19. **Mitochondria of Caco-2 KO ATP7B KO cells had structural impairments, even before copper treatment. (A)** Electron micrographs of mitochondria in situ (left panel, scale bar: 1000 nm; right panel, scale bar: 500 nm) displayed mitochondria structural alterations in Caco-2 ATP7B KO cells (red arrows). It was visible the loss of cristae organization with swelling of the mitochondria. ATP7B KO cells treated with 100µM $CuCl_2$ further displayed detachment of the inner mitochondria membrane (black arrow). **(B)** Mitochondria were divided in four stages, based on cristae structure, membrane integrity and matrix density. **(C, D)** In Caco-2 KO cells, there was a significant decrease in Stage I mitochondria in comparison to Caco-2 WT cells. **(D)** Treatment with 100µM $CuCl_2$ lead to a significant increase in Stage IV mitochondria in Caco-2 WT cells, with no significant changes in Caco-2 KO cells, upon treatment. Data are the mean ± SD of N=3, n=232 to 253 (D). One-way analysis of variance with the Kruskal-Wallis test (Dunn's multiple comparisons), after column analysis (identify outliers). *Significance to Caco-2 WT control. *P<.05.

High resolution respirometry studies revealed that, also in untreated Caco-2 KO cells, the basal routine (R) vs leak (L) (R/L) and maximum respiratory capacities at the electron transport chain (E) vs leak (E/L ratio) were significantly decreased in comparison to WT cells (Figure 20.A). Upon Cu treatment of the KO cells, oxygen consumption linked to Complex II (Succinate (S)-linked pathway) was significantly increased in comparison to untreated KO cells. This effect was observed upon succinate (Figure 20.B), but also upon glycerol-3-phosphate (Gp) addition (Figure 20.C), which could indicate a possible compensatory mechanism towards Complex I damage. Cytochrome c oxidase (Complex IV)-linked respiration was also elevated in Caco-2

KO cells (Figure 20.D), which correlated with the proteome analysis that showed increased protein expression of different ATP synthase subunits (ATP5SL and ATPAF1) (Figure 18.C, Figure 20.E).

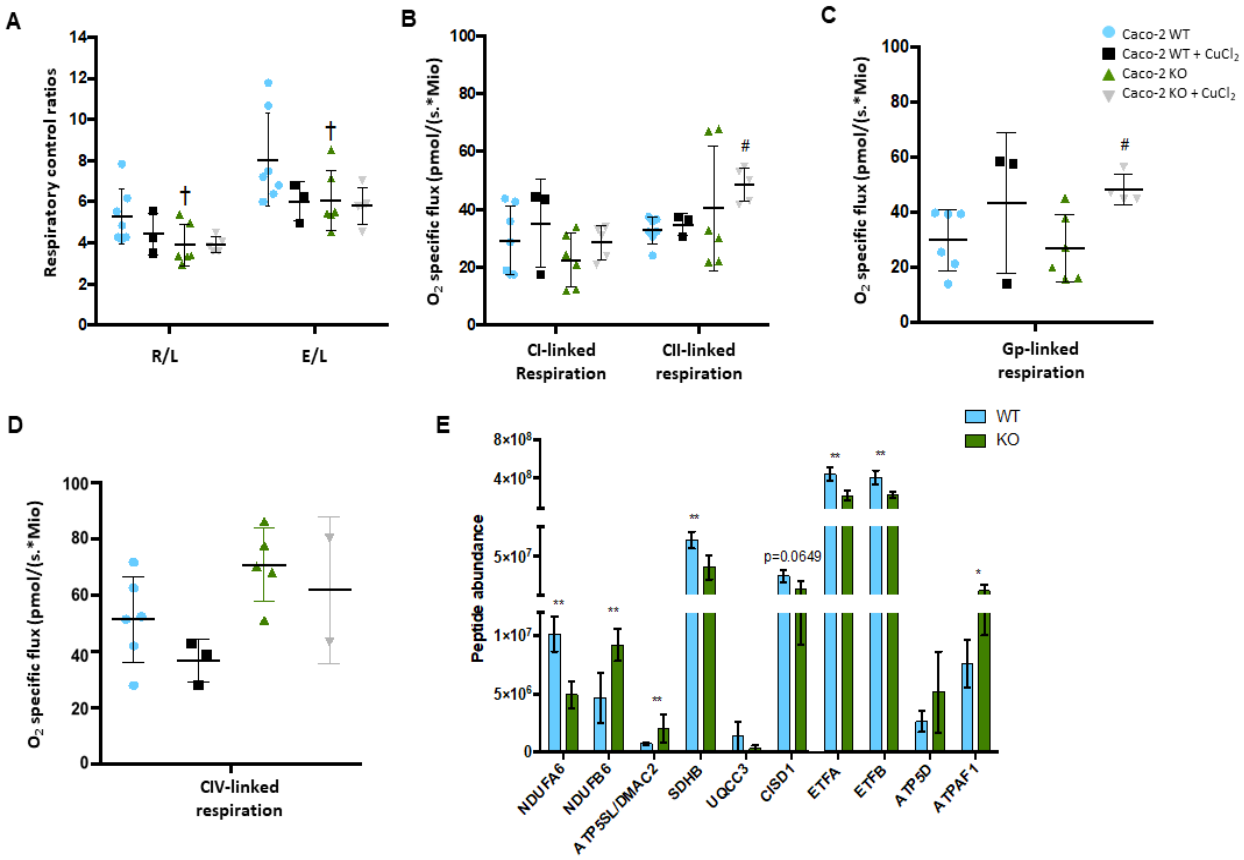

Figure 20. **Caco-2 ATP7B KO cells had decreased mitochondria function and OXPHOS-linked protein abundance.** **(A)** The Respiratory to Control ratio (RCR), defined as routine to leak respiration (R/L), and the electron transport system to leak respiration (E/L) was decreased in both mitochondria-coupled conditions in the ATP7B KO cells. **(B)** Mitochondria complex II-linked (S-linked respiration) and **(C)** Gp-linked oxygen consumption were significantly increased in ATP7B KO cells upon 100μM $CuCl_2$ treatment. **(D)** Mitochondria complex IV-linked respiration was increased in ATP7B KO cells without $CuCl_2$ treatment. **(E)** Protein abundance of key proteins linked to OXPHOS complexes assembly and electron transport in the mitochondria were significantly downregulated, with upregulation of complex V (ATP synthase) assembly units (ATP5SL/DMAC2 and ATPAF1). Peptide abundance: total amount of identified peptides normalized towards the total amount of peptides in 10 μg of protein. Proteins are represented with their correspondent gene symbol. Data are the mean ± SD of N=3-7 (A-C), N=2-6 (D) N=3 (E). Two-way analysis of variance (A) with Dunnett's multiple comparisons test, One-way analysis of variance with the Kruskal-Wallis test (Dunn's multiple comparisons) after column analysis (identify outliers) (B-D) and Two-tailed t-test (Mann-Whitney) (E). *Significance to Caco-2 WT control. #Significance to Caco-2 KO control. †Significance to control Caco-2 KO in comparison to control Caco-2 WT cells. $^{*,\#,\dagger}$P<.05; **P<.01. *Abbreviations:Atpaf1, ATP synthase mitochondrial F1 complex assembly factor; Atp5d, ATP synthase subunit delta; Atp5sl/Dmac2, Distal membrane-arm assembly complex protein 2; Cisd1, CDGSH iron-sulfur domain-containing protein 1; Etfa, Electron transfer flavoprotein subunit alpha; Etfb, Electron transfer flavoprotein subunit beta; Ndufa6, NADH dehydrogenase [ubiquinone] 1 alpha subcomplex subunit 6; Ndufb6, NADH dehydrogenase [ubiquinone] 1 beta*

subcomplex subunit 6; Nme4, Nucleoside diphosphate kinase; Sdhb, Succinate dehydrogenase [ubiquinone] iron-sulfur subunit; Uqcc3, Ubiquinol-cytochrome c reductase complex assembly factor 3.

A parallel analysis of mitochondrial oxygen consumption (OCR), and extracellular acidification rate (ECAR) in the Seahorse XF Analyzer, corroborated the abovementioned results. Again, at basal level, Caco-2 KO cells had no spare respiratory capacity (SRC), i.e. no difference between oxygen consumption linked to ATP production and maximal respiratory capacity (Figure 21.A). Thus, when forced to ATP production, OXPHOS runs at maximum in the KO cells. An additional Cu challenge decreased the mitochondrial metabolic potential in Caco-2 KO in comparison to WT cells (Figure 21.B), although equal Cu accumulation was observed for both cell lines (Figure 17.A). Caco-2 KO cells were more glycolytic, with a significant increase in the ECAR, in comparison to Caco-2 WT cells, at basal levels. Upon Cu treatment, the ECAR increased in both cell lines, with a higher increase observed for the KO cells (Figure 21.C). This increase is higher when mitochondria ATP production is inhibited (via oligomycin) however, the difference between Caco-2 KO control and Cu treated cells was lower (Figure 20.C, D). A higher glycolytic activity is also observed by the medium acidification of the Caco-2 KO cells in comparison to the WT cells (Figure 21.F).

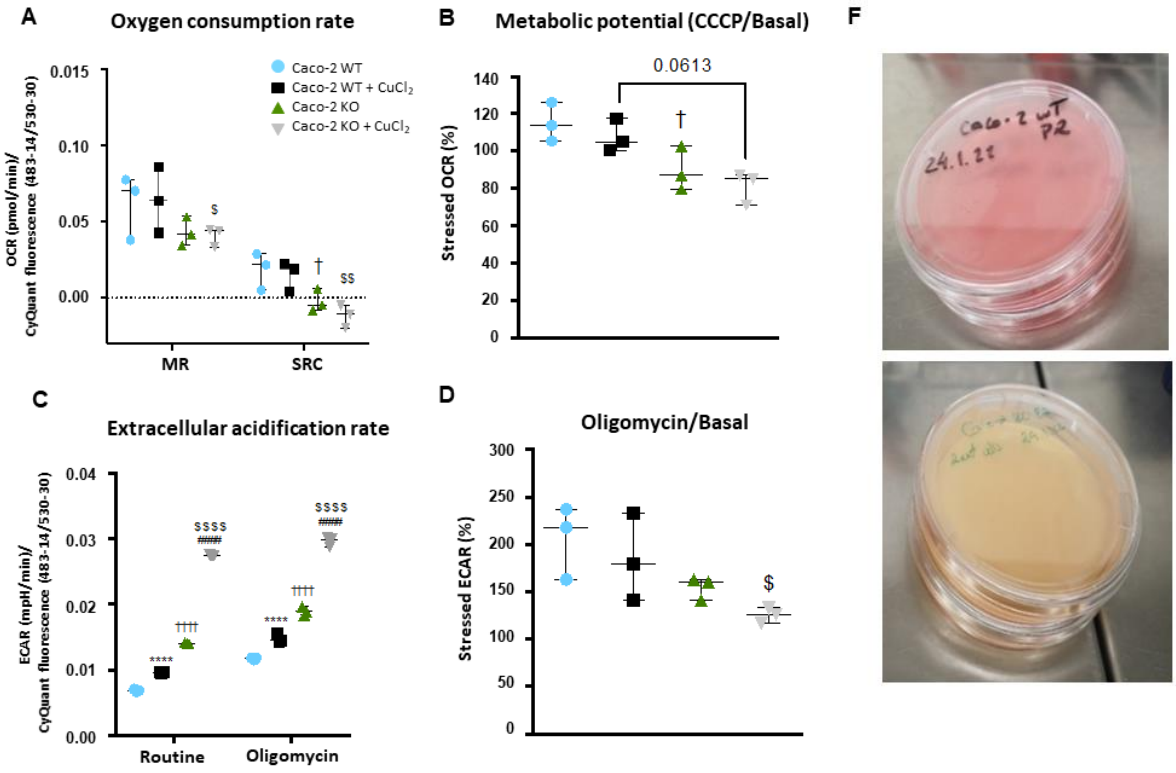

Figure 21. **Caco-2 ATP7B KO cells were metabolically different from the Caco-2 WT cells. (A)** Mitochondria maximum respiratory capacity (MR) and spare respiratory capacity (SRC) of KO cells were decreased in comparison to WT cells, in particular when treated with 100μM $CuCl_2$. These results reflect in a decreased **(B)** metabolic potential [(CCCP linked OCR/Baseline OCR) x 100] of the KO cells. **(C)** The extracellular acidification rate (ECAR) was significantly higher in KO cells without treatment, further increasing upon 100μM $CuCl_2$ treatment. Nonetheless, the ECAR upon oligomycin incubation in relation to the basal acidification values, **(D)** was significantly decreased amongst KO and WT $CuCl_2$ treated cells. **(F)** Media acidification of Caco-2 WT cells (upper figure) and Caco-2 KO cells (down figure) was observed in a higher extent in the KO cells, under the same culture conditions. Data are the mean ± SD of N=3, n=3 (A-D). Two-way analysis of variance with Dunnett's multiple comparisons test (A) or Sidak's multiple comparisons test (C), and One-way analysis of variance (B, D) with the Kruskal-Wallis test (Dunn's multiple comparisons), after column analysis (identify outliers). *Significance to Caco-2 WT Control. #Significance to Caco-2 KO Control. †Significance to control Caco-2 KO in comparison to control Caco-2 WT cells. $Significance to treated Caco-2 KO in comparison to equally treated Caco-2 WT cells. †, $P<.05; **, $$P<.01; ****, ####, ††††, $$$$P<.0001

3.1.2.2 Lipid metabolism is altered in ATP7B KO Caco-2 cells

Changes in lipid metabolism were previously reported in *Atp7b*$^{-/-}$ mice intestine[74], and in Caco-2 ATP7B KO cells[97]. Moreover, proteomic analysis from untreated KO vs WT cells (Figure 18.C) revealed alterations in the abundance of proteins linked to fat processing and storage. Thus, FFA mixture alone or in combination with Cu was applied to Caco-2 KO cells to investigate toxicity and lipid accumulation differences in comparison to Caco-2 WT cells. In this experiment, Cu was added to the cells in the histidine bound form (Cu-His) and Caco-2 KO cells were again more sensitive towards Cu treatment, with a significant decrease in overall ATP cellular content at 200µM Cu-His (Figure 22.A). Again, no differences in Cu content were observed between Caco-2 KO and WT cells (Figure 22.B), as previously observed with 100µM $CuCl_2$ treatment (Figure 17.A). This result showed that Cu accumulation in the cells was independent of the delivery form of the metal, since both $CuCl_2$ and Cu-His treatments resulted in comparable Cu levels in KO and WT cells. A 24 hours' 200µM Cu-His treatment, followed by a BSA-KOH or FFA-BSA treatment for another 24 hours, decreased ATP cellular content in Caco-2 KO cells, in comparison to WT cells, which was not further decreased by the co-treatment, i.e. 200µM Cu-His plus 500µM FFA-BSA for 24 hours, after 24 hours 200µM Cu-His pre-treatment (Figure 22.C). Additionally, the cellular fatty acid content was significantly increased with co-treatment in Caco-2 KO cells, in comparison to equally treated WT cells. However, no significant increase was observed in the cellular fatty acid content, normalised towards cells mass, between FFA-BSA treated cells and non-treated controls, for both cell lines (Figure 22.D).

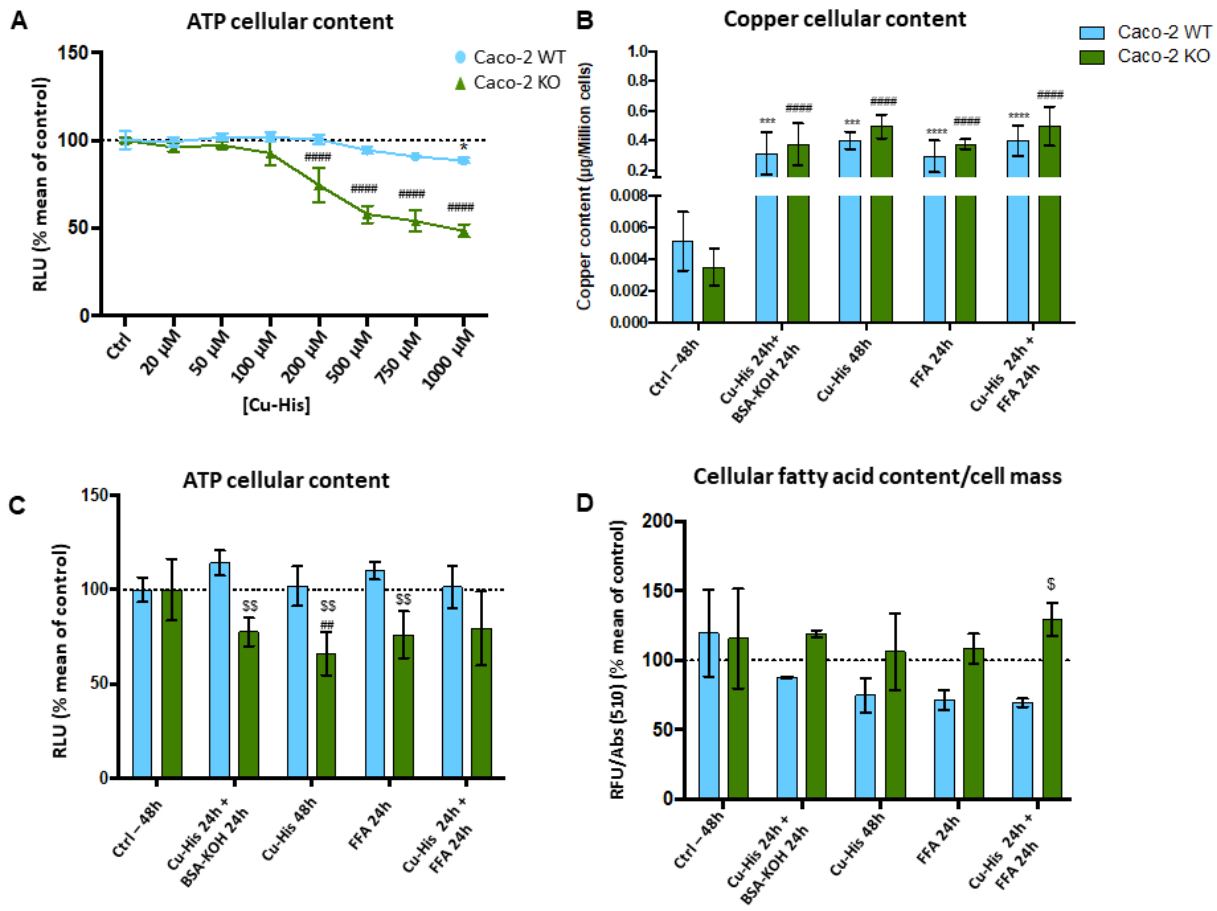

Figure 22. **Caco-2 ATP7B KO cells accumulated fatty acids, even before a FFA mixture treatment, in comparison to Caco-2 WT cells (A)** Caco-2 KO cells were more sensitive do Cu-His treatment, with a significant decrease of ATP cellular content at 200µM Cu-His. **(B)** Treatment with 200µM Cu-His 24h + BSA-KOH 24h, 200µM Cu-His 48h and with 200µM Cu-His 24h + 500µM FFA 24h increased cellular Cu content to the same levels for both Caco-2 WT and Caco-2 KO cells. **(C)** Incubation of cells with FFA following Cu-His treatment did not decrease ATP cellular content in comparison to Cu-His + BSA-KOH control. **(D)** Quantification of cellular fatty acid content, normalised to total cell mass, showed a significant increase in Caco-2 KO cells upon co-treatment (200µM Cu-His + 500µM FFA), in comparison with equally treated Caco-2 WT cells. Data are the mean ± SD of N=3, n=3 (A,C), N=2-4 (B), N=2, n=3 (D). Two-way analysis of variance with Dunnett's multiple comparisons test (A) or Sidak's multiple comparisons test (B-D), after column analysis (identify outliers). *Significance to Caco-2 WT Control. #Significance to Caco-2 KO Control. $Significance to treated Caco-2 KO in comparison to equally treated Caco-2 WT. $^{*,\$}$P<.05; $^{\#\#,\$\$}$P<.01; ***P<.001; $^{****,\#\#\#\#}$P<.0001

Fluorescence microscopy analysis showed an increase in BODYPI staining in the KO cells, without and with 200µM Cu-His treatment, in comparison to WT cells (Figure 23). Incubation of both cell lines with the FFA mixture resulted in an increase of BODIPY staining, again more prominent in KO cells. Furthermore, the accumulation of lipid droplets in the cytosol of the KO cells corroborated the previous finding by the proteome analysis that predicted a

dysregulation of lipid metabolism linked to a possible increase in cellular TG storage. Immunostaining for mitochondria is less intense in the KO cells, for all conditions (Figure 23).

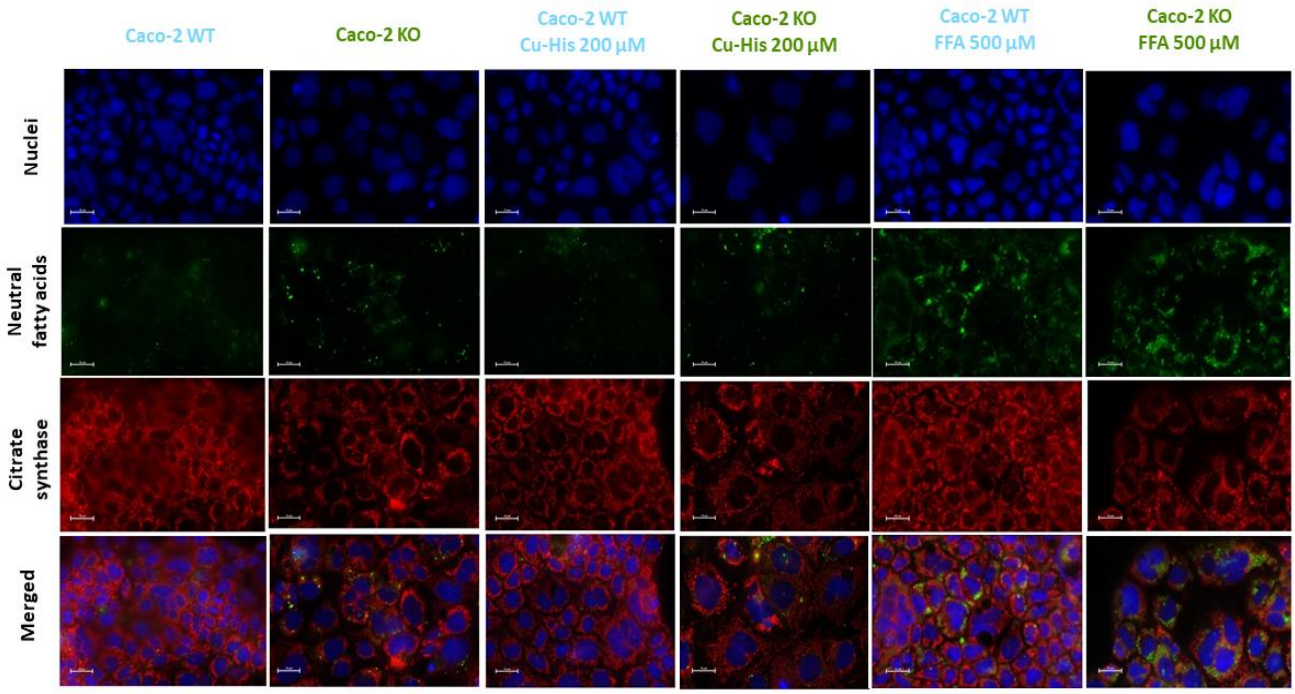

Figure 23. **Lipid droplets content was increased in Caco-2 ATP7B KO.** Cells treated for 48 hours with 500µM FFA had increased staining with BODIPY (green), in comparison to the respective non-treated controls, for both Caco-2 WT and ATP7B KO cells. In Caco-2 KO controls, lipid staining was increased at basal levels in comparison to WT cells, as well as with Cu-His treatment. Immunostaining for mitochondria (red) showed a decrease staining intensity for KO cells at basal conditions, and also with treatments. Scale bar: 10 µm. Fields were chosen randomly and at least 2-3 pictures were taken with the same settings with 60x magnification (Eclipse Ti-S Inverted Research Microscope, Nikon).

3.1.3 Loss of barrier integrity in a human Wilson disease enterocyte cell model

From our findings in the LPP *Atp7b*$^{-/-}$ rats and Caco-2 KO cells, we hypothesized that enterocyte bioenergetic stress and reduced cell-cell contacts may be connected. Indeed, several reports have linked mitochondrial dysfunction in enterocytes to impaired intercellular barrier integrity[245-247]. Thus, we investigated the intercellular barrier tightness in Caco-2 WT and KO monolayers by biophysically assessing their trans epithelial electrical resistance (TEER). The formation of a cell barrier connected by tight junctions (TJ) alters the electrical resistance, created by the flux of ions moving through this barrier. These changes can be monitored by TEER measurement, which is indicative of barrier integrity. In addition, the capacitance (Ccl) of the cellular monolayer can be assessed, providing information on membrane morphology (folding, microvilli formation, etc.), cell layer thickness, and composition[206, 248]. Caco-2 cells, both WT and KO, were continuously differentiated for 21 days in a Transwell® system to form an enterocyte-like barrier. From the 14th day of differentiation, TEER and Ccl were measured and it was observed that the TEER of the KO cellular barriers was consistently, and significantly, lower compared to controls (Figure 24.A, E), while the Ccl was consistently higher (Figure 24.B, F). Apparent permeability (Papp) of the barriers was also determined, showing an increased barrier permeability of the KO cells at 16 days of differentiation (Figure 24.C). As observed in the LPP *Atp7b*$^{-/-}$ rats (Figure 15), electron micrographs showed less electron-dense protein accumulations at the desmosome contact sites, and a strong widening of TJ in Caco-2 KO, but not in Caco-2 WT cells (Figure 24.D), especially at 16 days of differentiation. After 21 days, the Papp was not significantly different between KO and WT cells (Figure 24.C), and the intercellular spaces did not present such widening as it was observed at 16 days. However, Caco-2 WT cells still had more electron-dense desmosome-like structures after 21 days of differentiation, in comparison to KO cells (Figure 24.D).

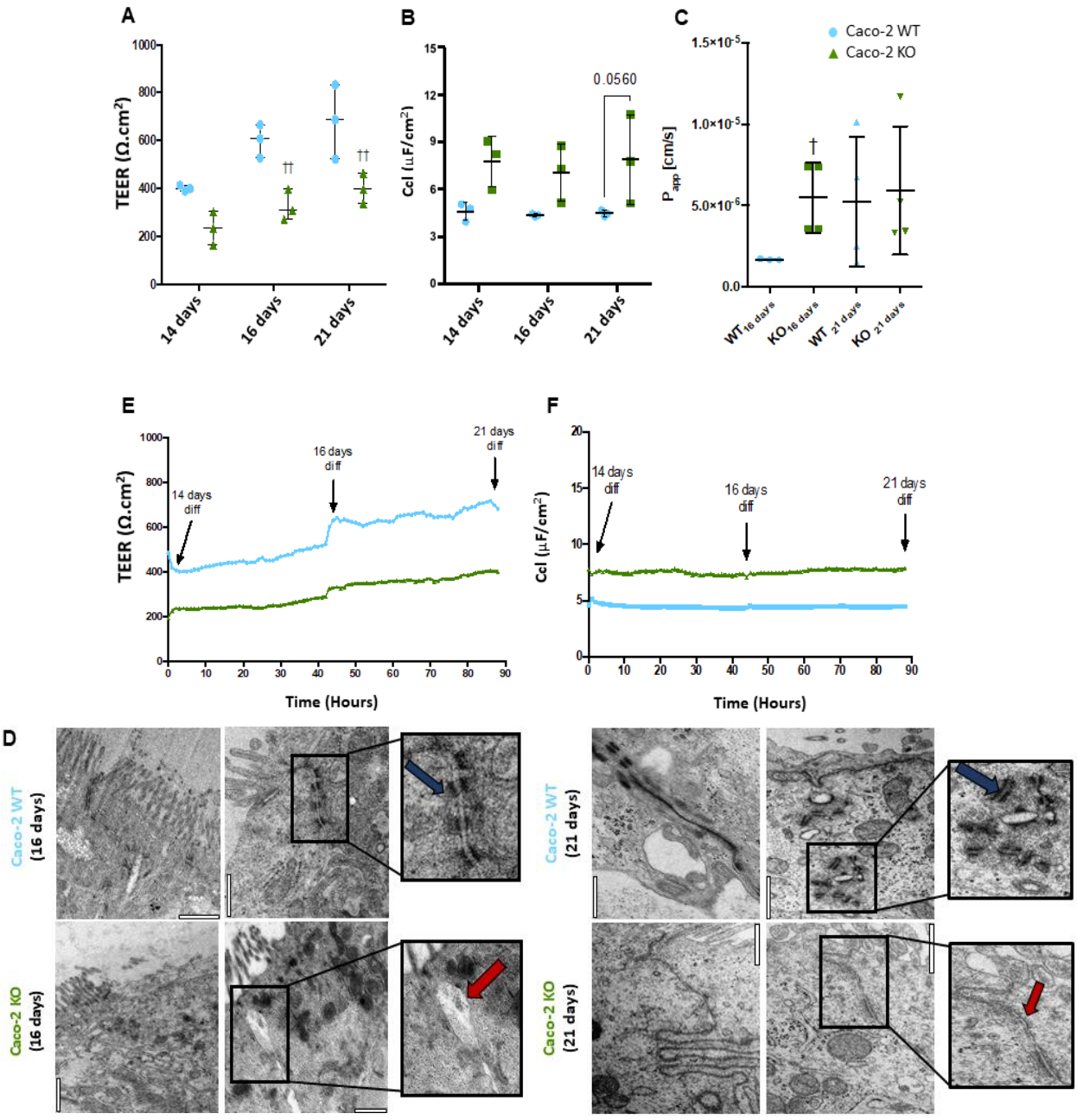

Figure 24. **Caco-2 KO cells present decreased barrier integrity upon differentiation.** ATP7B KO cells had consistently lower **(A)** TEER (Ω.cm^2) in comparison to Caco-2 WT cells. **(B)** Capacitance values of ATP7B KO cells were higher in comparison to WT cells, with no significant time-dependent alterations. **(C)** The apparent permeability (Papp) of the Caco-2 KO monolayers after 16 was lower in comparison to WT cells. **(E)** Representative time dependent measurement of the TEER and **(F)** Ccl, from the 14th until the 21st day of differentiation (Mean values only). **(D)** Electron micrographs of Caco-2 cells differentiated in a Transwell® system for 16 or 21 days with normal medium, changed every 2-3 days (left panel, except Caco-2 WT 21 days, scale bar: 1000 nm; right panel and Caco-2 WT 21 days from the left panel, scale bar: 500 nm). Caco-2 KO cells did not form tight barriers at 16 days of differentiation, which was observed by the intercellular spaces depicted by the red arrows. The formation of protein dense-desmosome-like structures was observed in the Caco-2 WT cells (blue arrows), but was missing in the Caco-2 KO cells, even after 21 days of differentiation (red arrow). **(C)** Data are the mean ± SD of N=3 (A,B) and N= 3-4. One-way analysis of variance with Dunn´s multiple comparisons test (C)

or Two-way analysis of variance with Sidak's multiple comparisons test (A, B), after column analysis (identify outliers). †Significance to control Caco-2 KO in comparison to control Caco-2 WT cells. †P<.05; ††P<.01.

Furthermore, analysis of the proteome from WT and Caco-2 KO cells demonstrated a significant reduction in the expression of important TJ constituting proteins, such as occludin and claudin-4 (Table S3), while other binding proteins responsible for the integrity of cell-cell adhesions were also negatively altered, e.g., nectin, vinculin (VCL), actin, myosin, and catenin beta-1 (CTNNB1) (Figure 25).

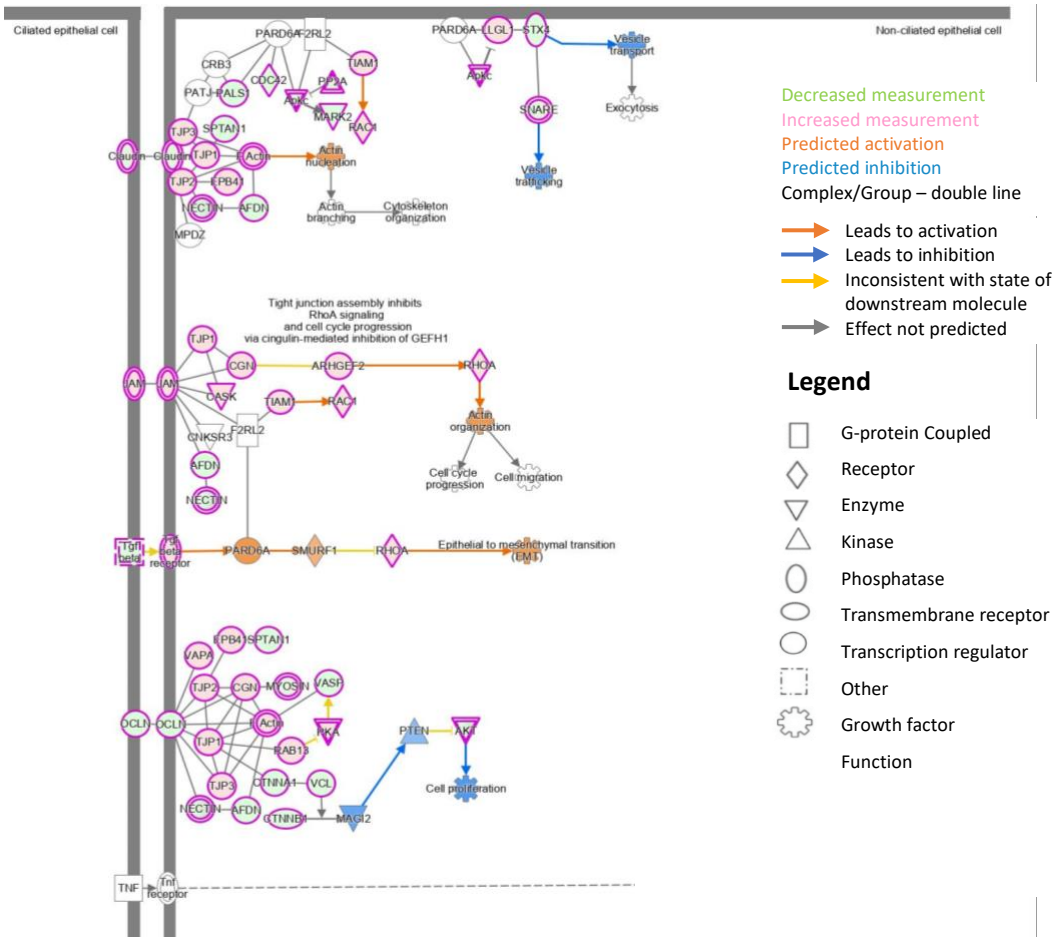

Figure 25. **Caco-2 KO cells present decreased barrier tightness.** Canonical pathway analysis of proteomics data comparing ATP7B KO and WT cells shows decreased expression of several proteins involved in the formation of tight-junctions at the epithelial barrier, with prediction of increased tight junction's permeability (Qiagen, Ingenuity pathway analysis)

The enterocyte-like barriers of Caco-2 WT and KO cells challenged with Cu revealed a higher impairment in WT cells, rather than in KO cells, with a significant decrease in TEER at 21 days of differentiation/14 days of treatment (Figure 26.A, B). Immuno-fluorescent monolayer staining against claudin-5 (Figure 26.C), an integral membrane protein component of TJ strands[249, 250], further confirmed the decreased tightness in the Caco-2 KO cells barrier, with

worsening upon Cu challenge, especially in WT cells. As observed before for non-differentiated Caco-2 cells (Figure 17.A), cellular Cu content was not significantly different between differentiated Caco-2 WT and KO cells, before and after treatment with 100µM $CuCl_2$ (Figure 26.D). Increased barrier leakiness resulted in a decreased Cu content in the apical side (Figure 26.E), with a consequent significant increase in the basolateral side (Figure 26.F), in Cu-treated WT cells. The inflammation marker Interleukin-8 (IL-8) was increased in both WT and KO cells upon Cu treatment (Figure 26.G). After 21 days of differentiation/14 days of treatment, IL-8 amount was decreased in treated KO cells, in comparison with 16 days of differentiation/9 days of treatment. Inversely, IL-8 amount increased in treated WT cells with increasing treatment time (Figure 26.G). Thus, an inflammatory environment accompanies the increase in barrier leakiness.

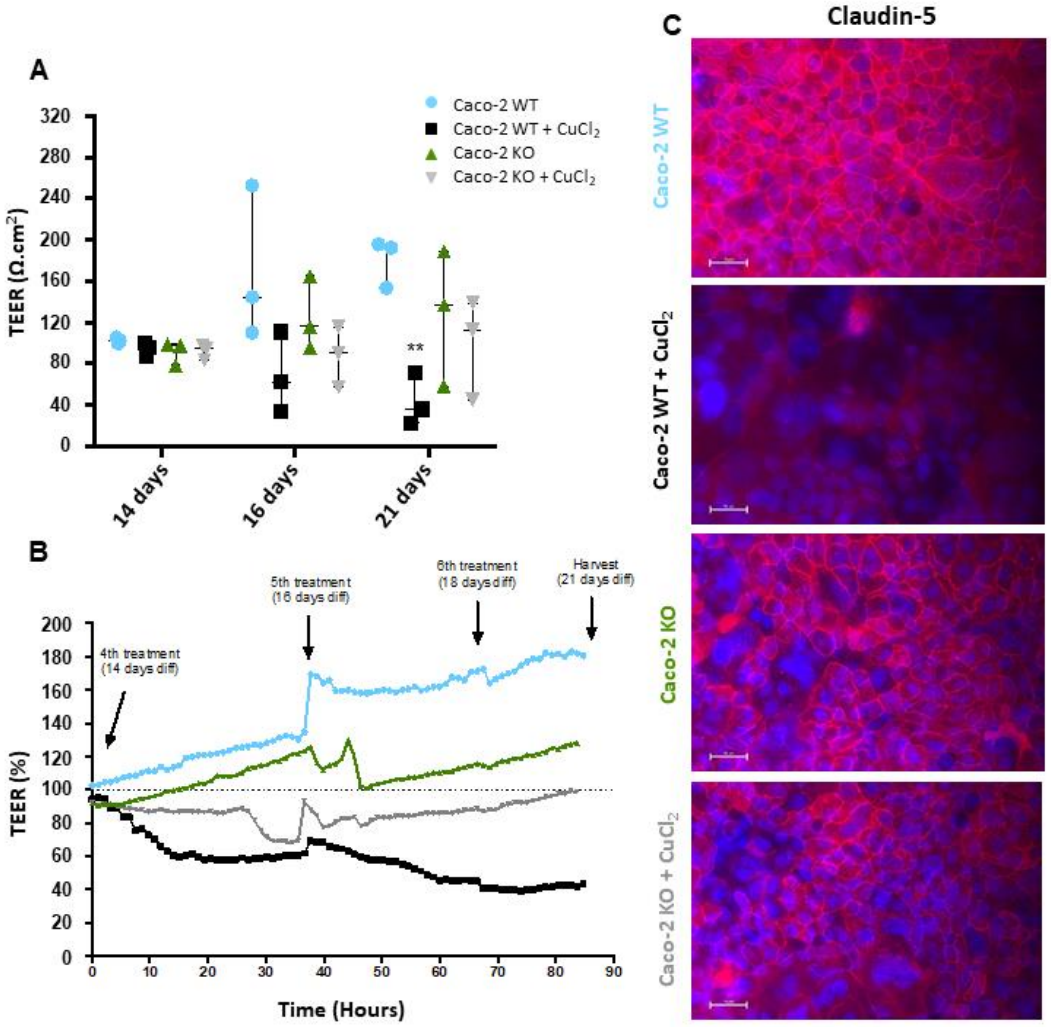

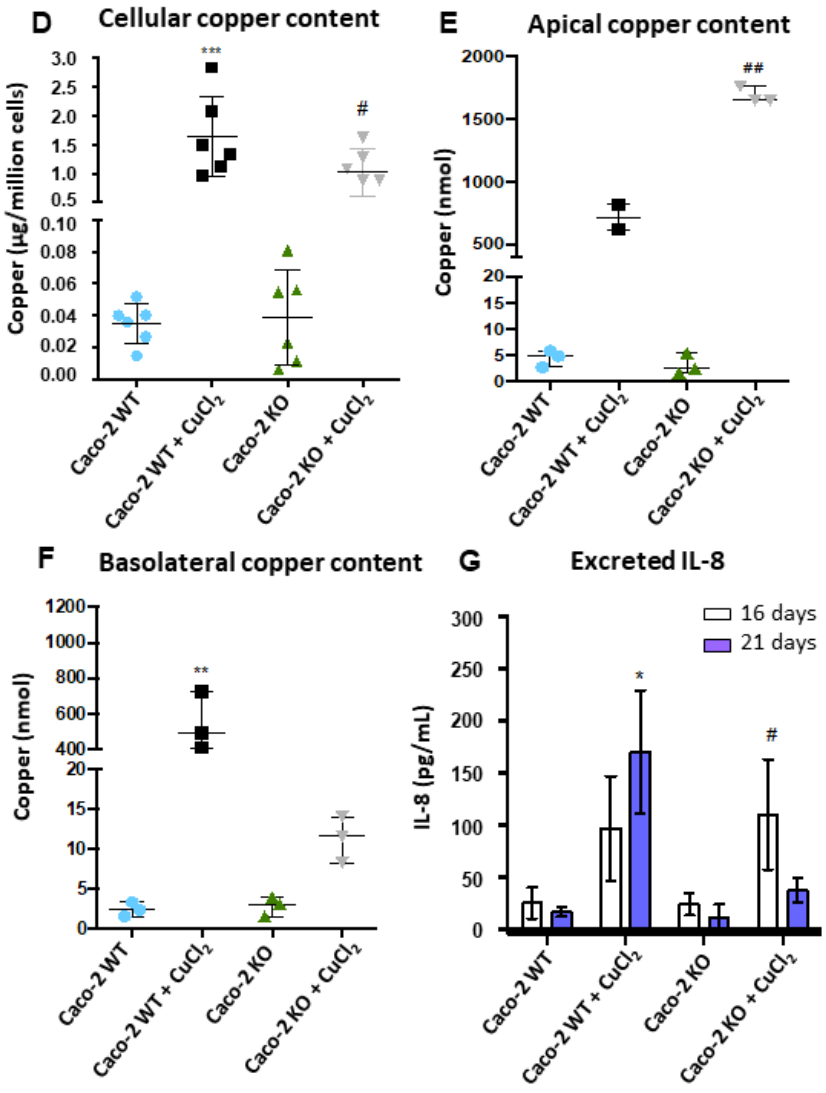

Figure 26. **Copper chloride disrupted tight junctions in differentiated Caco-2 cells. (A)** Treatment with 100µM $CuCl_2$ lead to a time dependent decrease of the TEER, with the highest decrease observed in the Caco-2 WT cells. **(B)** Representative time dependent measurement of the TEER (Mean values only). **(C)** Immunocytochemistry staining against the TJ protein claudin-5 showed a continuous staining of the cell margins in control WT cells, that is disrupted in control KO cells, and further affected by $CuCl_2$ treatment, especially in WT cells (scale bars: 10 µm). **(D)** Cellular Cu content in Caco-2 cells, differentiated for 21 days, increased upon $CuCl_2$ treatment, more significantly in the WT cells. **(E)** The Cu content in the apical (luminal side) media was significantly higher in KO cells, upon treatment. **(F)** In the basolateral (interstitial fluid side) media, Cu content increased significantly in treated WT cells. **(G)** Interleukin-8 secretion was similar for all conditions at 16 days, with Cu treatment causing an increase in inflammation. At 21 days, inflammation progressed in WT cells, but decreased in KO cells. Data are the mean ± SD of N=3-4 (A, B, E, F) and N=5-6 (D). Two-way analysis of variance with Sidak's multiple comparisons test (A), after column analysis (identify outliers) and One-way analysis of variance (D-G) with the Kruskal-Wallis test (Dunn's multiple comparisons), after column analysis (identify outliers). *Significance to Caco-2 WT Control. #Significance to Caco-2 KO Control. $^{*,\#}P<.05$; $^{**,\#\#}P<.01$;$^{***}P<.001$

3.1.4 Methanobactin beneficial effects in the Wilson disease enterocyte cell model

Despite the lack of an increased cellular Cu content in Caco-2 KO cells in comparison to WT cells, we nevertheless came with the question if the high affinity Cu chelator methanobactin (MB) could, to some extent, reverse the impairments caused by the decrease of ATP7B expression. This was done under the rationale that, while overall Cu may be unchanged in basal WT vs KO cells, the intracellular Cu distribution may be altered, thereby causing negative effects that are Cu related. Methanobactin has an enormous Cu affinity to typically provide their hosts with vitally needed environmental Cu[251]. As our group has previously reported, MB is highly effective in depleting deleterious liver Cu in LPP *Atp7b*$^{-/-}$ animals, thereby restoring mitochondrial bioenergetic capacity and thus avoiding liver failure[69, 108]. A Zn stabilized MB was used here, as it has been shown to prevent temperature dependent MB inactivation, due to prolonged incubations at elevated temperatures (37°C), without causing deficits in Cu binding[108]. A 24 hours' treatment of Caco-2 KO cells with MB (Zn) significantly improved mitochondrial activity (Figure 27.A). A prolonged treatment with MB, from the 7th day of differentiated KO cells on, up to 21 days of differentiation, improved the TEER values (Figure 27.B). This finding was further supported by increased presence of the TJ proteins occludin and tight junction protein 1 (TJP-1)/ZO-1 in MB-treated ATP7B KO monolayers (Figure 27.C). At ultrastructural level, TJ of MB-treated KO monolayers appeared with increased electron density due to desmosome formation, whereas untreated KO like-enterocytes mostly had semi-desmosomal structures only (Figure 27.D, quantification in Figure 27.E). In addition, MB treatment resulted in reduced intracellular Cu, with no significant changes in Zn and Fe (Figure

27.F). Thus, the high affinity Cu chelator treatment improved mitochondrial dysfunction, and promoted an increase in barrier formation and tightness of Caco-2 ATP7B KO like-enterocytes.

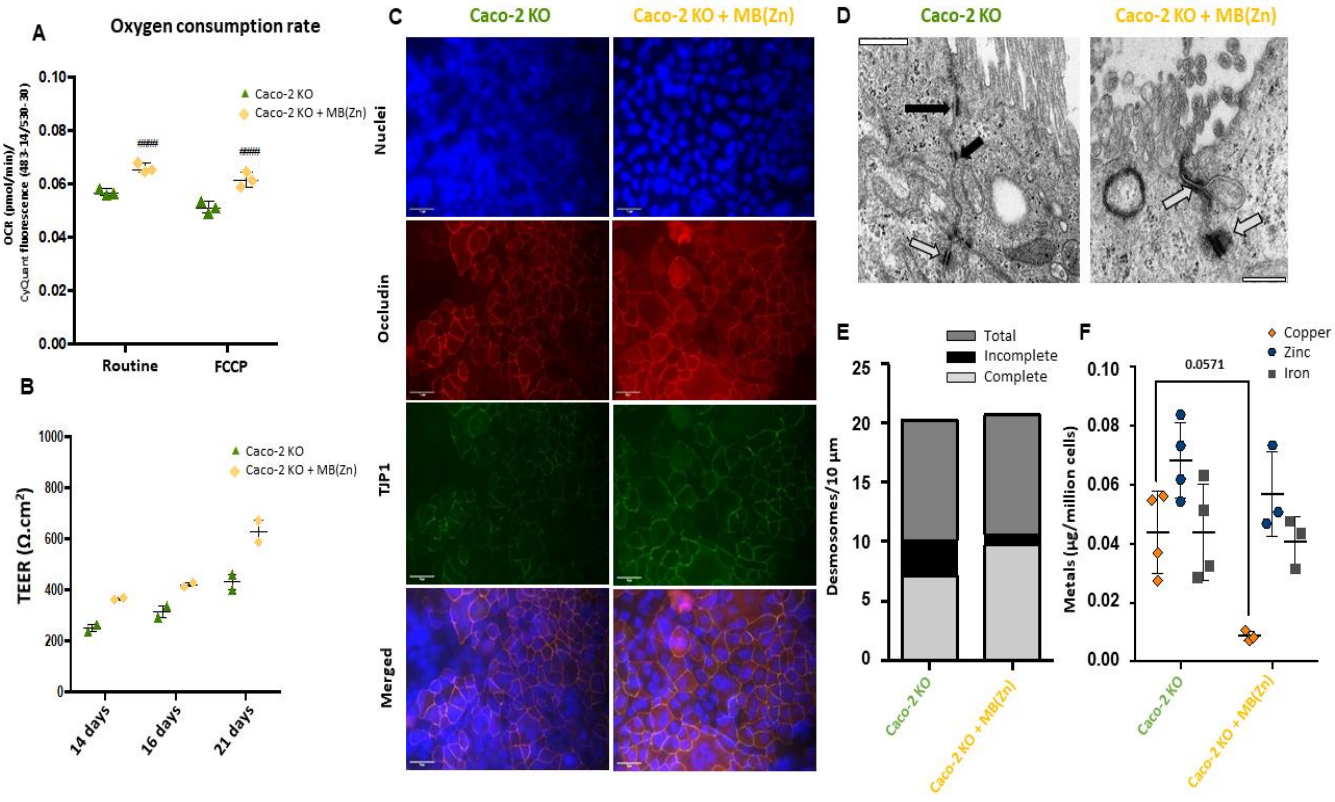

Figure 27. **Methanobactin decreased the metabolic stress, and improved barrier leakiness in Caco-2 ATP7B KO cells.** Changes in cellular metabolism were observed in KO cells upon treatment with 50µM MB(Zn). **(A)** The oxygen consumption rate (OCR) was improved, as well as the **(B)** TEER, measured from the 14th day, until de 21st day of differentiation. **(C)** Immunocytochemistry staining against the TJ proteins occludin and TJP1/ZO-1, showed an increased intensity of the staining upon MB(Zn) treatment of the KO cells (scale bars: 10 µm). **(D)** Electron micrographs of KO cells, differentiated in a Transwell® system for 18 days (scale bar: 500 nm), indicated that MB(Zn) promoted an increase of the electron dense areas at the intercellular junctions. The number of complete desmosome-like structures (grey arrows) was higher in KO cells treated with MB(Zn), with more incomplete desmosome-like structures (black arrows) observed in the control. **(E)** Quantification of the desmosome-like structures was performed with ImageJ for 10 images per condition (Total desmosome like-structures: dark-grey; complete desmosome like-structures: light-grey; incomplete desmosome like-structures: black). **(F)** Copper content was decreased in KO cells upon MB(Zn) treatment, with a tendency for lower Zn, and no differences in Fe. Data are the mean ± SD of N=3, n=3 (A) N=2 (B) and N=3-4 (F). Two-way analysis of variance with Dunnett's multiple comparisons test after column analysis (identify outliers). #Significance to Caco-2 KO Control. ####P<.0001

3.2 Development of a new nutritional approach for Wilson Disease

3.2.1 Mushroom extracts improve cellular viability in a lipotoxicity *in vitro* model.

Steatosis is an early and prime feature in Wilson disease (WD)[65]. Thus, we aimed to develop a new nutritive approach that may either ameliorate liver damage or slow down disease progression. As diverse edible mushrooms have been reported to provide liver protective effects[134, 135, 252], in order to identify a potential edible or medicinal mushroom species that, on the one hand, has low or inexistent toxicity towards hepatocytes and, on the other hand, can be protective in a lipotoxic hepatic environment, a first screening in the hepatocellular carcinoma cell line HepG2 was performed. Seven mushroom species were selected and HepG2 cells incubated, dose-dependently, with both ethanol and aqueous extracts. Cell metabolic activity and cell viability (as a measure of total cells mass) were evaluated, and the results for the highest concentration applied (1000µg/mL) were summarized in Table 17. For the aqueous extracts, metabolic activity and cell viability significantly decreased in HepG2 cells treated with *Ganoderma lucidum* and *Cantharellus cibarius*. By contrast, ethanol extracts at a concentration of 1000µg/mL revealed to reduce both metabolic activity and viability (Table 17). The only exception was *Agaricus bisporus* aqueous and ethanol extracts that did not decrease cell metabolic activity or cell viability at 1000 µg/mL. Ethanolic extracts from *Lentinula edodes, Macrolepiota procera* and *Boletus edulis* induced a significant decrease in cell metabolic activity (61%, 68% and 76%, respectively). *Boletus edulis, C. cibarius and G. lucidum* ethanol extracts significantly decreased cell viability (70%, 81% and 87%, respectively). The treatment with *Pleurotus ostreatus* ethanolic extract induced a significant decrease in cell metabolic activity of 36%, and a decrease in cell viability of 26%. On contrary, the aqueous extract from *P. ostreatus* had no cytotoxic effect on HepG2 cells, up to 1000µg/mL (Table 17).

Table 17. **Summary table of cell metabolic activity and cell viability values** (% to the mean of controls) of HepG2 cells treated with 1000µg/mL of aqueous or ethanol extracts from seven different mushroom species, for 24 hours.

	Cell metabolic activity		*Cell viability*	
	Extract 1000 µg/mL		Extract 1000 µg/mL	
Mushroom species	Aqueous	Ethanol	Aqueous	Ethanol
Agaricus bisporus	_	_	_	_
Boletus edulis	_	***↓76%	_	*↓70%
Cantharellus cibarius	↓27%	↓52%	*↓36%	***↓81%
Ganoderma lucidum	*↓12%	↓48%	↓20%	***↓87%
Lentinula edodes	_	*↓61%	_	*↓59%
Macrolepiota procera	_	***↓68%	_	***↓68%
Pleurotus ostretaus	_	*↓36%	_	↓26%

↓ (decrease); *P<.05, **P<.01, ***P<.0001

The ethanol extracts were likely to contain both polar and nonpolar metabolites, including terpenoids, sterols, fatty acids, polypeptides and amino acids[253]. Conversely, aqueous extracts were likely to contain water-soluble compounds including carbohydrates such as polysaccharides and small amounts of proteins and minerals[253, 254]. Therefore, considering the composition of both extracts and their cytotoxic profile, aqueous extracts were selected to test the potential protective effect on HepG2 cells treated with 125 µM FFA-BSA mixture for 24 hours, followed by 125 µM FFA-BSA mixture for another 24 hours. Co-treatment with the aqueous mushrooms extracts was applied together with the second incubation of FFA-BSA mixture. The treatment of HepG2 cells with the FFA-BSA mixture alone caused a decrease of 23% in cell metabolic activity in comparison to non-treated controls (Figure 28.A). Three concentrations of aqueous extracts from the different species were applied: 250, 500 and 1000 µg/mL. *Agaricus bisporus, L. edodes and M. procera* significantly increased cell metabolic activity back to non-treated control values for all applied concentrations. *Cantharellus cibarius, G. lucidum* and *P. ostreatus* significantly increased, dose-dependently, the cell metabolic activity (Figure 28.A). With regards to cell viability, cells treated only with the FFA-BSA mixture had a 12% decrease, in comparison to non-treated controls (Figure 28.B). Mushroom aqueous extracts did not induce significant changes in HepG2 cell viability, except for *A. bisporus* at 1000 µg/mL, *C. cibarius* at 500 and 1000 µg/mL, and *P. ostreatus*, which increased cellular viability, dose-dependently, at 500 and 1000 µg/mL (Figure 28.B). The ATP

cellular content of HepG2 cells treated with 125 µM FFA-BSA for 24 hours + 125 µM FFA-BSA/aqueous extracts for 24 hours was measured, and both *A. bisporus* and *P. ostreatus* aqueous extracts increased overall ATP content by 25%, in comparison to FFA-BSA treated HepG2 cells (Figure 28.C). With regards to lipid accumulation, cells treated with the FFA-BSA mixture had a fat increase of 63%, compared to non-treated controls (Figure 28.D). Mushroom aqueous extracts did not significantly revert this accumulation in the HepG2 cells, when compared to FFA-BSA treated controls (Figure 28.D). Nonetheless, *P. ostreatus* aqueous extract dose-dependently decreased lipid accumulation, even though the effect was not statistically significant (Figure 28.D).

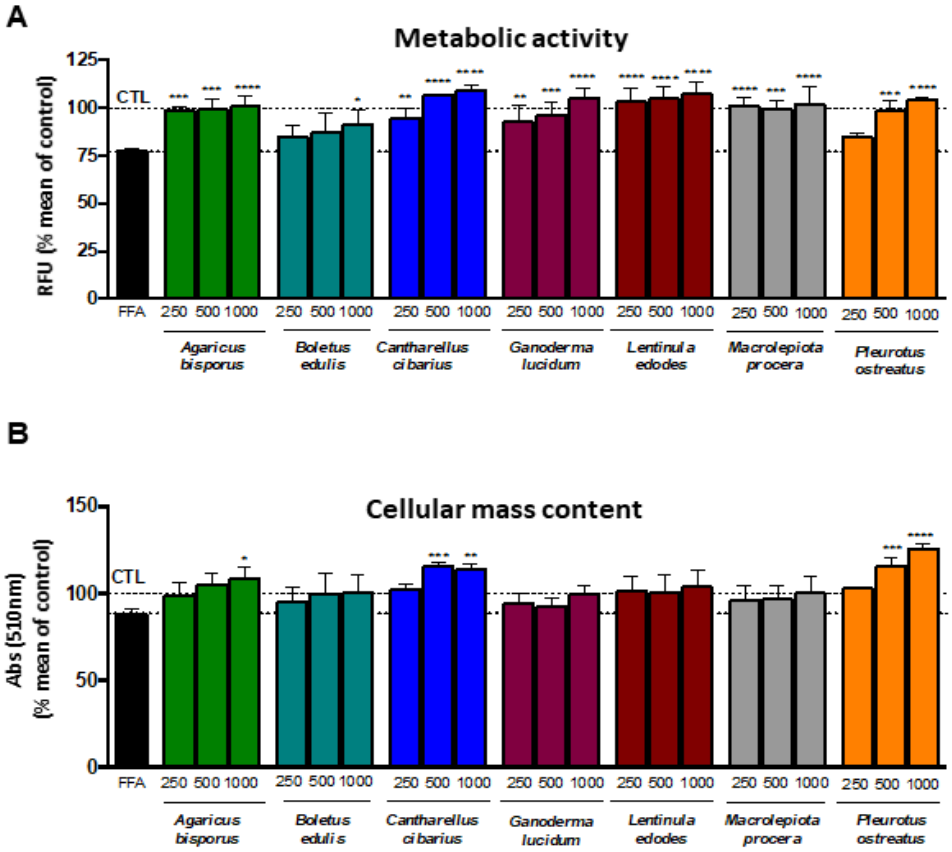

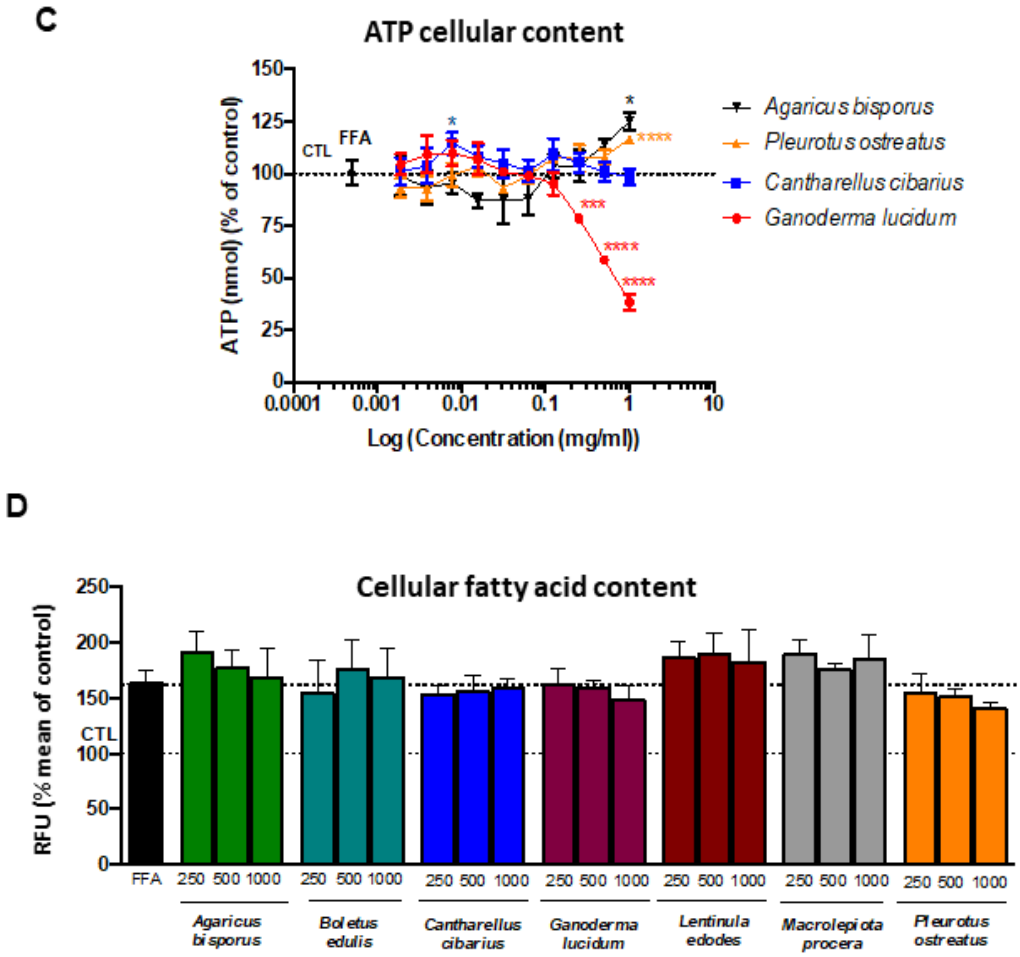

Figure 28. **Evaluation of cellular toxicity and protective effect of seven mushroom extracts against *in vitro* fattening of HepG2 cells.** Treatment of HepG2 cells was performed by incubation with 125µM of a FFA-BSA mixture for 24h + 125µM of FFA-BSA mixture and aqueous extracts from *Agaricus bisporus*, *Boletus edulis*, *Cantharellus cibarius*, *Ganoderma lucidum*, *Lentinula edodes*, *Macrolepiota procera* and *Pleurotus ostreatus* with the following concentrations: 250, 500 e 1000 µg/mL, for an additional 24 hours **(A, B, D)**. The total duration of the assays was 48 hours. Determination of the total ATP cellular content was done, dose-dependently (1.9 up to 1000 µg/mL), for the aqueous extracts from *A. bisporus, P. ostreatus, C. cibarius* and *G. lucidum*, for 24 hours **(C).** In comparison to the FFA-BSA control (FFA), the *P. ostreatus* aqueous extract was the least toxic to HepG2 cells, amongst the seven mushrooms on **(A)** cell metabolic activity and **(B)** cell viability. **(C)** Treatment of HepG2 cells with 125µM of FFA-BSA mixture for 24h + 125 µM of FFA-BSA mixture and mushroom aqueous extracts of *A. bisporus* and *P. ostreatus* for an additional 24 hours, increased ATP cellular content in comparison to the FFA-BSA control (FFA). **(D)** Lipid accumulation in HepG2 cells treated with 125µM of FFA-BSA mixture for 24h + 125µM of FFA-BSA mixture and mushroom aqueous extracts (250, 500 and 1000 µg/mL), for an additional 24 hours, were consistently improved with *A. bisporus* and *P. ostreatus*. Data are the mean ± SEM of N=3, n=3. Two-way analysis of variance with Sidak's multiple comparisons test. *P<.05; **P<.01; ***P<.001; ****P<.0001

Based on the evidence gathered in the *in vitro* model for hepatic lipotoxicity, *Pleurotus ostreatus* was the species selected for further studies.

3.2.2 *Pleurotus ostreatus* accumulates zinc dose-dependently in their mycelium.

3.2.2.1 Pleurotus ostreatus growth in solid substrate

Several fungi have the capacity to accumulate metals in their mycelium and carpophores (i.e. fruiting bodies), namely Cu and Zn[180, 255-257]. The metal binding capacity of *Pleurotus ostreatus*, and other members of the *Pleurotus* genus is well documented in the literature[192, 256, 258]. Thus, a nutritional strategy using *P. ostreatus* was develop to combine the beneficial effects towards hepatic steatosis, and promotion of Cu excretion in the intestine. To achieve the second therapeutic effect, *P. ostreatus* was cultivated in a Zn-enriched substrate (Figure 29.A), and both carpophores and mycelia harvested and dried. The goal was to develop of a more tolerable Zn formulation ("bio-zinc") to help in the treatment of WD patients.

Metal analysis revealed no significant changes in Cu content in mycelia (Figure 29.B), and a significant, and dose-dependent increase in Zn, in comparison to the control, non-enriched mycelia (Figure 29.C). In the carpophores, no significant differences were observed for both Cu (Figure 29.D) and Zn (Figure 29.E) content. The content of the heavy metal cadmium was significantly, and dose-dependently, decreased in the carpophores of zinc-enriched *P. ostreatus* (Figure 29.F).

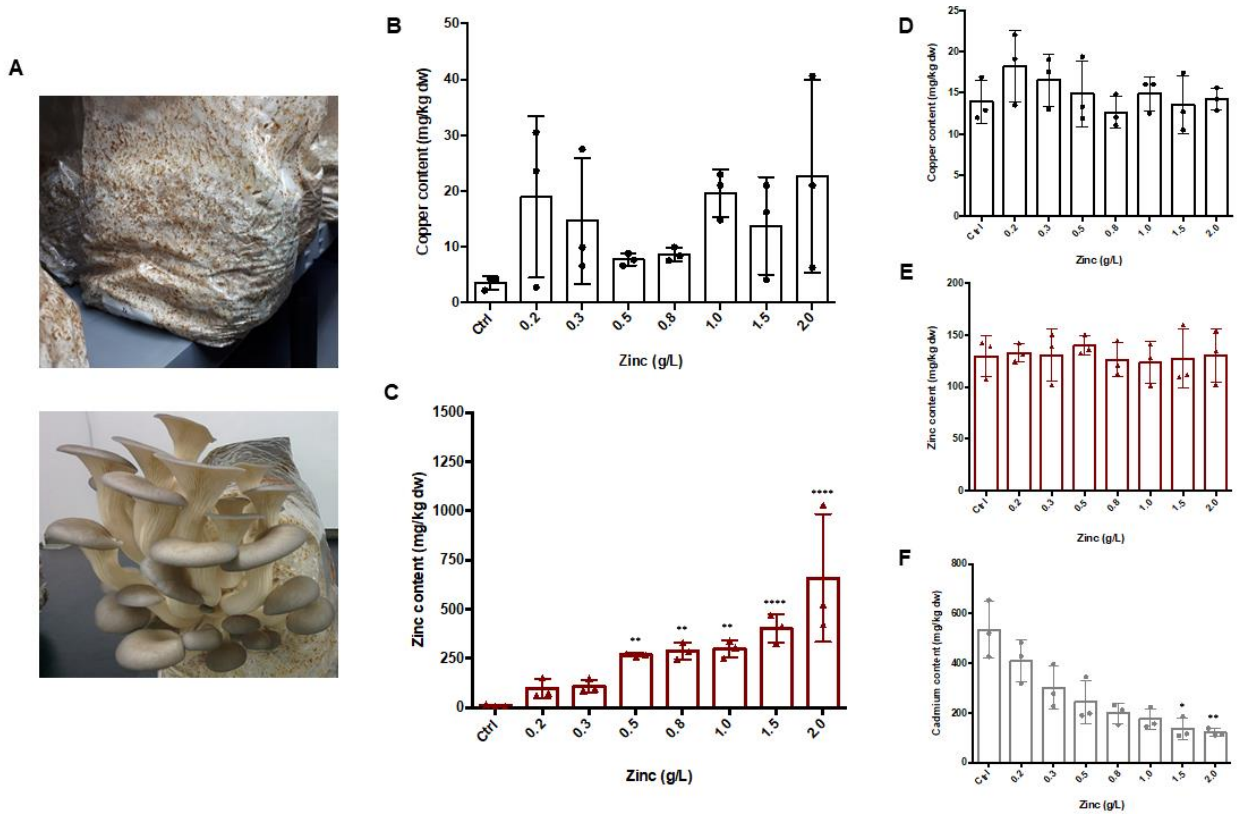

Figure 29. **Pilot study: zinc content increased, dose-dependently, in the mycelium of *Pleurotus ostreatus*. (A)** Mycelia and carpophores of *P. ostreatus* grown on Zn-enriched solid substrate. **(B)** Copper and **(C)** Zn content [mg/Kg dry weight, dw] in the mycelia, in contrast with **(D)** Cu and **(E)** Zn content [mg/Kg dry weight, dw] in the carpophores of *P. ostreatus*. The mycelium of *P. ostreatus* (M2191; provided by Mycelia BVBA, Belgium) was cultivated on a Zn-enriched substrate (68% water and 32% substrate composed by 80% pine pellets supplemented with 20% biologic lucerne pellets and increasing doses of Zinc sulphate heptahydrate, $ZnSO_4.7H_2O$). **(F)** Cadmium content [mg/Kg dry weight, dw] decreased, dose dependently in the carpophores of *P. ostreatus* with increasing doses of Zn in the substrate. Data are the mean ± SD of N=3 (B-F). Two-way analysis of variance with Dunnett´s multiple comparison test. *P<.05; **P<.01; ****P<.0001

For the next studies, focus was put on the mycelium, following the same growth conditions, and three different concentrations of $ZnSO_4.7H_2O$: 0.5, 1.5 and 2g/L. This time, mycelium from all three conditions, plus control, was harvested and cleared from substrate debris, before freeze-drying (Figure 30.A). The Cu content in mycelia was around 2-fold higher in comparison to the initial study (Figure 30.B), while Zn content (Figure 30.C), significantly, and dose-dependently increased in the mycelia. A protein extract from the *P. ostreatus* control and Zn-enriched mycelia was prepared to determine the Zn content in whole extract, and after dialysis against membranes with different cut-offs (0.1-0.5, 20 and 100KDa). The protein content of *P. ostreatus* control and Zn-enriched mycelia protein extract (Figure 30.D) was not significantly different. However, the Zn concentration was 2-fold higher in the protein extract

of the Zn-enriched mycelium, shown here as the Zn concentration before dialysis (Figure 30.E). After dialysis, protein content was significantly reduced in both control and Zn-enriched mycelia (Figure 30.E), while Zn content was significantly increased in the dialysed of the Zn-enriched mycelia protein extract with a cut-off of 0.5-1KDa. However, it was decreased upon dialysis with a cut-off of 20KDa, and more prominently with a cut-off of 100KDa (Figure 30.F). The Zn-to-protein ration after dialysis was significantly increased with the cut-offs of 0.5-1 and 20KDa (Figure 30.G), implying that Zn is probably bound to low-molecular weight proteins.

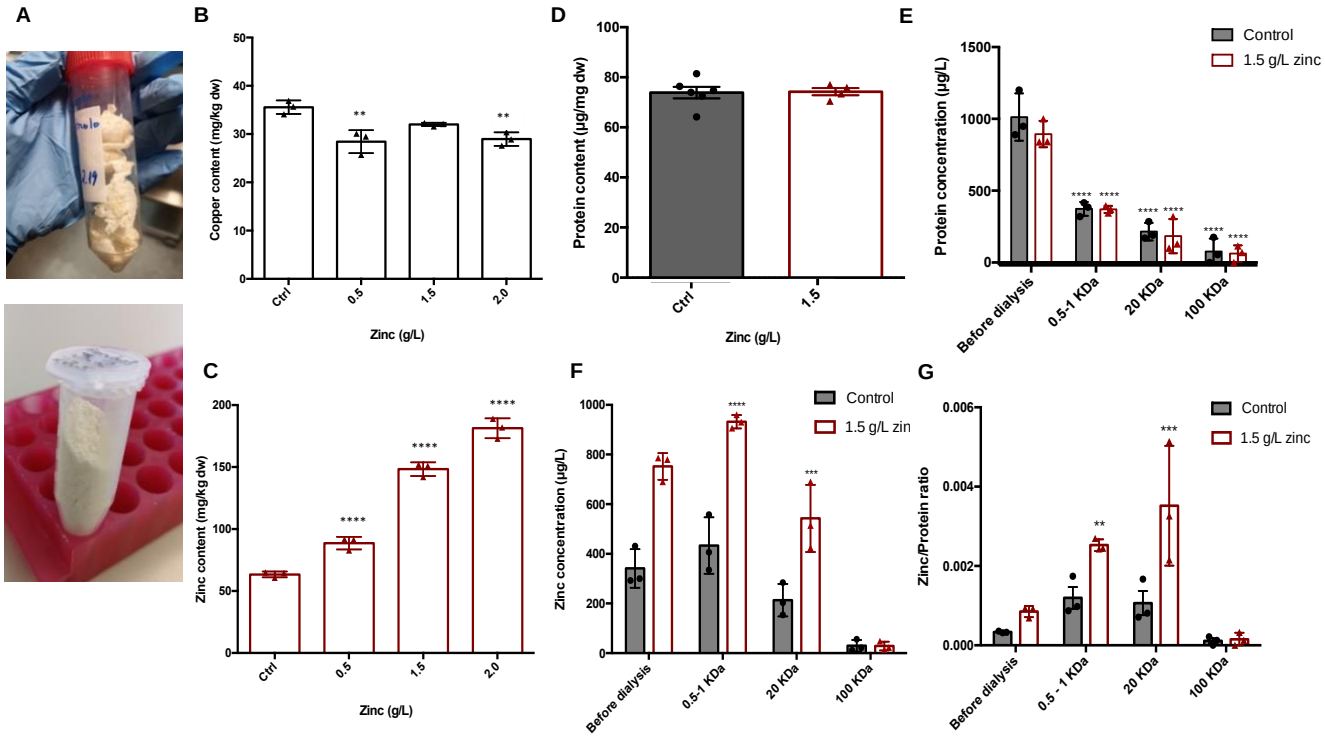

Figure 30. **Mycelium focused study: zinc content increased, dose-dependently, in the mycelium of *Pleurotus ostreatus*. (A)** Mycelium of *P. ostreatus* grown on Zn-enriched solid substrate, before and after lyophilization plus grinding. **(B)** Copper and **(C)** Zn content [mg/Kg dry weight, dw] in the mycelium of *P. ostreatus*. **(D)** Protein content in a protein extract from control and Zn-enriched *P. ostreatus* dried mycelia, grown in solid substrate, obtained through mechanic cell disruption in the tissue homogeneiser Precellys24 (Bertin Instruments). **(E)** Protein content, **(F)** Zn content and **(G)** Zn-to-protein ratio of the control and Zn-enriched *P. ostreatus* mycelia protein extract, before and after dialysis with different molecular weight cut-offs (0.5-1, 20 and 100KDa), 1:500 against dialysis buffer. Data are the mean ± SD of N= 3 (B,C,E-G) and N=4-5 (D). Two-way analysis of variance with Dunnett's or Sidak's multiple comparisons test after column analysis (identify outliers). **P<.01; ***P<.001; ****P<.0001

3.2.2.2 Pleurotus ostreatus growth in liquid substrate

The results from the *P. ostreatus* mycelium growth in solid substrate were important to establish the conditions for the mycelium growth in liquid culture (Figure 31.). The growth of *P. ostreatus* mycelium in synthetic semi-defined liquid medium was developed and optimized for non-toxic $ZnSO_4.7H_2O$ concentrations. The composition of the medium was adapted from previous studies with the same mushroom species[192, 259, 260]. The mycelium was grown for 7-9 days and, after recovering and freeze-drying (Figure 31.A), the metal content was determined (Figure 31.B). A study by Poursaied *et al.*[192] reported an accumulation of 840 mg/kg dry weight of Zn in the mycelium of *Pleurotus florida*, after 15 days of culture, with a Zn concentration in the medium of 100 mg/L. In the present study, the Zn accumulation (Figure 31.B) was 470 mg/kg dry weight with a Zn medium concentration of 13 mg/L. Moreover, in comparison to the mycelium growth in the solid substrate (see Figure 30.C), the Zn uptake was 2.5-fold higher (Figure 31.B). A protein extract was prepared from the mycelium produced in liquid culture and, as observed with the mycelium from solid culture (Figure 30.D), there were no differences in protein content between control and Zn-enriched mycelia (Figure 31.C). Afterwards, the protein extract from both control and Zn-enriched mycelia were dialysed, similar as for the mycelia grown in solid culture (Figure 30.E, F). No differences were observed in Zn concentration before and after dialysis (Figure 31.D), which was reflected in the Zn-to-protein ratio that increased around 6-fold, independently of the cut-off (Figure 31.E). In both situations, i.e. mycelium from either solid or liquid culture, Zn was bound to proteins with a molecular size lower than 100KDa. However, in the liquid culture setting, the Zn content in the protein extract of the Zn-enriched mycelium was around 3.5-fold higher in comparison to the mycelium grown in solid culture (Figure 30.F).

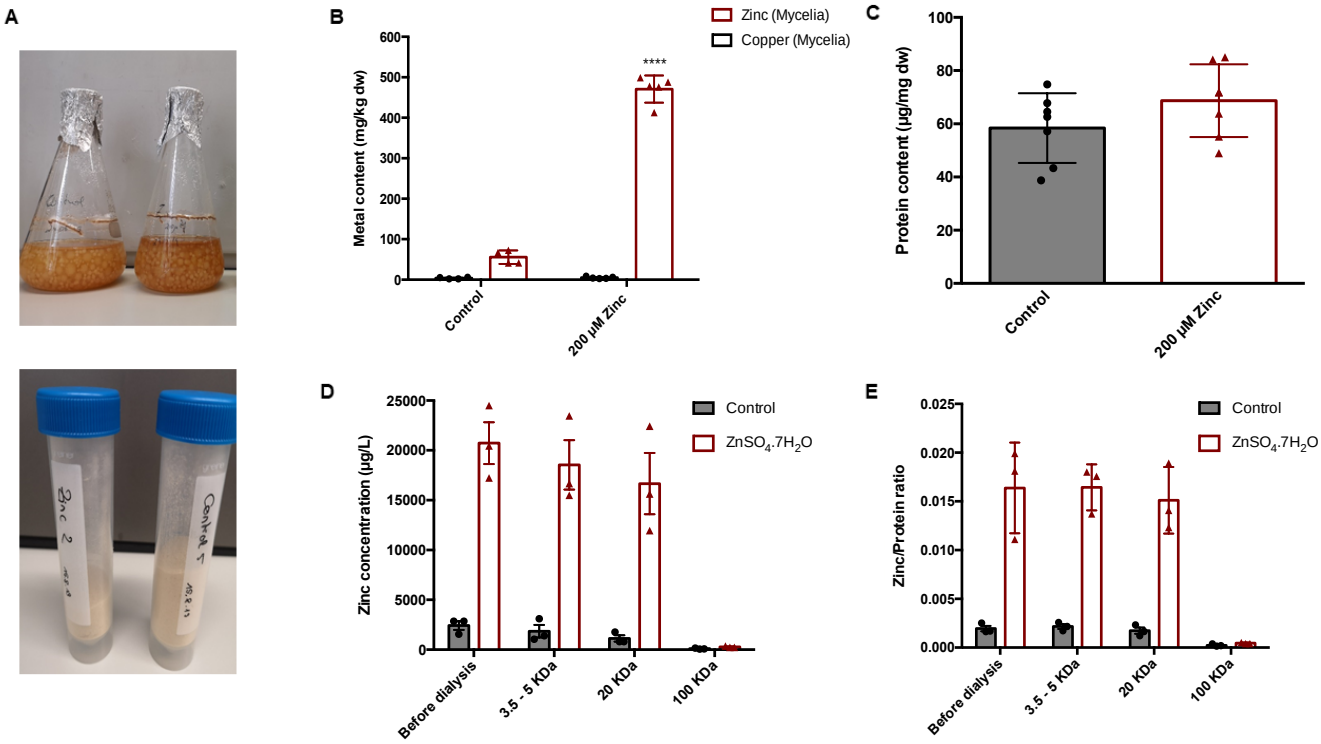

Figure 31. **Zinc content increased in the mycelium of *Pleurotus ostreatus* grown on Zn-enriched liquid substrate. (A)** Mycelium of *P. ostreatus* grown on Zn-enriched liquid substrate, before and after recovering with lyophilization and grinding. **(B)** Copper and Zn content [mg/Kg dry weight, dw] in the mycelium of *P. ostreatus* grown in liquid culture, without or with 200µM Zn supplementation. **(C)** Protein content in a protein extract from control and Zn-enriched *P. ostreatus* dried mycelia, grown in liquid substrate, obtained through mechanic cell disruption in the tissue homogeneiser Minilys (Bertin Instruments). **(D)** Zinc content in the control and Zn-enriched *P. ostreatus* mycelia protein extract, before and after dialysis with different molecular weight cut-offs (3.5-5, 20 and 100 KDa), 1:500 against dialysis buffer. **(E)** Zinc-to-protein ratio of the control and Zn-enriched *P. ostreatus* mycelia protein extract, before and after dialysis with different molecular weight cut-offs (3.5-5, 20 and 100 KDa), 1:500 against dialysis buffer. Data are the mean ± SD of N= 4-5 (B), N=5-7 (C) and N=3 (D, E). Two-way analysis of variance with Dunnett's multiple comparisons test after column analysis (identify outliers).***P<.001; ****P<.0001

3.2.3 The zinc-enriched mycelium protein extract ameliorates *in vitro* copper toxicity.

The Caco-2 cells *in vitro* model was used to study the potential capacity of the *P. ostreatus* Zn-enriched mycelium protein extract (ZM(PO)) to "detoxify" Cu and to protect from Cu-induced barrier damage. Previous studies in this model had reported Cu toxicity and positive therapeutic effects of Zn towards barrier integrity[261-263]. In patients with Wilson disease (WD), Zn salts induce the expression of metallothioneins (MT) in the enterocytes. These cysteine-rich proteins are intracellular metal chelators with higher affinity for Cu than Zn, therefore promoting a systemic increased Cu excretion via enterocyte desquamation[46]. A similar effect was the rationale to take place upon ZM(PO) treatment. First, preliminary studies with non-differentiated Caco-2 cells allowed the evaluation of the cytotoxicity of an inorganic Zn salt. A significant decrease in lysosomal/other vesicular compartments acidification (Figure 32.A), ATP cellular content (Figure 32.B) and cellular viability (Figure 32.C) was observed at 500µM Zinc sulphate heptahydrate ($ZnSO_4.7H_2O$). Incubation with 18.5µM ZM(PO) (i.e. 18.5µM Zn) caused no significant decrease of lysosomal/other vesicular compartments acidification (Figure 32.D), ATP cellular content (Figure 32.E) or cellular viability (Figure 32.F); while incubation with 37µM ZM(PO) (i.e. 37µM Zn) induced a decrease in lysosomal/other vesicular compartments acidification in comparison to 18.5µM ZM(PO). Therefore, we used 18.5µM ZM(PO) in further experiments. The *P. ostreatus* control mycelia (M-Ctrl(PO)) had no cytotoxic effect on Caco-2 cells, with corresponding volumes of protein extract applied to the cells as the ZM(PO): 37µM ZM(PO) - M-Ctrl(PO), and 18.5µM ZM(PO) - M-Ctrl(PO) 1:2 (Figure 32.D-F).

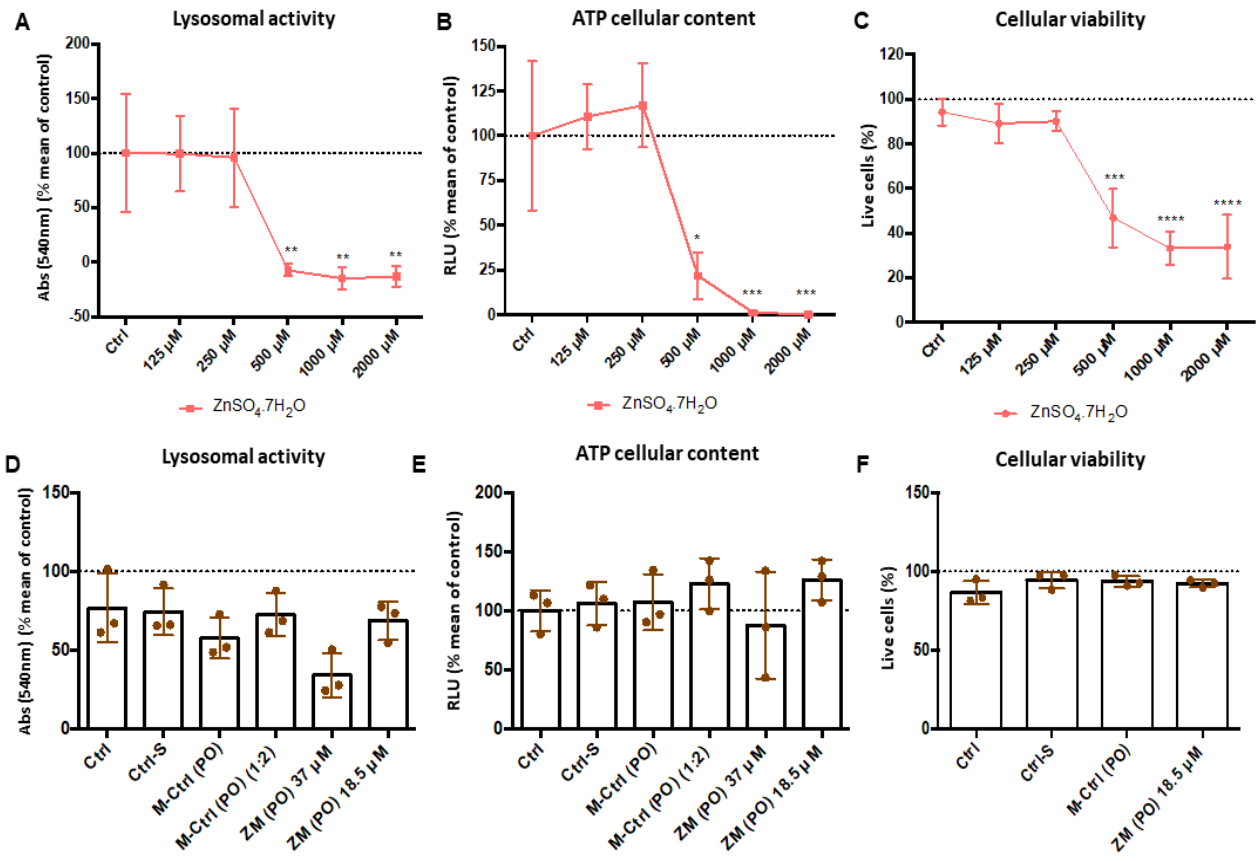

Figure 32. **Caco-2 WT cells were sensitive to zinc at high concentrations.** Increasing $ZnSO_4.7H_2O$ concentrations significantly decreased **(A)** Lysosomal/other vesicular compartments acidification, **(B)** ATP cellular content, and **(C)** Cellular viability of Caco-2 WT at 500-2000µM. Treatment of Caco-2 WT cells with control (M-Ctrl(PO)) or Zn-enriched *P. ostreatus* mycelia protein extract (ZM(PO)), did not significantly decreased **(D)** lysosomal/other vesicular compartments acidification, **(E)** ATP cellular content and **(F)** Cellular viability, at a concentration of 18.5 and 37µM Zn (equal respective volume for control condition). Data are the mean ± SD of N=3, n=3. Two-way analysis of variance with Sidak's multiple comparisons test (A-F), after column analysis (identify outliers). *P<.05; **P<.01; ***P<.001; ****P<.0001; Ctrl-S: solvent control

To investigate the capacity of ZM(PO) to decrease cellular Cu content, a 48 hours' incubation of non-differentiated Caco-2 cells with 200µM $CuCl_2$, 200µM $CuCl_2$ + M-Ctrl(PO) 1:2, or 200µM $CuCl_2$ + 18.5µM ZM(PO) was performed. Co-treatment with 18.5µM ZM(PO) improved cellular viability in comparison to 200µM $CuCl_2$ (Figure 33.A), and significantly decreased cellular Cu content (Figure 33.B). Afterwards, differentiated Caco-2 cells were treated with 20µM ZM(PO) (the concentration was adjusted from 18.5 to 20µM, i.e. 20µM Zn, for the sake of simplification). No significant changes were observed in barrier structure upon 21 days of differentiation plus 48 hours' treatment with 20µM ZM(PO) (Figure 33.C). Cellular Zn content after treatment with 20µM ZM(PO) was slightly increased, and Cu content reduced, but not significantly (Figure 33.D).The co-incubation with 37µM ZM(PO) resulted in an increase of Cu

in the cells (Figure 33.D), as well as an increase in the expression of MT1/2 (Figure 33.E). Treatment with 20 or 37µM ZM (PO) also increased MT1/2 expression, in comparison to non-treated control and Cu-treated cells (Figure 33.E).

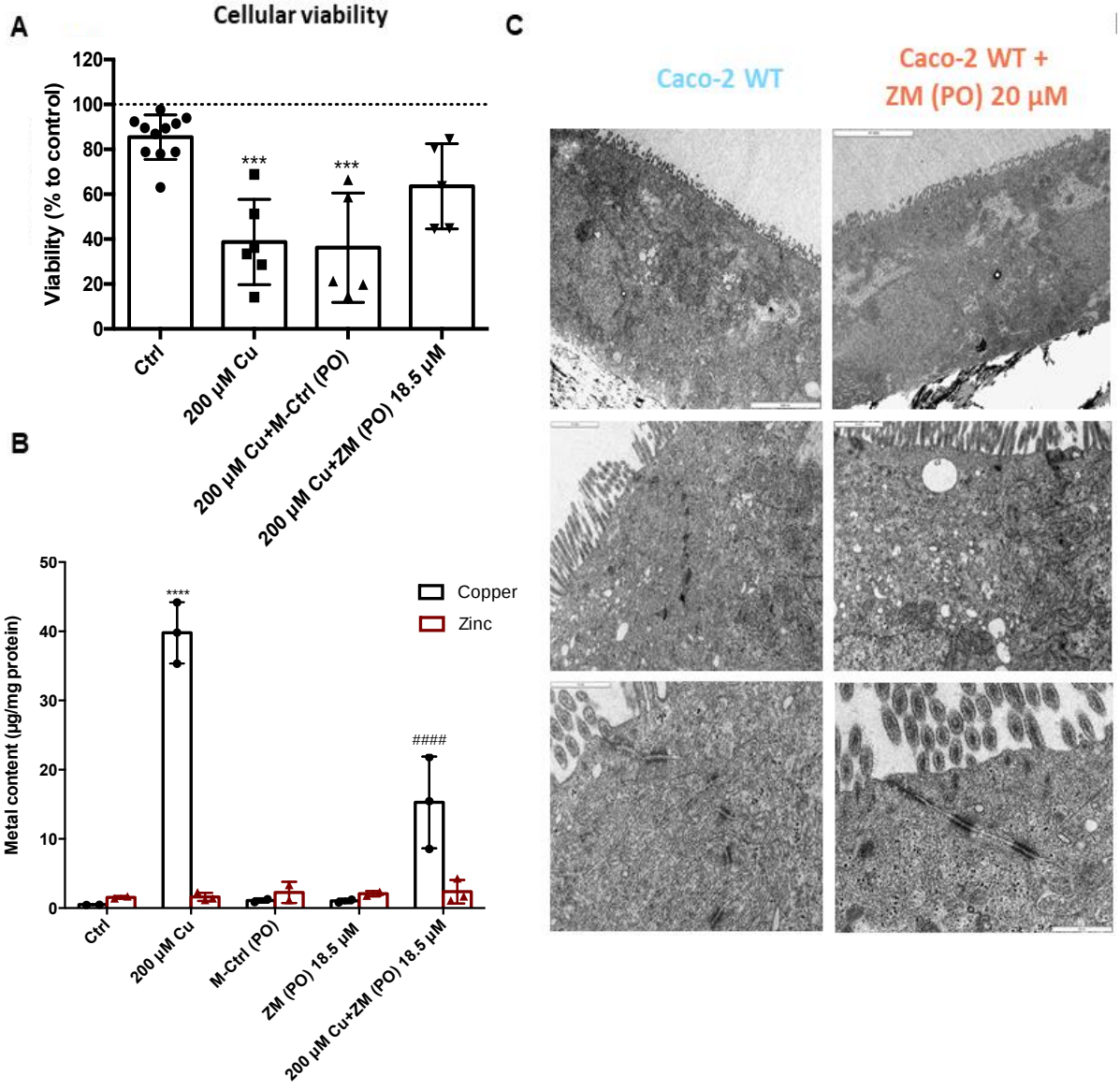

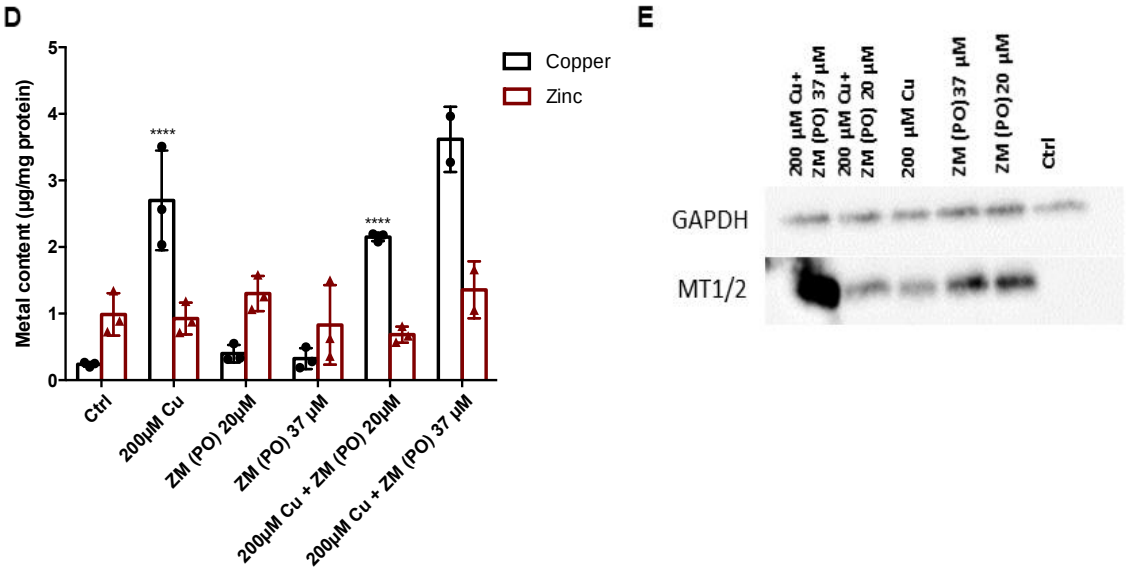

Figure 33. ***Pleurotus ostreatus*** **zinc-enriched mycelium protein extract protected Caco-2 WT against copper toxicity.** ZM(PO) 18.5 µM/Zn improved **(A)** cell viability, as percentage of live cells, and decreased **(B)** cellular copper content in Caco-2 WT cells upon 48 hours co-treatment with 200µM $CuCl_2$. **(C)** Caco-2 WT cells, differentiated for 21 days in a Transwell® system, were treated for 48 hours with 200µM $CuCl_2$, ZM(PO) 37 or 20µM/Zn, and correspondent double treatments. **(D)** A tendency for cellular Cu content decrease, and increase **(E)** metallothioneins (MT1/2) expression was observed with ZM(PO) 37 and 20 µM/Zn and ZM(PO) 37 µM/Zn + 200µM $CuCl_2$ treatment. Data are the mean ± SD of N=11-5 (A) and N=2-3 (B, D), N=1 (E). Two-way analysis of variance with Sidak's multiple comparisons test (A, D), or Dunnett's multiple comparisons (B) test after column analysis (identify outliers). ***, ###P<.001; ****P<.0001. #Comparison towards 200µM $CuCl_2$ treatment condition.

Prolonged treatment with 100µM $CuCl_2$ decreased the TEER of differentiated Caco-2 cells overtime. Co-incubation with 20µM ZM(PO) had a positive impact on the cellular barrier integrity, since TEER increased in comparison to Cu treated cells (Figure 34.A). No significant differences were observed in Ccl, in comparison to control (Figure 34.B). In a single proof of principal experiment, a decrease in cellular Cu content (Figure 34.C) was observed with the co-treatment of 100µM $CuCl_2$ and 20µM ZM(PO). Furthermore, less Cu was present in the basolateral compartment upon treatment with ZM(PO) (Figure 34.E), with an increase in Zn content on the apical compartment of the Transwell® system (Figure 34.D). Immuno-fluorescent monolayer staining against claudin-5 (Figure 34.F), an integral membrane protein component of Tight junctions (TJ) strand, is decreased in Caco-2 cells treated with Cu, with expression and structural organization of the TJ recovered upon co-treatment with ZM(PO).

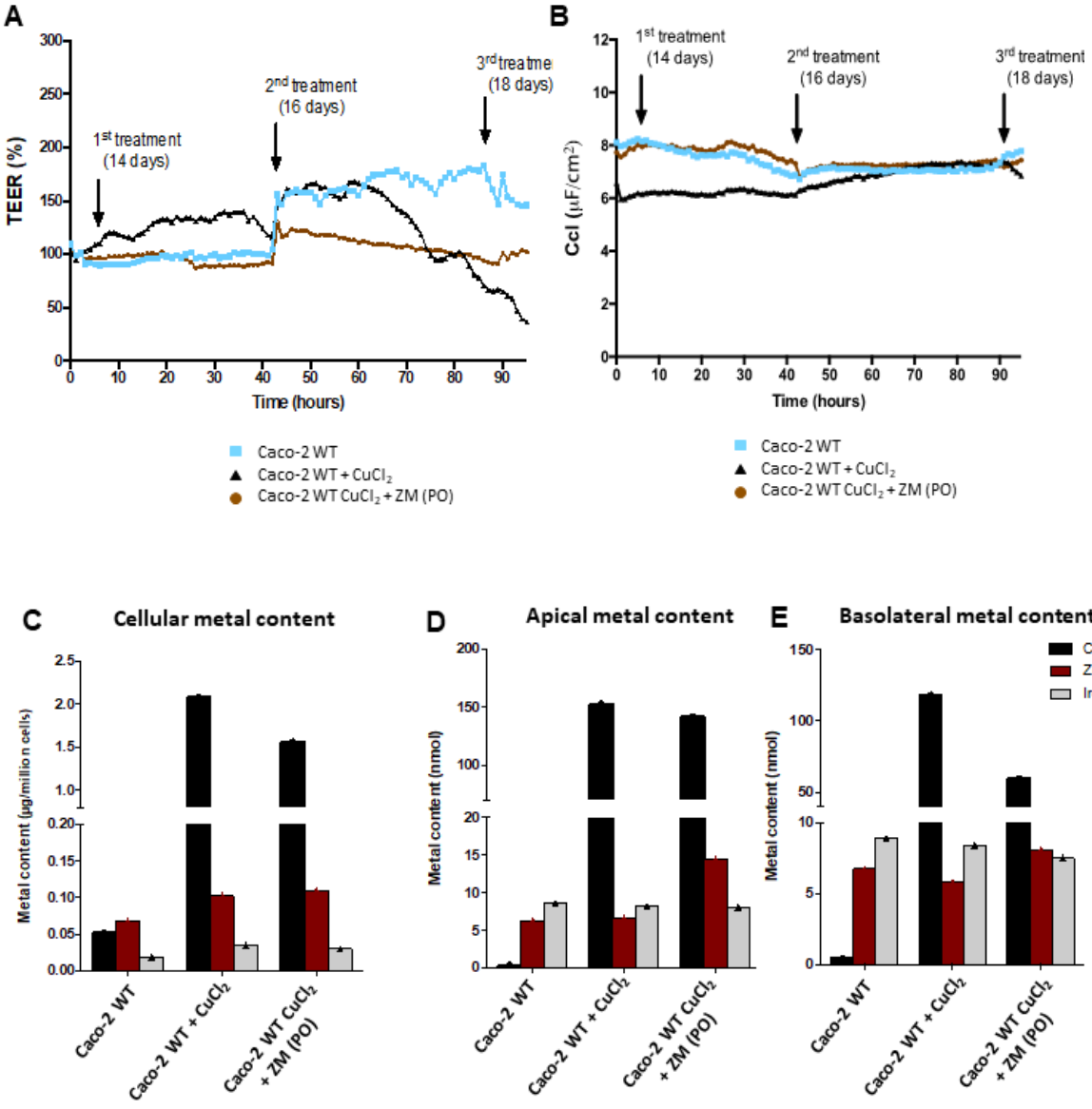
A
TEER (%)
1st treatment (14 days)
2nd treatment (16 days)
3rd treatme (18 days)
Time (hours)
Caco-2 WT
Caco-2 WT + CuCl2
Caco-2 WT CuCl2 + ZM (PO)
B
Ccl (µF/cm2)
1st treatment (14 days)
2nd treatment (16 days)
3rd treatment (18 days)
Time (hours)
Caco-2 WT
Caco-2 WT + CuCl2
Caco-2 WT CuCl2 + ZM (PO)
C
Cellular metal content
Metal content (µg/million cells)
Caco-2 WT
Caco-2 WT + CuCl2
Caco-2 WT CuCl2 + ZM (PO)
D
Apical metal content
Metal content (nmol)
Caco-2 WT
Caco-2 WT + CuCl2
Caco-2 WT CuCl2 + ZM (PO)
E
Basolateral metal content
Copper
Zinc
Iron
Metal content (nmol)
Caco-2 WT
Caco-2 WT + CuCl2
Caco-2 WT CuCl2 + ZM (PO)

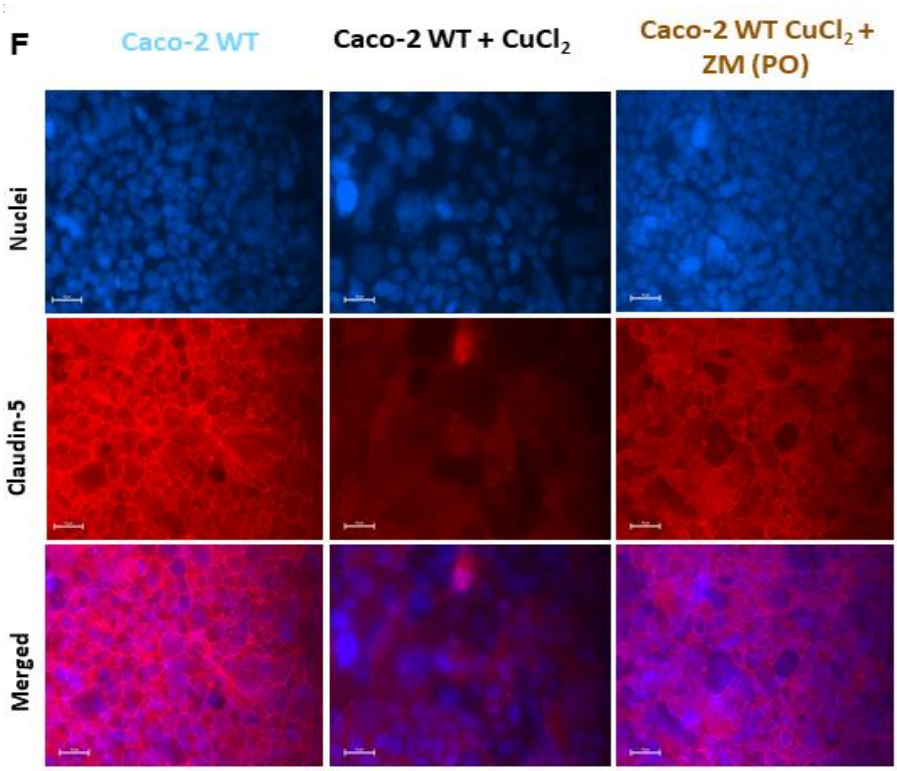

Figure 34. **Disruption of tight junctions in differentiated Caco-2 WT cells was ameliorated by *Pleurotus ostreatus* zinc-enriched mycelium protein extract. (A)** Treatment with 100μM $CuCl_2$ lead to a time dependent decrease of the TEER, which was increased by the co-treatment with ZM(PO) 20μM/Zn. **(B)** Capacitance values (Ccl) were not significantly changed amongst treatments. **(C)** Cellular Cu content in Caco-2 WT cells, differentiated for 21 days, increased with $CuCl_2$ treatment, with a decrease upon co-treatment with ZM(PO) 20μM/Zn. **(D)** The Zn content in the apical (luminal side) medium was increased with ZM(PO) 20μM/Zn, while Cu content was decreased. **(E)** In the basolateral (interstitial fluid side) medium, Cu content decreased with the co-treatment with ZM(PO) 20μM/Zn, in comparison to 100μM $CuCl_2$ treatment. **(F)** Immunocytochemistry staining against the TJ protein claudin-5 showed a continuous staining of the cell margins in control Caco-2 WT cells, that was disrupted with $CuCl_2$, but recovered with the co-treatment with ZM(PO) 20μM/Zn (scale bars: 10 μm).

In order to evaluate the effects of the Zn-enriched mycelium protein extract in the Caco-2 ATP7B KO cells, 100µM $CuCl_2$ treatment, as well as treatment with 20µM ZM(PO), and respective co-treatment, started at the 4th day until the 21st day of differentiation. An early treatment time-point was applied since no significant toxicity of Cu was observed in Caco-2 KO cells treated from the 7th day of differentiation (Figure 26.A, B). With this setting, a decrease in barrier tightness was observed with 100µM $CuCl_2$, as well as an improvement of the TEER in the co-treatment (Figure 35.A). However, all treatments caused a decrease in the TEER, as percentage related to the starting point, in comparison to control. No significant effects were observed in the Ccl values (Figure 35.B). Immuno-fluorescent monolayer staining against occludin and TJP1/ZO-1 (Figure 35.C) showed a decrease in the fluorescence intensity for all treatments, in comparison to control (untreated Caco-2 KO cells). Nonetheless, co-treatment of the cells with 100µM $CuCl_2$ + 20µM ZM(PO) improved occluding-related fluorescence in comparison to Cu treatment alone.

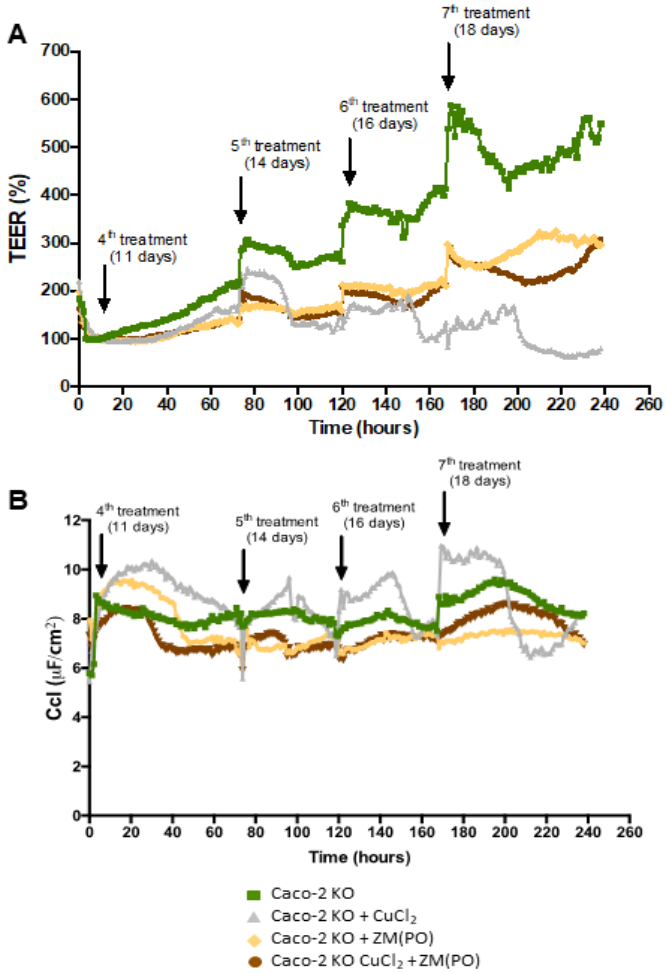

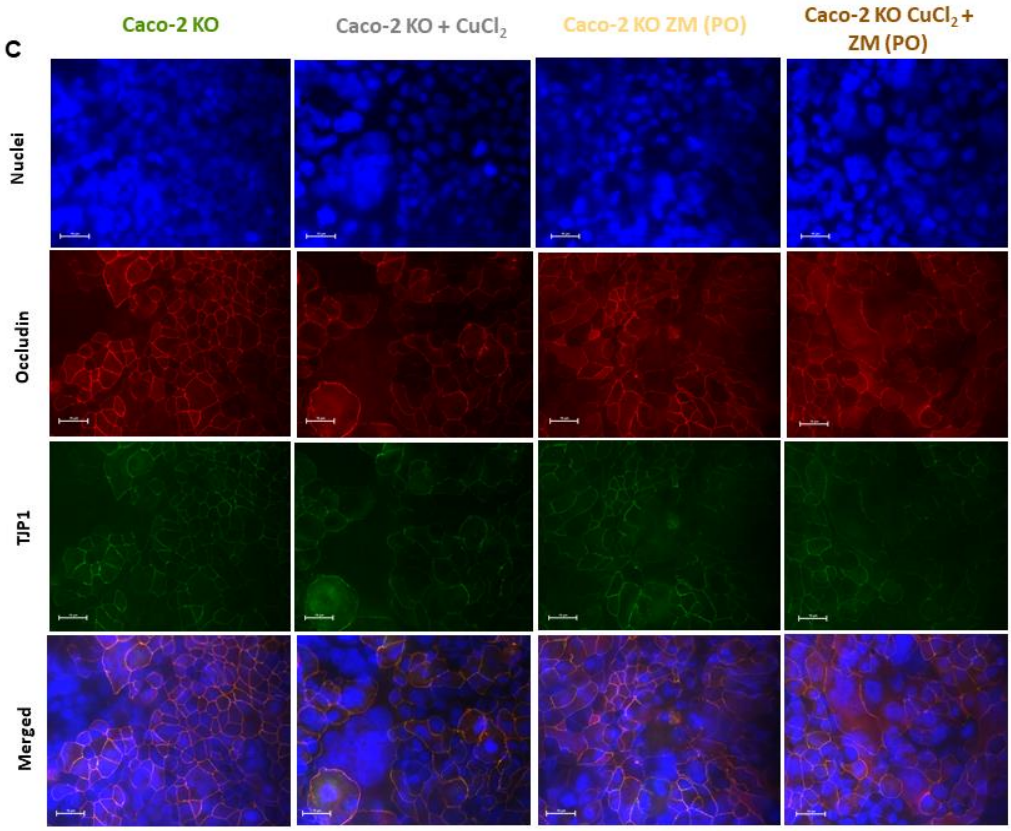

Figure 35. **Caco-2 ATP7B KO cells were sensitive to copper treatment, with amelioration of the TJ disruption upon zinc-enriched mycelium protein extract co-treatment. (A)** Treatment with 100μM $CuCl_2$ lead to a time dependent decrease of the TEER in KO cells, differentiated for 21 days and treated from the 4th day of differentiation. Co-treatment with ZM(PO) 20 μM/Zn improved TEER values. **(B)** Capacitance values (Ccl) were not significantly changed amongst treatments. **(C)** Immunocytochemistry staining against the TJ proteins occludin and TJP1/ZO-1, showed an increased intensity of the staining upon 100μM $CuCl_2$ + ZM(PO) 20 μM/Zn treatment, in comparison to 100μM $CuCl_2$ (scale bars: 10 μm).

Thus, the Zn-enriched protein extract obtained from the *P. ostreatus* mycelium is protective against Cu toxicity in differentiated Caco-2 cells. This protective effect is more pronounced in the WT cells, in comparison to KO.

3.3 Feeding of *Pleurotus ostreatus* zinc-enriched mycelium promoted zinc absorption, and changed duodenal metal content in LPP rats

Zinc salts are a relevant therapeutic strategy for Wilson disease (WD) patients that is frequently used as a maintenance treatment to reduce Cu absorption in the GIT[112]. Intake of Zn promotes a lower systemic Cu through upregulation of high affinity Cu molecules such as metallothioneins (MT) [111, 113] in the enterocytes and a higher excretion at the intestinal site via enterocyte desquamation[35, 100]. Despite being more often applied as a second therapy option, with the side effects caused by Cu chelators, Zn is growing as a first-line alternative to normalize "free" Cu levels[111, 264, 265]. However, prolonged treatment is required to increase MT levels in the intestine, which can lead to GIT irritability and inflammation. Other setbacks of the treatment are the necessity of changing Zn formulation from time to time, and the obligation of avoiding food consumption together with ingestion of the Zn salts[103, 110]. Treatment of LEC rats (a previously widely used WD animal model[266]) with Zn salts mimics the effects observed in WD patients (Table S4), with increased MT expression, decreased Cu levels and increased Zn levels in liver and intestine. However, Zn levels tend to decrease with long treatment regiments (Table S4). The Zn-enriched mycelium is an alternative to the Zn salts since it is design to be taken up together with the food, an provide an extracellular source of Zn bound MT which may lead to a direct Cu excretion via Cu-mushroom-MT. This way providing further Zn in a less irritating form. To evaluate the effect of the Zn-enriched mycelium from *P. ostreatus* on Cu and Zn levels in different tissues, as well as excretion vs. absorption, three LPP *Atp7b*$^{-/-}$ female rats at the age of 84 days were fed a diet supplemented with the powdered Zn-enriched mycelium (see 2.10.1). Having this *in vivo* setting is crucial to the proof of concept because a full functional digestive system is needed to better understand the effects of the enriched diet.

The health status of the animals was assessed at different time points (see Figure 6). As observed by the body weight (BW), as well as ALT, AST and Bilirubin values (Table 18), at the end of the study, all three animals were in a different health condition. Animal number 1 (LPP 1383) reached disease state, animal number 2 (LPP 1384) presented with a stage of diseased onset, while animal number 3 (LPP 1385) still had AST levels below 200 U/L (Table 18).

Table 18. **Summary table of LPP *Atp7b*$^{-/-}$ health status from the 1st day of the study, until the day of the 2nd metabolic cage.**

Animal	*Time (days)*	*Study time point*	*Age (days)*	*BW (g)*	*ALT (U/L)*	*AST (U/L)*	*Bili (mg/dl)*	*Health state*
LPP *Atp7b* $^{-/-}$ 1 (1383)	1	F1	84	171	38.4	86.6	<0.5	Healthy
	6	MC1	90	186	55.6	86.2	<0.5	Healthy
	12	F2	97	191	120	142	<0.5	Healthy (ALT>100)
	20	MC2	105	173	591	-	12	Diseased (Bili > 0.5)
LPP *Atp7b* $^{-/-}$ 2 (1384)	1	F1	84	170	33.3	88.8	<0.5	Healthy
	6	MC1	90	190	35.3	81.4	<0.5	Healthy
	12	F2	97	196	65.8	111	<0.5	Healthy
	20	MC2	105	189	297	210	<0.5	Diseased onset (AST>200)
LPP *Atp7b* $^{-/-}$ 3 (1385)	1	F1	84	186	38.4	86.6	<0.5	Healthy
	6	MC1	90	203	40.9	105	<0.5	Healthy
	12	F2	97	203	40.5	134	<0.5	Healthy
	20	MC2	105	203	142	142	<0.5	Healthy (ALT>100)

F1 – start of the first feeding cycle; MC1 – metabolic cage after F1; F2 - start of the second feeding cycle; MC2 – metabolic cage after F2; ALT: alanine aminotransferase; AST: aspartate aminotransferase; Bili: Bilirubin

Figure 36 depicts the development of the three animals at the abovementioned time points of the study. A clear decrease in BW was observed (Figure 36.A) for animal 1 in between the start of the 2nd feeding cycle (F2) and the 2nd metabolic cage (MC2). For all three animals, an increase in ALT (Figure 36.B) and AST (Figure 36.C) levels, between F2 and MC2, clearly showed onset of liver disease in this time frame.

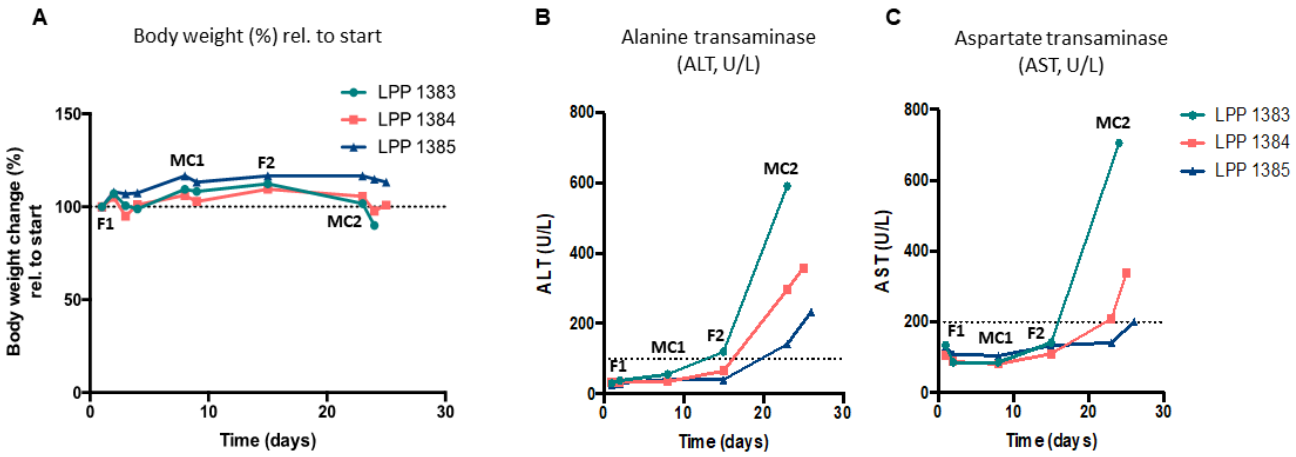

Figure 36. **Wilson disease rats, LPP *Atp7b*$^{-/-}$, had increase liver damage overtime.** Animals fed a Zn-enriched mycelium diet experienced a change in **(A)** body weight, relative to the start of the study, that was more prominent for animal number 1 during F2. This decline in body weight was correlated with an increase of **(B)** alanine transaminase (ALT, U/L) and **(C)** aspartate transaminase (AST, U/L) values, that were also observed for animals number 2 and 3, after the start of F2. F1: 1st feeding cycle; F2: 2nd feeding cycle; MC1: 1st metabolic cage; MC2: 2nd metabolic cage.

Food and water intake were measured for a period of 24 hours, from the moment the animals were placed in the MC. Results for MC1 showed that food intake was comparable amongst animals, with a higher water intake for animal number 2 (Figure 37.A). Copper (Figure 37.B) and Zn (Figure 37.C) excretion via the faeces was also comparable amongst animals, with a tendency for a higher excretion/intake ratio for Zn (Figure 37.D). Compared to historical data of LPP *Atp7b*$^{-/-}$ (N=4) aged-matched controls fed a normal chow diet, also kept for 24 hours in a MC, a significant increase in Zn excretion/intake ratio was observed for the LPP *Atp7b*$^{-/-}$ fed the Zn-enriched mycelium diet (Figure 37.E).

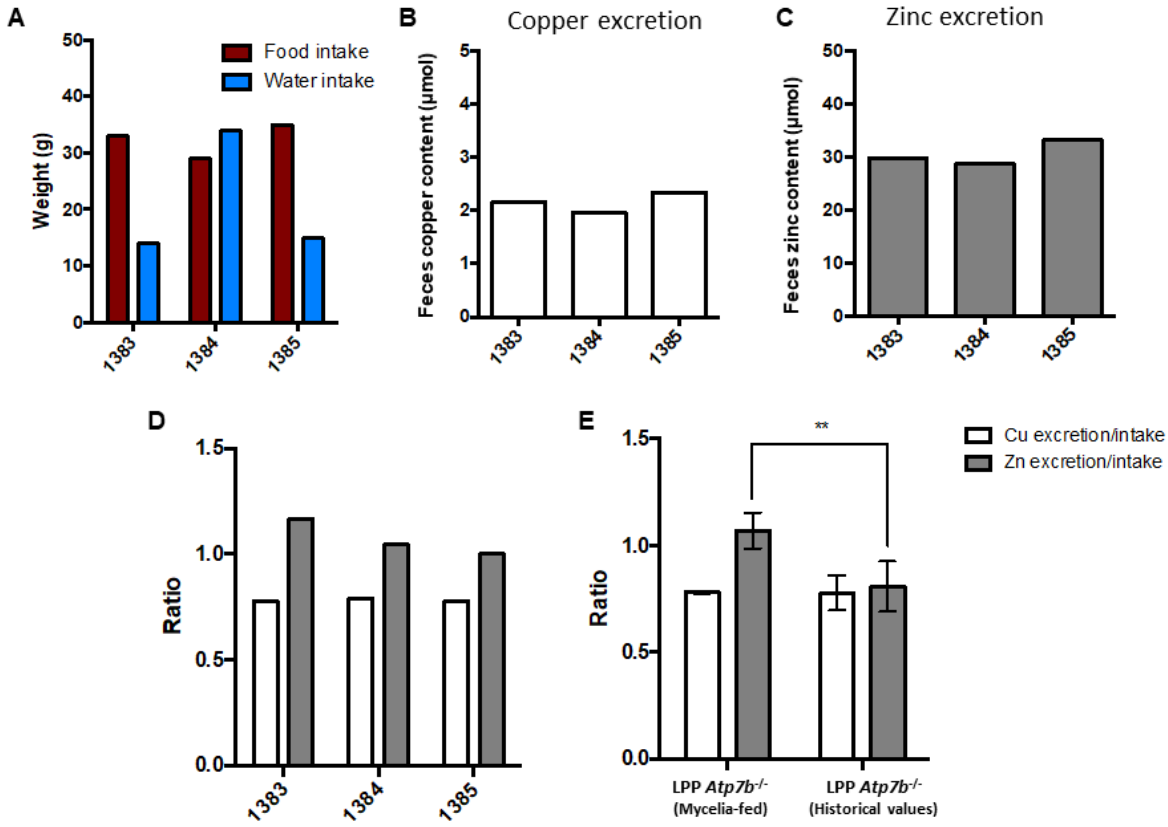

Figure 37. **A zinc-enriched mycelium diet promoted similar metal excretion in all three LPP *Atp7b*$^{-/-}$-fed animals, after the 1st feeding cycle.** After a period of 24 hours in a metabolic cage, **(A)** food intake was similar amongst animals, with increased water intake for animal number 2. **(B)** Copper and **(C**) Zn content in absolute values in the faeces was similar for all animals, with higher **(D)** Zn excretion/intake ratio in comparison with the Cu excretion/intake ratio. **(E)** Comparison with historical controls (age-matched LPP *Atp7b*$^{-/-}$ animals, fed a normal chow diet) showed an increase in Zn excretion via the feaces for mycelium-fed animals. Data are the mean ± SD of N=3 for mycelium-fed animals, and N=4 for LPP *Atp7b*$^{-/-}$ historical controls. Two-way analysis of variance with Sidak's multiple comparisons test after column analysis (identify outliers). **P<.01

After F2, animals number 2 and 3 were placed in a MC for 24 hours (MC2), while animal number 1 was kept in the normal cage, since the animals' health status did not allow the 24 hours MC experiment. Food and water intake were comparable between animals number 2 and 3 (Figure 38.A) and decreased for animal number 1. Copper (Figure 38.B) and Zn (Figure 38.C) excretion values via the faeces were lower in animal number 1, as expected from the lower food intake. For animals number 2 and 3, Cu and Zn excretion via the faeces was comparable (Figure 38.B, C) but lower in comparison to the values from MC1 (Figure 37.B, C), especially for Zn. The ratio excretion/intake was similar for both animals (Figure 38.D), as well as in comparison to historical values obtained for aged-matched LPP *Atp7b*$^{-/-}$ controls fed a normal chow diet (Figure 38.E).

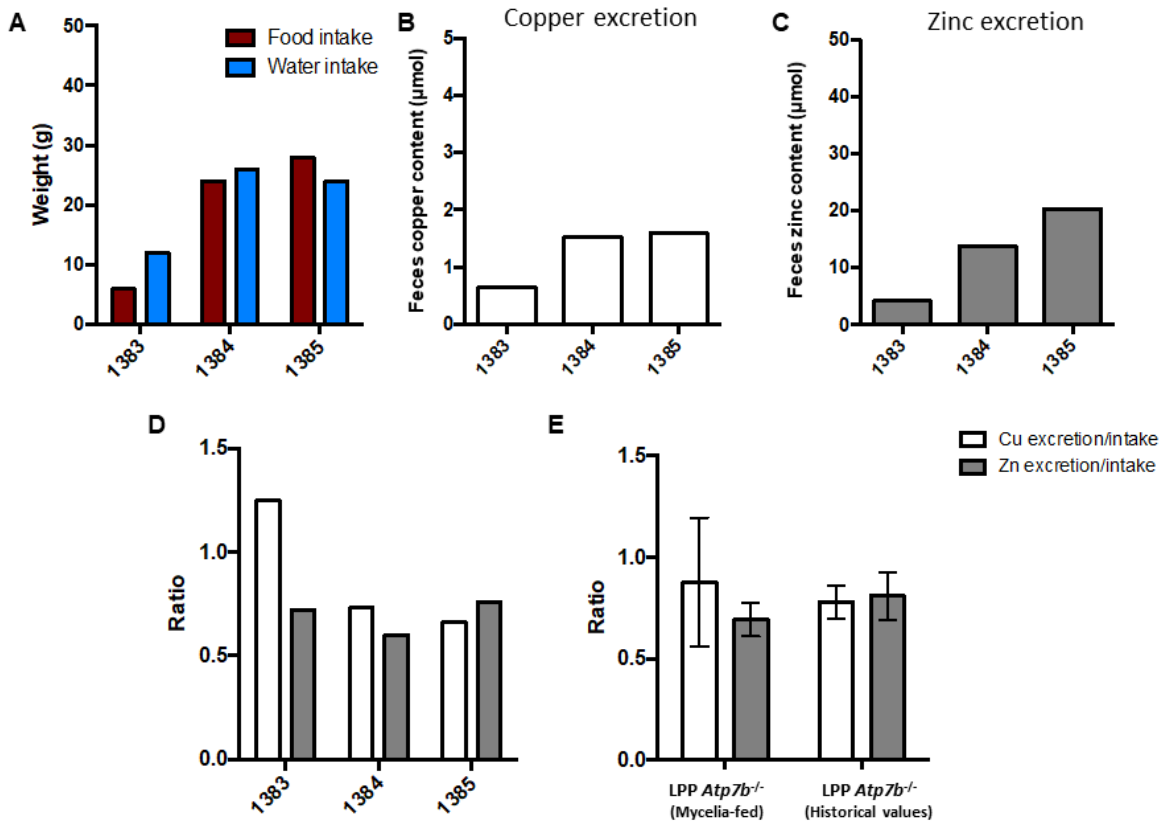

Figure 38. **A zinc-enriched mycelium diet promoted similar metal excretion, in still healthy LPP *Atp7b*$^{-/-}$-fed animals, after the 2nd feeding cycle.** After a period of 24 hours in a metabolic cage, **(A)** food intake was similar for animals number 2 and 3, with a decrease observed for animal number 1. **(B)** Copper and **(C**) Zn content in absolute values in the faeces was lower in animal number 1, with higher **(D)** Cu excretion/intake ratio in comparison with the still healthy animals. **(E)** Comparison with historical controls (age-matched *LPP Atp7b*$^{-/-}$ animals, fed a normal chow diet) showed no significant differences in both Cu and Zn excretion via the faeces for mycelium-fed animals. Data are the mean ± SD of N=3 for mycelium-fed animals, and N=4 for LPP *Atp7b*$^{-/-}$ historical controls.

Since food intake was similar between the two feeding cycles but Zn excretion about half as high in the second cycle, we can say that Zn absorption conversely increased from the 1st feeding cycle to the 2nd feeding cycle. Urine Cu and Zn excretion values for MC1 were in a comparable range for all three animals (Figure 39.A, B), with a higher Zn excretion observed for animal number 3 (Figure 39.B). The ratio excretion/intake was again comparable amongst animals (Figure 39.D), and the Zn ratio was lower in mycelium fed-animals in comparison to historical aged-matched LPP *Atp7b*$^{-/-}$ control rats fed a normal chow diet (Figure 39.E).

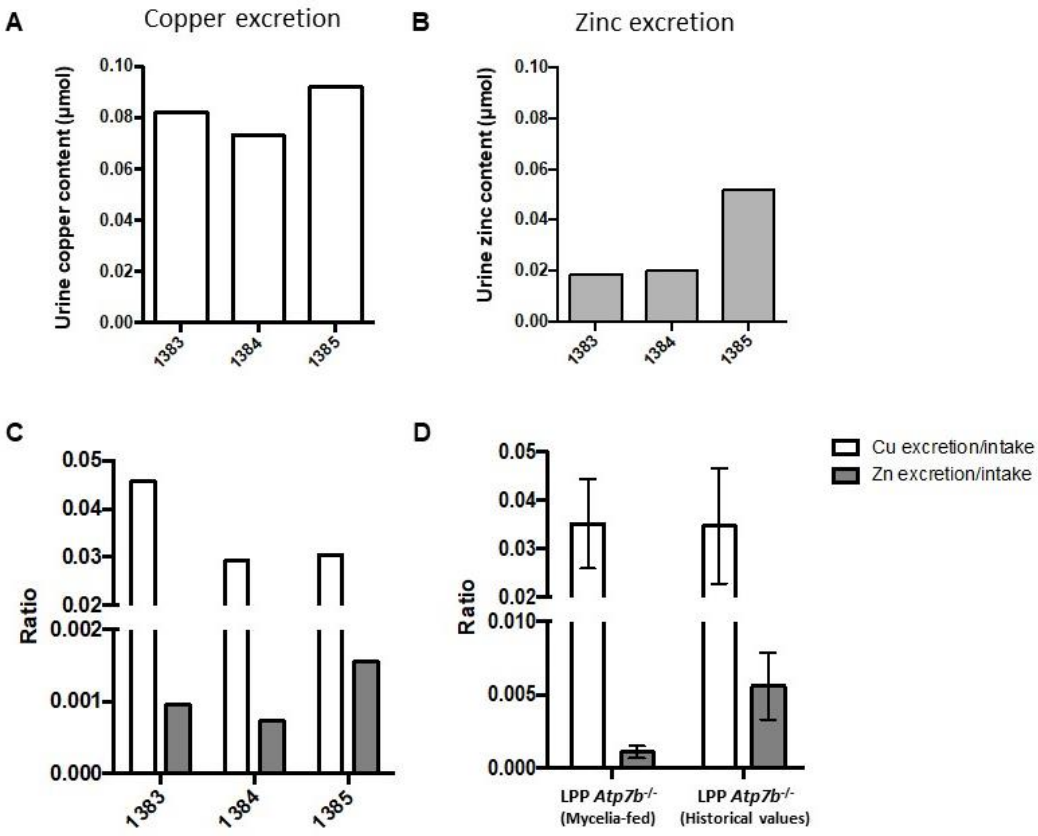

Figure 39. **A zinc-enriched mycelium diet promoted an increase in zinc excretion, in comparison to historical LPP *Atp7b*$^{-/-}$ controls, after the 1st feeding cycle.** After a period of 24 hours in a metabolic cage, **(A)** Cu and **(B)** Zn content in the urine was similar for all animals, with higher Zn content for animal number 3. **(C)** Copper excretion/intake ratio was higher than the Zn excretion/intake ratio. **(D)** Comparison with historical controls (age-matched LPP *Atp7b*$^{-/-}$ animals, fed a normal chow diet) showed a decrease in Zn excretion via the urine for mycelium-fed animals. Data are the mean ± SD of N=3 for mycelium-fed animals, and N=4 for LPP *Atp7b*$^{-/-}$ historical controls.

After F2, urine excretion values for Cu and Zn (Figure 40.A, B), during MC2 did not differ between animals number 2 and 3, as well as the ratios (Figure 40.C). The ratio excretion/intake of Zn was lower in the mycelium-fed animals (Figure 40.D), as observed for MC1 (Figure 39.D).

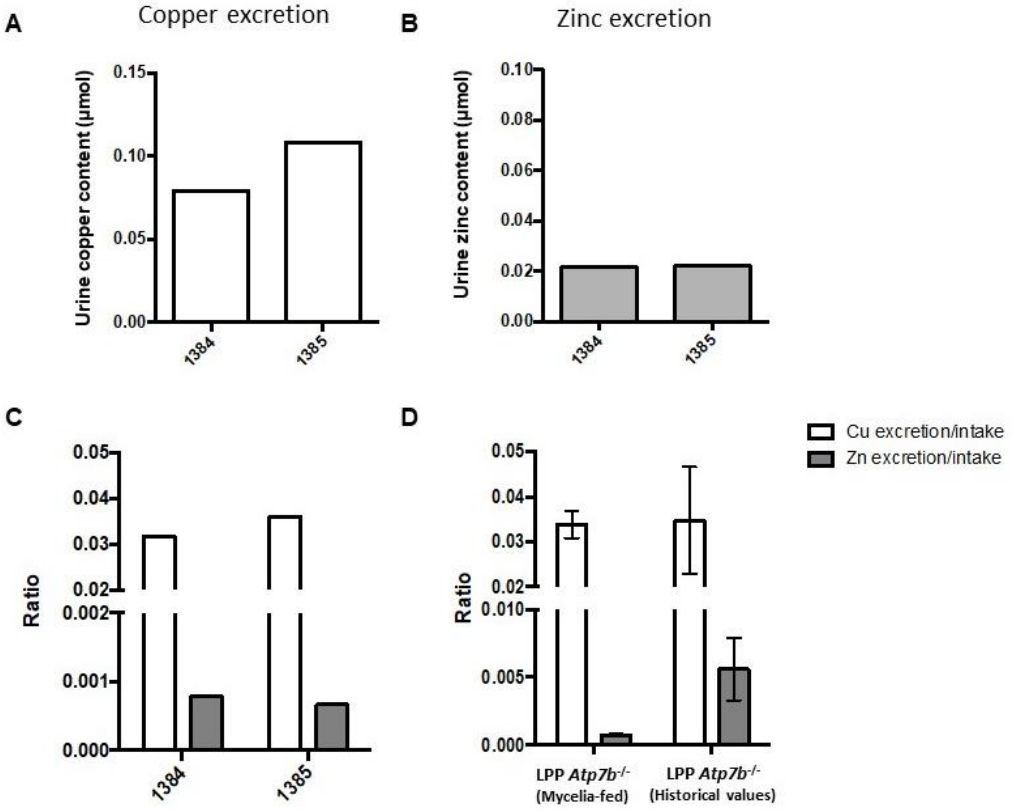

Figure 40. **A zinc-enriched mycelium diet promoted similar metal excretion, in LPP *Atp7b*$^{-/-}$-fed animals, after the 2nd feeding cycle.** After a period of 24 hours in a metabolic cage, **(A)** Cu and **(B**) Zn content in the urine was comparable for animals number 2 and 3. **(C)** Copper and Zn excretion/intake ratio was similar for both still healthy animals. **(D)** Comparison with historical controls (age-matched LPP *Atp7b*$^{-/-}$ animals, fed a normal chow diet) showed a decrease in Zn excretion via the urine for mycelium-fed animals. Data are the mean ± SD of N=3 for mycelium-fed animals, and N=4 for LPP *Atp7b*$^{-/-}$ historical controls.

The tissue metal content indicated that Cu level was increased in the duodenum of mycelium-fed animals, in comparison with jejunum/ileum sections of the intestine, and in comparison to LPP *Atp7b*$^{+/-}$ normal fed animals (Figure 41.A). Furthermore, duodenal Cu content was increased in mycelium-fed animals in comparison to LPP *Atp7b*$^{-/-}$, aged and health status (i.e. diseased animals) matched-animals, also fed a normal diet (Figure 41.D). Zinc content was increased in the intestine of mycelium-fed animals, with no differences between duodenum and jejunum/ileum (Figure 41.B). When compared with LPP *Atp7b*$^{-/-}$ fed a normal diet, Zn content was increased (Figure 41.E). In regards to Fe, no differences were observed in between mycelium-fed LPP *Atp7b*$^{-/-}$ and LPP *Atp7b*$^{+/-}$ normal fed animals (Figure 41.C). However, Fe content in the duodenum was increased in mycelium-fed animals in comparison to normal-fed LPP *Atp7b*$^{-/-}$ (Figure 41.F).

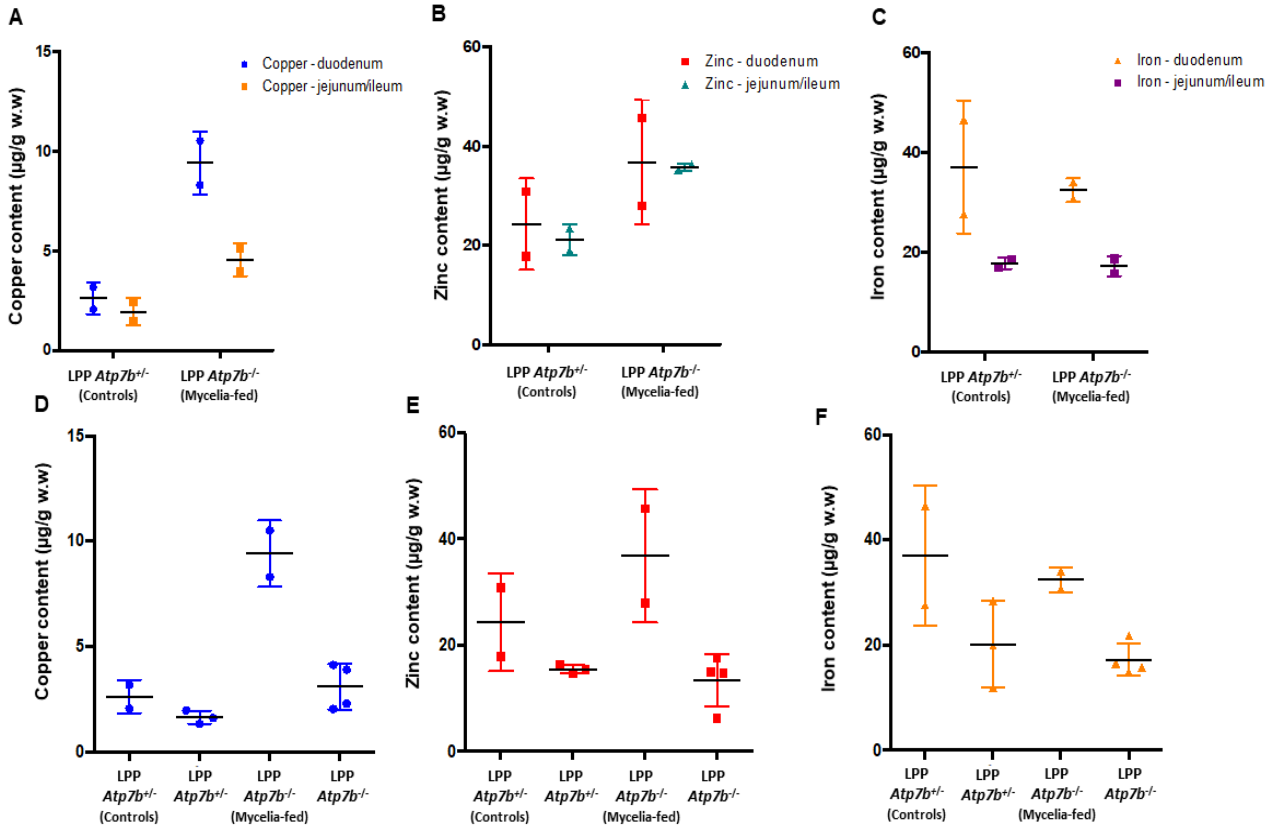

Figure 41. **Copper content was increased in the duodenum homogenates of LPP *Atp7b*$^{-/-}$ mycelium-fed animals.** **(A)** Copper content doubles in the duodenum of LPP *Atp7b*$^{-/-}$ mycelium-fed animals, in comparison to normal fed LPP *Atp7b*$^{+/-}$ and LPP *Atp7b*$^{-/-}$ controls. Copper content in the jejunum/ileum was lower, especially for LPP *Atp7b*$^{-/-}$ mycelium-fed animals, in comparison to duodenum, in the same animals. **(B)** Zinc content was tendentially increased in LPP *Atp7b*$^{-/-}$ mycelium-fed animals, in comparison to normal fed LPP *Atp7b*$^{+/-}$ controls, with no differences observed between duodenum and jejunum/ileum. **(C)** Iron content was increased in the duodenum, in comparison to jejunum/ileum, with no differences between *LPP Atp7b*$^{-/-}$ mycelium-fed animals and normal fed LPP *Atp7b*$^{+/-}$ controls. Metal content in the duodenum of LPP *Atp7b*$^{-/-}$ mycelium-fed animals was higher in comparison with aged-matched LPP *Atp7b*$^{-/-}$, that were fed a normal chow diet. **(D)** Copper content was similar in between LPP *Atp7b*$^{+/-}$ animals and increased in LPP *Atp7b*$^{-/-}$ mycelium-fed animals. Same results were observed for **(E)** Zn and **(F)** Fe content in the duodenum. Data are the mean± SD of N=2 for LPP *Atp7b*$^{-/-}$ mycelium-fed animals and LPP *Atp7b*$^{+/-}$ controls, and N=3-4 for LPP *Atp7b*$^{+/-}$ and LPP *Atp7b*$^{-/-}$, fed a normal chow diet.

These results pointed towards changes in duodenal metal content upon feeding with a Zn-enriched mycelium diet. From previous studies it is known that Cu levels in both liver homogenates and purified mitochondria are significantly elevated in LPP *Atp7b*$^{-/-}$ animals[68, 69]. In this study, isolated mitochondria from the duodenum of mycelium-fed animals did not

differ from LPP *Atp7b*$^{+/-}$ normal fed animals in terms of Cu (Figure 42.A), Zn (Figure 42.B) or Fe (Figure 42.C) content.

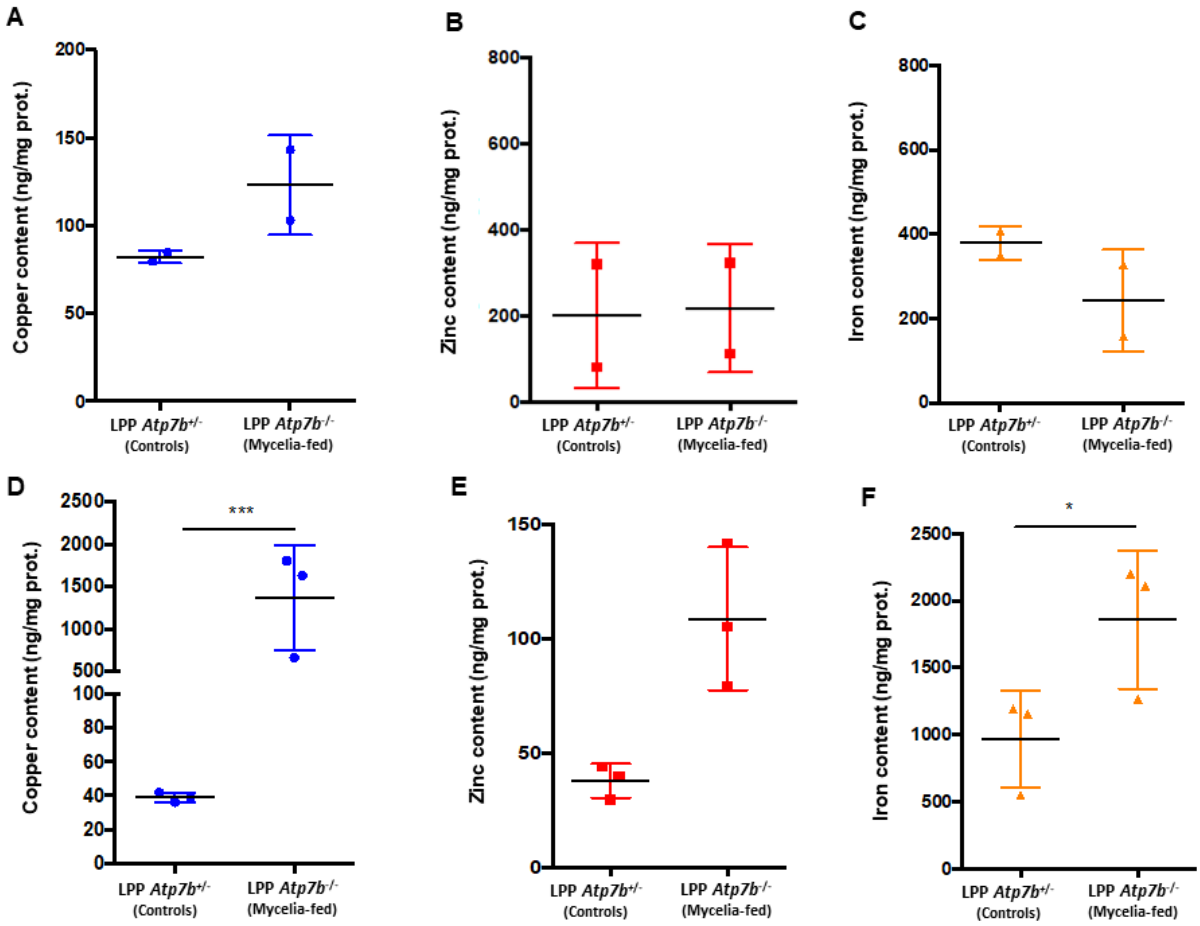

Figure 42. **Metal content in mitochondria, isolated from the duodenum of LPP *Atp7b*$^{-/-}$ mycelium-fed animals, was not different from LPP *Atp7b*$^{+/-}$ controls. (A)** Copper, **(B)** Zn and **(C)** Fe content in isolated mitochondria from duodenum did not change significantly in between LPP *Atp7b*$^{-/-}$ mycelium-fed animals and LPP *Atp7b*$^{+/-}$ controls. On the other hand, **(D)** Cu, **(E)** Zn and **(F)** Fe values in mitochondria isolated from liver were elevated in LPP *Atp7b*$^{-/-}$ mycelium-fed animals, in comparison to LPP *Atp7b*$^{+/-}$ controls. Data are the mean ± SD of N=2 for LPP *Atp7b*$^{-/-}$ mycelium-fed animals and LPP *Atp7b*$^{+/-}$ controls (A-C), and N=3 for LPP *Atp7b*$^{-/-}$ mycelium-fed animals and LPP *Atp7b*$^{+/-}$ controls (D-F). Two-tailed t-test (Mann-Whitney) after column analysis (identify outliers). *P<.05, ***P<.001

With regards to other organs, LPP *Atp7b*$^{-/-}$ mycelium-fed animals had significantly more Cu in the liver and kidneys (Figure 43.A), with no significant differences for brain, heart and spleen (Figure 43.D), in comparison to LPP *Atp7b*$^{+/-}$ animals. Zinc content in liver, heart, spleen and brain was also similar (Figure 43.B, E), with a significant increase observed in the kidneys (Figure 43.E). Concerning Fe, there was no significant differences in liver, heart or spleen (Figure 43.C), as well as no differences were observed for brain and kidney (Figure 43.F), comparing mycelium-fed and LPP *Atp7b*$^{+/-}$ normal fed animals.

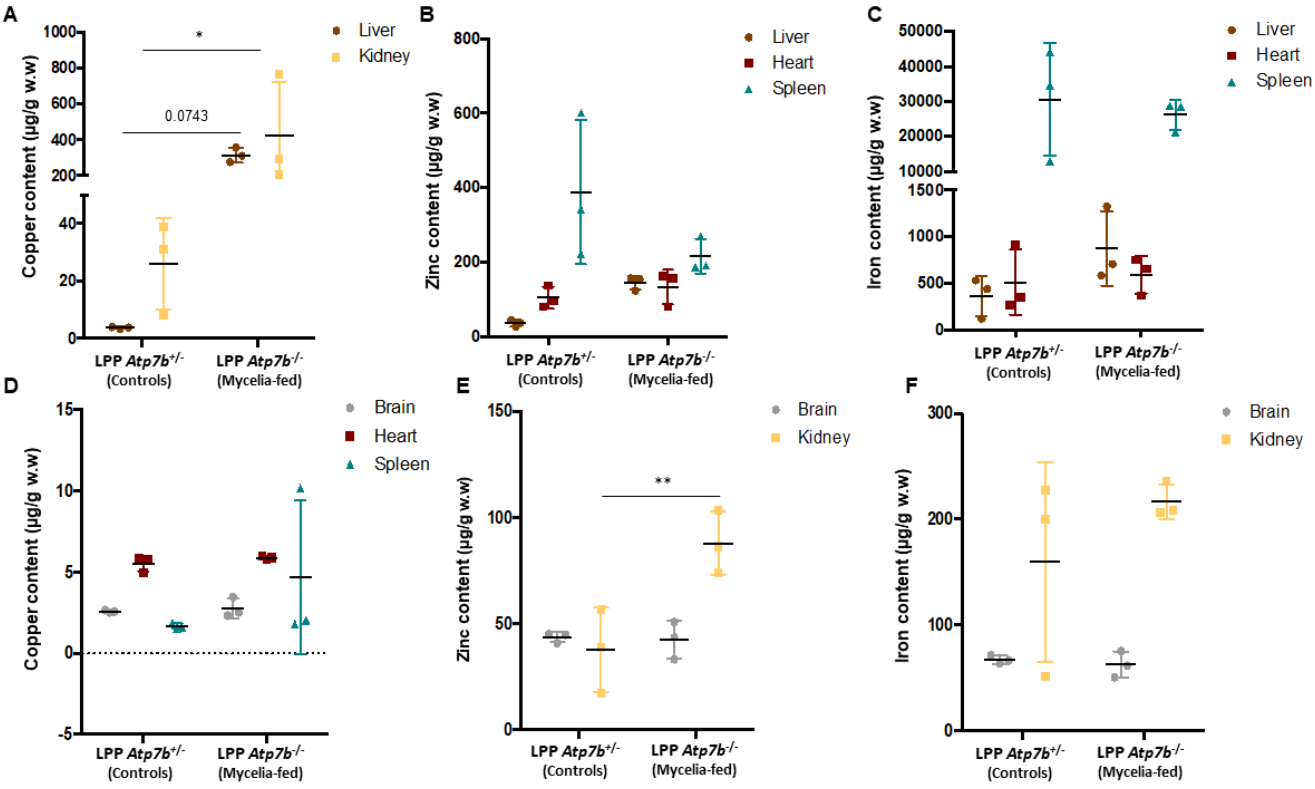

Figure 43. **Copper and Zn content was elevated in the liver and kidney homogenates of LPP *Atp7b*$^{-/-}$ mycelium-fed animals.** Analysis of metal content in different organs of LPP *Atp7b*$^{-/-}$ mycelium-fed animals, in comparison to LPP *Atp7b*$^{+/-}$ controls, showed an increase in **(A)** Cu levels in the liver and kidneys, and **(E)** Zn levels in the kidneys of LPP *Atp7b*$^{-/-}$ mycelium-fed animals. No significant differences were observed for **(D)** Cu and **(B, E)** Zn content in brain, heart and spleen, as well as for Fe content in **(C)** liver, heart, spleen, **(F)** brain and kidneys. Data are the mean ± SD of N=3 for LPP *Atp7b*$^{-/-}$ mycelium-fed animals and LPP *Atp7b*$^{+/-}$ controls. Two-way analysis of variance with Sidak's multiple comparisons test after column analysis (identify outliers). *P<.05, **P<.01

4. Discussion

4.1 Intestinal alterations in Wilson Disease

4.1.1 Intestinal damage in LPP animals, an *in vivo* model for Wilson Disease

Wilson disease (WD) is a life-threatening condition caused by the malfunction of the Cu transporter ATP7B. The disruption in the metabolism of Cu primarily leads to excessive metal accumulation in liver and brain of WD patients, with later problems also found in kidneys and heart. Even though the liver plays an important and central role in Cu homeostasis, the intestine as the site of Cu uptake, is also a key organ with respect to the regulation of body Cu levels[34]. Notwithstanding, its contribution to WD pathology is not yet fully understood and, only recently, studies indicated that ATP7B malfunction might have a different role in the intestine than in the liver[74, 95]. In *Atp7b*$^{-/-}$ rats (strain name: LPP), a well-established *in vivo* model for WD, liver tissue necrosis, fibrosis and inflammatory infiltrations were observed upon disease[68, 70], comparable to WD patients (untreated)[68].

In this study, structural alterations in the intestine of diseased LPP *Atp7b*$^{-/-}$ rats were observed, with a reduction of goblet cells and cell content in the lamina propria of the duodenum, as well as increased mucosal associated lymphatic tissue in the colon (Figure 8). A decrease in goblet cell number, and consequent alteration of the intestinal mucus layer, is a known result of chronic inflammation and may be associated with inflammatory bowel disease and ulcerative colitis[267]. Especially in the small intestine, the proper formation of a mucus layer is imperative to avoid bacterial infections with goblet cells as primary activators of the immune system[268]. In addition, alterations in the gut microbiota can also affect mucus-layer formation and increase inflammation, ultimately leading to increased gut permeability[267]. In fact, two studies reported altered gut microbiota in WD patients that correlated with increased inflammation[269], low concentration of intestinal short chain fatty acids (SCFAs), increased gut permeability, alterations in glucose metabolism and immune response, and decreased abundance of probiotics that affect other physiological functions[270]. Thus, alterations in the duodenum and colon of LPP *Atp7b*$^{-/-}$ rats could be linked to alterations in the gut microbiota, and/or inflammation as a consequence of a “leaky” barrier. Indeed, the proteomics data from still healthy LPP *Atp7b*$^{-/-}$ duodenum showed a predicted activation of pathways linked to inflammation, namely the complement and coagulation cascades, Toll-like receptor and B-cell receptor signalling pathways (Figure 13.A). In diseased LPP *Atp7b*$^{-/-}$ animals, a predicted activation of the nuclear receptor factor kappa B (NF-kB) pathway was also observed (Figure 14). Copper treatment in differentiated Caco-2 cells induced the production of Interleukin-8

(IL-8) for both wild-type (WT) and ATP7B KO cells (Figure 26), further strengthening the hypothesis of a Cu-linked inflammation scenario in the intestine, with ATP7B malfunction.

In the liver of LPP *Atp7b*$^{-/-}$ animals, Cu accumulation largely precedes the disease state[69]. In the duodenum, a significant increase of Cu levels was only observed in diseased LPP *Atp7b*$^{-/-}$ (Figure 9.A), in comparison to non-affected LPP *Atp7b*$^{+/-}$ animals, demonstrating a different regulation of Cu in the intestine. Nevertheless, a relative increase of Cu in the cytosolic fraction was observed in still healthy LPP *Atp7b*$^{-/-}$ (Figure 10.D), in comparison to non-affected LPP *Atp7b*$^{+/-}$ animals. In agreement with these findings, the proteome analysis of the rats' duodenum revealed a significant increase in cytosolic metallothioneins isotypes 1 and 2 (MT1/2) abundance, and a decrease in the Cu transporter CTR1, already before disease onset (Figure 9.D).

These results show that, before an overall significant Cu increase, the intestine is adapting against a possible systemic Cu overload. These findings agreed with published data on lower Cu content[74, 271] and increased MT expression in the intestine of *Atp7b*$^{-/-}$ mice[271], indicating a different regulation of intestinal Cu in comparison to liver Cu, which could be linked to potential differences in the function of the ATP7B transporter at these two sites. In the intestine, it was suggested that ATP7B rather has a role in the sequestration of Cu in intracellular vesicles for maintenance of Cu homeostasis in the enterocytes[95]. In the liver, its main function is to deliver Cu to the secretory pathway for excretion into the bile[272]. In further agreement, Medici *et al.* also reported an increase in Cu content in the intestine of LEC rats at 13 weeks-old, but only in animals with clear signs of acute hepatitis (ALT and AST values above normal)[273]. In WD patients, the mechanisms linked to Cu uptake also seem to adapt. The Cu transporter CTR1, which is responsible for more than 50% of Cu influx from the luminal side[274] was downregulated in the intestine of WD patients (mRNA and protein content), while the expression of the Cu transporter ATP7A, responsible for Cu transport to the blood, was increased[275].

Hepatic mitochondria damage is a hallmark of WD[69, 243] , with clear structural alterations observed in WD patients[36, 68, 243, 276]. In LPP *Atp7b*$^{-/-}$ rats, hepatic mitochondrial Cu accumulation, as well as structural and functional alterations were observed even before the onset of hepatitis, that occurs in these animals when they are 90-100 days of age[69]. Hence, the mitochondrial structure was analysed in the different intestinal sections of LPP *Atp7b*$^{-/-}$ still healthy and diseased animals. In still healthy animals, mitochondrial structure alterations were visible in both duodenum tissue and upon isolation (Figure 11), while in jejunum and

ileum, these alterations were more prominent in diseased animals (Figure 11). In agreement, the abundance of several proteins linked to mitochondrial organization and bioenergetic processes were altered in LPP *Atp7b*$^{-/-}$ intestinal proteomes (Figure 12.B). Namely Hspd1/Hsp60 and Opa1, responsible for mitochondrial structure regulation, as well as Atp5f1, and different proteins linked to Complex III assembly and activity (Uqcrq, Uqcrh, Coq4 and Lyrm7) were significantly downregulated in LPP *Atp7b*$^{-/-}$ animals. Alterations in cellular bioenergetics were observed in the proteome analysis by the decreased abundance of Acetyl-coA metabolism and citric acid cycle enzymes, such as isocitrate dehydrogenase [NAD] subunit beta (IdH3), and increased abundance of glycolysis (hexokinase-1), ketogenesis and creatine metabolism (Glycine amidinotransferase – Gatm). In addition, the observed predicted inhibition of the nuclear receptor LXR/RXR heterodimer in diseased animals, may lead to changes in the regulation of lipoprotein processing and transport (Figure 14), with a subsequent predicted inhibition of cholesterol transport and efflux, and upregulation of cholesterol biosynthesis (Figure 12.A, Figure 14). These results are in agreement with Pierson *et al.*, who showed loss of chylomicrons and apopoliprotein B mislocalization in *Atp7b*$^{-/-}$ mice enterocytes[74]. Furthermore, inhibition of LXR/RXR signalling, together with inflammation, was also observed in the livers of *Atp7b*$^{-/-}$ mice. Here, treatment with a LXR agonist significantly ameliorated liver damage and inflammation, without affecting the liver Cu content[277]. In the *Atp7b*$^{-/-}$ global knockout mice, liver damage and disease progression were more pronounced than in hepatic specific knockouts, with marked alterations in lipid metabolism, mitochondrial function and increased inflammatory response[72]. These results strengthen the role of extrahepatic organs, namely the intestine, in the pathogenesis of WD. In the liver of high-caloric fed LPP *Atp7b*$^{-/-}$ rats, Einer and co-workers[70] also observed an increase in lipid biosynthesis enzymes, with an increase in TG levels. Their proteomics data indicated a significant increase (around 4-fold) in the levels of nearly all enzymes in the cholesterol biosynthesis pathway, which consequentially caused elevation of bile salts in high-caloric fed LPP *Atp7b*$^{-/-}$ rats. The proteomic comparison also showed a slight increase in the levels of ketogenic mitochondrial enzymes. However, since serum levels of 3-hydroxybutyrate were comparable in high-caloric vs normal fed *Atp7b*$^{-/-}$ animals, the authors concluded that there were no significant alterations in this pathway. Nonetheless, our data in the intestine also pointed to a predicted increase in ketogenesis.

Finally, intestinal damage in LPP *Atp7b*$^{-/-}$ animals was detected by a significant decrease in the abundance of tight-junction (TJ) associated proteins, such as cadherin 1, 5 and 17, in still

healthy LPP *Atp7b*$^{-/-}$ animals (Figure 15.A), together with an observed decrease of electron-dense desmosome areas, and intercellular space widening, in comparison to non-affected LPP *Atp7b*$^{+/-}$ animals (Figure 15.B). Evidences of intestinal barrier problems were reported for NAFLD and NASH patients. In biopsy-confirmed NAFLD patients, gut permeability was increased in comparison to healthy controls, and correlated with small intestinal bacteria overgrowth and severity of steatosis. However, there was no correlation with hepatic inflammation or fibrosis. The content of duodenal ZO-1 was reduced in both crypts and villi of NAFLD patients, in comparison to healthy controls[278]. In a meta-analysis study[279], the authors reported that 39.1% of NAFLD patients had evidence for intestinal permeability, compared to 6.8% of healthy controls. The incidence of permeability was higher in NASH patients (49.2%), in comparison to NAFLD patients and healthy controls. In WD patients, or respective animal models, no data is available for the consequences of ATP7B malfunction in intestinal barrier permeability.

In conclusion, alterations in the upper intestine of still healthy LPP *Atp7b*$^{-/-}$ rats, namely the increase in MT1/2 and decreased CTR1, the relative Cu increase in cytosol, mitochondrial structure damage along with inflammatory signalling and decreased TJ-proteins abundance, demonstrated intestinal impairments/adaptations even before overt liver disease in these animals.

4.1.2 Copper sensitivity and mitochondrial damage in a Wilson Disease enterocyte cell model

From the results obtained in the LPP animals, we reasoned that enterocyte bioenergetic stress and reduced cell-cell contacts may be intertwined in WD. In fact, several reports have linked mitochondrial dysfunction to impaired cellular barrier integrities[245-247]. Thus, mitochondrial function and barrier tightness were evaluated in a well-established, and widely used enterocyte *in vitro* model, Caco-2 cells [202, 203, 280]. In parallel, Caco-2 cells bearing a *ATP7B* mutation (ATP7B KO)[97] were used. Hardly any ATP7B originated peptides were detected in these cells (Figure 16.A) and, in agreement with Guttmann and co-workers[97], they were more sensitive to Cu (Figure 16.C-F), especially with respect to ATP cellular content (Figure 16.D). Their liver counterpart, the HepG2 ATP7B KO cells, were also reported to be more sensitive to Cu challenge[281]. However, despite the increased sensitivity, we found no significant changes in cellular Cu content between Caco-2 WT and KO cells, before and after Cu treatment (Figure 17.A). This finding was not in line with Guttmann *et al.*[97], since they reported a significant increase in Caco-2 KO cellular Cu content upon Cu treatment, in comparison to WT cells. Interestingly, in HepG2 ATP7B KO, also no difference was observed between intracellular Cu levels of HepG2 WT and KO cells after Cu treatment[281]. Different results could be due to different sample preparations and/or different normalization strategies for the metal content. In fact, Guttmann and co-workers normalized Cu content against protein amount, and not against cell number, as presented in this study. However, metal content was also normalized by protein content (data not shown), and the results were similar to the ones in Figure 17. In isolated mitochondria, at basal or Cu loaded conditions, no differences were observed in Cu content between Caco-2 WT and KO cells (Figure 17.D). Thus, increased ATP depletion in the KO cells upon Cu treatment (Figure 16.D) might not be a direct consequence of Cu overload. Nonetheless, this indicates that mitochondria damage was already present in the Caco-2 KO cells at basal conditions, as observed for the LPP *Atp7b*$^{-/-}$ rats (Figure 11, Figure 12). Such damage would rather be due to ATP7B malfunction that might lead to Cu misplacement in the cell, instead of an overwhelming Cu load. Indeed, proteome analyses from Caco-2 WT vs KO cells, at basal conditions, clearly pointed towards mitochondrial dysfunction with a significant predicted inhibition of oxidative phosphorylation (Figure 18.A, B), and decreased ATP production (Figure 18.B). Moreover, and in accordance with the animal model (LPP *Atp7b*$^{-/-}$ rats) (Figure 13), a predicted activation of cellular stress response and alterations in the

expression of proteins linked to lipid metabolism were observed in KO cells, in comparison to WT (Figure 18.A, C). Of note are also the changes in the relative abundance of key proteins that ensure proper lysosomal acidification, such as ATP6V1F, ATP6V0A1 and ATP6V0D1, as well as proteins that are linked to lysosomal degradation of carbohydrates (GALC, HEXA, GLB1, NAGLU, MAN2B1 and FUCA1), and lipids (LIPA) (Figure 18.C). As mitochondria, lysosomes are important organelles in metal homeostasis. There are increasing evidence that several proteins involved in Cu homeostasis, such as the high-affinity Cu transporters CTR1/2, ATP7A/B and MT, associate with, and depend on lysosomes to store and transport Cu[282]. In particular, hepatic ATP7B interplays with the lysosomes to regulate cytosolic Cu content[283] and, as recently reported, also interacts with the microtubule-associated proteins 1 light chain 3 beta (LC3B) to promote Cu clearance via the autophagosome-lysosome fusion, promoting Cu-induced autophagy that was shown to be impaired in HepG2 ATP7B KO cells[284]. In addition, reduction of the cellular capacity to eliminate dysfunctional organelles, such as mitochondria, can lead to its accumulation. This situation is indeed observed in Caco-2 KO cells (Figure 19), with a significant decrease of mitochondria with clear cristae, and electron-dense matrixes (Stage I), and an increase of mitochondria with no visible cristae and swelling (Stage IV), without additional Cu treatment. As expected, mitochondria function was also compromised in Caco-2 KO cells, already at basal conditions (Figure 20, Figure 21). As mitochondria Complex-I linked respiratory spare capacity seems to be depleted in the KO cells (Figure 20.A, Figure 21.A), cellular rescue mechanisms come into play, such as the increase in Complex II-linked O_2 consumption, most prominently after Cu treatment (Figure 20.B, C), increased abundance of ATP synthase structural proteins (Figure 20.E) and a metabolic shift towards glycolysis (Figure 21.C, F).

In addition to Cu accumulation and marked mitochondria dysfunction in the liver, steatosis is also a common feature of WD patients[65]. In fact, misdiagnosis of WD for NAFLD/NASH can occur due to the overlap of several clinical criteria[285]. In LPP *Atp7b*$^{-/-}$ animals, a Western diet significantly, and in a short period of time, increased liver damage[70]. On contrary, *Atp7b*$^{-/-}$ mice fed a Western diet did not show significant changes in comparison to controls, and even displayed reduced liver inflammation[286]. However, it is important to note that the composition of the Western diet was different in-between studies, and the animal models per se already have a different disease outcome[287]. Even though it is clear that Cu and lipid metabolism are intertwined in WD, the mechanisms are still far from being fully comprehended[61, 288]. Since Cu and fatty acids are known to be absorbed in the upper part of the intestine[34, 289], it would be

legit to hypothesize on an important role of the intestine in the first processing of both. Pierson and co-workers shed light on this topic, reporting an impairment in lipid processing in the intestine of *Atp7b*$^{-/-}$ mice[74]. In ATP7B KO Caco-2 cells, the study by Guttmann and co-workers[97] demonstrated that these cells have disturbed lipid metabolism with increased small lipid droplets accumulation in the cytosol upon Cu treatment. Furthermore, they observed an increase in intracellular TG accumulation, with decreased secretion, when incubated with oleic acid[97]. Treatment of Caco-2 KO cells with a FFA mixture mimicking a high-fat diet[70], decreased ATP cellular content, and increased intracellular lipid accumulation, in comparison to FFA-treated WT cells (Figure 22.C, D). A co-treatment with Cu further increased intracellular lipid accumulation in the KO, in comparison to equally treated WT cells (Figure 22.D). Interestingly, staining for neutral fatty acids with BODIPY revealed an increase in lipid droplets in the ATP7B KO cells, even without FFA treatment (Figure 23), which corroborates the proteome analysis that indicated lipid metabolism changes (Figure 18), and the published reports in both animals[74] and cell model[97].

In conclusion, Caco-2 ATP7B KO cells have increased sensitivity to Cu, expressed by mitochondria structural and functional impairment already at basal conditions, together with alterations in lipid metabolism, as well as indications towards cellular stress linked to a decreased lysosomal activity. Moreover, in agreement with the data from still healthy LPP *Atp7b*$^{-/-}$ animals, no significant increase in Cu content was observed in comparison to Caco-2 WT cells, indicating a different ATP7B function in the intestine than in the liver, as in the latter, pathognomonic effects are linked to Cu excess.

4.1.3 Loss of barrier integrity is a feature of the Wilson Disease enterocyte model

The loss of barrier tightness in the GIT is a feature of several inflammatory diseases that affects not only the intestine but also the liver[50, 290]. In WD, indications of cellular barrier dysfunction were first suggested by Stuerenburg concerning the blood-brain barrier (BBB)[291]. He observed an increase of the ratio: albumin in cerebrospinal fluid vs albumin in the serum of patients with neurological manifestation of the disease, which could be related to a disturbance in the BBB. Borchard and co-workers reported a significant decrease in the transepithelial electrical resistance (TEER) of primary porcine brain capillary endothelial cells after a 48-hour treatment with Cu-albumin. This decrease was rescued by co-treatment with the Cu-chelator – WTX101 (Bis-choline tetrathiomolybdate)[104].

To follow up the observations that indicated malformation of tight barriers in LPP *Atp7b*$^{-/-}$ rat intestine, in comparison to LPP *Atp7b*$^{+/-}$ controls, we investigated the barrier tightness in Caco-2 WT and KO monolayers by biophysically assessing their TEER. Caco-2 cells have the capacity to regulate Cu uptake[292], and metal toxicity was previously reported in WT cells, with Cu treatment leading to a decrease in TEER, alterations in cytoskeleton maintenance and assembly[262, 293], increased inflammation and gut barrier dysfunction (decreased TJ expression)[294]. In our study, after 16 days of differentiation in a Transwell® system, KO cells did not form as tight barriers as the WT (Figure 24-26). Moreover, a prolonged Cu challenge to these barriers was more damaging to WT than KO cells (Figure 26), with a significant increase in Cu transport through the barrier (Figure 26.F), and inflammation (Figure 26.G). Previous studies with Caco-2 cells showed that prolonged Cu exposure can induce phenotypic changes, including a significant upregulation of SOD, MT and total GSH[295, 296]. Furthermore, in HepG2 ATP7B KO cells, continuous cultivation in medium containing Cu conferred resistance to these cells, in comparison with non-pre-treated HepG2 ATP7B KO cells[297]. Hence, although it is clear that the barrier integrity is compromised due to the ATP7B mutation, Caco-2 KO cells seemed to have developed some resistance towards Cu, most likely as a result of passaging and differentiation in a serum-containing medium that may result, for example, in the downregulation of CTR1, as observed in the intestine of the LPP rats and WD patients.

4.1.4 Methanobactin improves bioenergetics deficits and barrier integrity in the Wilson Disease enterocyte model

Currently, the first line treatments of WD patients are Cu chelators (e.g., D-penicillamine (DPA), Trientine), which are largely able to re-establish Cu homeostasis in the liver (although at higher levels)[116]. Alternatively, zinc salts induce lower Cu net intake and higher excretion at the intestinal site[35, 100], via increased high affinity Cu-binding MT abundance[111, 113]. Recently, the high-affinity Cu chelator peptide methanobactin (MB) has proven its enormous capacity to de-copper WD rat livers and liver mitochondria, thereby ameliorating mitochondria structure and function and, consequently, improving disease condition[70, 108]. Therefore, to test whether mitochondrial dysfunction and increased barrier leakiness in ATP7B KO Caco-2 cells could be therapeutically ameliorated by high affinity Cu chelation, we employed a Cu binding MB. As a result, mitochondrial function (Figure 27.A) and barrier impairment was improved (Figure 27.B-E), with a significant decrease in cellular Cu content (Figure 27.F). Thus, despite the fact that cellular Cu content did not increase in Caco-2 KO cells in comparison to WT (Figure 17.A), a positive effect was still obtained with MB, which efficiently depleted Cu from ATP7B KO Caco-2 cells. These results further support the hypothesis that ATP7B malfunction in Caco-2 KO cells may rather be caused by Cu mislocalization, than simple Cu excess. Such altered presence, e.g. in the cytosol, may interfere with lipid handling, which would then affect membrane compositions e.g. from mitochondria. In fact, it is hypothesized that Cu interferes with fatty acid desaturase and elongase activities. Copper supplementation in calfs increased Δ-9-desaturase activity, with an increase in fatty acid unsaturation, and decreased stearic acid in phosphatidylcholine and phosphatidylethanolamine in liver and heart[298]. Furthermore, cardiolipin (phospholipid specifically located at the mitochondrial inner membrane thereby directly contributing to its organization[299]) content was increased in the liver and heart, but decreased in muscle tissue. These results indicate that high Cu levels can change fatty acid composition of phospholipids, thus promoting alterations in membrane fluidity[298].

4.2 Development of a new nutritional approach for Wilson Disease

Copper induced liver damage is the major hallmark in WD, with steatosis and hepatic mitochondrial structure alterations as the two earliest pathognomonic features[36, 65, 69, 243]. We therefore aimed to develop a new nutritive approach that may ameliorate liver damage or slow down disease progression. The rationale for this was that the current treatments are not without unwanted reactions, i.e. Cu-chelator treatments may come with neurological worsening and other severe side effects due to long-term treatment[101-103]. Moreover, the alternative treatment by zinc salts is linked to gastric inflammation observed in approximately 30% of WD patients[111, 116, 117]. Typically, these treatments must follow a strict time schedule mostly in between meals thereby causing severe compliance issues. On top of that, treatment costs are elevated[300]. The beneficial effects of mushrooms in different pathologic scenarios, such as cancer, obesity, diabetes, NAFLD, inflammatory conditions, amongst others, is extensively described in the literature[134, 135]. Besides liver protective effects, mushrooms are further known to have a high metal binding capacity. Therefore, a mushroom-enriched diet may provide an additional but co-nutritive approach to ameliorate liver damage in WD.

4.2.1 Mushroom extracts have the potential to improve cellular viability in a lipotoxicity *in vitro* model

Aqueous and ethanol extracts from seven different edible mushrooms species (*Agaricus bisporus*, *Boletus edulis*, *Cantharellus cibarius*, *Ganoderma lucidum*, *Lentinula edodes*, *Macrolepiota procera* and *Pleurotus ostreatus*) were selected to treat HepG2 cells. Cytotoxicity was stronger with the ethanol extracts, while decreased cellular viability with aqueous extracts was observed only for *G. lucidum* and *C. cibarius* (Table 17). For *G. lucidum*, several reports have shown its capacity to reduce viability and growth of cancer-derived cell lines in culture[51, 301-303]. For *C. cibarius*, less studies were reported thus far, however both ethanol/methanol[304] and aqueous extracts[49] had cytotoxic effects *in vitro*. HepG2 cells treated with a free fatty acids (FFA) mixture that mimics the FA composition in the liver of mice fed a Western-like diet (45% calories from fat)[305], were used as an *in vitro* model of lipotoxicity[199, 200]. This FFA treatment was previously reported to induce, on one hand, a time-dependent increase in neutral lipid content, with increased cellular ROS, and decreased mitochondrial membrane potential (ΔΨ) in HepG2 cells[306]. On the other hand, it increased Complex III, IV and V protein expression levels[306]. In the present study, metabolic activity and cellular viability

were decreased in FFA-treated HepG2 cells (Figure 28.A, B), while cellular lipid content was increased (Figure 28.D), with no difference in ATP cellular content (Figure 28.C), in comparison to non-treated control cells. Co-treatment of HepG2 cells with the FFA mixture and mushroom aqueous extracts revealed positive effects for *P. ostreatus* for all evaluated parameters, i.e. cellular metabolic activity and viability, ATP cellular content, and intracellular lipid accumulation (Figure 28). The protective effect of two polysaccharide-peptides (PSI/II) extracted from *Pleurotus citrinopileatus* against FFA (palmitic and oleic acid, 1:2 respectively)-treated HepG2 cells was previously reported. Cellular viability of HepG2 cells treated with the FFA was significantly decreased, with increased TG and ALT/AST levels, and decreased cellular SOD activity, in comparison to non-treated control cells. Treatment with PSI/II for 48 hours significantly reversed the observed effects and stimulated FFA oxidation, observed by the increase in PPAR-α, CPT1 and ACOX1 gene expression[307]. Similar effects were observed with treatment of high-fat diet induced obese mice with a *P. citrinopileatus* water extract. In comparison to non-treated obese animals, supplementation with the mushroom water extract reduced body weight, serum levels of TG, cholesterol, LDL, AST, creatinine and nonesterified FA levels, and improved glucose tolerance[308]. In animal models fed a high-caloric diet (either high-fat or high-fat and high-cholesterol), different extracts from *P. ostreatus* improved liver damage and the activity of antioxidant enzymes, decreased liver and/or circulating amount of FA and ameliorated glucose metabolism[150, 309]. Thus, the beneficial effects of the *P. ostreatus* aqueous extract against *in vitro* lipotoxicity reported in this study are supported by previous reports of *Pleurotus spp*. liver protection in fatty acids accumulation/high-fat diet scenarios.

4.2.2 The mushroom *Pleurotus ostreatus* accumulates zinc in their mycelium

Metal accumulation in fungi is well documented[180, 192, 255, 256, 258], mostly from the perspective of environmental myco-remediation, but also with the aim of understanding metabolic alterations in the fungi upon metal overload[182, 192, 258, 259, 310], or explore their capacity to detoxify another living organism[311].

In line with the idea of developing a "liver protective" nutritional approach for WD, *P. ostreatus* was chosen to explore a double strategy that combines the beneficial effects against liver steatosis, described by the literature and corroborated in this work, and the potential capacity to decrease Cu absorption in the GIT, that is currently accomplished with zinc salts in WD patients[110-112, 264].

The growth of the mushroom *P. ostreatus* in a Zn-enriched solid substrate resulted in a dose-dependent increase of Zn in the mycelium (Figure 29.C, Figure 30.B), but not in the carpophores (i.e. fruiting bodies), as initially hypothesized. The dialysis of the protein extract showed a complete loss of Zn at a higher cut-off (100KDa), with an increase of the Zn-to-protein ratio with a cut-off equal or below 20KDa (Figure 30.F, G; Figure 31.D, E). These results indicate that Zn, or at least a major part of it, is bound to proteins in the mycelium of *P. ostreatus*, as previously shown for other mushroom species[182, 312]. The hypothesized mechanism for the high tolerance of mushrooms towards metal overload is the upregulation of intracellular metal chelators such as GSH and MT[182]. The same results were observed for the Zn-enriched mycelium of *P. ostreatus* grown in a liquid culture setting (Figure 31), with the exception that, in liquid culture, the Zn content in the mycelium was 2-fold higher in comparison to the mycelium grown in solid culture (Figure 31.B, Figure 30.E). Different reports have shown the capacity of *Pleurotus spp.* to accumulate Zn[192], but also Fe[191] and Se[313, 314], or even both Zn and Se[315, 316] in their mycelium. To the best of our knowledge, this is the first report of a Zn-enriched protein extract obtained from the mycelium of *P. ostreatus,* grown in a Zn-enriched liquid substrate. The cultivation of the Zn-enriched mycelium in liquid culture contributes to better control the biomass production for *in vitro* model studies, as well as to study the mechanisms linked to its high tolerance for metal accumulation.

4.2.3 The zinc-enriched mycelium protein extract ameliorates *in vitro* copper toxicity

The use of *Pleurotus ostreatus* mycelium to develop new nutritional strategies with bio-medical effects has very recently gained momentum[317]. In fact, a study by Cardoso *et al.*, demonstrated that mycelium from *P. ostreatus* contained higher amounts of bioactive compounds, like ergosterol and phenolic compounds, and had higher antioxidant activity in different cancer-derived cell lines, in comparison to the carpophores[318]. Caco-2 cells were also previously used to study the transport, metabolism and effects of functional foods[319], including *Pleurotus spp.*[320, 321]. As a preventive strategy, fermentation supernatants (FS) from *P. eryngii* increased gene expression levels of different tight-junctions (TJ) proteins (ZO-1, occluding and claudin-1) in Caco-2 cells treated with lipopolysaccharides[321]. Also, FS from *P. eryngii*, *P. ostreatus* and *Cyclocybe cylindracea* protected Caco-2 cells from the genotoxic agent tert-butyl hydroperoxide (*t*-BOOH)[320].

To evaluate a potential positive effect of *P. ostreatus* Zn-enriched mycelium protein extract (ZM(PO)) against Cu toxicity in Caco-2 cells, a first screening was performed. At a concentration of 37μM ZM(PO), correspondent to the Zn content in the protein extract, the extract caused a decrease in cellular lysosomal acidification (Figure 32.D), in contrast to the protein extract from the control mycelium (M-Ctrl(PO)) (Figure 32.D). At a lower concentration, 18.5μM ZM(PO), no differences were observed in comparison to M-Ctrl(PO) 1:2 and untreated control cells (Figure 32.D). Treatment of Caco-2 cells with zinc sulphate had no significant cellular toxic effects up to 250μM (Figure 32.A-C). Thus, the effect observed for 37μM ZM(PO) could be related to other compounds present in the protein extract, or to the lysis buffer used in the extract preparation. However, since the effect of M-Ctrl(PO) was not as prominent, the toxicity observed was probably not caused by the lysis buffer but by other compounds, such as polysaccharides, proteoglycans and polypeptides, which have been reported to have *in vitro* antitumoral activity[322-324]. Importantly, in the presence of Cu, 18.5μM ZM(PO) co-treatment in the Caco-2 cells improved cellular viability and decreased cellular Cu content, in comparison to the co-treatment with M-Ctrl(PO) (Figure 33.A, B). In differentiated Caco-2 cells treated with 200μM $CuCl_2$ for 48 hours, cellular Cu content was also tendentiously reduced upon co-treatment. Expression of MT was increased upon treatment with ZM(PO), which is in line with our initial hypothesis of increasing MT upon Zn treatment, that is a known

mechanism of zinc salts therapy in WD patients[111, 264]. A 7-days treatment with Cu induced a decrease in TEER of around 50% that was partially rescued by the co-treatment with ZM(PO) (Figure 34.A), with increased expression of the TJ protein claudin-5 (Figure 34.F). As observed for the 48 hours treatment (Figure 33.D), a tendency of decreased cellular Cu content was observed, as well as a decrease in the basolateral Cu content (Figure 34.C-E). Meaning, treatment with the ZM(PO) potentially improved barrier leakiness, thus less Cu was present in the basolateral compartment (mimicking the blood stream). In differentiated ATP7B KO Caco-2 cells treated for 17 days, Cu treatment also reduced the TEER to about half, in comparison to the beginning of treatment, with an ameliorating effect observed upon co-treatment with ZM(PO) (Figure 35.A). The expression of the TJ protein occludin was increased upon co-treatment, with no clear improvement for TJP1/ZO-1 (Figure 35.C). Interestingly, supplementation with lentinan, a compound extracted from the mushroom *Lentinula edodes*, had beneficial effects in the gut barrier of a high-fat diet-induced NASH mouse model. Treatment with lentinan significantly increased mRNA and protein levels of the TJ proteins occludin and ZO-1 in the mice jejunum, in comparison to high-fat fed, non-treated mice[325]. Moreover, an improvement in microbiota dysbiosis, as well as liver steatosis and inflammation was reported in this study, further strengthening the role of the gut-liver axis in liver disease, and the therapeutical potential of mushrooms compounds. Also, as observed before, the Caco-2 WT enterocyte-like barrier is more sensitive to a prolonged Cu challenge than KO cells (Figure 26). Thus, to test whether ZM(PO) was able to rescue the damage caused by Cu to the barrier of the KO cells, an early treatment was applied. In both cases, WT and KO cells, a rescue effect was observed. However, further biological replicates are needed to draw firm conclusions from these results. Furthermore, an increased number of replicates, as well as a prolonged treatment with M-Ctrl(PO), together with a co-treatment with Cu, would be needed to distinguish between mycelium only or Zn-enriched mycelium protein extract effects. Taken together, this is the first report on the positive therapeutic effects of a *P. ostreatus* Zn-enriched mycelium protein extract on Cu-treated Caco-2 cells. These effects were observed in both non-differentiated cells (decreased intracellular Cu content and increased cellular viability), and enterocyte-like barrier forming cells (improvement of cell barrier integrity by potential decreased in Cu content and increased MT expression).

4.3 Feeding of *Pleurotus ostreatus* zinc-enriched mycelium promoted zinc absorption, and changed duodenal metal content in LPP rats

Several studies reported the beneficial effects of Zn salts supplementation in LEC animals, actually mimicking the effects observed in WD patients namely increased MT expression, decreased Cu and increased Zn levels in liver and intestine, and decreased liver damage[273, 326-330]. However, only few reports exist on feeding LEC rats, or rats in general with *Pleurotus spp.* mycelia. Recently, Ogbmida *et al*. reported the metalloprotective role of *Pleurotus tuberregium* in rats exposed to arsenic and chromium[311]. Also, different extracts from *Pleurotus spp*. Zn-enriched mycelium have proven *in vivo* hepatoprotective and antioxidative effects[187, 331, 332]. The promising results observed with the enterocyte-like *in vitro* model prompted the idea to feed LPP *Atp7b*$^{-/-}$ rats with a *Pleurotus ostreatus* Zn-enriched mycelium nutrition. In our study, three LPP *Atp7b*$^{-/-}$ female rats were fed in two cycles, each for one week, separated by one week of normal chow feeding (Figure 6.A, Table 10). This first pilot study was conducted with the following questions: 1) Do the animals eat the Zn-enriched mycelium food?; 2) Does the feeding changes Cu, and also Zn, excretion levels via the faeces?; 3) Is there any change in Cu, but also Zn excretion via the urine?; 4) Does the feeding alter metal contents in the duodenum?, and 5) Does the health status of the animals improves upon feeding?

With regards to our first question in this study (*1) Do the animals eat the zinc-enriched mycelium food?),* all three animals ate the Zn-enriched mycelium food (Figure 37.A, Figure 38.A). When we moved to our second question (*2) Does the feeding changes Cu, and also Zn, excretion levels via the faeces?,* it was difficult to compare the data in this study with historical data since the diet prepared with the Zn-mycelium powder had a different composition (around 50% water) from the normal chow diet fed to the historical controls (LPP *Atp7b*$^{-/-}$). Therefore, it is not possible to directly compared food intake and metal values in the faeces and urine. After the 1st feeding cycle, Cu and Zn absolute content in the faeces was similar for all treated animals (Figure 37.B-D). When comparing the metal ratio of excretion vs intake to normal-fed LPP *Atp7b*$^{-/-}$ rats, Zn values were significantly elevated for the Zn-enriched mycelium-fed animals (Figure 37.E). At the end of the 2nd feeding cycle, food and water intake, as well as Cu and Zn excretion via the faeces was reduced for animal number 1 (LPP 1383), which correlated with the animal's diseased condition. Zinc excretion vs intake ratios were

also reduced (Figure 38.E) in comparison to the values from the 1st feeding cycle (Figure 37.E). This result points towards an increase in Zn intake with prolonged feeding of the animals with the Zn-enriched mycelium. The third main question was *(3) Is there any change in Cu, but also Zn excretion via the urine?* With regards to this, of note is the decreased ratio of Zn excretion vs. intake in the urine, in comparison to normal-fed LPP *Atp7b*$^{-/-}$ rats, observed after the 1st and 2nd feeding cycles (Figure 39.D, Figure 40.D). Thus, although there was no clear evidence of an increased Cu excretion via the faeces, Zn intake and retention seemed to increase from the 1st to the 2nd feeding cycle. Regarding the fourth question *(4) Does the feeding alter metal contents in the duodenum?*, in the intestine of LPP *Atp7b*$^{-/-}$ fed a Zn-enriched mycelium diet, Cu content was increased in the duodenum, in comparison to the jejunum/ileum sections (Figure 41.A). Furthermore, Cu, but also Zn and Fe levels, were elevated in the duodenum of Zn-enriched mycelium fed animals, in comparison to normal-fed, age and health status matched animals (Figure 41.D-F). Once more, both LPP *Atp7b*$^{+/-}$ study controls, and *LPP Atp7b*$^{-/-}$ historical controls, were fed a normal chow-diet, instead of an equivalent paste diet, hindering the possibility of a direct comparison of results. In isolated mitochondria from the duodenum, no significant differences were observed for all evaluated metals (Figure 42.A-C) while in liver mitochondria, Cu and Fe were significantly elevated when compared to LPP *Atp7b*$^{+/-}$ fed a normal diet (Figure 42.D-F). Looking at the values for tissue homogenates, as expected, Cu was significantly elevated in the liver and kidneys of LPP *Atp7b*$^{-/-}$, in comparison to LPP *Atp7b*$^{+/-}$ animals (Figure 43.A). In addition, Zn was also significantly elevated in the kidneys of LPP *Atp7b*$^{-/-}$ animals (Figure 43.E), which could be related to the observed decrease in Zn excretion via the urine (Figure 39.D, Figure 40.D). With regards to other organs, LPP *Atp7b*$^{-/-}$ mycelium-fed animals had significantly more Cu in the liver and kidneys (Figure 43.A), with no significant differences for brain, heart and spleen (Figure 43.D). Zinc content in liver, heart, spleen and brain was also not different (Figure 43.B, E), with a significant increased observed in the kidneys (Figure 43.E). Concerning Fe levels, there was no significant differences in liver, heart or spleen (Figure 43.C), as well as no differences were observed for brain and kidney (Figure 43.F), comparing mycelium-fed and LPP *Atp7b*$^{+/-}$ normal fed animals. Last but not least, our fifth question was *5) Does the health status of the animals improves upon feeding?* No improvement in their health status was observed with the Zn-enriched food (Table 18, Figure 36). This result was, however, expected, since at the age of 84 days, Cu levels in the liver of the treated animals are already massively elevated[69]. As Zn therapies are known to work on a long-term treatment basis, the time frames of Zn-enriched mycelium feeding in

this pilot study were too short to be effective in this respect. Consequently, at the end of the study, animal number 1 (LPP 1383) presented with liver disease (Bili > 0.5 mg/dL), animal number 2 (LPP 1384) with a disease onset scenario (AST > 200 U/L), and animal number 3 (LPP 1385) was still healthy but with an ALT value about 100 U/L (Table 18).

In summary, feeding the LPP *Atp7b*$^{-/-}$ animals with a *Pleurotus ostreatus* Zn-enriched mycelium diet was well tolerated, had an impact on duodenal metal content and on Zn excretion vs. intake in the intestine. Further studies have to address the correct feeding controls, as well as early feeding time points and longer treatment periods.

5. Conclusions and Future work

The view how metals may negatively impact human health is about to change. New evidences have shown that, despite what was previously thought, metal-related ROS production via Fenton reactions might not be the main route by which essential metals, such as copper and iron, cause cellular stress and even death. In the last years, ferroptosis and cuproptosis have been described as new metal-linked types of cell death, unraveling new molecular targets and mechanisms for metal toxicity. In parallel, particularly copper imbalance, is now pointed as a feature to different diseases, from metabolic to neurological conditions. Wilson disease is the prototype of a copper-storage disease, caused by mutations in the copper transporter ATP7B. In Wilson disease (WD), mitochondrial function and structure alterations, as well as steatosis, are early hepatic pathologic features that arise from an increase in copper levels, and before any oxidative stress is found in the liver. In metabolic disorders, namely NAFLD, mitochondrial dysfunction and steatosis are also early pathological signs, with copper imbalance being correlated with disease progression. However, there is no consensus whether copper deficient or overload is the cause or consequence in this scenario. Current treatment options for WD patients are not ideal. From several side effects to challenging treatment schedules that affect patient's compliance, both copper chelators and zinc salts have their pitfalls.

In line with this, the hypothesis of this research work was that a zinc-enriched mushroom could represent a nutritive approach to potentially improve the therapeutic outcome in WD by directly binding Cu in the diet and/or promoting Cu binding in the enterocytes with lower GIT irritation and, simultaneously, to ameliorate liver damage, especially hepatic steatosis.

Contrary to the hepatic phenotype of WD, little is known about ATP7B malfunction in the intestine and the resulting pathophysiology. Therefore, it became important to enhance the knowledge about the intestinal impairment in WD, to better understand the effect of the mushroom-enriched diet. As so, the first aim of this work was to study potential alterations in the intestine of WD rats (LPP *Atp7b*$^{-/-}$), and Caco-2 ATP7B KO cells. This study demonstrated mitochondrial structural alterations with changes in intestinal cellular bioenergetics for both intestinal models, as it happens in the liver. In the Caco-2 ATP7B KO cells, such mitochondrial dysfunction was present already at basal conditions (i.e. without additional Cu treatment). Nonetheless, the Cu chelator methanobactin improved mitochondrial function and barrier integrity in the Caco-2 KO cells. This result initiated the hypothesis that, in the intestine, ATP7B malfunction may rather lead to Cu misdistribution than to its simple excess as the main pathologic issue, contrary to liver, where a clear Cu overload is observed. Furthermore, the new finding of impaired tight barrier formation observed in the LPP rats (*Atp7b*$^{-/-}$), as well as

in Caco-2 ATP7B KO cells, was in line with the mitochondrial dysfunction, and with other liver diseases, such as NAFLD. Thus, the idea of a new nutritional approach gained momentum, especially with reported positive effects of mushrooms on gut microbiota and intestinal metabolism overall.

The second aim of this research was to select a mushroom species to develop the zinc-enriched mushroom. To this end, seven edible and medicinal mushroom species with proven health beneficial effects towards liver disease: *Agaricus bisporus*, *Boletus edulis*, *Cantharellus cibarius*, *Ganoderma lucidum*, *Lentinula edodes*, *Macrolepiota procera* and *Pleurotus ostreatus*, were used and from that, the aqueous extract from *P. ostreatus* selected.

Whereat, the goal was to find a new nutritive approach, complementary to currently approved treatments for WD that would lower the systemic copper burden of patients, in a more bio and food friendly form, and with combinatory beneficial effects, e.g. concerning steatosis. As so, the third aim of this work was the development of a zinc-enriched *P. ostreatus* based on 1) the evidence of health benefits of the species; 2) the promising results in the *in vitro* lipotoxicity model; 3) the species ability to accumulate metals, and 4) the premise of providing a healthier approach of a bio-zinc formulation for Wilson disease patients. To this end, the protocol for the mycelium growth in a zinc-enriched liquid culture, as well as the protocol to obtain a zinc-enriched *P. ostreatus* mycelium protein extract were developed and optimized. The fourth and final aim of this research work was to develop a new dietary approach to help reduce Cu absorption in the GIT. To this, Caco-2 WT and ATP7B KO cells were treated with the zinc-enriched *P. ostreatus* mycelium protein extract, which resulted in an increase in copper protective metallothioneins and an improvement of the intestinal barrier integrity. In LPP rats, preliminary results pointed towards an increase in Zn uptake, along with Cu retention in the duodenum, with two weeks of feeding with the zinc-enriched *P. ostreatus* mycelium. Taken together, both *in vitro* and *in vivo* results encourage the pursuing of new nutritional approach in the future, not only for Wilson disease, but also for other gut-liver related conditions like NAFLD.

Due to the novelty of this nutritional approach, a considerable time was needed for the development of the zinc-enriched mycelium and the correspondent protein extract. Also, the Caco-2 cell model was first established in the laboratory, together with the ATP7B KO cell model, which allowed the evaluation of the mitochondrial bioenergetic defects, along with the study of the protective effects of the zinc-enriched *P. ostreatus* mycelium protein extract against Cu toxicity and barrier impairment.

The promising results obtained with regards to the intestinal phenotype leave several questions to be answered in the future, namely: 1) How does ATP7B malfunction cause the encountered intestinal damages; is there in fact a problem of copper mislocalization? 2) Is cuproptosis happening in the enterocytes? and 3) What are the mechanisms behind the "leaky" barrier? To this end, ATP production will be determined in isolated mitochondria from both cells (Caco-2 cells WT and ATP7B KO) and animals (LPP *Atp7b*$^{+/-}$ vs LPP *Atp7b*$^{-/-}$), along with cellular fractionation to analyse the Cu content in whole cells/tissue, cytosol and mitochondria.

Lipidomic analysis of isolated mitochondria, as well as protein immunodetection and gene expression of key proteins linked to Cu metabolism (MT, GSH and CCO), lysosomal/vesicular transport and autophagy will be performed for both models. In the cellular model, the same analysis will be conducted in cells after Cu treatment, and Cu + Cu-chelators (DPA, TTM and MB), plus flow cytometry to evaluate lysosomal activity in these conditions. To follow up with the second and third questions, Caco-2 WT and ATP7B KO cells will be grown in high-glucose (25mM) and glucose-free/galactose media. Under these conditions, different substrates will be tested (octanoylcarnitine, glutamate and beta-hydroxybutyrate), to evaluate the cellular energetic dependency of the cells, independently of the TCA cycle. Target proteins in cuproptosis (mostly belonging to the pyruvate dehydrogenase complex) will be quantified via immunodetection, and a potential rescue effect with lipoamide will be studied. Caco-2 WT and ATP7B KO cells, in both media, will be differentiated in the Transwell® system to evaluate the potential effect of glucose depletion on the enterocyte-like barrier formation and further infer on the role of mitochondria in the process. Also in differentiated Caco-2 cells, more replicates of the treatments with the zinc-enriched protein extract obtained from the *P. ostreatus* mycelium will be performed, to infer on the results from the pilot study with regards to the putative protective effect against Cu toxicity. In parallel, non-enriched protein extract and zinc-salt treatments will be used as controls. Moreover, a model for *ex-vivo* digestion will be used to mimic the digestion of the zinc-enriched *P. ostreatus* mycelium in the presence of Cu, to evaluate the capacity of *P. ostreatus* to bind the metal in the GIT, even before absorption.

To further explore the potential of a zinc-enriched *P. ostreatus* mycelium diet, a longer feeding study, already approved by the Regierung von Oberbayern (Munich, Germany), will be conducted in LPP rats, with the correspondent controls. We expect to see beneficial effects of such diet approach, in particular: 1) a delay on the diseased onset, 2) a reduced copper uptake

in the upper intestine (duodenum) and, 3) an improvement of intestinal impairment. To this end, in addition to the analysis already presented in the pilot study, feaces samples will be collected to analyse the microbiota populations and *in vivo* intestinal permeability assays will be attempted. In the collected tissue samples, priority will be given to the evaluation of inflammation and barrier-tightness markers.

6. Bibliography

1. Bost, M. (2016). Dietary copper and human health: Current evidence and unresolved issues. *Journal of Trace Elements in Medicine and Biology*, 35:107-15.

2. Barceloux, DG. (1999). Copper. *Journal of Toxicology: Clinical Toxicology*, 37:217-30.

3. Blockhuys, S. (2017). Defining the human copper proteome and analysis of its expression variation in cancers. *Metallomics,* 9:112-123.

4. Tsang, T. (2021). Copper biology. *Current Biology*, 31:R421-r427.

5. Vonk, WI. (2008). Relevance of animal models for understanding mammalian copper homeostasis. T*he American Journal of Clinical Nutrition*, 88:840s-5s.

6. Maung, MT. (2021). The molecular and cellular basis of copper dysregulation and its relationship with human pathologies. *The FASEB Journal*, 35:e21810.

7. Chowdhury, R. (2018). Environmental toxic metal contaminants and risk of cardiovascular disease: systematic review and meta-analysis. *The BMJ*, 362:k3310

8. Antonucci, L. (2017). Non-Alcoholic Fatty Liver Disease and Nutritional Implications: Special Focus on Copper. *Nutrients*, 18;9(10):1137

9. Morrell, A. (2017). The role of insufficient copper in lipid synthesis and fatty-liver disease. *International Union of Biochemistry and Molecular Biology Life*, 69:263-270.

10. Aigner, E. (2010). A Role for Low Hepatic Copper Concentrations in Nonalcoholic Fatty Liver Disease. *The American Journal of Gastroenterology*, 105:1978-85.

11. Prohaska, JR. (1986). Genetic diseases of copper metabolism. *Clinical Physiology and Biochemistry*, 4:87-93.

12. Mark, S. (1999). Wilson's disease and Menkes disease. *American Journal of Physiology-Gastrointestinal and Liver Physiology*, 276:G311-G314.

13. Tümer, Z. (2010). Menkes disease. *European Journal of Human Genetics*, 18:511-518.

14. Cox, DW. (2002). Copper transporting P-type ATPases and human disease. *Journal of Bioenergetics and Biomembranes*, 34:333-8.

15. Bhattacharjee, A. (2017). Cellular copper homeostasis: current concepts on its interplay with glutathione homeostasis and its implication in physiology and human diseases. *Metallomics*, 9:1376-1388.

16. Krężel, A. (2017). The Functions of Metamorphic Metallothioneins in Zinc and Copper Metabolism. *International Journal of Molecular Sciences*, 18(6):1237.

17. Blades, B. (2021). Copper and lipid metabolism: A reciprocal relationship. *Biochimica et Biophysica Acta - General Subjects*, 1865 (11):129979.

18. Sutton, HC. (1989) On the participation of higher oxidation states of iron and copper in Fenton reactions. *Free Radical Biology and Medicine*, 6 (1):53-60.

19. Gaetke, LM. (2014). Copper: toxicological relevance and mechanisms. *Archives of Toxicology*, 88:1929-38.

20. Zischka, H. (2019). Chapter 6 - Cellular Copper Toxicity: A Critical Appraisal of Fenton-Chemistry-Based Oxidative Stress in Wilson Disease. In: Weiss, KH. (2019). Wilson Disease: Pathogenesis, Molecular Mechanisms, Diagnosis, Treatment and Monitoring. *Academic Press*, 65-81.

21. Barber, RG. (2021). Copper Toxicity Is Not Just Oxidative Damage: Zinc Systems and Insight from Wilson Disease. *Biomedicines*, 9(3):316.

22. Rae, TD. (1999). Undetectable intracellular free copper: the requirement of a copper chaperone for superoxide dismutase. *Science*, 284:805-8.

23. Tsvetkov, P. (2022). Copper induces cell death by targeting lipoylated TCA cycle proteins. *Science* 375 (6586):1254-1261.

24. Zimnicka, AM. (2007). Human copper transporter hCTR1 mediates basolateral uptake of copper into enterocytes: implications for copper homeostasis. *Journal of Biological Chemistry*, 282(36):26471-80.

25. van den Berghe, PV. (2009). New developments in the regulation of intestinal copper absorption. *Nutrition Reviews*, 67(11):658-72.

26. Moriya, M. (2008). Copper is taken up efficiently from albumin and alpha2-macroglobulin by cultured human cells by more than one mechanism. *American Journal of Physiology-Cell Physiology*, 295(3):C708-21.

27. Roberts, EA. (2008). Diagnosis and treatment of Wilson disease: an update. *Hepatology*, 47(6):2089-111.

28. Banci, L. (2010). Affinity gradients drive copper to cellular destinations. *Nature*, 465:645-648.

29. Członkowska, A. (2018). Wilson disease. *Nature Reviews Disease Primers*, 4(1):21.

30. Lutsenko, S. (2010). Human copper homeostasis: a network of interconnected pathways. *Current Opinion in Chemical Biology*, 14(2):211-7.

31. Roberts, EA. (2008). Diagnosis and treatment of Wilson disease: an update. *Hepatology*, 47(6):2089-111.

32. Turnlund, JR. (1998). Copper absorption, excretion, and retention by young men consuming low dietary copper determined by using the stable isotope 65Cu. *American Journal of Clinical Nutrition*, 67(6):1219-25.

33. Linder, MC. (1996). Copper biochemistry and molecular biology. *The American Journal of Clinical Nutrition*, 63(5):797S-811S.

34. Linder, MC. (2020). Copper Homeostasis in Mammals, with Emphasis on Secretion and Excretion. A Review. *International Journal of Molecular Sciences*, 21(14):4932.

35. European Association for Study of Liver (EASL). (2012). Clinical Practice Guidelines: Wilson's disease. *Journal of Hepatology*, 56(3):671-85.

36. Ferenci, P. (2004). Pathophysiology and Clinical Features of Wilson Disease. *Metabolic Brain Disease*, 19(3-4):229-239.

37. Ferenci, P. (2014). Phenotype-genotype correlations in patients with Wilson's disease. *Annals of the New York Academy Sciences*, 1315:1-5.

38. Gitlin, JD. (2003). Wilson disease. *Gastroenterology*,125(6):1868-77.

39. Stattermayer, AF. (2015). Hepatic steatosis in Wilson disease-Role of copper and PNPLA3 mutations. *Journal of Hepatology*, 63(1):156-63.

40. Wu, F. (2015). Wilson's disease: a comprehensive review of the molecular mechanisms. *International Journal of Molecular Sciences*, 16(3):6419-31.

41. Wilson, SAK. (1912). Progressive lenticular degeneration: a familial nervous disease associated with cirrhosis of the liver. *Brain*, 34:295-507.

42. Frydman, M. (1985). Assignment of the gene for Wilson disease to chromosome 13: linkage to the esterase D locus. *Proceedings of the National Academy of Sciences USA*, 82(6):1819-21.

43. Kerkar, N. (2018). Clinical and translational perspectives on WILSON DISEASE. *Academic Press*.

44. Schilsky, ML. (2015). Wilson disease: Epidemiology and pathogenesis. Available at: https://www.uptodate.com/contents/wilson-disease-epidemiology-and-pathogenesis

45. Liu, J. (2017). Epidemiology, diagnosis, and treatment of Wilson's disease. I*ntractable and Rare Disease Research*, 6(4):249-255.

46. Coffey, AJ. (2013). A genetic study of Wilson's disease in the United Kingdom. *Brain*, 136(Pt 5):1476-87.

47. García-Villarreal, L. (2001). High prevalence of the very rare wilson disease gene mutation Leu708Pro in the Island of Gran Canaria (Canary Islands, Spain): A genetic and clinical study. *Hepatology (Baltimore, Md.)*, 32(6):1329-36.

48. Artursson, P. (1990). Epithelial transport of drugs in cell culture. I: A model for studying the passive diffusion of drugs over intestinal absorptive (Caco-2) cells. *Journal of Pharmaceutical Sciences*, 79(6):476-82.

49. Lemieszek, MK. (2019). Branched mannans from the mushroom Cantharellus cibarius enhance the anticancer activity of natural killer cells against human cancers of lung and colon. *Food & Function*, 10:5816-5826.

50. Vancamelbeke, M. (2017). The intestinal barrier: a fundamental role in health and disease. *Expert Review of Gastroenterology and Hepatology*, 11(9):821-834.

51. Wu, TS. (2001). Cytotoxicity of Ganoderma lucidum triterpenes. *Journal of Natural Products* ,64(8):1121-2.

52. Dzieżyc-Jaworska, K. (2019). Clinical manifestations of Wilson disease in organs other than the liver and brain. *Annals of Translational Medicine*,7(Suppl2):S62.

53. Rosencrantz, R. (2011). Wilson disease: pathogenesis and clinical considerations in diagnosis and treatment. *Seminars in Liver Disease*, 31(3):245-59.

54. Zischka, H. (2018). Mitochondrial copper homeostasis and its derailment in Wilson disease. *The International Journal of Biochemistry and Cell Biology*, 102:71-75.

55. Tao, TY. (2003). Hepatic copper metabolism: insights from genetic disease. *Hepatology*, 37(6):1241-7.

56. Horn, D. (2008). Mitochondrial copper metabolism and delivery to cytochrome c oxidase. *International Union of Biochemistry and Molecular Biology Life*, 60(7):421-9.

57. Protasoni, M. (2021). Mitochondrial Structure and Bioenergetics in Normal and Disease Conditions. *International Journal of Molecular* Sciences, 22(2):586.

58. Ruiz, LM. (2021). Role of Copper on Mitochondrial Function and Metabolism. *Frontiers in Molecular Biosciences*, 8:711227.

59. Vest, KE. (2013). Copper import into the mitochondrial matrix in Saccharomyces cerevisiae is mediated by Pic2, a mitochondrial carrier family protein. *Journal of Biological Chemistry*, 288(33):23884-92.

60. Scheiber, IF. (2017). Pathogenesis of Wilson disease. *Handbook of Clinical Neurology*, 142:43-55.

61. Jason, LB. (2013) The Role of Copper as a Modifier of Lipid Metabolism. In: Valenzuela, R. (2013) Lipid Metabolism. *Rijeka: IntechOpen*, Chapter 3.

62. Caldwell, SH. (1999). Mitochondrial abnormalities in non-alcoholic steatohepatitis. *Journal of Hepatology*, 31(3):430-4.

63. Le, TH. (2004). The zonal distribution of megamitochondria with crystalline inclusions in nonalcoholic steatohepatitis. *Hepatology*, 39(5):1423-9.

64. Gerosa, C. (2019). Liver pathology in Wilson's disease: From copper overload to cirrhosis. *Journal of Inorganic Biochemistry*, 193:106-111.

65. Liggi, M. (2013). The relationship between copper and steatosis in Wilson's disease. *Clinics and Research in Hepatology and Gastroenterology*, 37(1):36-40.

66. Anstee, QM. (2019). From NASH to HCC: current concepts and future challenges. *Nature Reviews Gastroenterology and Hepatology*, 16(7):411-428.

67. Ahmed, S. (2005). A new strain of rat for functional analysis of PINA. *Molecular Brain Research*, 137:63-69.

68. Lichtmannegger, J. (2016). Methanobactin reverses acute liver failure in a rat model of Wilson disease. *Journal of Clinical Investigation*, 126(7):2721-35.

69. Zischka, H. (2011). Liver mitochondrial membrane crosslinking and destruction in a rat model of Wilson disease. *Journal of Clinical Investigation*, 121(4):1508-18.

70. Einer, C. (2019). A High-Calorie Diet Aggravates Mitochondrial Dysfunction and Triggers Severe Liver Damage in Wilson Disease Rats. *Cellular and Molecular Gastroenterology and Hepatology*, 7(3):571-596.

71. Huster, D. (2007). High copper selectively alters lipid metabolism and cell cycle machinery in the mouse model of Wilson disease. *Journal of Biological Chemistry*, 282(11):8343-55.

72. Muchenditsi, A. (2021). Systemic Deletion of Atp7b Modifies the Hepatocytes' Response to Copper Overload in the Mouse Models of Wilson Disease. *The FASEB Journal*, 11(1):5659

73. Muchenditsi, A. (2017). Targeted inactivation of copper transporter Atp7b in hepatocytes causes liver steatosis and obesity in mice. *American Journal of Physiology-Gastrointestinal and Liver Physiology*, 313(1):G39-g49.

74. Pierson, H. (2018). The Function of ATPase Copper Transporter ATP7B in Intestine. *Gastroenterology*, 154(1):168-180.e5.

75. Sauer, SW. (2011). Severe dysfunction of respiratory chain and cholesterol metabolism in Atp7b(-/-) mice as a model for Wilson disease. *Biochimica et Biophysica Acta*, 812(12):1607-15.

76. Porcu, C. (2018). Copper/MYC/CTR1 interplay: a dangerous relationship in hepatocellular carcinoma. *Oncotarget*, 9(10):9325-9343

77. Chen, C. (2021). Copper exposure association with prevalence of non-alcoholic fatty liver disease and insulin resistance among US adults (NHANES 2011–2014). *Ecotoxicology and Environmental Safety*, 218(9):112295.

78. Heffern, MC. (2016). In vivo bioluminescence imaging reveals copper deficiency in a murine model of nonalcoholic fatty liver disease. *Proceedings of the National Academy of Sciences of the United States of America*, 113(50):14219-14224.

79. Song, M. (2012). High fructose feeding induces copper deficiency in Sprague-Dawley rats: a novel mechanism for obesity related fatty liver. *Journal of* Hepatology, 56(2):433-40.

80. Tallino, S. (2015). Nutrigenomics analysis reveals that copper deficiency and dietary sucrose up-regulate inflammation, fibrosis and lipogenic pathways in a mature rat model of nonalcoholic fatty liver disease. *The Journal of Nutritional Biochemistry*, 26(10):996-1006.

81. Buzzetti, E. (2016). The multiple-hit pathogenesis of non-alcoholic fatty liver disease (NAFLD). *Metabolism*, 65(8):1038-48.

82. Borchard, S. (2018). The exceptional sensitivity of brain mitochondria to copper. *Toxicology In Vitro*, 51:11-22.

83. Tang, D. (2022). Cuproptosis: a copper-triggered modality of mitochondrial cell death. C*ell Research - Nature*, 32(5):417-418.

84. Di Ciaula, A. (2020). Liver Steatosis, Gut-Liver Axis, Microbiome and Environmental Factors. A Never-Ending Bidirectional Cross-Talk. *Journal of Clinical Medicine*, 9(8):2648.

85. Ohtani, N. (2020). Role of the Gut–Liver Axis in Liver Inflammation, Fibrosis, and Cancer: A Special Focus on the Gut Microbiota Relationship. *Hepatology Communications*, 3(4):456-470.

86. Lu, J. (2020). Gut Microbiota in Liver Disease: What Do We Know and What Do We Not Know? *Physiology*, 35(4):261-274.

87. Vancamelbeke, M. (2017). The intestinal barrier: a fundamental role in health and disease. *Expert Review of Gastroenterology and Hepatology*, 11(9):821-834.

88. König, J. (2016). Human intestinal barrier function in health and disease. *Clinical and Translational Gastroenterology*, 7(10):e196.

89. Groschwitz, KR. (2009). Intestinal barrier function: molecular regulation and disease pathogenesis. J*ournal of Allergy Clinical Immunology*, 124(1):3-20; quiz 21-2.

90. Sawada, N. (2013) Tight junction-related human diseases. *Pathology International*, 63(1):1-12.

91. Vermette, D. (2018). Tight junction structure, function, and assessment in the critically ill: a systematic review. *Intensive Care Medicine Experimental*, 6(1):37.

92. Zihni, C. (2016). Tight junctions: from simple barriers to multifunctional molecular gates. *Nature Reviews Molecular Cell Biology*, 17:564-580.

93. Günzel, D. (2017) Claudins: vital partners in transcellular and paracellular transport coupling. *Pfluegers Archiv - European Journal of Physiology*, 469(1):35-44.

94. Balda, MS. (2000). Multiple domains of occludin are involved in the regulation of paracellular permeability. *Journal of Cellular Biochemistry*, 78:85-96.

95. Weiss, KH. (2008). Localization of the Wilson disease protein in murine intestine. *Journal of Anatomy*, 213(3):232-40.

96. Okayasu, T. (1992). Inherited copper toxicity in Long-Evans cinnamon rats exhibiting spontaneous hepatitis: a model of Wilson's disease. *Pediatric Research - Nature*, 31(3):253-7.

97. Guttmann, S. (2020). ATP7B knockout disturbs copper and lipid metabolism in Caco-2 cells. *PLoS One*, 15(3):e0230025.

98. Przybyłkowski, A. (2013). Intestinal expression of metal transporters in Wilson's disease. *Biometals,* 26(6):925-934.

99. Ding, X. (2011). The significance of copper chelators in clinical and experimental application. *The Journal of Nutritional Biochemistry*, 22(4):301-310.

100. Roberts, EA. (2018) Update on the Diagnosis and Management of Wilson Disease. *Current Gastroenterology Reports*, 20(12):56.

101. Rodriguez-Castro, KI. (2015). Wilson's disease: A review of what we have learned. *World Journal of Hepatology*, 7(29):2859-70.

102. Merle, U. (2007). Clinical presentation, diagnosis and long-term outcome of Wilson's disease: a cohort study. *Gut*, 56(1):115-20.

103. Schilsky, ML. (2017) Wilson Disease: Diagnosis, Treatment, and Follow-up. *Clinical Liver Disease*, 21(4):755-767.

104. Borchard, S. (2022). Bis-choline tetrathiomolybdate prevents copper-induced blood-brain barrier damage. *Life Science Alliance*, 5(3):e202101164.

105. Stremmel, W. (2019) Bis-choline Tetrathiomolybdate as Old Drug in a New Design for Wilson's Disease: Good for Brain and Liver? *Hepatology*, 69(2):901-903.

106. Weiss, KH. (2017). Bis-choline tetrathiomolybdate in patients with Wilson's disease: an open-label, multicentre, phase 2 study. *The Lancet Gastroenterology &* Hepatology, 2(12):869-876.

107. Krentz, BD. (2010). A comparison of methanobactins from Methylosinus trichosporium OB3b and Methylocystis strain Sb2 predicts methanobactins are synthesized from diverse peptide precursors modified to create a common core for binding and reducing copper ions. *Biochemistry*, 49(47):10117-30.

108. Lichtmannegger, J. (2016). Methanobactin reverses acute liver failure in a rat model of Wilson disease. *The Journal of Clinical Investigation*, 126(7):2721-2735.

109. Brewer, GJ. (2001). Zinc acetate for the treatment of Wilson's disease. *Expert Opinion on Pharmacotherary*, 2(9):1473-7.

110. Brewer, GJ. (1993). Treatment of Wilson's Disease with Zinc XII: Dose Regimen Requirements. *The American Journal of the Medical* Sciences, 305(4):199-202.

111. Camarata, MA. (2019). Zinc Maintenance Therapy for Wilson Disease: A Comparison Between Zinc Acetate and Alternative Zinc Preparations. *Hepatology Communications*, 3(8):1151-1158.

112. Schilsky, ML. (2001). Treatment of Wilson's disease: What are the relative roles of penicillamine, trientine, and zinc supplementation?, *Current Gastroenterology Reports*, 3(1):54-59.

113. Sturniolo, GC. (1999). Zinc therapy increases duodenal concentrations of metallothionein and iron in Wilson's disease patients. *American Journal of Gastroenterology*, 94(2):334-8.

114. Brewer, GJ. (2005). Wilson's disease: clinical management and therapy. Journal of Hepatology, 42 Suppl(1):S13-21.

115. Hedera, P. (2019). Clinical management of Wilson disease. *Annals of Translational Medicine*, 7(Suppl2):S66.

116. Mohr, I. (2019). Current anti-copper therapies in management of Wilson disease. *Annals of Translational Medicine*, 7(Suppl2):S69.

117. Wiernicka, A. (2013). Gastrointestinal side effects in children with Wilson's disease treated with zinc sulphate. *World Journal of Gastroenterology*, 19(27):4356-62.

118. Lindequist, U. (2005). The pharmacological potential of mushrooms. *Evidence Based Complementary Alternative Medicine*, 2(3):285-99.

119. Pettigrew, J. (2011) Iconography in Bradshaw rock art: breaking the circularity. *Clinical and Experimental Optometry*, 94(5):403-17.

120. Weyrich, LS. (2017). Neanderthal behaviour, diet, and disease inferred from ancient DNA in dental calculus. *Nature*, 544(7650):357-361.

121. Carod-Artal, FJ. (2015). Hallucinogenic drugs in pre-Columbian Mesoamerican cultures. *Neurología* (English Edition), 30(1):42-49.

122. Winkelman, M. (2019) Introduction: Evidence for entheogen use in prehistory and world religions. *Journal of Psychedelic Studies*, 3(2):43-62.

123. Roncero-Ramos, I. (2017). The beneficial role of edible mushrooms in human health. *Current Opinion in Food Science*, 14:122-128

124. Chang, R. (1996). Functional properties of edible mushrooms. *Nutrition Reviews*, 54(11 Pt2):S91-3.

125. USDA (2018). Food data central: Mushrooms, Raw (Survey(FNDDS), 342623). Volume 2019, Available at: https://fdc.nal.usda.gov/fdc-app.html#/food-details/1103362/nutrientsamp

126. Friedman, M. (2016) Mushroom Polysaccharides: Chemistry and Antiobesity, Antidiabetes, Anticancer, and Antibiotic Properties in Cells, Rodents, and Humans. *Foods*, 5(4):80.

127. Martel, J. (2017). Anti-obesogenic and antidiabetic effects of plants and mushrooms. *Nature Reviews Endocrinology*, 13(3):149-160.

128. Ferreira, IC. (2009) Antioxidants in wild mushrooms. *Current Medicinal Chemistry*, 16(12):1543-60.

129. D De, D. (2012). Medicinal mushrooms in prevention and control of diabetes mellitus. *Fungal diversity*, 56(1):1-29

130. Wasser, SP. (2011) Current findings, future trends, and unsolved problems in studies of medicinal mushrooms. *Applied Microbiology and Biotechnology*, 89(5):1323-32.

131. Wu, HT. (2014). In vivo and in vitro anti-tumor effects of fungal extracts. *Molecules*, 19(2):2546-56.

132. Royse, DJ. (2017). Current overview of mushroom production in the world. In: Zied, D. (2017), Edible and medicinal mushrooms: technology and applications. *Wiley Online Library*, Chapter 2:5-13.

133. Shirur, M. (2021). Sustainable Production of Edible and Medicinal Mushrooms: Implications on Mushroom Consumption. In: Hebsale Mallappa, VK. (2021). Climate Change and Resilient Food Systems: Issues, Challenges, and Way Forward. *Singapore: Springer Singapore*, 315-346.

134. Fontes, A. (2019). Antioxidant Versus Pro-Apoptotic Effects of Mushroom-Enriched Diets on Mitochondria in Liver Disease. *International Journal of Molecular Sciences*, 20(16):3987.

135. Fontes, A. (2022). Mushrooms on the plate: Trends towards NAFLD treatment, health improvement and sustainable diets. *European Journal of Clinical Investigation*, 52(3):e13667.

136. Das, M. (2022). Modulation of obesity associated metabolic dysfunction by novel lipophilic fraction obtained from Agaricus bisporus. *Life Sciences*, 305:120779.

137. Gallego, P. (2021). White Button Mushroom Extracts Modulate Hepatic Fibrosis Progression, Inflammation, and Oxidative Stress In Vitro and in LDLR-/- Mice. *Foods*, 10(8):1788.

138. Tan, Y. (2022). Chemical profiles and health-promoting effects of porcini mushroom (Boletus edulis): A narrative review. Food Chemistry, 390:133199.

139. Lemieszek, MK. (2019). Cantharellus cibarius branched mannans inhibits colon cancer cells growth by interfering with signals transduction in NF-κB pathway. *International Journal of Biological Macromolecules*, 134:770-780.

140. Qu, Y. (2021). Structural analysis and macrophage activation of a novel β-glucan isolated from Cantharellus cibarius. *International Journal of Molecular Medicine*, 47(4):50.

141. Lee, HA. (2020). Ganoderma lucidum Extract Reduces Insulin Resistance by Enhancing AMPK Activation in High-Fat Diet-Induced Obese Mice. *Nutrientes*, 12(11):3338.

142. BO, A. (2020). Ganoderma Lucidum from Red Mushroom Attenuates Formaldehyde-Induced Liver Damage in Experimental Male Rat Model. *Biology*, 9(10):313.

143. Pan, H. (2019). Autophagic flux disruption contributes to Ganoderma lucidum polysaccharide-induced apoptosis in human colorectal cancer cells via MAPK/ERK activation. C*ell Death and Disease*, 10(6):456.

144. Seweryn, E. (2021). Health-Promoting of Polysaccharides Extracted from Ganoderma lucidum. *Nutrients,* 13(8):2725.

145. Kamiyama, T. (2022). Preventing Recurrence of Hepatocellular Carcinoma After Curative Hepatectomy With Active Hexose-correlated Compound Derived From Lentinula edodes Mycelia. *Integrative Cancer Therapies*, 21:15347354211073066.

146. López-Cauce, B. (2022). Lentinula edodes extract increases goblet cell number and Muc2 expression in an intestinal inflammatory model of Trichinella spiralis infection. *Biomedicine and Pharmacotherapy*, 150:112937.

147. Chen, HP. (2018). Anti-Proliferative and Anti-Inflammatory Lanostane Triterpenoids from the Polish Edible Mushroom Macrolepiota procera. *Journal of Agricultural and Food Chemistry*, 66(12):3146-3154.

148. Georgiev, YN. (2022). Structural Features and Immunomodulatory Effects of Water-Extractable Polysaccharides from Macrolepiota procera (Scop.) Singer. *Journal of Fungi*, 8(8):848.

149. Abdel-Monem, NM. (2020). Exopolysaccharide-peptide complex from oyster mushroom (Pleurotus ostreatus) protects against hepatotoxicity in rats. *Biochemistry and Biophysics Reports*, 24:100852.

150. Dong, Y. (2019). Characterization and anti-hyperlipidemia effects of enzymatic residue polysaccharides from Pleurotus ostreatus. *International Journal of Biological Macromolecules* 129:316-325.

151. Duan, Z. (2020). Structural characterization of phosphorylated Pleurotus ostreatus polysaccharide and its hepatoprotective effect on carbon tetrachloride-induced liver injury in mice. *International Journal of Biological Macromolecules*, 162:533-547.

152. Chiu, HF. (2017). Triterpenoids and polysaccharide peptides-enriched Ganoderma lucidum: a randomized, double-blind placebo-controlled crossover study of its antioxidation and hepatoprotective efficacy in healthy volunteers. *Pharmaceutical Biology*, 55(1):1041-1046.

153. Sasidharan, S. (2010). In vitro antioxidant activity and hepatoprotective effects of Lentinula edodes against paracetamol-induced hepatotoxicity. *Molecules*, 15(6):4478-89.

154. Jayakumar, T. (2006). Antioxidant activity of the oyster mushroom, Pleurotus ostreatus, on CCl4-induced liver injury in rats. *Food and Chemical Toxicology*, 44(12):1989-1996.

155. Zhang, Y. (2016). Antidiabetic effect of polysaccharides from Pleurotus ostreatus in streptozotocin-induced diabetic rats. *International Journal of Biological Macromolecules*, 83:126-32.

156. Xiao, Y. (2019). The effect of boletus polysaccharides on diabetic hepatopathy in rats. *Chemico-Biological Interactions*, 308:61-69.

157. Adamska, I. (2022). Possibilities of Using Macrolepiota procera in the Production of Prohealth Food and in Medicine. *International Journal of Food Science*, 2022:5773275.

158. Calvo, MS. (2016) A Retrospective Study in Adults with Metabolic Syndrome: Diabetic Risk Factor Response to Daily Consumption of Agaricus bisporus (White Button Mushrooms). *Plant Foods for Human Nutrition*, 71(3):245-51.

159. Jayasuriya, WJ. (2015). Hypoglycaemic activity of culinary Pleurotus ostreatus and P. cystidiosus mushrooms in healthy volunteers and type 2 diabetic patients on diet control and the possible mechanisms of action. *Phytotherapy Research*, 29(2):303-9.

160. Schneider, I. (2011). Lipid lowering effects of oyster mushroom (Pleurotus ostreatus) in humans. *Journal of Functional Foods*, 3(1):17-24.

161. Yu, S. (2016). Diets Containing Shiitake Mushroom Reduce Serum Lipids and Serum Lipophilic Antioxidant Capacity in Rats. *The Journal of Nutrition*, 146(12):2491-2496.

162. Chen, MH. (2014). Antidiabetic and Antihyperlipidemic Effects of Clitocybe nuda on Glucose Transporter 4 and AMP-Activated Protein Kinase Phosphorylation in High-Fat-Fed Mice. *Evidence Based Complementary Alternative Medicine*, 2014:981046.

163. Kanaya, N. (2011). Protective effects of white button mushroom (Agaricus bisporus) against hepatic steatosis in ovariectomized mice as a model of postmenopausal women. *PLoS One*, 6(10):e26654.

164. Hiraki, E. (2017). Anti-obesity activity of Yamabushitake (Hericium erinaceus) powder in ovariectomized mice, and its potentially active compounds. *Journal of Natural Medicines*, 71(3):482-491.

165. Gil-Ramírez, A. (2016). Modulation of cholesterol-related gene expression by ergosterol and ergosterol-enriched extracts obtained from Agaricus bisporus. *European Journal of Nutrition*, 55(3):1041-57.

166. Gil-Ramírez, A.(2016). Water-Soluble Compounds from Lentinula edodes Influencing the HMG-CoA Reductase Activity and the Expression of Genes Involved in the Cholesterol Metabolism. *Journal of Agricultural and Food Chemistry*, 64(9):1910-20.

167. Nakahara, D. (2020). Effect of mushroom polysaccharides from Pleurotus eryngii on obesity and gut microbiota in mice fed a high-fat diet. *European Journal of Nutrition*, 59(7):3231-3244.

168. Caz, V. (2015). Modulation of Cholesterol-Related Gene Expression by Dietary Fiber Fractions from Edible Mushrooms. *Journal of Agricultural and Food Chemistry,* 63(33):7371-80.

169. Kundakovic, T. (2013). Therapeutic properties of mushrooms in managing adverse effects in the metabolic syndrome. *Current Topics in Medicinal Chemistry*, 13(21):2734-44.

170. Li, M. (2021). Role of dietary edible mushrooms in the modulation of gut microbiota. *Journal of Functional* Foods, 83:104538.

171. Vamanu, E. (2021). Therapeutic Properties of Edible Mushrooms and Herbal Teas in Gut Microbiota Modulation. *Microorganisms*, 9(6):1262.

172. Hess, J. (2018). Impact of Agaricus bisporus Mushroom Consumption on Gut Health Markers in Healthy Adults. *Nutrients*, 10(10):1402.

173. Hess, J. (2017). Impact of Agaricus bisporus mushroom consumption on satiety and food intake. *Appetite*, 117:179-185.

174. Chang, CJ. (2018). Antrodia cinnamomea reduces obesity and modulates the gut microbiota in high-fat diet-fed mice. *International Journal of Obesisty - Nature*, 42(2):231-243.

175. Chang, CJ. (2015). Ganoderma lucidum reduces obesity in mice by modulating the composition of the gut microbiota. *Nature Communications*, 6:7489.

176. Chang, CJ. (2017). Corrigendum: Ganoderma lucidum reduces obesity in mice by modulating the composition of the gut microbiota. *Nature Communications*, 8:16130.

177. Liang, Z. (2018). Hypolipidemic, Antioxidant, and Antiapoptotic Effects of Polysaccharides Extracted from Reishi Mushroom, Ganoderma lucidum (Leysser: Fr) Karst, in Mice Fed a High-Fat Diet. *Journal of Medicinal Food*, 21(12):1218-1227.

178. Liang, Z. (2019). Ganoderma lucidum Polysaccharides Prevent Palmitic Acid-Evoked Apoptosis and Autophagy in Intestinal Porcine Epithelial Cell Line via Restoration of Mitochondrial Function and Regulation of MAPK and AMPK/Akt/mTOR Signaling Pathway. *International Journal of Molecular Sciences*, 20(3):478.

179. Alonso, J. (2003). The concentrations and bioconcentration factors of copper and zinc in edible mushrooms. *Archives of Environmental Contamination and Toxicology*, 44(2):180-8.

180. Chatterjee, S. (2017). Mushrooms: from nutrition to mycoremediation. *Environmental Science and Pollution Research (International)*, 24(24):19480-19493.

181. Svoboda, L. (2000). Concentrations of mercury, cadmium, lead and copper in fruiting bodies of edible mushrooms in an emission area of a copper smelter and a mercury smelter. *Science of The Total Environment,* 246(1):61-7.

182. Bellion, M. (2006). Extracellular and cellular mechanisms sustaining metal tolerance in ectomycorrhizal fungi. *FEMS Microbiology Letters*, 254(2):173-81.

183. Leonhardt, T. (2014). Metallothionein-like peptides involved in sequestration of Zn in the Zn-accumulating ectomycorrhizal fungus Russula atropurpurea. *Metallomics*, 6(9):1693-701.

184. Nowakowski, P. (2021). EVALUATION OF TOXIC ELEMENT CONTENT AND HEALTH RISK ASSESSMENT OF EDIBLE WILD MUSHROOMS. *Journal of Food Composition and Analysis*, 96:103698.

185. Orywal, K. (2021). Health risk assessment of exposure to toxic elements resulting from consumption of dried wild-grown mushrooms available for sale. *Plos one*, 16(6):e0252834.

186. Xu, N. (2017). Antioxidant and anti-hyperlipidemic effects of mycelia zinc polysaccharides by Pleurotus eryngii var. tuoliensis. *International Journal of Biological Macromolecules*, 95:204-214.

187. Zhang, J. (2015). The antioxidative effects of acidic-, alkalic-, and enzymatic-extractable mycelium zinc polysaccharides by Pleurotus djamor on liver and kidney of streptozocin-induced diabetic mice. *BMC Complementary and Alternative Medicine*, 15:440.

188. Zhang, J. (2015). Purification, Characterization and Hepatoprotective Activities of Mycelia Zinc Polysaccharides by Pleurotus djamor. *Carbohydrate Polymers*, 136:588-97.

189. Serafin Muñoz, AH. (2006). Se-enriched mycelia of Pleurotus ostreatus: distribution of selenium in cell walls and cell membranes/cytosol. *Journal of Agricultural and Food Chemistry*, 54(9):3440-4.

190. Milovanović, I. (2014). Potential of Pleurotus ostreatus Mycelium for Selenium Absorption. *The Scientific World Journal*, 2014:681834.

191. Almeida, SM. (2015). Iron bioaccumulation in mycelium of Pleurotus ostreatus. *Brazilian Journal of Microbiology*, 46(1):195-200.

192. Poursaeid, N. (2015). Improvement of zinc bioaccumulation and biomass yield in the mycelia and fruiting bodies of Pleurotus florida cultured on liquid media. *Applied Biochemistry and Biotechnology*, 175(7):3387-96.

193. Zheng, L. (2014). Antihyperlipidemic and hepatoprotective activities of mycelia zinc polysaccharide from Pholiota nameko SW-02. *International Journal of Biological Macromolecules*, 70:523-9.

194. Liu, Y. (2016). Structural characterization and antidiabetic activity of a glucopyranose-rich heteropolysaccharide from Catathelasma ventricosum. *Carbohydrates Polymers*, 149:399-407.

195. Liu, Y. (2015). Characterization of selenium-enriched mycelia of Catathelasma ventricosum and their antihyperglycemic and antioxidant properties. *Journal of Agricultural and Food Chemistry,* 63(2):562-8.

196. Liu, Y. (2013). Antidiabetic activity of mycelia selenium-polysaccharide from Catathelasma ventricosum in STZ-induced diabetic mice. *Food and Chemical Toxicology*, 62:285-91.

197. Conway, E. (2022). Sweeney T. Selenium-Enriched Mushroom Powder Enhances Intestinal Health and Growth Performance in the Absence of Zinc Oxide in Post-Weaned Pig Diets. *Animals (Basel)*, 12(12):1503

198. Khalili, M. (2015). Iron chelation and liver disease healing activity of edible mushroom (Cantharellus cibarius), in vitro and in vivo assays. *The Royal Society of Chemistry Advances*, 5(7):4804-4810.

199. Gómez-Lechón, MJ. (2007). A human hepatocellular in vitro model to investigate steatosis. *Chemico-Biological Interactions*, 165(2):106-16.

200. Yao, HR. (2011). Lipotoxicity in HepG2 cells triggered by free fatty acids. *American Journal of Translational Research*, 3(3):284-91.

201. Fogh, J. (1977). Absence of HeLa cell contamination in 169 cell lines derived from human tumors. *Journal of the National Cancer Institute*, 58:209-14.

202. Hidalgo, IJ. (1989). Characterization of the human colon carcinoma cell line (Caco-2) as a model system for intestinal epithelial permeability. *Gastroenterology*, 96(3):736-49.

203. Lea, T. (2015) Caco-2 Cell Line. In: Verhoeckx, K. (2015). The Impact of Food Bioactives on Health: in vitro and ex vivo models. *Springer International Publishing*, Chapter 10:103-111.

204. Angelis, ID. (2011). Caco-2 cells as a model for intestinal absorption. *Current Protocols in Toxicology*, Chapter 20:Unit20.6.

205. Nauli, AM. (2015). Using Caco-2 Cells to Study Lipid Transport by the Intestine. *Journal of Visualized Experiments*, (102):e53086.

206. nanoAnalytics GmbH. (2019). Technical Note cellZscope, cellZscope® - How it Works. Available at: https://scitech.com.au/uploads/pdf/nanotechnology/TN_cZs_How_It_Works.pdf.

207. Golowasch, J. (2009). Membrane capacitance measurements revisited: dependence of capacitance value on measurement method in nonisopotential neurons. *Journal of Neurophysiology*, 102(4):2161-75.

208. Hoppe-Tichy, T. (2005). Kupferhistidin-Lösung zur Behandlung von Menkes' Kinky Hair Syndrom: Herstellung und Stabilität. *Die Pharmazie - An International Journal of Pharmaceutical Sciences: Avoxa - Mediengruppe Deutscher Apotheker GmbH*, 60(3):205-207.

209. O'Brien, J. (2000). Investigation of the Alamar Blue (resazurin) fluorescent dye for the assessment of mammalian cell cytotoxicity. *European Journal of Biochemistry*, 267(17):5421-6.

210. Silva, FSG. (2016). Determination of Metabolic Viability and Cell Mass Using a Tandem Resazurin/Sulforhodamine B Assay. *Current Protocols in Toxicology*, 68:2.24.1-2.24.15.

211. Crouch, SP. (1993). The use of ATP bioluminescence as a measure of cell proliferation and cytotoxicity. *Journal of Immunological Methods*, 160(1):81-8.

212. Papazisis, KT. (1997). Optimization of the sulforhodamine B colorimetric assay. *Journal of Immunological Methods*, 208(2):151-8.

213. Vichai, V. (2006). Sulforhodamine B colorimetric assay for cytotoxicity screening. *Nature Protocols*, 1(3):1112-1116.

214. Greenspan, P. (1985). Nile red: a selective fluorescent stain for intracellular lipid droplets. *Journal of Cell Biology*, 100(3):965-73.

215. McMillian, MK. (2001). Nile Red binding to HepG2 cells: an improved assay for in vitro studies of hepatosteatosis. *In Vitro and Molecular* Toxicology, 14(3):177-90.

216. Kim, JS. (2011). Comparison of the automated fluorescence microscopic viability test with the conventional and flow cytometry methods. *Journal of Clinical Laboratory Analysis*, 25(2):90-4.

217. Kim, SI. (2016). Application of a non-hazardous vital dye for cell counting with automated cell counters. *Analytical Biochemistry*, 492:8-12.

218. Repetto, G. (2008). Neutral red uptake assay for the estimation of cell viability/cytotoxicity. *Nature Protocols*, 3(7):1125-31.

219. Bradford, MM. (1976). A rapid and sensitive method for the quantitation of microgram quantities of protein utilizing the principle of protein-dye binding. *Analytical Biochemistry*, 72:248-54.

220. Otero-Romaní, J. (2009). Inductively coupled plasma-optical emission spectrometry/mass spectrometry for the determination of Cu, Ni, Pb and Zn in seawater after ionic imprinted polymer based solid phase extraction. *Talanta*, 79(3):723-9.

221. Schmitt, S. (2015). Isolation of mitochondria from cultured cells and liver tissue biopsies for molecular and biochemical analyses. *Methods in Molecular Biology*, 1295:87-97.

222. Schmitt, S. (2013). A semi-automated method for isolating functionally intact mitochondria from cultured cells and tissue biopsies. *Analytical Biochemistry*, 443:66-74.

223. Bialkowska, AB. (2016). Improved Swiss-rolling Technique for Intestinal Tissue Preparation for Immunohistochemical and Immunofluorescent Analyses. *Journal of Visualized Experiments*, (113):54161.

224. Schulz, S. (2015). A protocol for the parallel isolation of intact mitochondria from rat liver, kidney, heart, and brain. *Methods in Molecular Biology*, 1295:75-86.

225. Meul, T. (2020). Mitochondrial Regulation of the 26S Proteasome. *Cell Reports*, 32(8):108059.

226. Navarro, P. (2014). General statistical framework for quantitative proteomics by stable isotope labeling. *Journal of Proteome Research*, 13(3):1234-47.

227. Lam, J. (2021). A Universal Approach to Analyzing Transmission Electron Microscopy with ImageJ. *Cells*, 10(9):2177.

228. Winey, M. (2014). Conventional transmission electron microscopy. *Molecular Biology of the Cell*, 25(3):319-23.

229. Gnaiger, E. (2020) Mitochondrial pathways and respiratory control: An Introduction to OXPHOS Analysis. 5th edition, *Bioenergetics Communications*.

230. Pesta, D. (2012). High-resolution respirometry: OXPHOS protocols for human cells and permeabilized fibers from small biopsies of human muscle. *Methods in Molecular Biology*, 810:25-58.

231. Sanderson, MJ. (2014). Fluorescence microscopy. *Cold Spring Harbor Protocols* 2014(10):pdb.top071795.

232. Dunst, S. (2019). Imaging Flies by Fluorescence Microscopy: Principles, Technologies, and Applications. *Genetics*, 211(1):15-34.

233. Bailey, CA. (1996). The use of the intestinal epithelial cell culture model, Caco-2, in pharmaceutical development. *Advanced Drug Delivery Reviews*, 22(1-2):85-103.

234. Camenisch, G. (1998). Estimation of permeability by passive diffusion through Caco-2 cell monolayers using the drugs' lipophilicity and molecular weight. *European Journal of Pharmaceutical Sciences*, 6(4):317-24.

235. Hubatsch, I. (2007). Determination of drug permeability and prediction of drug absorption in Caco-2 monolayers. *Nature Protocols*, 2(9):2111-2119.

236. Konishi, Y. (2002). Transepithelial transport of fluorescein in Caco-2 cell monolayers and use of such transport in in vitro evaluation of phenolic acid availability. *Bioscience, Biotechnology and Biochemistry*, 66(11):2449-57.

237. Crowther, JR. (1995) ELISA. Theory and practice. *Methods in Molecular Biology*, 42:1-218.

238. Sonnier, DI. (2010). TNF-α induces vectorial secretion of IL-8 in Caco-2 cells. *Journal of Gastrointestinal Surgery*, 14(10):1592-9.

239. Burnette, WN. (1981) "Western blotting": electrophoretic transfer of proteins from sodium dodecyl sulfate--polyacrylamide gels to unmodified nitrocellulose and radiographic detection with antibody and radioiodinated protein A. *Analytical Biochemistry*, 112(2):195-203.

240. Renart, J. (1979). Transfer of proteins from gels to diazobenzyloxymethyl-paper and detection with antisera: a method for studying antibody specificity and antigen structure. *Proceedings of the National Academy of Sciences*, 76(7):3116-20.

241. Towbin, H. (1979). Electrophoretic transfer of proteins from polyacrylamide gels to nitrocellulose sheets: procedure and some applications. *Proceedings of the National Academy of Sciences*, 76(9):4350-4.

242. Guo, D. (2005). Physical interaction and functional coupling between ACDP4 and the intracellular ion chaperone COX11, an implication of the role of ACDP4 in essential metal ion transport and homeostasis. *Molecular Pain*, 1:15.

243. Zischka, H. (2014). Pathological mitochondrial copper overload in livers of Wilson's disease patients and related animal models. *Annals of the New York Academy of Sciences,* 1315:6-15.

244. Sternlieb, I. (1968). Mitochondrial and fatty changes in hepatocytes of patients with Wilson's disease. *Gastroenterology*, 55(3):354-367.

245. JanssenDuijghuijsen, LM. (2017). Mitochondrial ATP Depletion Disrupts Caco-2 Monolayer Integrity and Internalizes Claudin 7. *Frontiers in Physiology*, 8:794.

246. Berger, E. (2016). Mitochondrial function controls intestinal epithelial stemness and proliferation. *Nature Communications*, 7:13171.

247. Borchard, S. (2022). Bis-choline tetrathiomolybdate prevents copper-induced blood-brain barrier damage. *Life Science Alliance*, 5(3):e202101164.

248. Linz, G. (2020). Cell barrier characterization in transwell inserts by electrical impedance spectroscopy. *Biosensors and Bioelectronics*, 165:112345.

249. Zeissig, S. (2007). Changes in expression and distribution of claudin 2, 5 and 8 lead to discontinuous tight junctions and barrier dysfunction in active Crohn's disease. *Gut*, 56(1):61-72.

250. Garcia-Hernandez, V. (2017). Intestinal epithelial claudins: expression and regulation in homeostasis and inflammation. *Annals of the New York Academy of Sciences*, 1397(1):66-79.

251. DiSpirito, AA. (2016). Methanobactin and the Link between Copper and Bacterial Methane Oxidation. *Microbiology and Molecular Biology Reviews*, 80(2):387 - 409.

252. Soares, AA. (2013). Hepatoprotective effects of mushrooms. *Molecules*, 18(7):7609-7630.

253. Lindequist, U. (2005). The pharmacological potential of mushrooms. *Evidence-Based Complementary and Alternative Medicine*, 2(3):285-99.

254. Beattie, KD. (2011). Ethanolic and aqueous extracts derived from Australian fungi inhibit cancer cell growth in vitro. *Mycologia*, 103(3):458-65.

255. Alonso, J. (2003). The concentrations and bioconcentration factors of copper and zinc in edible mushrooms. *Archives of Environmental Contamination and Toxicology*, 44(2):180-8.

256. Kapahi, M. (2017). Mycoremediation potential of Pleurotus species for heavy metals: a review. *Bioresoures and Bioprocessing*, 4(1):32.

257. Širić, I. (2016). Heavy metal bioaccumulation by wild edible saprophytic and ectomycorrhizal mushrooms. *Environmental Science and Pollution Research International*, 23(18):18239-52.

258. Dementyev, DV. (2015). Biosorption of (241)Am from aqueous solutions and its biochemical fractionation in Pleurotus ostreatus mycelium. *Doklady Biochemistry and Biophysics*, 460:34-6.

259. Muñoz, AH. (2005). Subcellular distribution of aluminum, bismuth, cadmium, chromium, copper, iron, manganese, nickel, and lead in cultivated mushrooms (Agaricus bisporus and Pleurotus ostreatus). *Biological Trace Element Research*, 106(3):265-77.

260. Vamanu, E. (2012). Biological activities of the polysaccharides produced in submerged culture of two edible Pleurotus ostreatus mushrooms. *Journal of Biomedicine and Biotechnology*, 2012:565974

261. Ferruzza, S. (2000). Copper uptake and intracellular distribution in the human intestinal Caco-2 cell line. *Biometals*, 13(2):179-85.

262. Ferruzza, S. (1999). Copper treatment alters the permeability of tight junctions in cultured human intestinal Caco-2 cells. *American Journal of Physiology*, 277(6):G1138-48.

263. Shao, Y. (2017). Zinc enhances intestinal epithelial barrier function through the PI3K/AKT/mTOR signaling pathway in Caco-2 cells. *Journal of Nutritional Biochemistry*, 43:18-26.

264. Avan, A. (2022). The Role of Zinc in the Treatment of Wilson's Disease. *International Journal of Molecular Sciences*, 23(16):9316.

265. Ranucci, G. (2014). Zinc monotherapy is effective in Wilson's disease patients with mild liver disease diagnosed in childhood: a retrospective study. *Orphanet Journal of Rare Diseases*, 9:41.

266. Terada, K. (1999). The Long-Evans Cinnamon rat: an animal model for Wilson's disease. *Pediatrics International*, 41(4):414-8.

267. Kim, YS. (2010). Intestinal goblet cells and mucins in health and disease: recent insights and progress. *Current Gastroenterology Reports,* 12(5):319-30.

268. Pelaseyed, T. (2014). The mucus and mucins of the goblet cells and enterocytes provide the first defense line of the gastrointestinal tract and interact with the immune system. *Immunological Reviews*, 260(1):8-20.

269. Geng, H. (2018). Association study of gut flora in Wilson's disease through high-throughput sequencing. *Medicine (Baltimore)*, 97(31):e11743.

270. Cai, X. (2020). Altered diversity and composition of gut microbiota in Wilson's disease. *Scientific Reports*, 10(1):21825.

271. Zhang, CC. (2018). Metallothionein is elevated in liver and duodenum of Atp7b(−/−) mice. *Biometals*, 31(4):617-625.

272. Bartee, MY. (2007). Hepatic copper-transporting ATPase ATP7B: function and inactivation at the molecular and cellular level. *Biometals*, 20(3-4):627-37.

273. Medici, V. (2005). Efficacy of zinc supplementation in preventing acute hepatitis in Long-Evans Cinnamon rats. *Liver International*, 25(4):888-95.

274. Hasan, NM. (2012). Regulation of copper transporters in human cells. *Current Topics in Membranes*, 69:137-61.

275. Przybyłkowski, A. (2013). Intestinal expression of metal transporters in Wilson's disease. *Biometals*, 26(6):925-34.

276. Gu, M. (2000). Oxidative-phosphorylation defects in liver of patients with Wilson's disease. *Lancet*, 356(9228):469-74.

277. Hamilton, JP. (2016). Activation of liver X receptor/retinoid X receptor pathway ameliorates liver disease in Atp7B(-/-) (Wilson disease) mice. *Hepatology*, 63(6):1828-41.

278. Miele, L. (2009). Increased intestinal permeability and tight junction alterations in nonalcoholic fatty liver disease. *Hepatology*, 49(6):1877-87.

279. Luther, J. (2015). Hepatic Injury in Nonalcoholic Steatohepatitis Contributes to Altered Intestinal Permeability. *Cellular and Molecular Gastroenterology and Hepatology*, 1(2):222-232.

280. Natoli, M. (2012). Good Caco-2 cell culture practices. *Toxicology In Vitro*, 26(8):1243-6.

281. Chandhok, G. (2014). The effect of zinc and D-penicillamine in a stable human hepatoma ATP7B knockout cell line. *PLoS One*, 9(3):e98809.

282. Polishchuk, EV. (2016). The emerging role of lysosomes in copper homeostasis. *Metallomics*, 8(9):853-62.

283. Polishchuk, EV. (2014). Wilson disease protein ATP7B utilizes lysosomal exocytosis to maintain copper homeostasis. *Developmental Cell*, 29(6):686-700.

284. Pantoom, S. (2021). Direct Interaction of ATP7B and LC3B Proteins Suggests a Cooperative Role of Copper Transportation and Autophagy. *Cell*s, 10(11):3118.

285. Schroeder, SM. (2021). Wilson disease and the differential diagnosis of its hepatic manifestations: a narrative review of clinical, laboratory, and liver histological features. *Annals of Translational Medicine*, 9(17):1394.

286. Gottlieb, A. (2022). Hepatic Steatosis in the Mouse Model of Wilson Disease Coincides with a Muted Inflammatory Response. *The American Journal of Pathology*, 192(1):146-159.

287. Reed, E. (2018). Animal models of Wilson disease. *Journal of Neurochemistry*, 146(4):356-373.

288. Mazi, TA. (2020). Lipid and energy metabolism in Wilson disease. *Liver Research*, 4(1):5-14.

289. Mu, H. (2004). The digestion of dietary triacylglycerols. *Progress in Lipid Research*, 43(2):105-33.

290. Mandato, C. (2021). The gut-liver axis as a target of liver disease management. *Hepatobiliary Surgery and Nutrition*, 10(1):100-102.

291. Stuerenburg, HJ. (2000) CSF copper concentrations, blood-brain barrier function, and coeruloplasmin synthesis during the treatment of Wilson's disease. *Journal of Neural Transmission (Vienna)*, 107(3):321-9.

292. Zerounian, NR. (2003). Regulation of copper absorption by copper availability in the Caco-2 cell intestinal model. *American Journal of Physiology-Gastrointestinal and Liver Physiology*, 284(5):G739-47.

293. Ferruzza, S. (2002). Iron and copper alter tight junction permeability in human intestinal Caco-2 cells by distinct mechanisms. *Toxicology In Vitro*, 16(4):399-404.

294. Ude, VC. (2017). Impact of copper oxide nanomaterials on differentiated and undifferentiated Caco-2 intestinal epithelial cells; assessment of cytotoxicity, barrier integrity, cytokine production and nanomaterial penetration. *Particle and Fibre Toxicology*, 14(1):31.

295. O'Doherty, C. (2020). Characterisation and proteomic profiling of continuously exposed Cu-resistant variants of the Caco-2 cell line. *Toxicology In Vitro*, 65:104773.

295. O'Doherty, C. (2020). Gene expression profiling of copper-resistant Caco-2 clones. *Metallomics*, 12(10):1521-1529.

297. Groba, SR. (2016). Establishment of Copper Resistance in an ATP7B Knockout Cell Line. *Zeitschrift für Gastroenterologie*, 54(12):1343-1404.

298. Jenkins, KJ. (1989). Influence of excess dietary copper on lipid composition of calf tissues. *Journal of Dairy Science*, 72(10):2582-91.

299. Schlame, M. (2009). The role of cardiolipin in the structural organization of mitochondrial membranes. *Biochimica et Biophysica Acta (BBA)-Biomembranes*, 1788(10):2080-2083.

300. Schilsky, ML. (2015). Costly choices for treating Wilson's disease. *Hepatology*, 61(4):1106-1108.

301. Liu, YW. (2009). Evaluation of antiproliferative activities and action mechanisms of extracts from two species of Ganoderma on tumor cell lines. *Journal of Agricultural and Food Chemistry*, 57(8):3087-93.

302. Lin, SB. (2003). Triterpene-enriched extracts from Ganoderma lucidum inhibit growth of hepatoma cells via suppressing protein kinase C, activating mitogen-activated protein kinases and G2-phase cell cycle arrest. *Life Sciences*, 72(21):2381-90.

303. Yu, Y. (2017). Ganoderma lucidum polysaccharide enhances radiosensitivity of hepatocellular carcinoma cell line HepG2 through Akt signaling pathway. *Experimental and Therapeutic Medicine*, 14(6):5903-5907.

304. Kolundzic, M. (2017). Cytotoxic and Antimicrobial Activities of Cantharellus cibarius Fr. (Cantarellaceae). *Journal of Medicinal Food*, 20(8):790-796.

305. Einer, C. (2017). Data on chow, liver tissue and mitochondrial fatty acid compositions as well as mitochondrial proteome changes after feeding mice a western diet for 6-24 weeks. *Data in Brief,* 15:163-169.

306. Amorim, R. (2021). Exploratory Data Analysis of Cell and Mitochondrial High-Fat, High-Sugar Toxicity on Human HepG2 Cells. *Nutrients*, 13(5):1723.

307. Huang, Y. (2022). In Vitro Hepatoprotective and Human Gut Microbiota Modulation of Polysaccharide-Peptides in Pleurotus citrinopileatus. *Frontiers in Cellular and Infection Microbiology*, 12:892049.

308. Sheng, Y. (2019). Anti-obesity and hypolipidemic effect of water extract from Pleurotus citrinopileatus in C57BL/6J mice. *Food Science and Nutrition*, 7(4):1295-1301.

309. Xiong, M. (2018). Antidiabetic Activity of Ergosterol from Pleurotus Ostreatus in KK-A(y) Mice with Spontaneous Type 2 Diabetes Mellitus. *Molecular Nutrition and Food Research*, 62(3).

310. Fontes Vieira, PA. (2013). Antioxidant activities, total phenolics and metal contents in Pleurotus ostreatus mushrooms enriched with iron, zinc or lithium. *LWT - Food Science and Technology*, 54(2):421-425.

311. Ogbomida, ET. (2018). Bioactive profiling and therapeutic potential of mushroom (Pleurotus tuberregium) extract on Wistar albino rats (Ratus norvegicus) exposed to arsenic and chromium toxicity. *Toxicology Reports*, 5:401-410.

312. Leonhardt, T. (2014). Metallothionein-like peptides involved in sequestration of Zn in the Zn-accumulating ectomycorrhizal fungus Russula atropurpurea. *Metallomics*, 6(9):1693-701.

313. Serafin Muñoz, AH. (2006). Se-Enriched Mycelia of Pleurotus ostreatus: Distribution of Selenium in Cell Walls and Cell Membranes/Cytosol. *Journal of Agricultural and Food Chemistry*, 54(9):3440-3444.

314. Milovanović, I. (2014). Potential of Pleurotus ostreatus mycelium for selenium absorption. *The Scientific World Journal*, 2014:681834.

315. Gąsecka, M. (2016). Phenolic composition and antioxidant properties of Pleurotus ostreatus and Pleurotus eryngii enriched with selenium and zinc. *European Food Research and Technology*, 242:723-732.

316. Yan, H. (2012). Antioxidant and Antitumor Activities of Selenium- and Zinc-Enriched Oyster Mushroom in Mice. *Biological Trace Element Research*, 150(1-3):236-241.

317. Włodarczyk, A. (2020). Pleurotus spp. Mycelia Enriched in Magnesium and Zinc Salts as a Potential Functional Food. *Molecules*, 26(1):162.

318. Cardoso, RVC. (2017). Development of nutraceutical formulations based on the mycelium of Pleurotus ostreatus and Agaricus bisporus. *Food & Function*, 8(6):2155-2164.

319. Iftikhar, M. (2020). Transport, metabolism and remedial potential of functional food extracts (FFEs) in Caco-2 cells monolayer: A review. *Food Research International*, 136:109240.

320. Boulaka, A. (2020). Genoprotective Properties and Metabolites of β-Glucan-Rich Edible Mushrooms Following Their In Vitro Fermentation by Human Faecal Microbiota. *Molecules*, 25(15):3554.

321. Saxami, G. (2021). Fermentation Supernatants of Pleurotus eryngii Mushroom Ameliorate Intestinal Epithelial Barrier Dysfunction in Lipopolysaccharide-Induced Caco-2 Cells via Upregulation of Tight Junctions. *Microorganisms*, 9(10):2071.

322. Cao, XY. (2015). Antitumor activity of polysaccharide extracted from Pleurotus ostreatus mycelia against gastric cancer in vitro and in vivo. *Molecular Medicine Reports*, 12(2):2383-9.

323. Facchini, JM. (2014). Antitumor activity of Pleurotus ostreatus polysaccharide fractions on Ehrlich tumor and Sarcoma 180. *International Journal of Biological Macromolecules*, 68:72-77.

324. Mishra, V. (2021). Promising anticancer activity of polysaccharides and other macromolecules derived from oyster mushroom (Pleurotus sp.): An updated review. *International Journal of Biological Macromolecules*, 182:1628-1637.

325. Yang, X. (2022). Lentinan Supplementation Protects the Gut-Liver Axis and Prevents Steatohepatitis: The Role of Gut Microbiota Involved. *Frontiers in Nutrition*, 8:803691-803691.

326. Gonzalez, BP. (2005). Zinc supplementation decreases hepatic copper accumulation in LEC rat: a model of Wilson's disease. *Biological Trace Element Research*, 105(1-3):117-34.

327. Medici, V. (2002). Metallothionein and antioxidant enzymes in Long-Evans Cinnamon rats treated with zinc. *Archives of Toxicology*, 76(6):509-16.

328. Santon, A. (2002). Interactions between Zn and Cu in LEC rats, an animal model of Wilson's disease. *Histochemistry and Cell Biology*, 117(3):275-81.

329. Santon, A. (2003). Effect and possible role of Zn treatment in LEC rats, an animal model of Wilson's disease. *Biochimica et Biophysica Acta*, 1637(1):91-7.

330. Santon, A. (2003). Metallothionein-1 and metallothionein-2 gene expression and localisation of apoptotic cells in Zn-treated LEC rat liver. *Histochemistry and Cell Biology*, 119(4):301-8.

331. Xu, N. (2017). Hepatoprotection of enzymatic-extractable mycelia zinc polysaccharides by Pleurotus eryngii var. tuoliensis. *Carbohydrate Polymers*, 157:196-206.

332. Zhang, J. (2016). Purification, characterization and hepatoprotective activities of mycelia zinc polysaccharides by Pleurotus djamor. *Carbohydrate Polymer*s, 136:588-97.

7. Annexes

7.1 Supplementary tables

Table S 1. **Atp7b knockout induces changes in the abundance of proteins directly linked to intestinal homeostasis in WD rats**

Gene Symbol	Description	Abundance ratio (*Atp7b* $^{-/-}$/ *Atp7b* WT)	Abundance ratio (*Atp7b* $^{-/-}$ diseased / *Atp7b* WT)	Cellular localization
Energy metabolism				
G6pc3	Glucose-6-phosphatase 3	0,28**	0,66	ER
Hk1	Hexokinase-1	1,75*	1,21	Cytoplasm, Mitochondrion
Pea15	Astrocytic phosphoprotein PEA-15	0,63	0,36****	Cytoplasm
Stxbp5	Syntaxin-binding protein 5	0,37*	0,84	Cell junction, Cell membrane, Cytoplasm
Pklr	Pyruvate kinase PKLR	0,51*	0,53***	Cell membrane, Cytosol
Myo1c	Unconventional myosin-Ic	1,77*	1,36	Cell membrane, Cytoplasm
Aqp3	Aquaporin-3	0,38*	0,73	Basolateral cell membrane
Aqp7	Aquaporin-7	0,25**	0,52*	Cell membrane, Cytoplasm, Cytoplasmic vesicle, Lipid droplet
Calm3	Calmodulin-3	0,56*	0,97	Cytoskeleton
Digestion and absorption				
Cel	Bile salt-activated lipase	4,40****	2,74****	Secreted
Pnlip	Pancreatic triacylglycerol lipase	3,63****	2,66****	Secreted
Amy2	Pancreatic alpha-amylase	4,62****	1,67**	Secreted
Pnliprp1	Inactive pancreatic lipase-related protein 1	3,21****	1,84***	Secreted

Pnliprp2	Pancreatic lipase-related protein 2	2,92***	2,06****	Secreted
Alpi	Intestinal-type alkaline phosphatase 1	0,57*	1,02	Cell membrane
Cpa2	Carboxypeptidase A2	4,06****	2,58****	Secreted
Cpa1	Carboxypeptidase A1	4,02****	2,58****	Secreted
Cpb1	Carboxypeptidase B	4,26****	2,74****	Secreted
Cpa3	Mast cell carboxypeptidase A (Fragment)	2,50**	1,33	Secreted
Lct	Lactase-phlorizin hydrolase	0,26****	0,53***	Apical cell membrane
Anpep	Aminopeptidase N	0,32***	0,68*	Cell membrane
Si	Sucrase-isomaltase	0,43**	0,67*	Apical cell membrane
Try3	Cationic trypsin-3	6,76****	3,16****	Secreted
Dgat1	Diacylglycerol O-acyltransferase 1	0,32***	0,80	ER
Asah2	Neutral ceramidase	0,26****	0,52***	Cell membrane, Golgi apparatus, Mitochondrion, Secreted
Slc16a10	Monocarboxylate transporter 10	0,43	0,64	Basolateral cell membrane
Slc15a1	Solute carrier family 15 member 1	0,45*	0,91	Cell membrane
Slc7a8	Large neutral amino acids transporter small subunit 2	0,50	0,92	Basolateral cell membrane
Slc6a19	Sodium-dependent neutral amino acid transporter B(0)AT1	0,47*	1,06	Apical cell membrane
Slc9a3	Sodium/hydrogen exchanger 3	0,31**	0,53**	Apical cell membrane
Slc9a3r1	Na(+)/H(+) exchange regulatory cofactor NHE-RF1	0,30****	0,51****	Apical cell membrane

Slc39a4	Zinc transporter ZIP4	0,59	0,67	Cell membrane
Slc12a1	Solute carrier family 12 member 1	0,57	0,44***	Apical cell membrane
Slc2a5	Solute carrier family 2, facilitated glucose transporter member 5	0,41*	0,65	Apical cell membrane
Slc52a3	Solute carrier family 52, riboflavin transporter, member 3	0,36*	0,67	Cell membrane
Slc26a3	Chloride anion exchanger	1,41	2,12****	Apical cell membrane
Slc9a3r2	Na(+)/H(+) exchange regulatory cofactor NHE-RF2	2,06*	1,06	Apical cell membrane
Slc4a1	Band 3 anion transport protein	2,02*	1,16	Basolateral cell membrane
Chp2	Calcineurin B homologous protein 2	0,22****	0,47***	Cell membrane, Cytoplasm, Nucleus
Clic5	Chloride intracellular channel protein 5	0,48*	0,79	Apical cell membrane, Golgi apparatus, Cytoplasm, Cytoskeleton
Metabolism				
Fabp2	Fatty acid-binding protein	0,55*	0,76	Cytoplasm
Sh3bp1	SH3 domain-binding protein 1	0,34**	0,61*	Cell junction, Cell projection, Cytoplasm, Nucleus, Tight junction
Sh3bp5	SH3 domain-binding protein 5	1,91*	1,43*	Cytoplasmic vesicle, Cell membrane, Mitochondrion
Duox2	Dual oxidase 2	2,49*	2,46**	Cell junction, Apical cell membrane
Podxl	Podocalyxin	0,38*	0,58*	Apical cell membrane
Abcg2	Broad substrate specificity ATP-binding cassette transporter ABCG2	0,45*	0,86	Apical cell membrane, Mitochondrion

Muc13	Mucin-13	0,53*	0,69*	Cell membrane, Secreted
S100g	Protein S100-G	2,08**	1,28	Apical and basolateral cell membrane, Cytoplasm, Secreted
Sycn	Syncollin	2,97***	1,43*	Peripheral membrane protein
Ppfia3	Liprin-alpha-3	2,28*	1,95**	Cytoplasm
Hmgb2	High mobility group protein B2	1,13	1,42*	Nucleus, Cytoplasm, Secreted
Nlrp6	NACHT, LRR and PYD domains-containing protein 6	0,28***	0,64*	Nucleus, Cell membrane, Cytoplasm,
Prkg2	cGMP-dependent protein kinase 2	0,43*	0,74	Apical cell membrane
Hnrnpm	Heterogeneous nuclear ribonucleoprotein M	0,41**	0,81	Nucleus
Reg3b	Regenerating islet-derived protein 3-beta	0,64	1,77*	Secreted
Acat2	Acetyl-CoA acetyltransferase	1,45	1,48*	Cytoplasm
Bdh1	D-beta-hydroxybutyrate dehydrogenase	0,26****	0,49***	Mitochondria
Bdh2	3-hydroxybutyrate dehydrogenase type 2	2,06*	1,69**	Cytoplasm
Hmgcs1	Hydroxymethylglutaryl-CoA synthase,	1,82	2,25****	Cytoplasm
Hmgcs2	Hydroxymethylglutaryl-CoA synthase	0,49*	0,82	Mitochondria
Crp	C-reactive protein	0,95	0,24****	Secreted
Tmem43	Transmembrane protein 43	1,91*	1,19	Nucleus, ER
Pacs1	Phosphofurin acidic cluster sorting protein 1	0,39*	0,55**	Golgi apparatus
Mrc2	C-type mannose receptor 2	2,14	0,82	Cell membrane

Reep6	Receptor expression-enhancing protein 6	0,17****	0,70	ER
Itsn1	Intersectin-1	0,46*	0,71	Cell junction, Cell membrane, Cell projection, Coated pit, Cytoplasm, Nucleus, Endosome
Snap91	Clathrin coat assembly protein AP180	2,62*	1,27	Cell membrane, Coated pit
Clta	Clathrin light chain A	0,48*	0,51***	Coated pit, Cytoplasm, Cytoskeleton
Ldlr	Low-density lipoprotein receptor	1,68	1,98***	Golgi apparatus, Endosome, Lysosome, Cell membrane

*P<.05, **P<.01, ***P<.001, ****P<.0001

Table S 2. **Atp7b knockout induces changes in the abundance of proteins directly linked to intestinal lipid metabolism in WD rats**

Gene Symbol	Description	Abundance ratio (*Atp7b* $^{-/-}$/ *Atp7b* WT)	Abundance ratio (*Atp7b* $^{-/-}$ diseased / *Atp7b* WT)	Cellular localization
Apoe	Apolipoprotein E	0,37*	0,27****	Secreted, Chylomicrons
Apoa4	Apolipoprotein A-IV	0,30****	0,50****	Secreted, Chylomicrons
Apoa1	Apolipoprotein A-I	0,59	0,72*	Secreted, HDL
Apoa2	Apolipoprotein A-II	0,21***	0,30****	Secreted, HDL
Apom	Apolipoprotein M	0,79	0,36**	Secreted, HDL
C3	Complement C3	1,49	0,47****	Secreted
C4	Complement C4	1,33	0,67*	Secreted
Tf	Serotransferrin	1,55	0,70*	Secreted
Cyp51a1	Lanosterol 14-alpha demethylase	2,23*	3,52****	ER, Cell membrane, Microsome
Fdft1	Squalene synthase	1,78	3,03****	ER, Cell membrane
Hpx	Hemopexin	1,46	0,71*	Secreted
Gc	Vitamin D-binding protein	1,50	0,62*	Secreted
A1bg	Alpha-1B-glycoprotein	0,61	0,08****	Secreted
Ahsg	Alpha-2-HS-glycoprotein	1,07	0,69*	Secreted
Clu	Clusterin	1,14	1,84***	Secreted, Nucleus, Mitochondria, Cell membrane, ER, Cytoplasm
Apoh	Beta-2-glycoprotein 1	1,53	0,63*	Secreted
Serpina1	Alpha-1-antiproteinase	0,34**	0,33****	Secreted
Ambp	Protein AMBP	1,17	0,49**	Secreted, Mitochondria, Cell membrane, ER, Cytoplasm
Orm1	Alpha-1-acid glycoprotein	1,85*	1,71**	Secreted
Ldlr	Low-density lipoprotein receptor	1,68	1,98***	Golgi apparatus, Endosome, Lysosome, Cell membrane

*P<.05, **P<.01, ***P<.001, ****P<.0001

Table S 3. **Atp7b knockout induces changes in the abundance of proteins directly linked to mitochondrion metabolism and cell-cell adhesion in Caco-2 cells.**

Gene Symbol	Description	Abundance ratio (Caco-2 KO / Caco-2 WT)	Cellular localization
Energy metabolism – Glycolysis/Gluconeogenesis and Lipid processing			
HK1	Hexokinase-1	1,69*	Mitochondrion, Cytosol
HKDC1	Hexokinase HKDC1	1,68*	Mitochondrion
PCK2	Phosphoenolpyruvate carboxykinase [GTP]	0,56**	Mitochondrion
SORD	Sorbitol dehydrogenase	0,40****	Mitochondrion
GLUD1	Glutamate dehydrogenase 1	0,33****	Mitochondrion, ER
THEM4	Acyl-coenzyme A thioesterase THEM4	3,74***	Mitochondrion, Cell membrane, Cytoplasm
ACADVL	Very long-chain specific acyl-CoA dehydrogenase	1,87**	Mitochondrion
ACOT13	Acyl-coenzyme A thioesterase 13	0,64*	Mitochondrion, Nucleus, Cytosol, Cytoskeleton
ACAA2	3-ketoacyl-CoA thiolase	0,61*	Mitochondrion
ACSL1	Long-chain-fatty-acid--CoA ligase 1	0,60*	Mitochondrion, ER, Peroxisome
HMGCS2	Hydroxymethylglutaryl-CoA synthase	0,50**	Mitochondrion
AMACR	Alpha-methylacyl-CoA racemase	0,48**	Mitochondrion, Peroxisome
SCP2	Sterol carrier protein 2	0,47***	Mitochondrion, ER, Peroxisome, Cytoplasm
ACADSB	Short/branched chain specific acyl-CoA dehydrogenase	0,43**	Mitochondrion
ACSS1	Acetyl-coenzyme A synthetase 2-like	0,40***	Mitochondrion
CPT1a	Carnitine O-palmitoyltransferase 1	0,39**	Mitochondrion

DECR1	2,4-dienoyl-CoA reductase	0,36****	Mitochondrion
CRAT	Carnitine O-acetyltransferase	0,35***	Mitochondrion, ER, Peroxisome
Tight-junctions			
OCLN	Occludin	0,65*	Cell membrane, TJ
CLDN4	Claudin-4	0,41**	Cell membrane, TJ
VASP	Vasodilator-stimulated phosphoprotein	0,61*	Cell membrane, cytoplasm, cytoskeleton, TJ

*P<.05, **P<.01, ***P<.001, ****P<.0001

Table S 4. **Results on the regulation of metallothioneins, copper and zinc content, in liver and intestine of LEC rats supplemented with zinc.**

			Parameters				
Groups	**Duration**	**Dose of Cu/Zn**	**Metallothioneins**	**Copper**	**Zinc**	**Conclusions**	**Publication**
LEC I - Zinc-diet (N=32); LEC II - Normal diet (N=32); LE III - Zinc diet (N=16); LE IV - normal diet (N=16)	6, 8, 10, 12 or 18 wks	Normal diet: 70 ppm; Zn diet: 1000 ppm	**Hepatic**			In LEC fed a zinc diet there was a delay in the onset of acute hepatitis and shorter time needed for recovery.	Gonzalez *et al.*[326]
			LEC II/LEC I: Strong immunostaining after 12 wks; hepatic Cu and Zn was associated with the MT fraction in LEC rats (12 and 20 wks)	LEC I : ↑ Cu at 12 wk; ↓ Cu at 18 and 20 wk); LEC II: no changes	LE III and IV: 25 µg/g ww. LEC I: 81± 3 µg/g ww (12 wks); LEC II: 61±8 µg/g ww (12 wks);		
			Intestinal				
			LEC I: ↑ 20 wks; LEC II: ↓ at 20 wks. Hepatic Cu and Zn associated with the MT fraction in LEC rats (12 wks)	LEC I : 10 ± 5 µg/g at 12 wks; LEC II: 6 ± 1 µg/g at 12 wks	LEC I : 26 ± 1 µg/g at 12 wks; LEC II: 26 ± 7 µg/g at 12 wks		
Treated 1 wk (T1)/Treated 2 wks (T2) (N=8); Untreated 1 or 2 wks (U1/U2) (N=5)	1 wk or 2 wks (80 mg zinc acetate in 2% glucose solution) by g. d.	Normal diet: 11.7 mg Cu/kg and 67.5 mg Zn/kg; Zn diet: plus 80 mg daily	**Hepatic**			In LEC fed a zinc diet: ↑ of Zn and MT tissue content, and a ↓ of Cu was observed in the liver and intestine.	Medici *et al.*[327]
			↑ at 1 wk, ↓ at 2 wks	U2 vs.T2 : ↓	↑ at 1 and 2 wks T1 vs.T2 : ↓		
			Intestinal				
			↑ at 1 and 2 wks	↓ at 1 wk	U1 vs T1: ↓ U2 vs T2: ↑		
Controls: 1 wk (N=8) or 2 wks (N=8); Treated: 8 wks (N=13).	1 or 2 wks (80mg/ml), or 8 wks (50mg/ml), in 2% glucose	Normal diet: 11.7 mg Cu/kg and 67.5 mg Zn/kg; Zn diet:	**Hepatic**			In LEC fed a zinc diet, it was observed a prevention of acute hepatitis onset. MT concentrations were	Medici *et al.*[273]
			A positive correlation between zinc and MT was found in the liver of Zn-treated rats after 1,2 and 8 wks	↓ in the treated group for all time points	↑ in the treated group for all time points		

	solution) by g. d.	plus 80 or 50 mg/ml daily	**Intestinal**			higher in all the organs studied after 8 wks	
				↓ in the treated group	↑ in the treated group		
Controls (N=10), 1 wk treatment (N=8), 2 wks treatment (N=8)	1 or 2 wks (80 mg/ml) by g. d.	Normal diet: 11.7 mg Cu/kg and 67.5 mg Zn/kg; Zn diet: plus 80 mg/ml daily	**Hepatic**			In LEC fed a zinc diet, tissue Zn and MT content was ↑ and Cu ↓ in the liver and kidneys. ↓ Zn with all treatments	Santon *et al.*[328]
			2 fold ↑ at 1 wk; 2 wks: no significant differences.	No significant differences after 1 wk. After 2 wks, Cu levels were 0.3 fold ↓	↑ in treated group for all time points, but a ↓ was observed from the 1st to the 2nd wks		
Controls (N=13), 8 wks treatment (N=13), Basal group (N=4)	8 wks (50mg/ml zinc acetate in 2% glucose solution) by g. d.	Normal diet: 11.7 mg Cu/kg and 67.5 mg Zn/kg; Zn diet: plus 80 mg/ml daily	**Hepatic**			In LEC fed a zinc diet, tissue Zn and MT content was ↑ and Cu and Fe ↓ in all organs. ↓ Oxidative stress and liver damage	Santon *et al.*[329]
			↑ in the treated group	↓ in the treated group	Not a significant difference		
			Intestinal				
			↑ in the treated group	Not a significant difference	Not a significant difference		
Controls (N=13), 8 wks treatment (N=13), Basal group (N=4)	8 wks (50mg/ml zinc acetate in 2% glucose solution) by g. d.	Normal diet: 11.7 mg Cu/kg and 67.5 mg Zn/kg; Zn diet: plus 80 mg/ml daily	MT-1 mRNA was ↑ with Zn treatment, with a 1.3 fold ↑ expression in comparison to untreated.	↓ Cu levels in the Zn-treated group	Hepatic Zn levels were ↑ 1.25-fold	In LEC fed a zinc diet, ↑ Zn and MT tissue content in the liver.	Santon *et al.*[330]

Cu: copper; Zn: zinc; MT: metallothioneins; wks: weeks; g.d: gavage daily; ↑ increase; ↓ decrease

7.2 Proof of licence for Figures 2 and 3

This Agreement between Helmholtz Zentrum München, Deutsches Forschungszentrum für Gesundheit und Umwelt (GmbH) -- Adriana Filipa Fontes ("You") and John Wiley and Sons ("John Wiley and Sons") consists of your license details and the terms and conditions provided by John Wiley and Sons and Copyright Clearance Center.

License Number - 5437560604242

Licensed Content Publisher - John Wiley and Sons

Licensed Content Publication - European Journal of Clinical Investigation

Licensed Content Title - Mushrooms on the plate: Trends towards NAFLD treatment, health improvement and sustainable diets

Portions - Figure 1 and Figure 2